

Dye-sensitized solar cells: Detailed studies focused on the molecular engineering of D-π-A dyes and the optimization of the application of ionic-liquid-based electrolytes

THÈSE N° 5824 (2013)

PRÉSENTÉE LE 5 JUILLET 2013

À LA FACULTÉ DES SCIENCES DE BASE
LABORATOIRE DE PHOTONIQUE ET INTERFACES
PROGRAMME DOCTORAL EN CHIMIE ET GÉNIE CHIMIQUE

ÉCOLE POLYTECHNIQUE FÉDÉRALE DE LAUSANNE

POUR L'OBTENTION DU GRADE DE DOCTEUR ÈS SCIENCES

PAR

Magdalena Anna MARSZALEK

acceptée sur proposition du jury:

Dr R. Hovius, président du jury
Prof. M. Graetzel, Dr S. M. Zakeeruddin, directeurs de thèse
Prof. J. Augustynski, rapporteur
Prof. A. Hagfeldt, rapporteur
Prof. K. Sivula, rapporteur



ÉCOLE POLYTECHNIQUE
FÉDÉRALE DE LAUSANNE

Suisse
2013

Study the Science of Art. Study the Art of Science.
Develop your senses - learn how to see.
Realize that everything connects with everything else.

— Leonardo da Vinci

Abstract

Dye-sensitised solar cells (DSCs) are the hybrid inorganic-organic photovoltaic devices, gaining recently much interest in academic and industrial communities. At the heart of the device there is a mesoporous nanoparticulate semiconductor layer made of titanium dioxide, which serves as a large-surface area support for the dye molecules that absorb the light. From a scientific point of view it is an enthralling system to investigate, optimize and develop. The device comprises of various materials and each of the components can be designed, fabricated and explored individually. Nonetheless, it has to be pointed out, that crucial for the device is the interplay between them. Commercialisation of the DSCs is already taking place. It is not surprising, because among all the emerging photovoltaic technologies this one is the least expensive and most efficient. Additionally, the materials used in the product are abundant and relatively non-toxic. The fabrication process is easy and can be easily automatized and upscaled.

The work presented in this thesis is focused on the application of the organic dyes in DSCs. The most common scheme, consisting of a donor, a π -conjugated bridge and an acceptor/anchoring unit (D- π -A), was employed for the studied molecules. The importance and role of particular building blocks was studied on the examples of 2,1,3-benzothiadiazole (BTDA) in a spacer group, phenyl and ethylenedioxythiophene (EDOT) in double anchoring configurations, and phenothiazine and carbazole as donors. One small part is devoted to the modification of the formula of the ionic-liquid based electrolytes.

Benzothiadiazole was found to be of particular interest in the design of highly efficient dyes due to the broadening the UV-Vis absorption spectrum. It was discovered that the place of this unit within the molecule is important, because too close proximity to the anchoring group led to unwanted back-electron transfer reaction. An additional phenyl ring, which introduced a torsion angle, proved to be a remedy for this issue. Building upon that, a D-A- π -A system

Abstract

with BTDA properly placed was further presented, where the dye aggregation problem was investigated and solved by the introduction of hexyl chains on the thiophene bridge.

Structure-property relations were scrutinised using the series of phenothiazine sensitizers. The optical properties of the molecules were tuned by increasing the length of the π -conjugation - from one double bond through 2,2'-bithiophene to 4H-cyclopenta[2,1-b:3,4-b]dithiophene (CPDT). It was found that the bithiophene-bearing molecule yielded the highest photocurrents, but suffered from a low open-circuit voltage. Alkyl-substituted CPDT solved this issue, however, a synergy effect was not obtained, because the current densities obtained for that molecule were lower due to the narrower absorption spectrum.

A set of dyes with two anchoring groups was investigated and tested for photovoltaic application. It was interesting to realize that these molecules indeed bind to the surface using both anchoring groups. The proof first was calculated theoretically and displayed via the minimum-energy structures, and later on shown experimentally, with Fourier Transform Infrared Spectroscopy (FTIR) measurements.

Finally, a study on the influence of the anions in ionic-liquid based electrolytes was conducted. 1-ethyl-3-methylimidazolium tetracyanoborate was replaced by various cations (derivatives of pyridinium, pyrrolidinium and triethylpropylammonium) either with tetracyanoborate or tricyanomethanide. Electrolytes with tricyanomethanide were less viscous than their tetracyanoborate counterparts, which improved the photovoltaic performance. Moreover, the upward conduction band shift was detected for the tricyanomethanide-containing devices, mainly attributed to its facilitated partial adsorption and suppression of the interfacial charge-transfer.

All the above presented concepts and their realisations made valuable contributions to the DSC field. The studies presented hereby are comprehensive and elegant examples of careful, logically planned scrutiny leading to a deeper understanding of the processes within the DSC. The extensive use of many different investigating techniques and the successful combination of obtained results allowed for drawing important conclusions upon which the base for further optimisation of DSCs may be built.

Keywords: Photovoltaics, dye-sensitized solar cells, organic sensitizers, donor-pi-acceptor systems, structure-property relation, benzothiadiazole, indoline, phenothiazine, carbazole, ionic liquids, tricyanomethanide, electron recombination

Zusammenfassung

Die Farbstoffsolarzelle - auch Grätzel-Zelle genannt - ist eine neuartige Photovoltaik-Technologie die seit ihrer Entdeckung Anfang der neunziger Jahre, sowohl im akademischen als auch industriellen Bereich viel Aufsehen erregt hat. Das Kernstück einer solchen Solarzelle ist eine nanoporöse Schicht eines partikelförmigen Halbleiters, z.B. TiO₂, auf dessen Oberfläche ein licht-absorbierender Farbstoff adsorbiert wird.

Die vorliegende Arbeit befasst sich mit neuen, organischen Farbstoffen und deren Anwendung in der Farbstoffsolarzelle. Das meistverwendete Strukturkonzept für den Aufbau solcher Farbstoffe ist das sogenannte D- π -A Konzept, welches grundsätzlich auf drei Elementen basiert: Einer Donor-Einheit (D), einer π -konjugierte Brücke und einer Akzeptor-Einheit (A), die gleichzeitig als Ankergruppe dient. Im speziellen wurde in dieser Arbeit der Einfluss folgender Struktureinheiten näher untersucht: 2,1,3-Benzothiadiazol (BTDA) als Teil der π -Brücke, Phenyl und 3,4-Ethylendioxythiophen (EDOT) als Teil der π -Brücke in Farbstoffen mit zwei Ankergruppen und schließlich Phenothiazin und Carbazol als Donor Gruppen. Ein weiteres Kapitel befasst sich mit der Optimierung von Elektrolyten auf Basis ionischer Flüssigkeiten. BTDA hat sich als besonders interessanter Baustein für die Entwicklung hocheffiziente Farbstoffe herausgestellt, da die Verwendung von BTDA zu einer Verbreiterung des Absorptionspektrums führte. Es zeigte sich, dass die genaue Position der BTDA Einheit im Farbstoffmolekül eine entscheidende Rolle spielt. Der Einsatz von BTDA in direkter Nähe zur Ankergruppe führte zur unerwünschten Rekombination zwischen Elektronen im TiO₂ und dem oxidierten Farbstoff. Dieses Problem konnte jedoch durch das Einfügen eines zusätzlichen Phenylrings behoben werden. Auf Basis dieses Konzept wurde eine weiteres Farbstoffsysteem mit dem Aufbau D-A- π -A untersucht. Ein hierbei auftretendes Problem – die verstärkte Aggregation der Farbstoffmoleküle - wurde genauer untersucht und letztendlich durch den Einsatz langer Alkylketten an der Thiophen-Brücke behoben.

Abstract

Eine weitere Struktur-Eigenschafts-Beziehung wurde anhand einer Serie von Phenothiazin-basierten Farbstoffen entwickelt. Die optischen Eigenschaften der Farbstoffe wurden durch den Einsatz unterschiedlich langer π -Brücken, namentlich Thiophen, 2,2'-Bithiophen sowie 4H-Cyclopenta[2,1-b:3,4-b']dithiophen (CPDT) variiert. Es zeigte sich, dass Solarzellen auf Basis des 2,2'-Bithiophen Farbstoffes die höchsten Photoströme erreichten aber unter einer geringen Leerlaufspannung litten. Letztere konnte durch die Verwendung von Alkyl-substituiertem CPDT erhöht werden, auch wenn eine synergetischer Effekt aufgrund des schmäleren Absorptionspektrums und dem daraus resultierenden, niedrigeren Photostrom nicht erreicht werden konnte.

Im Weiteren wurde eine Reihe von Farbstoffen mit zwei Ankergruppen untersucht und für die Herstellung von Farbstoffsolarzellen verwendet. Es konnte gezeigt werden, dass diese Art von Farbstoff in der Tat gleichzeitig mit beiden Ankergruppen an die Oberfläche des TiO₂ bindet. Die entsprechende Adsorptionsgeometrie wurde zunächst theoretisch berechnet und anschließend mit Hilfe von Fourier-Transform Infrarotspektroskopie experimentell bestätigt. Der letzte Teil der Arbeit befasst sich mit Elektrolyten auf Basis von ionischen Flüssigkeiten und im speziellen dem Einfluss des Anions der ionischen Flüssigkeit auf die Effizienz der Solarzelle. Im Vergleich zu Tetracyanoborat waren Elektrolyte mit Tricyanomethanid als Anion weniger viskos was in einer höheren Effizienz der Solarzellen resultierte. Weiterhin konnte im Falle von Tricyanomethanid eine Verschiebung des TiO₂ Leitungsbandes beobachtet werden, ein Effekt der auf die partielle Adsorption der Spezies der ionischen Flüssigkeit an der TiO₂ Oberfläche zurückzuführen war.

Die oben genannten Konzepte sowie deren Realisierung stellen einen wichtigen Fortschritt auf dem Gebiet der Farbstoffsolarzellen dar. Die vorgestellten Studien sind elegante und umfassende Beispiele für sorgfältig geplante Untersuchungen die zu einem besseren Verständnis der verschiedenen elektronischen Prozesse in der Farbstoffsolarzelle beitragen. Die umfangreiche Nutzung verschiedenster experimenteller Methode sowie die erfolgreiche Kombination der Ergebnisse erlaubte es wichtige Schlüsse zu ziehen, die eine vielversprechende Basis für die weitere Optimierung der Farbstoffsolarzelle darstellen.

Schlüsselwörter: Photovoltaik, Farbstoffsolarzelle, Organischer Farbstoff, Donor-pi-Akzeptor System, Struktur-Eigenschafts-Beziehung, Benzothiadiazol, Indolin, Phenotiazin, Carbazol, Ionische Flüssigkeit, Tricyanomethanide, Elektron-Loch-Rekombination

Contents

| | |
|---|-----------|
| Abstract (English/Deutsch) | v |
| 1 Introduction | 1 |
| 2 Fundamentals of dye-sensitized solar cells | 5 |
| 2.1 Harnessing the Sun: the photovoltaic effect | 5 |
| 2.2 Evolution of photovoltaic systems | 7 |
| 2.3 The concept of dye-sensitized solar cell | 11 |
| 2.3.1 The architecture of a dye-sensitized solar cell and its components. | 12 |
| 2.3.2 DSC's principles of operation | 16 |
| 2.4 Theoretical background of the processes within the devices and characterization methods | 20 |
| 2.4.1 J-V curves | 21 |
| 2.4.2 Quantum Efficiencies: IPCE and APCE | 24 |
| 2.4.3 Transient experiments | 26 |
| 2.4.4 Impedance Spectroscopy as a tool of the complex characterization of DSCs | 34 |
| 2.5 Bibliography | 42 |
| 3 Experimental methods | 47 |
| 3.1 UV-Vis spectroscopy, dye loading experiments | 47 |
| 3.2 Electrochemistry | 48 |
| 3.3 Viscosity measurements | 49 |
| 3.4 Fourier Transformed Infrared Spectroscopy | 49 |
| 3.5 Device fabrication | 50 |
| 3.6 Photovoltaic characterization | 53 |

Contents

| | |
|--|-----------|
| 3.7 External quantum efficiency - IPCE | 54 |
| 3.8 Transient photocurrent/photovoltage measurements | 54 |
| 3.9 Fluorescence spectroscopy and Time-correlated Single Photon Counting | 55 |
| 3.10 Photoinduced Absorption Spectroscopy | 56 |
| 3.11 Electrochemical Impedance Spectroscopy | 56 |
| 3.12 Bibliography | 58 |
| 4 The influence of the structural modifications of D-π-A dyes containing benzothiadiazole as a spacer. | 59 |
| 4.1 Introduction | 59 |
| 4.2 Preliminary studies with thieno[3,2-b]thiophene, bithiophene and biselenophene as bridging units | 60 |
| 4.2.1 Synthesis and characterization of the dyes | 60 |
| 4.2.2 Application in DSCs | 65 |
| 4.3 The effect of phenyl ring inserted between the benzothiadiazole and cyanoacrylic acid | 68 |
| 4.3.1 Synthesis and characterization of the phenyl-bearing dye | 68 |
| 4.3.2 Quantum chemical calculations | 70 |
| 4.3.3 Application in DSC | 74 |
| 4.3.4 Detailed investigation: transient measurements, laser study and EIS | 77 |
| 4.4 Conclusions | 83 |
| 4.5 Bibliography | 84 |
| 5 Molecular engineering on D-A-π-A dyes featuring indoline donor and benzothiadiazole bridge. | 85 |
| 5.1 Introduction | 85 |
| 5.2 Synthesis and characterization of the dyes WS-2 and WS-9 | 87 |
| 5.2.1 Design and synthesis | 87 |
| 5.2.2 Optical and redox properties | 89 |
| 5.2.3 Theoretical calculations | 90 |
| 5.2.4 The effect of an additional acceptor on the optical properties of the deprotonated form of the dye | 94 |

| | |
|---|------------|
| 5.3 Optimization of the photovoltaic performance | 96 |
| 5.3.1 General PV characterization including the effects of the dye-bath solvent and coadsorbents | 96 |
| 5.3.2 Apparent electron lifetime and electrochemical impedance spectroscopy | 101 |
| 5.3.3 Stability of the dyes and the devices | 102 |
| 5.4 Conclusions | 104 |
| 5.5 Bibliography | 105 |
| 6 Donor-π-Acceptors containing a 10-(1,3-dithiol-2-ylidene)anthracene unit for dye-sensitized solar cells. | 109 |
| 6.1 Introduction | 109 |
| 6.2 Synthesis and characterization of the dyes | 111 |
| 6.2.1 Synthetic route | 111 |
| 6.2.2 Optical and electrochemical properties | 112 |
| 6.3 Theoretical calculations | 114 |
| 6.3.1 Geometry of the molecules | 114 |
| 6.3.2 The character of the molecular orbitals | 117 |
| 6.4 Dye adsorption and photovoltaic performance | 120 |
| 6.4.1 Adsorption of the two-anchor dyes | 120 |
| 6.4.2 General PV characterization | 121 |
| 6.4.3 Charge recombination problem | 123 |
| 6.5 Conclusions | 125 |
| 6.6 Bibliography | 126 |
| 7 Tuning the photovoltaic performance of the D-π-A dyes with a phenothiazine and carbazole donor in dye-sensitized solar cells. | 129 |
| 7.1 Introduction | 129 |
| 7.2 Synthesis and characterization of the dyes V5, V7, V11 and V4 | 130 |
| 7.2.1 Chemical synthesis of the dye molecules | 130 |
| 7.2.2 Optical properties | 132 |
| 7.2.3 Electrochemistry - experimental determination of HOMO/LUMO | 133 |
| 7.2.4 Quantum chemical calculations | 134 |

Contents

| | | |
|-------------------------|---|------------|
| 7.3 | Evaluation of the photovoltaic performance | 135 |
| 7.3.1 | Overall photovoltaic characterization | 135 |
| 7.3.2 | IPCE comparison | 137 |
| 7.4 | Controlling the TiO ₂ interface - recombination rate and conduction band shift | 139 |
| 7.4.1 | V5-V7 comparison | 139 |
| 7.4.2 | Introduction of CPDT with alkyl side-chains | 141 |
| 7.4.3 | Electrochemical impedance study | 141 |
| 7.5 | Conclusions | 143 |
| 7.6 | Bibliography | 144 |
| 8 | Application of ionic liquids containing tricyanomethanide [C(CN)₃]⁻ or tetracyano-borate [B(CN)₄]⁻ anions in dye sensitized solar cells. | 147 |
| 8.1 | Introduction | 147 |
| 8.2 | Synthesis and characterization of ionic liquids | 148 |
| 8.2.1 | Synthetic route | 148 |
| 8.2.2 | Crystallography | 150 |
| 8.3 | Photovoltaic application evaluation | 151 |
| 8.3.1 | Electrolyte formulation and characterization | 151 |
| 8.3.2 | Photovoltaic performance | 153 |
| 8.3.3 | Conduction band shift induced by the counter-anions in the electrolyte | 155 |
| 8.4 | Conclusions | 156 |
| 8.5 | Bibliography | 156 |
| 9 | Summary and final conclusions | 161 |
| 9.1 | Bibliography | 165 |
| Acknowledgements | | 167 |
| Curriculum Vitae | | 171 |

1 Introduction

The herein presented PhD thesis entitled "Dye sensitized solar cells: detailed studies focused on the molecular engineering of D- π -A dyes and the optimization of the application of ionic-liquid-based electrolytes" is a composition of diverse studies conducted on different molecules - dyes and ionic liquids - with an aim not only to improve, but rather understand and predict the directions of the strategies leading to high-efficient and stable dye-sensitized solar cells.

The thesis starts with a general chapter entitled **Fundamentals of dye-sensitized solar cells**. In this chapter, first I would like to guide the reader through the basic ideas of capturing the solar energy and transforming it into electricity. Then I would like to provide the general overview of the current photovoltaic technologies and briefly mention the state-of-the-art concepts. Further, I would like to invite the reader to the fascinating world of dye-sensitized solar cells - the main subject of this work. I will present the device and the way it operates, and in the end I will introduce the more in-depth, theoretical description of the phenomena within the cell. This chapter will also provide the necessary foundations not only for the device's investigation methods, but also for understanding its elegance and beauty.

In the second chapter, **Experimental methods**, I would like to gather and present all methods that I personally used in this work. Most of the procedures apply to all of the following chapters (e.g. DSC characterization, EIS measurements), however, specified protocols will be indicated and presented for the cases that required special treatment. All of the used dyes^a

^aexcept the dye Z907

Chapter 1. Introduction

were synthesized by the collaborators and the synthetic routes are described in details in the relevant publications. Quantum chemical calculations details, as well as the ultrafast laser measurements' methodologies are provided also in the corresponding publications.

The results part could be in principle divided into two asymmetrical parts. The main interest of the thesis is put on the molecular engineering of organic D- π -A dyes. Four chapters are covering studies done on different molecules where the focus is put either on the π -bridge and its modifications, or anchoring groups. Last chapter in the results part, **Chapter 8**, describes the study on optimization of the ionic-liquid-based electrolytes in DSCs, focusing on the comparison between the tetracyanoborate and tricyanomethanide as counterions of the salt used in the formula.

Chapter 4 contains the study on the dyes incorporating benzothiadiazole (BTDA) in the conjugated bridge. In principle, this group extends the absorption spectrum to the long wavelengths. Nonetheless, when it was put directly next to the anchoring group, the photovoltaic performance was not satisfying. A subtle structural modification, namely the separation of BTDA from anchoring group by a phenyl ring, changed the geometry of the dye cation and the geometry of the frontier orbitals. The nature of the problem was resolved and explained using EIS and ultrafast laser spectroscopy. It is now clear why the proper spacing is required when BTDA unit is to be incorporated in the dye structure.

The concept proved in the **Chapter 4** was then applied in the next project, where in turn the dye aggregation was studied on the molecules with D-A- π -A architecture (BTDA was the extra acceptor next to the donor). The main modification, though, was the grafting of the hexyl chain on the thiophene-bridging unit. The influence of the solvent and the effect of the coadsorbent (chenodeoxycholic acid) was investigated thoroughly. Obtained results confirmed the impact of the solvent on the dye behaviour in the solution and further justified the use of a coadsorbent as beneficial in terms of photocurrent generation due to reducing the unwanted dye-dye interactions.

The improvement of stability could be realized via introducing more than one anchoring group in order to increase the binding strength of the molecule. A set of dyes with exTTF donors was equipped with two π -bridges with anchoring groups and the study is demon-

strated in the **Chapter 6**. It was calculated that the optimal geometry of minimal energy for these molecules would allow for grafting onto the surface via both anchors. This theoretical conclusion was then cross-checked with FTIR and the molecules were subjected to the photovoltaic evaluation.

Last chapter devoted to the dyes, **Chapter 7**, includes the work done on the molecules equipped with a phenothiazine donor. The optical properties of the dyes were tuned by introducing bridges with increasing degree of conjugation. The new molecules were characterized spectroscopically and electrochemically and employed as sensitizers in DSC.

The thesis is summarized and concluded in the final **Chapter 9**.

2 Fundamentals of dye-sensitized solar cells

2.1 Harnessing the Sun: the photovoltaic effect

The Sun - our nearest star - is by far the most abundant source of energy. However, it has been merely 200 years since it was realized that it can be used to create the electricity. It is also rather sad to realize that this potential still cannot be efficiently used today and majority of the power being generated nowadays is based on the non-renewable sources like oil and coal.

Solar radiation. It has been roughly estimated that the amount of solar energy reaching the Earth's surface every hour could satisfy the whole yearly planet's energy need! The Sun can be perceived as a black-body (an ideal diffuse emitter), emitting at $T \approx 5500$ K following the Planck's law^a. Its spectrum is very broad, stretching out from the X-rays up to the radio waves with the peak at 525 nm (2.36 eV). Nevertheless, the main fraction of the wavelengths lies between 100 nm and 1 mm - where half of the light is in the infrared region (which makes our planet warm and habitable for most of the known life forms), 40% is visible light and 10% is the ultraviolet. The atmosphere, though, protects the planet's surface from the excessive high-energy radiation and affects the shape of the solar spectrum (Figure 2.1). The atmospheric extinction is caused mainly by three effects:

^aPlanck's law is an energy distribution which relates the spectral radiance, \mathbf{B} , with the temperature of the emitter at a given wavelength: $B_\lambda(T) = \frac{2hc^2}{\lambda^5} \frac{1}{\exp\left(\frac{hc}{\lambda k_B T}\right) - 1}$

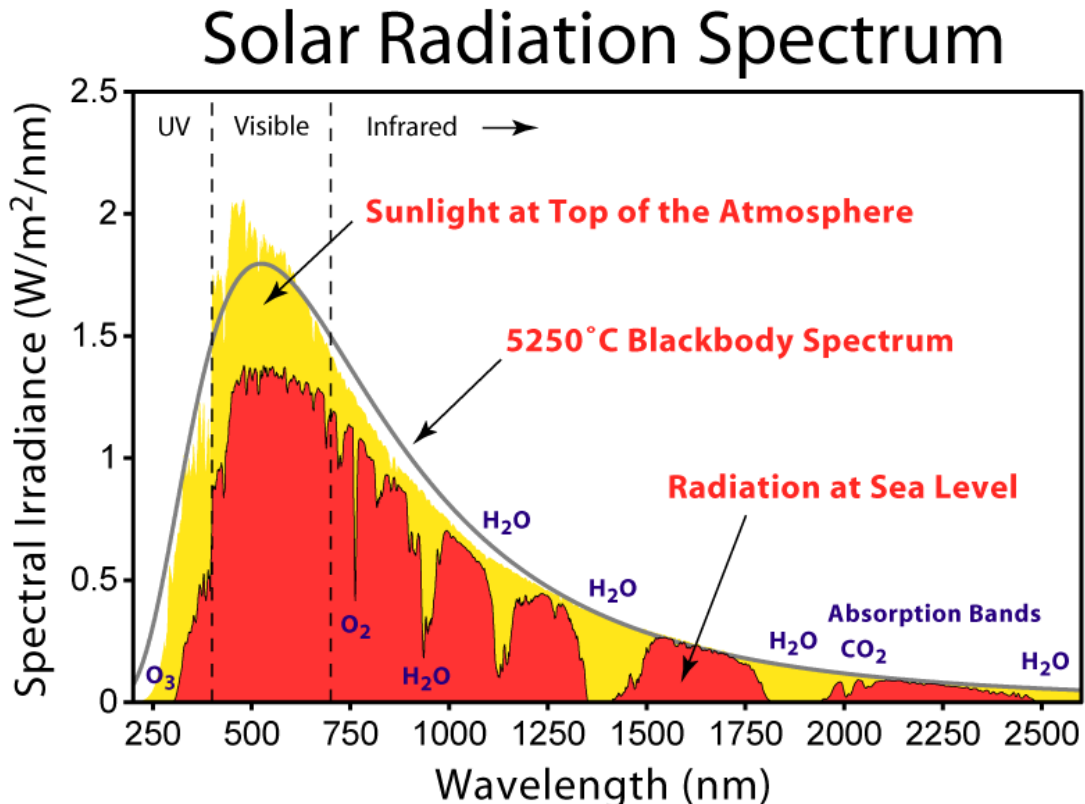


Figure 2.1: A comparison of a black-body radiation at 5250°C (solid grey line) with the solar irradiance spectrum at the top of the Earth's atmosphere (yellow) and after passing through the atmosphere (red). *The image was prepared by Robert A. Rhode and remains under the Creative Commons Attribution-Share Alike 3.0 Unported license.*

- Rayleigh scattering by air molecules (that is why the sky appears blue)
- scattering by aerosols, e.g. dust particles
- molecular absorption (termed also "telluric absorption") - water vapour, H₂O, CO₂, N₂O, O₂, CH₄ and fluorinated hydrocarbons which absorb in the infrared and ozone, O₃ that absorbs in the ultraviolet.

The attenuation depends on the path length (atmosphere thickness). The coefficient that defines this direct optical path length is called **air mass**, AM (Equation 2.1).

$$AM = \frac{l}{l_0} \approx \frac{1}{\cos z}, \quad (2.1)$$

where l_0 is path length normal to the Earth's surface at sea level and z is the zenith angle.

AM0 is then the value for the solar irradiation outside the atmosphere and AM1 is referred to the Sun shining directly overhead at the sea level ($z = 0^\circ$, the thickness of one atmosphere). Another very useful value is the AM1.5, which corresponds to the zenith angle of 48.2° . Most of the human habitats are situated at the latitudes where the Sun irradiation angle is close to that value (summer-winter variation, cloudy-sunny day variation), and in this way AM1.5 represents the overall yearly average solar irradiation. Therefore, it is an important indicator for photovoltaic measurements, where the sun simulators ought to resemble the solar spectrum as close as possible to the reality.

Photovoltaic effect. The photovoltaic effect was first observed and reported in 1839 by Alexandre-Edmond Bequerel - a silver coated platinum electrode immersed in the electrolyte generated photocurrent and photovoltage. This effect was widely studied later on, with the use of different materials (e.g. Se, copper-copper oxide films, PbS, Ti_2S). Today, the most popular solar cells are based on semiconductors and the so-called *p-n junction* (Figure 2.2). When two pieces of oppositely doped (*p* - positively, *n* - negatively) semiconductor are brought to an intimate contact (thermal equilibrium, no external bias) there is no net current flowing through the junction, however, there exist two balanced currents of the majority charge carriers induced by the diffusion. Since the Fermi levels in each type of the semiconductors are different, the flow of the majority charge carriers will lead to their equilibration and thus forming the difference in potential (*built-in potential*). The electric field will continue to grow (due to the displacement of charges and exposition of the stationary charges, i.e. dopants, impurities) and inhibit the current flow. The thin layer, where the majority charge carriers diffused out to the other side is called a *space-charge region*. Within this region, upon the photon absorption, an exciton is generated and then the effective separation of the charges occurs thanks to the electric field (the effect of the depletion of the majority charge carriers), allowing for the drift (Figure 2.3).

2.2 Evolution of photovoltaic systems

The first solar cell was constructed by Charles Fritts in 1883 (Se on Au layer), but was performing very, very poorly (< 1%). In the beginning of the next century, the golden era of quantum physics, mainly due to Max Planck's and Albert Einstein's efforts to understand the

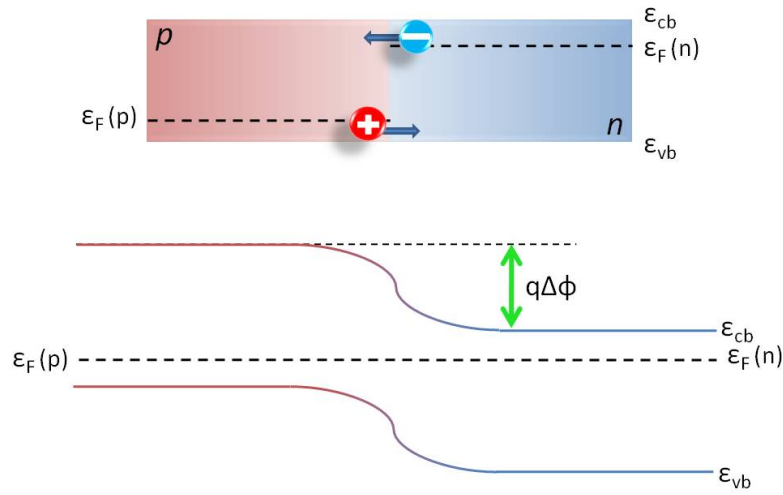


Figure 2.2: *Above:* n- and p-type semiconductors in contact. Majority charge carriers diffuse through the junction in the opposite directions - no net current is observed. *Below:* The creation of the uniform Fermi level throughout the material results in the generation of the built-in potential.

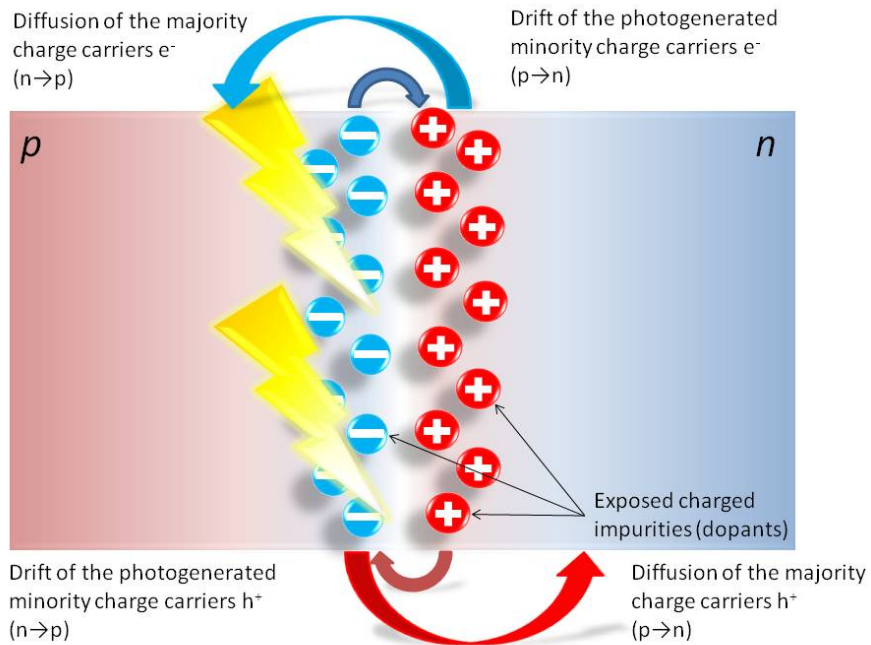


Figure 2.3: p-n junction after the absorption of a photon: the arrows show the types and directions of the currents flowing through the junction.

2.2. Evolution of photovoltaic systems

nature of light, the concept of conversion of the abundant and free sunlight to electricity was revisited. A Polish scientist, Jan Czochralski, developed a method to grow ultra pure crystals of semiconductors (mainly Si), which undoubtedly helped in constructing more efficient devices. However, the field started to blossom in 1950's when the first modern semiconductor cells based on the p-n junctions were constructed at Bell Laboratories. Then the "space-race" stimulated the research, as solar energy was found to be an ideal solutions for powering the satellites and the growing trend continued over the next two decades. Nowadays, when someone thinks about the solar cells, the first thing that comes to one's mind is the calculator powered by them - it was first introduced in 1978. Today solar cells are not only used to supply electricity to small portable devices, but whole power plants are being constructed in many places around the globe. Silicon solar cells are for now the leader in the market, but the researchers have many new materials, approaches and concepts how to stop wasting the free energy that is emitted by the Sun and reaching the Earth's surface in an efficient and cheap way. The current record efficiencies for all the technologies developed for solar conversion are presented in the Figure 2.4. The comments on the particular devices' groups are given below.

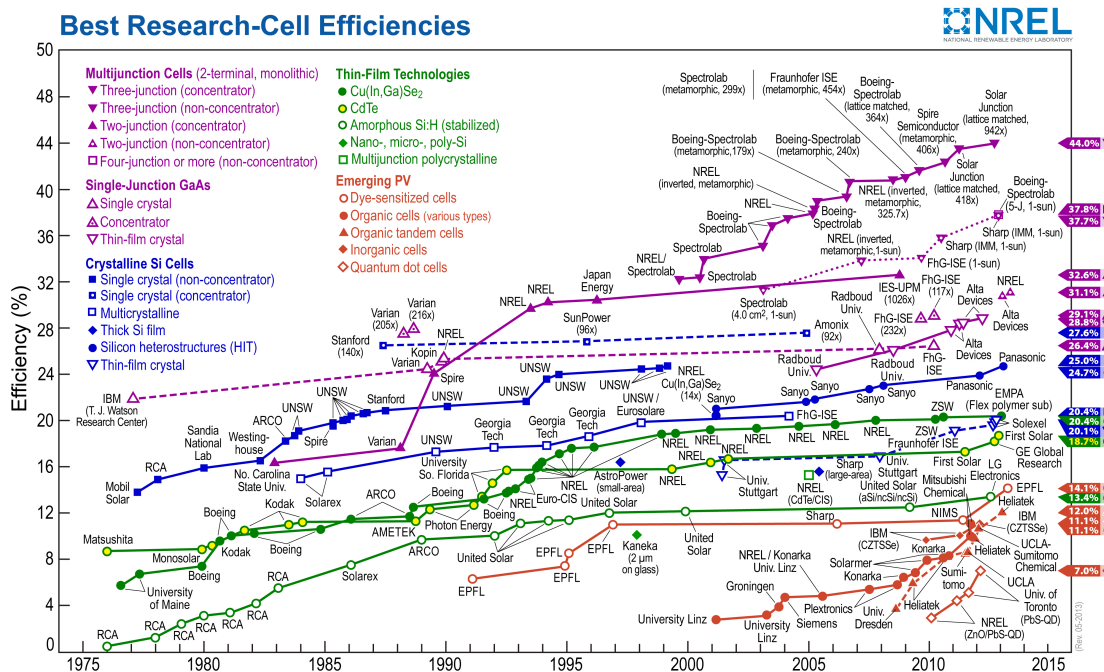


Figure 2.4: Research cell efficiency records. Source: National Renewable Energy Laboratory website www.nrel.gov/ncpv, 10.06.2013

Chapter 2. Fundamentals of dye-sensitized solar cells

Classic solar cells - Si, GaAs. Czochralski's method of growing large and pure single crystals allowed for fabrication devices of efficiencies (~ 25%) reaching almost the theoretical limit¹ (29% for a silicon solar cell, $E_g = 1.1$ eV)^b. Unfortunately, these cells are very expensive to fabricate, because the costs of the crystal growth and the subsequent material loss during the cutting of the ingots are too large. The solution would be the concept to use less pure multicrystalline Si, however the record efficiencies are much lower (20.4%). The more disordered structure provides more recombination channels, i.e. point defects, dislocations and grain boundaries. Up to date, the most efficient single crystal solar cell is made of GaAs with the efficiency reaching up to 26.4%. Due to the very high costs of production, this material is used almost exclusively for extraterrestrial applications.

Thin film technologies. In order to reduce the costs of the fabrication the new, natural concept of employing thinner, polycrystalline layers has emerged. The range of applicable materials has been expanded - apart from amorphous Si (a-Si) there is also CdTe, Cu(InGa)Se₂ (CIGS) or Cu₂ZnSn(SSe)₄ (CZTS). CIGS is an unquestionable leader among these technologies, reaching 20.4% efficiency. The bandgap of this materials is tunable and depends on the content of Ga (the bandgap varies from 1.04 eV (CuInSe₂) to 2.4 eV (CuGaSe₂)). A CdTe cell can convert solar energy with 18.3% efficiency. a-Si seems to be the less efficient material (only 13.4%), mainly because of the persisting problems with degradation after the exposure to light. The origin of this phenomenon is not very clear, however it may be related to the escape of hydrogen from the material, leading to dangling (unsaturated) bonds. The light accelerates this process and increase the density of the defects and, as a result, to the increase of the recombination current (Staebler-Wronski effect).

Emerging technologies. With the blossom of nanotechnology and material science in broad sense a few new approaches have entered the photovoltaics arena. A shift from crystalline semiconductors to polymers (and so-called *small molecules*) manifested itself in organic photovoltaic cells. The concept is based on the highly conjugated systems, of which HOMO and LUMO would form spatially distributed energy levels resembling a conduction and a valence band in a classic semiconductor. The record efficiency for these systems went up to

^b Shockley-Queisser limit is a theoretically estimated limit efficiency for a solar cell based on a single p-n junction, derived on the thermodynamical grounds.

11.1%, however, the main issue is a too short path for the charge diffusion to the contacts and the stability in the air. The champion in this field is indubitably a dye-sensitized solar cell, to which this thesis is devoted in its entirety.

2.3 The concept of dye-sensitized solar cell

It has been 22 years since the seminal paper by Grätzel and O'Regan² was published, however, the idea of photoelectrochemical solar cell is much older and dates back to the 19th century. In 1873 Vogel introduced a concept of the suitably chosen dyes which enable sensitization of silver halide emulsion to the red light³. Later on it was found that the most effective system was a monolayer of the dye adsorbed onto the surface. A lot of progress was made in 1970's, with particular contributions of Heinz Gerischer, Helmut Tributsch and Melvin Calvin^c. Model systems, like rhodamine B adsorbed on ZnO electrode⁴, were used to explain the processes of sensitization. Taking the inspiration directly from the nature, the chlorophyll was used in combination with ZnO monocrystals⁵ and photosynthetic membranes⁶. The key process of sensitization is the charge transfer from the dye molecule, which absorbs the light of energy lower than the bandgap of the semiconductor, to its conduction band in the form of an electron. The efficiencies achieved at that time were not very high, however, it has to be made clear that the photosynthesis reaction within the plants yields the solar energy conversion efficiencies lying in the wide range of 0.1–8% (mostly 3–6%). The highest efficiency reported for a dye-sensitized cell is 12.3% at 1 Sun illumination (13.0% at 0.1 Sun) - the cell was made using a specially optimized nanoporous TiO₂ layer to minimize the diffusion issues related to the use of a novel redox mediator - bulky tris(bipyridyl) Co(II/III) complex and judiciously tailored porphyrin dye in combination with a highly-efficient D-π-A dye⁷. This shows how important is the architecture of the device and each of its components. Everything connects to everything else.

In this section, first, I would like to present the device itself and enlist the processes that are happening during the cell's operation. A dye-sensitized solar cell is a successful combination of a few materials, properties of which were carefully tailored on a molecular level (dye),

^cMelvin Calvin was awarded the Nobel Prize in Chemistry in 1961 (along with Andrew Benson and James Bassham) for discovery of the *Calvin cycle* (reductive pentose phosphate cycle) - a cycle of light independent reactions taking place in the stroma of chloroplasts during photosynthesis

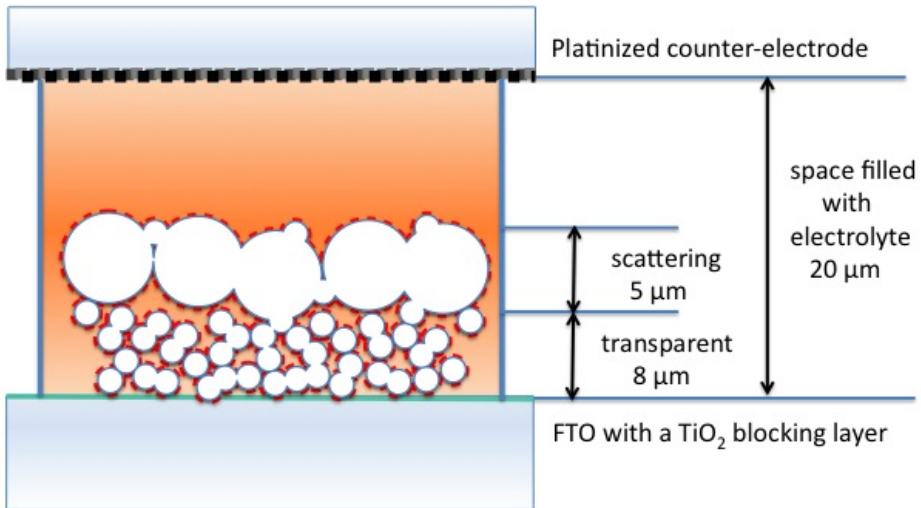


Figure 2.5: A scheme of a cross-section of a dye-sensitized solar cell.

nanoscale (TiO_2 film) and in a macroscopic view (electrolyte composition). The recent advances regarding the materials will be herein presented. The second section will deal with the operation principle of DSC, highlighting all the steps from the photon absorption to current extraction.

2.3.1 The architecture of a dye-sensitized solar cell and its components.

Today's dye-sensitized solar cells are made in a sandwich configuration - the heart of the device, which is a 20–25 μm -thick layer of various materials, is trapped between two pieces of conducting glass. There are attempts to fabricate a flexible DSC using Ti foil as a substrate for the photoanode, nevertheless, the glass device is the most convenient to make in the laboratory conditions. The schematic of a DSC is presented in the Figure 2.5. The main components of the cell are: a semiconductor scaffold stained with the dye and deposited on a transparent electrode (photoanode), electrolyte with a redox mediator and a counter-electrode.

2.3. The concept of dye-sensitized solar cell

On the bottom (Figure 2.5) there is a photoanode with a sensitized TiO_2 nanostructure. In most cases the light enters the device from this side, so that the good transparency (80–90% at 550 nm) of the glass is necessary to ensure a large number of incident photons. The glass is conductive, which means it is covered by a very thin layer of a transparent conductive oxide - fluorine doped tin oxide (FTO) is a material of choice. The products which fulfill the highest standards for DSC application purposes are NSG10 (Nippon Sheet Glass, Japan), TEC7 and TEC15 (Pilkington, UK) - the digits correspond to the resistivity of the materials in Ω/\square . The photoanode substrate is typically covered with a blocking layer made of TiO_2 , deposited according to the procedure described in the Chapter 3, section 3.5 Device fabrication. The layer considerably reduces the unwanted recombination processes (see *infra DSC's principles of operation*) and ensures very good ohmic contact between the FTO and proper TiO_2 mesoporous layer.

Nanostructured semiconductor layer. The DSC revolution started actually from the application of the mesoporous TiO_2 layer consisting of 20 nm-sized nanoparticles². Flat substrates made of rather large crystallites had been used before and although the photovoltaic effect had been also observed therein, the efficiencies had not been that spectacular. Only the introduction of a highly porous structure with a large surface area sparked the intensive research in the field. Carefully prepared films of connected regular nanoparticles of narrow size distribution provide the desired large surface area for dye adsorption and maintain the transparency in the visible regions^d. The thickness of such films can be varied, however, typically used are 6 to 8 μm thick layers of a porosity of ~60–70%. A scattering layer is applied on the top of the transparent layer. It consists of much larger particles (400 nm \varnothing) and it helps to reduce the optical losses. The thickness of the scattering layer varies between 3 and 6 μm . The nowadays most extensively used TiO_2 structure is not ideal, though. From a purely geometrical view, the best configuration would be a forest-like grown array of nanotubes/nanorods, preferably porous, so that the large surface area requirement would be fulfilled, but the enhancement would come from the reduction of the diffusion issues. The diffusion - actually - of both charges: electrons in the semiconductor and also the ions in electrolyte. In terms of electron transport, it is clear that the transport along the simple linear structure would be much faster.

^dOther materials, e.g. ZnO have also been studied, however TiO_2 remains the leader as of today.

Chapter 2. Fundamentals of dye-sensitized solar cells

The reduction of the tortuosity of the film would be very much beneficial especially in case of the cells with ionic liquid-based electrolyte, where their viscosities cause the diffusion problems for the electrolyte trapped within the spongy semiconductor structure.

Sensitizers. The nanostructured TiO₂ absorbs the photons up to ~380 nm, so that in order to harvest more of the solar spectrum reaching the Earth's surface, the dye molecules, acting as antennas, are chemically bound to its surface. Each dye molecule being in an intimate contact with the semiconductor can inject one electron upon the absorption of one quantum of energy, therefore in order to maximize the performance the large surface is needed. The choice of dye molecules is almost infinite, however, there are a few criteria to be fulfilled in order to ensure the sensitization to occur and - even more - to make it very efficient.

- a) The dye molecule has to be **soluble** in a suitable solvent to be transferred to the TiO₂ surface (typically dipping for 4 to 18 hours) - but not to be desorbed by the solvent used for the electrolyte.
- b) The dye has to be **attached to the surface** of the semiconductor via a chemical bond. This is typically realized by a carboxylic group, but phosphonic group is also an option. An expected result is a monolayer of the dye grafted neatly on the semiconductor surface.
- c) **Energetics** of the molecule has to be optimized in such a way that the excited state level lies sufficiently higher than the conduction band edge of the semiconductor (for an efficient electron injection) and its ground state redox potential lies lower than the redox potential of the redox couple in the electrolyte (for an efficient dye reduction).
- d) The dye's absorption spectrum should be broad, preferably extended to the red/infrared (**panchromatic**), with large optical cross-section throughout the whole absorption spectrum for effective light harvesting.
- e) **Non-aggregation** is an important feature, because it is believed that non-radiative decay of the excited state to the ground state reduces the electron injection efficiency.
- f) The molecule has to be **stable** - in terms of electrochemistry^e and in terms of decomposition under illumination or attachment to the semiconductor surface (strong chemical

^enumber of the red/ox turnovers under illumination - 10⁸ corresponds to ~20 years of the exposure to the sunlight

bond preventing the desorption).

Historically, the most efficient (and extensively studied in the first few years after the 1991 breakthrough) dyes used to be Ru complexes^{8–12} (extensive review¹³). The highest efficiency reported for a Ru-complex with I⁻/I₃⁻ redox couple is 11.5%¹⁴. Fully organic dyes open up a whole new universe of countless possibilities¹⁵. The most popular dye pattern follows a donor connected with an electron acceptor by a π -conjugated bridge (D- π -A) structure. To this day, the most efficient cell is constructed with the use of a mixture of two dyes: a zinc porphyrin dye and a D- π -A dye with triphenylamine donor, a cyclopentadithiophene bridge and a cyanoacrylic acid as an acceptor/anchoring group⁷. The co-sensitization concept was used in this work in order to complement the porphyrin spectrum with a valley in the green region with the D- π -A panchromatic dye. The use of two different molecules also helped with the reduction of the number of aggregates. It is very common to use neutral (not light absorbing) molecules as co-adsorbents (e.g. chenodeoxycholic acid, CDCA, bis-(3,3-dimethylbutyl)-phosphinic acid, DINHOP, 3-phenylpropionic acid, PPA) for highly aggregating dyes - they are believed to act already in the dipping solutions and break the dye clusters, but also to co-graft on the surface along with the dye molecules and separate them physically, blocking the paths of a non-radiative energy transfers.

Electrolytes. The space between the two electrodes is filled with the electrolyte containing a redox couple for the dye regeneration. In this work I focused only on devices with liquid (volatile) or ionic-liquid-based electrolytes, however, it can be successfully replaced with a solid state hole transporting material. Most successful trials were achieved using the 2,2',7,7'-tetrakis(N,N-di-*p*-methoxyphenylamine)-9,9-spirobifluorene (spiro-MeOTAD) and the highest efficiency reported for a solid-state DSC is 6.1%¹⁶. Liquid electrolytes based on organic solvents (ethanol, acetonitrile, acetonitrile/valeronitrile) have a longer tradition and the most popular redox couple remains still iodide/triiodide. Recently, the search of more efficient redox shuttle have intensified around new concepts (different redox shuttles, tailoring the dyes to provide effective shielding from the redox species, etc.), however, the attempts of use alternative redox mediators had been performed years ago^{17,18} (a review¹⁹). The re-design of the dyes with blocking alkoxy-chains and successful reduction of the recombination rate has led to the fruitful use of alternative mediators such as cobalt complexes²⁰, but also revive

Chapter 2. Fundamentals of dye-sensitized solar cells

the interest in other molecules, for instance ferrocene/ferrocenium²¹ or disulfide/thiolate²². There are also attempts to replace the organic solvent with water^{23,24} or totally eliminate the solvent - leading to ionic-liquid-based electrolytes. Ionic liquids are non-volatile, which feature makes them ideal in terms of stability. However, their rather large viscosity (in comparison to the acetonitrile-based electrolytes) causes the mass transport issues within devices. Nowadays, the state-of-the-art system is the eutectic melt of imidazole salts of markedly lowered viscosity²⁵, allowing for performances at the 8.2% level.

Counter-electrodes. The device is completed with a counter-electrode. Typically, it is a FTO glass piece covered with a layer of a catalyst for the redox couple regeneration reaction. Since iodide/triiodide is still the most popular redox mediator, platinum remains the natural choice. Fine particles of Pt are chemically stable and provide sufficient overvoltage for the triiodide reduction. Other possibilities include carbon (in various forms: graphite, carbon black, carbon nanotubes and nanoplatelets²⁶), conducting polymers (e.g. poly(3,4-ethylenedioxythiophene) - PEDOT - especially in application with electrolyte with Co complexes²⁷). In some cases, a very thin layer of gold could help improve the fill factor.

2.3.2 DSC's principles of operation

We believe that for the 3500 million years, when the first photosynthetic organisms appeared on the Earth, Nature has adjusted and optimized the process of photosynthesis along the evolutionary road. Yet, it is rather complicated mechanism, which could be divided into two main phases: light-dependent (photon absorption, electron hopping from Photosystem II to Photosystem I, synthesis of adenosine triphosphate, ATP, and the reduced form of nicotinamide adenine dinucleotide phosphate, NADPH, production of O₂) and "dark" reactions - the Calvin cycle, where CO₂ is transformed into simple organic compounds, like glucose and adenosine diphosphate, ADP, is formed - all these involving many, many chemical reactions. Having in mind that DSC in a way mimics the natural photosynthesis, we could proudly say that this time mankind did better job than the Mother Nature^f. The number of steps involved in the photocurrent generation cycle in a perfect (lossless) DSC is 6 (see Figure 2.6). In reality,

^fOne has also keep in mind, that in photosynthesis the goal is to store the light energy in a form of chemical bond, and in photovoltaics we are interested in production of a potential difference and then a current.

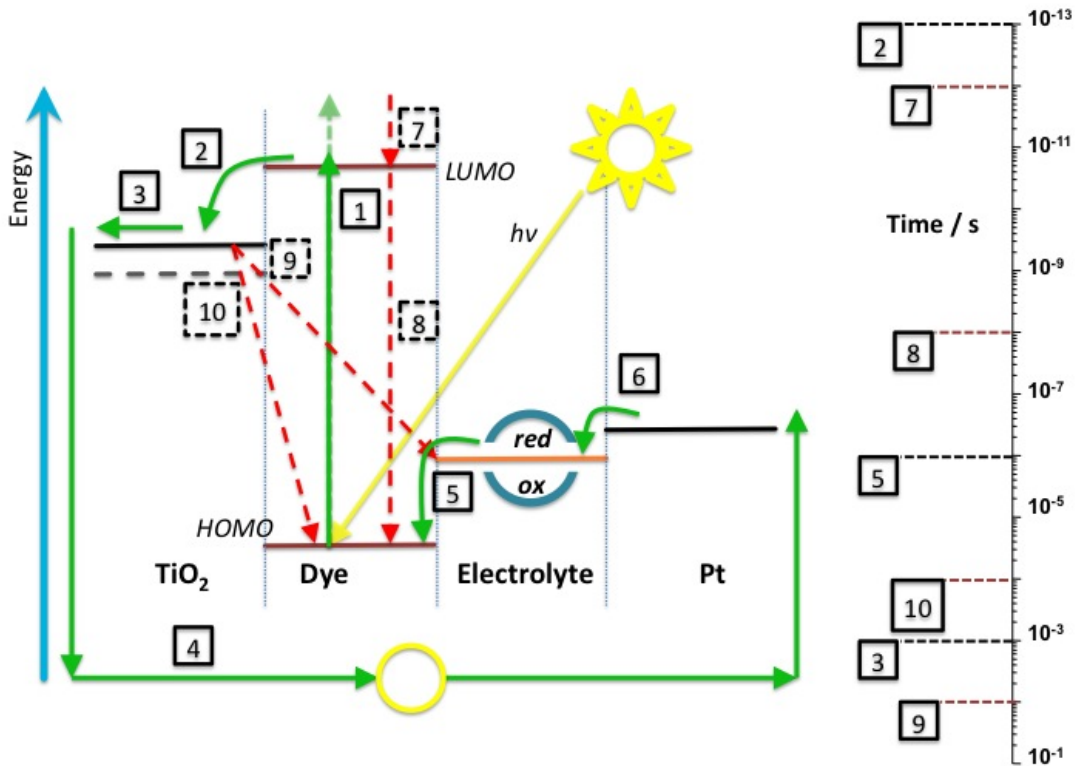


Figure 2.6: *Left:* Energy-level diagram for a dye-sensitized solar cell. The electron transfer processes are depicted with arrows (green - desired cycle path, red - unwanted loss channels). *Right:* A time scale of the processes within a DSC.

there are some unwanted phenomena occurring, reducing the overall efficiency of the device. The processes happening during cell's operation are presented in the Figure 2.6 and they are briefly described below (the numbers in the square brackets correspond to the labels in the Figure 2.6).



Photon absorption. As stated above, the monolayer of the dye grafted on the semiconductor surface helps to absorb most of the solar spectrum reaching the Earth's surface. A photon of energy $E \geq |HOMO-LUMO|$ is absorbed [1] by the molecule in a ground state (S) and promotes it to the excited state (S^*) (Equation 2.2). The excess of energy could be eliminated by the

Chapter 2. Fundamentals of dye-sensitized solar cells

relaxation [7] to the lowest vibrational state (10^{-12} s) and then emitted [8] (fluorescence - 10^{-8} s - or phosphorescence, when inter-system crossing is involved) (Equation 2.3). These processes do not contribute to the generation of electron in the conduction band of the semiconductor.



Electron injection. The process of the electron injection [2] from the excited state of the dye molecule into the conduction band of the semiconductor (Equation 2.4) is one of the fastest known physical phenomena²⁸ and it occurs on the femtosecond scale. This is a crucial step, because this is the moment when the charge separation takes place. Typically, the dyes are designed in such a way, that the process is quantitative as the LUMO of the dye lies sufficiently high above the conduction band edge. Nevertheless, the position of the latter can be modified by the local adsorption of some species (e.g. *tert*-butyl pyridine - causing the upward shift) or intercalation of small cations, like Li^+ , bringing the conduction band edge down.

Electron transport. The injected electrons have to travel through the mesoporous network to the external contact [3]. The thickness of the film varies from 3 to 12–15 μm , however, the actual path that the charge has to cover is longer due to the tortuosity induced by the mesoporous network of nanocrystallites. The fact that electrons are charged molecules would imply that the main mechanism of transport would be the gradient of the field, nonetheless, the electric field is effectively shielded by the ions in the electrolyte surrounding the particles, so that it is claimed that the electrons coupled with these ions undergo ambipolar diffusion. Additionally, the retention time in the film is prolonged by the fact of the occurrence of the electron traps within the band gap - the electrons experience multiple trapping/de-trapping events (detailed description is given in the section 2.4.3 Transient measurements). The time scale at which the transport occurs is in the ms/sub-ms range.



Dye regeneration. After the electron injection the dye molecule becomes oxidized, therefore it has to be consequently reduced to ensure the continuous operation of the device (Equation 2.5). This is done by the reduced form of the redox mediator present in the electrolyte [5].

2.3. The concept of dye-sensitized solar cell

The HOMO level of the dye has to be placed lower than the redox potential of the redox couple (it was shown that the difference as small as 150 mV is sufficient²⁹). If the process lasts microseconds, than the lifetime of the oxidized state should be in the range of hundreds of seconds.



Reduction of the redox mediator. The oxidized form of the redox mediator needs to be reduced and this takes place at the counter-electrode [6], where the electrons from the external circuit [4] are being collected (Equation 2.6). The ions diffuse to the electrode. Only in the case of a viscous medium with high concentration of the redox species, i.e. ionic liquid or gel electrolyte, can the transport be enhanced by the occurrence of the hopping Grotthus-like mechanism²⁵ involving the formation and cleavage of the chemical bonds in the temporarily formed associates. Upon the arrival to the counter-electrode the oxidized form is brought to the reduced state. The reaction is supposed to be rapid due to the use of a catalyst at the counter-electrode surface.



Electron recombination. The main source of the losses in the performance of DSC can occur via two channels: recombination of the electrons with the oxidized redox species in the electrolyte [9] and much less common recombination with the oxidized dye molecule [10]. It is believed that even in the high-performing cells ~10% of electrons readily injected into the conduction band recombines with the electrolyte (Equation 2.7). This leads to the lowering of the output voltage, because the quasi-Fermi level determined by the population of electrons in the trap states and conduction band is lowered. The mechanism of the reaction is not fully understood and remain ambiguous, as the formation of radicals or the participation of molecular I₂ is suspected in a multistep process^{30,31}. The recombination with the electrolyte occurs at a timescale comparable to the electron transport, however, in order to obtain a well-performing device, it has to be much slower than the transport. In case of 1-electron

Co complexes the blocking of this reaction must be very efficient (as it is very rapid) and is realized by employing bulky complexes (so as to hinder the diffusion close to the TiO₂ surface) and insertion of the shielding groups on the dye molecules.

The second recombination channel is not observed very frequently in the devices, as most of the dye molecules are designed in such a way to ensure effective charge separation^g. The recombination with the dye (Equation 2.8), termed **geminate recombination**, typically competes with the dye regeneration realized via the electrolyte and that is why the appropriate design of the dye molecule (the spread of the electron cloud) proves to be very important.

2.4 Theoretical background of the processes within the devices and characterization methods

In this section I would like to present a detailed physical description and quantification of both: processes occurring within dye-sensitized solar cells as well as concepts underlying the methods widely used to investigate them. In general, the characterization methods could be divided into three groups:

- I) **Steady-state characteristics** including basic J-V measurement and IPCE experiment for a general evaluation of a particular device. In these cases the charge density within the semiconductor layer does not vary with time. The process of photogeneration of electrons (in a very broad sense, including all the steps presented in the previous section) combined with the rate of transport of the charges through the semiconductor film is in the equilibrium with the loss-generating processes (e.g. various channels of recombination).
- II) **Time-resolved methods** giving more insight into the fundamental processes occurring at various time-scales. Ultra-fast femtosecond lasers are used for observing the kinetics of electron injection from the excited dye to the conduction band of a semiconductor, but for slower processes, e.g. dye recombination a nanosecond laser is sufficient. Even slower processes, namely the transport of the injected electrons within the semiconductor film

^gNevertheless, the story presented in the Chapter 4 is a very elegant example of the identification and smart solution of this kind of problem.

2.4. Theoretical background of the processes within the devices and characterization methods

and their recombination with the redox mediator, can be readily accessed with small-perturbation techniques (voltage and current decays) provided by a short red diode pulse superimposed on the steady white-light bias.

III) **Frequency-dependent techniques**, in particular Electrochemical Impedance Spectroscopy. This powerful method gives access to the multiple interfaces within the device and leads to a deeper understanding of the interplay between various components of the DSC. Additionally, the technique provides the parameters that are obtainable by the steady-state methods, which allows for an easy cross-check of the results.

All of these techniques were used by the author in the scope of this thesis to characterize and investigate the fabricated dye-sensitized solar cells. From the very basic ones (J-V, IPCE) to the much more complicated (EIS), the gradual comprehension of their application to the devices allowed for a deeper understanding of the complexity (but also the beauty!) of the physics of DSCs.

2.4.1 J-V curves

A common definition of a solar cell says that it is a "photoelectric cell which, when exposed to light, can generate and support an electric current without being attached to any external voltage source"³². A solar cell (in general) can be perceived as a current source (I_{photo}) connected with a diode(s) in parallel (I_{01} and I_{02}), but due to its non-ideality, a shunt resistance (R_{shunt}) is also a part of an equivalent circuit (Figure 2.7)³³. The shunt current (I_{shunt}) is induced by the charge recombination processes. Series resistance (R_{series}) is an element that groups together the contact resistances at the interfaces, the bulk resistance and the sheet resistances of the transparent glass supports.

Under illumination the overall current generated by the device is described by the very general Equation 2.9 .

$$I = I_{photo} - I_{dark} - I_{shunt} \quad (2.9)$$

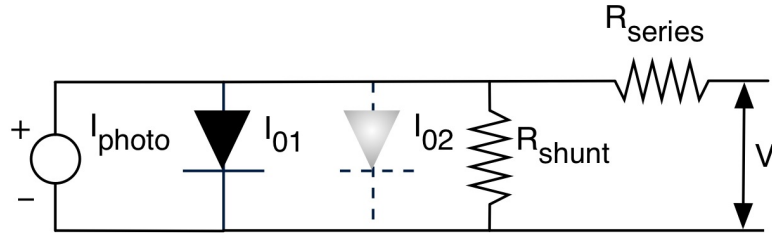


Figure 2.7: The equivalent circuit of a solar cell.

I_{photo} is the photogenerated current, originating from the absorbed photons^h. I_{dark} is the current flowing in the cell when it is not illuminated and is nothing else than a simple diode current (Equation 2.10)

$$I_{dark} = I_0 \left[\exp\left(\frac{qV}{k_B T}\right) - 1 \right], \quad (2.10)$$

where I_0 is a reverse saturation current, q an elementary charge, k_B - Boltzmann's constant and T - temperature. However, in practice, another diode is added to the equivalent circuit. This diode contains an ideality factor and it gives fitting results much closer to the measured curves (Equation 2.11). It is also very common to combine these two diode expressions, as shown in the Equation 2.12, and introduce an empirical ideality factor, m , which is 1 for the ideal case and never larger than 2. Shunt current, I_{shunt} , is obtained via the Ohm's law.

$$I = I_{photo} - I_{01} \left[\exp\left(\frac{q(V + IR_{series})}{k_B T}\right) - 1 \right] - I_{02} \left[\exp\left(\frac{q(V + IR_{series})}{2k_B T}\right) - 1 \right] - \frac{V + IR_{series}}{R_{shunt}} \quad (2.11)$$

$$I = I_{photo} - I_0 \left[\exp\left(\frac{q(V + IR_{series})}{mk_B T}\right) \right] - \frac{V + IR_{series}}{R_{shunt}}, \quad 1 \leq m \leq 2 \quad (2.12)$$

A typical I-V curve is presented in the Figure 2.8. Here we follow the convention where applied voltage bias is positive and the measured photocurrent is negative. By using the Figure 2.8 one can also examine the undesired effects of the increasing R_{series} , causing the reduction of

^hThis is in agreement with the two fundamental laws of photochemistry: the **Grotthuss-Draper law** stating that only photons absorbed by the system can cause a photochemical change, and the **Stark-Einstein law** quantifying the occurring processes to one per each single absorbed photon of an adequate energy.

2.4. Theoretical background of the processes within the devices and characterization methods

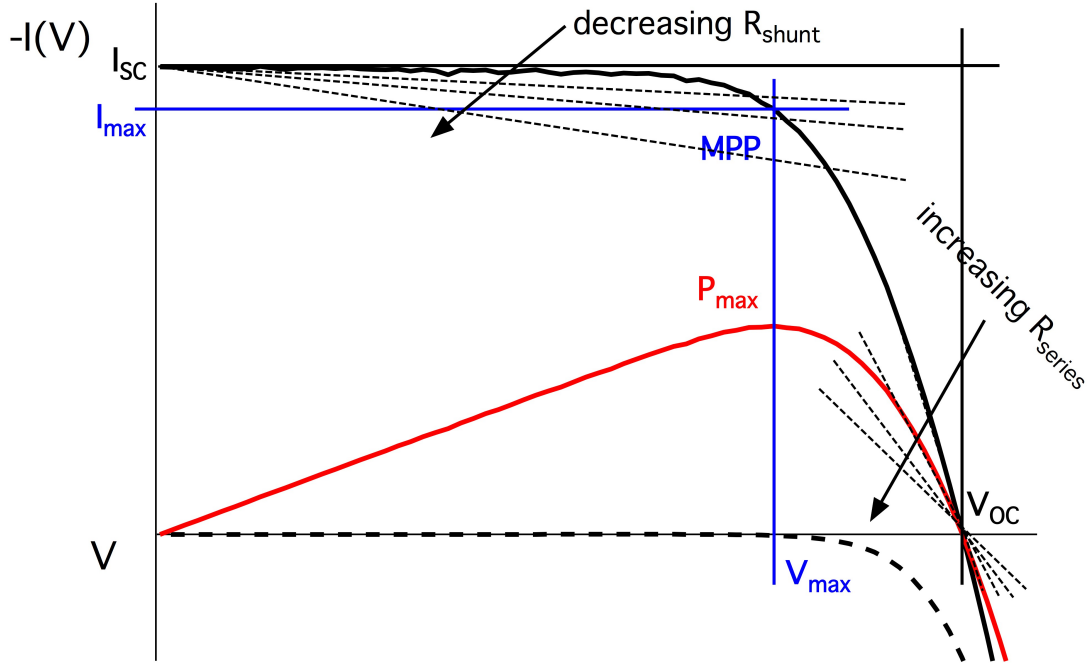


Figure 2.8: A typical IV curve of a solar cell: in the dark (black dashed line) and under illumination (black solid line). Power, as a product of current and potential is represented by the red line. The maximum power point (MPP) is indicated. The ratio of areas of two rectangles: blue ($I_{max} \times V_{max}$) and black one ($I_{SC} \times V_{OC}$) gives the fill factor. Additionally, the influence on the curve's slopes by the variations of R_{shunt} and R_{series} is demonstrated.

the "steepness" of the curve, and the diminishing R_{shunt} , leading to the loss of its "flatness". In order to find the expression for two important parameters of the solar cell: short-circuit current, I_{SC} , and open-circuit voltage, V_{OC} , one has to refer to the ideal solar cell case, where $R_{series} \rightarrow 0$ and $R_{shunt} \rightarrow \infty$. At short-circuit conditions ($V = 0$) all the generated current is extracted and taking into consideration the assumptions about R_{series} and R_{shunt} it is clear that

$$I_{SC} \approx I_{photo}. \quad (2.13)$$

On the opposite, when the cell is kept at open-circuit conditions and there is no net current

flowing ($I = 0$), the characteristic diode equation (Equation 2.12) gives

$$V_{OC} \approx \frac{mk_B T}{q} \ln \left(\frac{I_{photo}}{I_0} + 1 \right). \quad (2.14)$$

General formula for electric power, $P = I \times V$, applies also here, and the plot is included in the Figure 2.8 (red line). It is worth noting, that under the extreme conditions, i.e. I_{SC} and V_{OC} , no power can be generated. The maximum power, P_{max} , is derived under the conditions described as Maximum Power Point, MPP(I_{max} , V_{max}). Fill factor (FF) is a parameter related to the MPP and is often described as a measure of the "squareness" of the curve. For good DSCs typical values are in the range of 0.78–0.8. Fill factor is the ratio of the areas of two rectangles under the IV curve, determined by the values of voltages and currents at MPP and open/short-circuit conditions (Equation 2.15):

$$FF = \frac{I_{max} \times V_{max}}{I_{SC} \times V_{OC}}. \quad (2.15)$$

Finally, the overall efficiency, η , (Equation 2.16) can be presented as the product of the above-introduced parameters (maximum extractable power) normalized to the incident solar power (P_{in}).

$$\eta = \frac{P_{max}}{P_{sun}} = \frac{I_{max} \times V_{max}}{P_{sun}} = \frac{I_{SC} \times V_{OC} \times FF}{P_{in}}. \quad (2.16)$$

In this way it was shown that this simple experiment provides the most basic characteristics (I_{SC} , V_{OC} , FF and η) of the device. In order to enable direct comparison between various cells, the value of the short-circuit current is normalized to the cell active (illuminated) area and expressed as short-circuit *current density*, J_{SC} - hence J-V curves. The determination of the active cell area is possible by using the masks with a defined aperture³⁴. It is a very important issue, recently discussed extensively by Snaith³⁵.

2.4.2 Quantum Efficiencies: IPCE and APCE

Due to the almost infinite variation of possible dyes that could be used to sensitize TiO_2 , especially in the case of DSCs it is extremely interesting to measure the spectral response of

2.4. Theoretical background of the processes within the devices and characterization methods

the devices. Spectral response, $SR(\lambda)$, is defined as the ratio of the photocurrent generated upon the illumination by a monochromatic light to the spectral irradiance of that particular wavelength. The expression for the External Quantum Efficiency, also recognized as the Incident Photon-to-current Conversion Efficiency (IPCE), which is the ratio of the collected charges to the photons falling on the cell, is presented below (Equation 2.17).

$$IPCE(\lambda) = \frac{hc}{q\lambda} SR(\lambda) = \frac{hc}{q} \frac{J_{SC}(\lambda)}{\lambda P_{in}(\lambda)} = \frac{\text{collected } e^-(\lambda)}{\text{incident photons}(\lambda)}, \quad (2.17)$$

where h is Planck's constant, c the speed of light in the vacuum and q an elementary charge. IPCE takes into consideration the whole population of photons being shone on the device, but makes no distinction between the ones being actually absorbed and the others - being either reflected, or transmitted. The shape of the resulting plot is a signature of the dye adsorbed onto the semiconductor surface, sometimes influenced also by the absorption of species in the electrolyte. The area under the curve after integration yields short-circuit current density (Equation 2.18).

$$J_{SC} = \int_{\lambda_i}^{\lambda_f} qIPCE(\lambda)\phi(\lambda) d\lambda, \quad (2.18)$$

where $\phi(\lambda)$ is the incident photon flux at a given wavelength. Typically, this integrated current is used to cross-check with the result achieved with a J-V experiment. IPCE, nevertheless, carries much more in-depth information about the device. Its value reflects the convolution of the fundamental processes within DSC: the amount of absorbed photons (light harvesting efficiencyⁱ, LHE) and efficiencies of injecting (η_{inj}) and collecting (η_{col}) electrons (Equation 2.19). APCE, Absorbed Photon-to-current Conversion Efficiency, also known as the Internal Quantum Efficiency, related to this part of incident light which was absorbed and caused the generation of photoelectrons. It approximates the efficiency of the direct generation of the current within the devices and - in case of low values - indicates problems related to either poor electron injection, or obstacles with the delivery of the charges to the current collectors.

$$IPCE(\lambda) = LHE(\lambda) \times \underbrace{\eta_{inj}(\lambda) \times \eta_{col}(\lambda)}_{APCE} \quad (2.19)$$

ⁱalso referred as **absorptance**, $\mathcal{A} = 1 - 10^{-A}$ - not to confuse with the *absorbance*, $A = -\log_{10}\left(\frac{I}{I_0}\right)$, where I denotes the intensity of light.

Recently, a very detailed description was given by Barnes et al.³⁶, for utilization of IPCE measurements to determine the electron injection efficiency, η_{inj} , and electron diffusion length, L . The cells ought to be measured from the front- and the backside. Illumination from the working electrode side yields higher IPCEs, because more light is absorbed close to the glass substrate and the electron diffusion length is shorter. Counter-electrode side illumination is influenced by the light absorption by Pt deposited on the substrate and also by the species present in the electrolyte. Obviously, the electrons are generated further away from the working electrode contact, therefore the measured diffusion length is the longest possible. It is thus possible to estimate if the TiO_2 layer is thin enough to ensure unimpeded transport of charges.

2.4.3 Transient experiments

In this section the focus will be put on the processes happening in the devices after the photon absorption and electron injection in the conduction band of TiO_2 . Ideally, all photogenerated electrons should be transported through the film to the back contact and therein collected. The driving force for the electrons' movement most logically should be the gradient of electron concentration^{37,38}, nevertheless, due to the application of the mesoporous semiconductor sponge-like structure, which can be interpreted as two intertwined networks: TiO_2 and electrolyte, the electrons in the semiconductor are coupled by weak electric field with the ions in the electrolyte. Thus, the diffusion of the charges is described as ambipolar³⁹. Moreover, based on the observations that the electron transport depends on the light intensity, it was proposed that the charges undergo constant oscillations between the conduction band and some states (trap states) placed below the band (multi-trap model)^{40,41}.

Electron trapping. The multi-trap model was first introduced for disordered semiconductors and later on was adapted for nanoporous semiconductors by Vanmaekelbergh and de Jongh⁴². It was shown that there is an exponential population (Equation 2.20) of electronic states (distributed energetically) lying below the conduction band of the nanoporous TiO_2 , and there is more "shallow" states, from which the electrons can be freed thermally, than deeper lying traps (in practice, once the electron is trapped there, the probability of de-trapping is thermodynamically very low). It is also worth noting, that the density of trapped electrons

2.4. Theoretical background of the processes within the devices and characterization methods

increases slower than the population of the electrons in the conduction band with the upward shift of the quasi-Fermi level.

$$g(E_{trap}) = \frac{N_{t,0}}{k_B T} \exp\left(-\frac{E_c - E_{trap}}{k_B T}\right), \quad (2.20)$$

where $N_{t,0}$ is the total trap states' density. The trap occupancy is determined by the Fermi-Dirac distribution. One should get familiar with the two conditions to which the DSCs is exposed during the operation: strong illumination (high bias) and low-light conditions (low bias), as presented in the Figure 2.9. The former situation determines large population of electrons in the conduction band or in its energetical vicinity - in fact, the fraction of the electrons undergoing trapping/de-trapping processes is much larger than these being in the conduction band. The quasi-Fermi level lies close to the conduction band, hence the V_{OC} is high. The trapping/de-trapping processes are then very frequent - so that the transport (hopping of the electron) is rather fast; on the other hand, the recombination rate is high as well. For low light bias, when there are less electrons generated, they would occupy mostly the deeper traps, so that both, transport and recombination rates, are slower. A very detailed and elegant mathematical description is given by Bisquert and Vikhrenko⁴³ - *quasi-static approximation* - or Peter⁴¹.

Electron transport. It was mentioned briefly above that the driving force for the electrons' movement is supposed to be the gradient of their concentration, indicating a diffusive process. Taking into consideration the fact that the species in question are charged particles, the more appropriate expression would include rather the gradient in the electrochemical potential, $\frac{\partial \mu_i}{\partial x}$. The electrochemical potential of an electron within the film is described by the Equation 2.21:

$$\overline{\mu}_i = \mu_i^0 + k_B T \ln\left(\frac{n_i}{n_i^0}\right) + z_i q \varphi, \quad (2.21)$$

where φ is the inner potential, n are the concentrations of both: the actual species and species at the conditions for the standard chemical potential, μ_i^0 . The flux of the electrons, J_i , is described by the Equation 2.22, where u_i is the charge mobility. After inserting the spatial derivative of the chemical potential and introducing the Einstein electrical mobility relation,

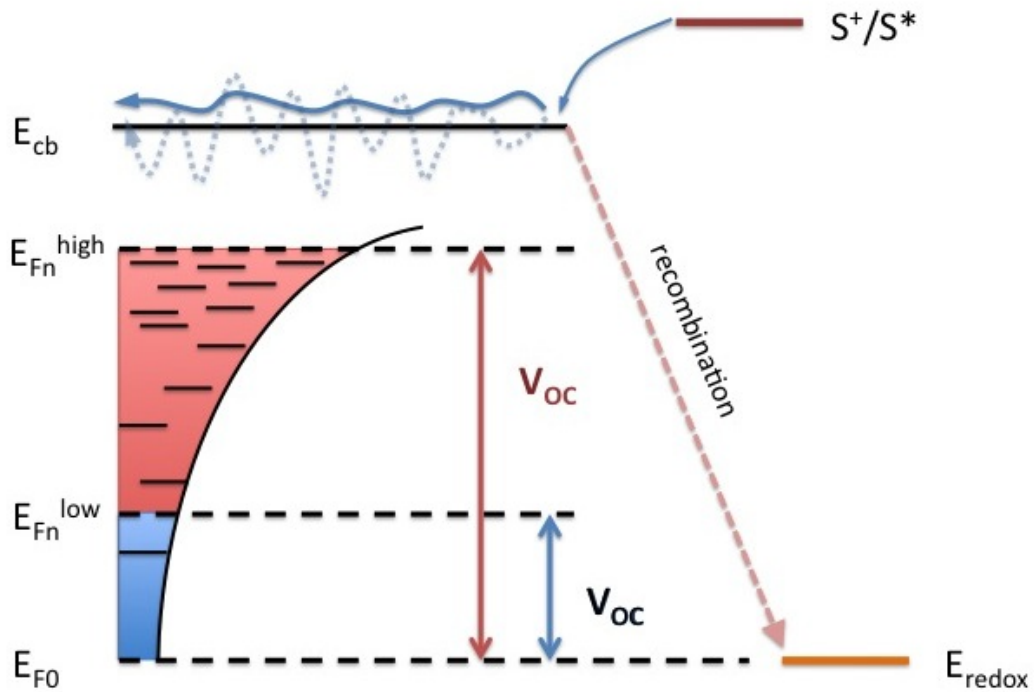


Figure 2.9: Electron trap distribution under high-(red) and low-light (blue) conditions. In the dark Fermi level is in equilibrium with the electrolyte redox potential. Upon illumination it is shifted upwards (and is called the quasi-Fermi level), and the resulting difference is measured as V_{OC} .

$D = \frac{u_i k_B T}{q}$, one can group the terms into a diffusive^j and a drift part.

$$J_i = -\frac{z_i n_i u_i}{q} \frac{\partial \mu_i}{\partial x} = -\frac{u_i k_B T}{q} \frac{\partial n_i}{\partial x} - z_i u_i n_i \frac{\partial \varphi}{\partial x} = \underbrace{-D_i \frac{\partial n_i}{\partial x}}_{\text{diffusion}} - \underbrace{z_i n_i u_i \frac{\partial \varphi}{\partial x}}_{\text{drift}} \quad (2.22)$$

Because of the high concentration of ions in the electrolyte, it is generally accepted that the electric field accompanying the charges within the semiconductor is effectively balanced out. The coupling between the opposite charges is strong enough to classify the diffusion as ambipolar. Taking into consideration also the back reaction (recombination with triiodide) a general **continuity equation**, describing the temporal changes of the electron concentration

^jFirst Fick's law of diffusion: $J = -D \frac{\partial n}{\partial x}$

2.4. Theoretical background of the processes within the devices and characterization methods

in the conduction band, n_c , can be written down (Equation 2.23)⁴⁴:

$$\frac{\partial n_c}{\partial t} = \underbrace{\alpha I_0 \exp(-\alpha x)}_{\text{injection}} - \underbrace{N_{t,0} \left(\frac{\partial f}{\partial t} \right)}_{\text{trapping/de-trapping}} + \underbrace{D_0 \frac{\partial^2 n_c}{\partial t^2}}_{\text{diffusion}} - \underbrace{\frac{n_c - n_{eq}}{\tau_0}}_{\text{recombination}}, \quad (2.23)$$

where α is the absorption coefficient, I_0 is the incident light intensity, $N_{t,0}$ and f are number of trapped electrons and the probability of such an event, respectively. The solutions of this equation, either under steady-state conditions, or with perturbations can be found in the literature^{40,45,46}. There exist also solutions under non-steady-state conditions⁴⁷. One of the most important findings after its analysis was the fact, that the diffusion coefficient is not constant and is a function of the quasi-Fermi level. This was confirmed experimentally by the observation of the changes of D_0 with light intensity. Therefore the **effective** diffusion coefficient, D_n , is expressed by the Equation 2.24. It is also worth mentioning that quasi-Fermi level also varies with the distance from the back contact under short-circuit conditions, whereas it remains constant at open-circuit.

$$D_n = \left(1 + \frac{\partial n_c}{\partial n_t} \right) D_0. \quad (2.24)$$

Recombination rate - electron lifetime. As the DSC under operation remains at quasi-equilibrium involving many processes (photon absorption, electron injection, transport and collection), one cannot forget about the loss processes, which are constantly occurring. As described in the Figure 2.6, there are a few loss channels for injected electrons. Here I will focus mainly on the interception of the injected electron by the triiodide, widely known as recombination. The V_{OC} depends on the concentration of the triiodide and the critical reaction (Equation 2.7) is linear in respect to the concentration of I_3^- . Therefore, this first order reaction^{45,48} is taken into consideration. The parameter, that is often used to characterize loss processes in the DSCs, is known as **apparent electron lifetime** and is related closely to the recombination rate. One has to keep in mind, that within the device there is a constant interplay of various processes, therefore the apparent electron lifetime is a convolution of the recombination processes and the trapping/de-trapping events. It is then clear, that upon decreasing light intensity, the occupancy of the trapping states is lower and electron lifetimes

become longer. Additionally, under high illumination the population of occupied trap states grows larger and that is why the apparent electron lifetime in this case is longer than the true conduction band lifetime.

In order to define the electron lifetime⁴⁹, let U_n be the recombination rate, linear in electron density (Equation 2.25). The decay of population is noted down with the Equation 2.26. In terms of measurements, we are interested in small perturbations applied to the device in the steady-state, which generate an extra population of electrons Δn , (however, $\Delta n \ll n$) that decays in a similar manner (Equation 2.27). The electron lifetime can therefore be expressed as the reciprocal of the partial derivative of recombination rate (Equation 2.28).

$$U_n = k_{rec} n \quad (2.25)$$

$$\frac{dn}{dt} = -U_n(n) \quad (2.26)$$

$$\frac{d\Delta n}{dt} = -\left(\frac{\partial U_n}{\partial n}\right)_n \Delta n \quad (2.27)$$

$$\tau_n = \left(\frac{\partial U_n}{\partial n}\right)_n^{-1} \quad (2.28)$$

If there were no trapping/de-trapping phenomena occurring, then the electron lifetime could be extracted in a very simple way from the photovoltage decay measurement. Photovoltage, which is a difference between the Fermi level (in the dark) and quasi-Fermi level (under illumination) could be expressed by the Equation 2.29:

$$V_{photo} = \frac{k_B T}{q} \ln \frac{n_c}{n_c^0} = \frac{k_B T}{q} \ln \frac{I_0 \tau_n [1 - \exp(-\alpha d_{film})]}{d_{film} n_c^0} \quad (2.29)$$

$$\tau_n = -\frac{k_B T}{q} \left(\frac{dV_{photo}(t)}{dt} \right)^{-1} \quad (2.30)$$

A **total voltage decay experiment** is performed in such a way that the device is brought to the steady-state equilibrium under illumination at open-circuit and then the light is switched off and in the very same moment the cell is being short-circuited. This kind of experiment can be used to test the quality of blocking layers applied in the DSCs. The voltage decay over

2.4. Theoretical background of the processes within the devices and characterization methods

time can be fitted with a single exponential. In our lab, however, we utilize the **transient** technique for **photovoltage decays** under various light intensities. A device under steady-state condition at open-circuit (V_{OC} is determined by the light intensity) is perturbed with a short red pulse, which cause a small increase in V_{OC} . If the perturbation is small enough to maintain the linearity of the response, then the decay to the initial V_{OC} can be fitted with a single exponential (Equation 2.31)

$$V(t) = V_0 + A \exp\left(-\frac{t}{\tau_n}\right) \quad (2.31)$$

A slightly modified total photovoltage decay can yield additional information about the charge density within the film. Unlike in the original experiment, where the steady-bias light was switched off simultaneously with the short-circuiting the cell, this time the cell's shorting is delayed with regards to the switching off the light, allowing first for some fraction of accumulated charges to recombine with I_3^- , and then collecting the remaining charges in the form of current. A series of photovoltage decays short-circuited after varying amount of time since switching-off the light is performed and the temporal integrals of the corresponding currents results in the number of charges, ΔQ , that had been stored in the film (Equation 2.32, where p is the film porosity and q an elementary charge).

$$n_c = \frac{\Delta Q}{qd(1-p)} \quad (2.32)$$

This kind of experiment is sometimes called **charge extraction** and provides the profile of the density of states within the film.

Cell capacitance and density of states. It has been mentioned that the quasi-Fermi level is not constant throughout the film at short-circuit condition, whereas for open-circuit indeed it is. Both, recombination and transport, are processes strongly depending on the concentration of the electrons, therefore it is wise to study these phenomena at well-determined conditions so as to be able to compare the results for different systems - in other words the comparison between the devices is only valid when the ratios of the trapped electrons to free electrons in the conduction band are equal. One can also take into consideration the quasi-Fermi level offset in relation to the conduction band, provided that the trap distribution is the same in

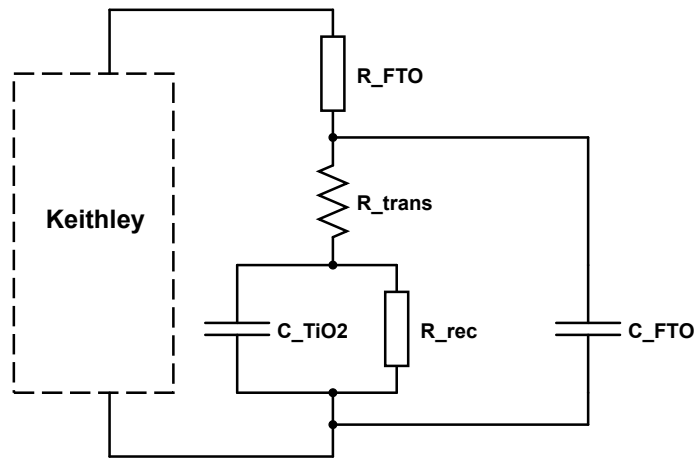


Figure 2.10: A simple model describing some DSC interfaces and components in terms of electric circuit elements⁵⁰. TiO_2 /electrolyte interface is a parallel connection of a capacitor C_{TiO_2} and recombination resistance, R_{rec} ; analogously FTO/electrolyte: $C_{FTO} \parallel R_{FTO}$. R_{trans} is the transport resistance within the TiO_2 film.

compared devices. Nevertheless, at the early stage of DSC development the electron transport was almost always studied under short-circuit conditions. The diffusion coefficients and diffusion lengths were obtained from the **transient photocurrent decays**. The experiments were performed analogously to the transient photovoltage decays, but they were problematic - scientifically, because of the obvious, above-stated reason - and technically, because it is not easy to bias and keep the cell under steady-state condition close to the short-circuit. From the experiment a number of charges could be derived (from the temporal integral of the area under the current decaying after the small perturbation). This ΔQ was used to form the expression for the cell capacitance (Equation 2.33):

$$C_{\text{TiO}_2} = \frac{\Delta Q}{\Delta V_{max}}, \quad (2.33)$$

where ΔV_{max} is the peak height of the transient photovoltage. This formula is not valid, when the numerator and the denominator originate from two extremely different conditions (short-circuit and open-circuit, respectively) and thence cannot be combined.

2.4. Theoretical background of the processes within the devices and characterization methods

Deeper understanding of the processes occurring in the DSC, with the emphasis on the profiles of quasi-Fermi levels at various conditions, led O'Regan et al. to the introduction of a more rigorous way to determine the transport rate and cell capacitance⁵⁰. One can be tempted to obtain the photocurrent decay close to the short circuit conditions and apply to the Equation 2.33, but the RC limitation occurs and the measured value is far from the real one. However, when a photocurrent transient caused by a small perturbation is measured closed to the open-circuit condition, the simple Equation 2.33 holds and corresponds well to the capacitance values obtained for instance via EIS. Nevertheless, the *clou* of the new concept is the extraction of the charge transport rate from the **transient photovoltage rise time**. The DSC can be simplified to an electrical circuit presented in the Figure 2.10. The two interfaces: TiO₂/electrolyte and FTO/electrolyte are represented by the parallel connections of a resistor and a capacitor. Typically, $C_{TiO_2} > C_{FTO}$. In-between the interfaces, a resistor in series characterizes the transport within the TiO₂ film. Illumination of the cells at V_{OC} causes a build-up of the charges at both capacitors, C_{TiO_2} and C_{FTO} , but there is no current flowing through the resistors. A small perturbation (red diode pulse) injects extra charges into the C_{TiO_2} causing the rise of voltage. The equilibrium between the two capacitors is lost, but could be regained by the flow of a fraction of these charges through the R_{trans} to C_{FTO} . The process is limited by the rate of the charging of C_{FTO} ($C_{FTO} < C_{TiO_2}$) and is characterized by the time constant in Equation 2.34. The same equilibrium could be reached by applying external voltage bias equal to V_{OC} . This time the additional charge on C_{TiO_2} (a result of the red diode pulse) will be driven out of the cell, because the external bias is applied continuously. The bottleneck of the process will then come from the resistors. There are two cases:

- 1) $R_{trans} > R_{FTO}$ - the limiting factor is the transport within TiO₂;
- 2) $R_{trans} < R_{FTO}$ - there is an overall RC limitation which makes it impossible to derive the transport time of the device.

For the first case, the transport time time constant is expressed in the Equation 2.35. Combination of Equations 2.34 and 2.35 yields an elegant formula (Equation 2.36) for the transport time that could be obtained from the photovoltage rise measurement, provided that the particular

capacitances are known ($C_{FTO} \approx 15\mu F$ and method of obtaining C_{TiO_2} is presented above).

$$\tau_{rise} = R_{trans} \times C_{FTO} \quad (2.34)$$

$$\tau_{trans} = R_{trans} \times C_{TiO_2} \quad (2.35)$$

$$\tau_{trans} = \tau_{rise} \times \frac{C_{TiO_2}}{C_{FTO}} \quad (2.36)$$

The final comment on the above presented physical description of the fundamental processes and their probing techniques is that due to the occurrence of the trap states in the nanostructured semiconductor band gap, that is characteristic and unique for each device, it is of the highest importance to compare the devices always with regards to the density of states. Comparison according to the V_{OC} is relative and thus almost always not valid, and it can cause misinterpretations such as under- or overestimated conduction band shifts.

2.4.4 Impedance Spectroscopy as a tool of the complex characterization of DSCs

Impedance spectroscopy is a well-established electrochemical method designed to study interfacial processes. The beauty of DCS lies in its interfaces, be it TiO_2 /dye/electrolyte, or FTO/ TiO_2 , or finally electrolyte/Pt-counter-electrode, so it was only a matter of time to apply this approach to study this complex system. Indeed, to this day EIS remains the most versatile technique, giving non-invasive and simultaneous access to almost all processes within the DSC (except the electron injection, because it is too fast). The blossom of DSC triggered the research also in other, related fields - the standard theories present in electrochemistry at that time could not truly address all the issues and give an appropriate description of the interfacial processes. Nanostructured mesoporous TiO_2 layer not only provided an interface of enormously large surface area, but also possessed characteristic electron transport features. The concept of **transmission line**^{51,52} was developed after realisation that such transport is inseparably connected with interfacial and recombination processes. Another important achievement is a treatment the conduction band in disordered TiO_2 as chemical capacitance⁵³. Nowadays, the extensive theories developed over the last 10 years enable the use of this technique as a standard cell characterization tool.

2.4. Theoretical background of the processes within the devices and characterization methods

Impedance - basics. Impedance (Equation 2.37) is a generalized resistance in AC circuits determined from a small voltage perturbation at a frequency ω and as such follows Ohm's law. It is a complex value, where its real part is called *resistance*, **R**, and the imaginary part - *reactance*, **X**. The magnitude of impedance is given by the ratio of the amplitudes of voltage to current and the phase is the phase shift/phase angle of a current in relation to voltage⁵⁴.

$$Z = \frac{|\Delta V| \exp(i\omega t)}{|\Delta I| \exp[i(\omega t + \theta)]} = |Z| \exp(i\theta) = \underbrace{|Z| \cos(\theta)}_{R} + i \underbrace{|Z| \sin(\theta)}_{X} \quad (2.37)$$

If the phase shift θ is equal to 0, then impedance is a real number and characterizes a purely **resistive** element. **Inductive** element (Equation 2.38) has no real part and the AC voltage is leading the AC current by $\frac{\pi}{2}$ ($\theta > 0$). Negative phase shifts are characteristic for **capacitive** elements (Equation 2.39) and an ideal one also has no real part - only imaginary - with AC voltage lagging AC current by $\frac{\pi}{2}$. For fitting purposes in DSC applications, due to the surface roughness and complicated interface, there is a need to introduce a modified capacitance as a circuit element describing a double layer: a **constant-phase element** (Equation 2.40) where the phase angle is independent of the frequency and is constant. The graphical representations of the circuit elements on the complex plane are shown in the Figure 2.11.

$$Z_{inductive} = \omega L \exp\left(i\frac{\pi}{2}\right) \quad (2.38)$$

$$Z_{capacitive} = \frac{1}{\omega C} \exp\left(-i\frac{\pi}{2}\right) \quad (2.39)$$

$$Z_{CPE} = \frac{1}{(i\omega)^n Q} \quad (2.40)$$

Application to DSCs. Impedance measurements of DSC used to be very time consuming, however, the reward was an almost complete picture of the particular components of the device and their interplays. Nowadays the electrochemical setups (potentiostats and frequency response analyzers) enable fast (~ 30 min) yet sensitive experiments. A cell is connected to the setup and a steady voltage bias is applied - either in the dark or under illumination. Then an AC voltage perturbation is applied within a frequency range 1 mHz to 10 MHz. During the

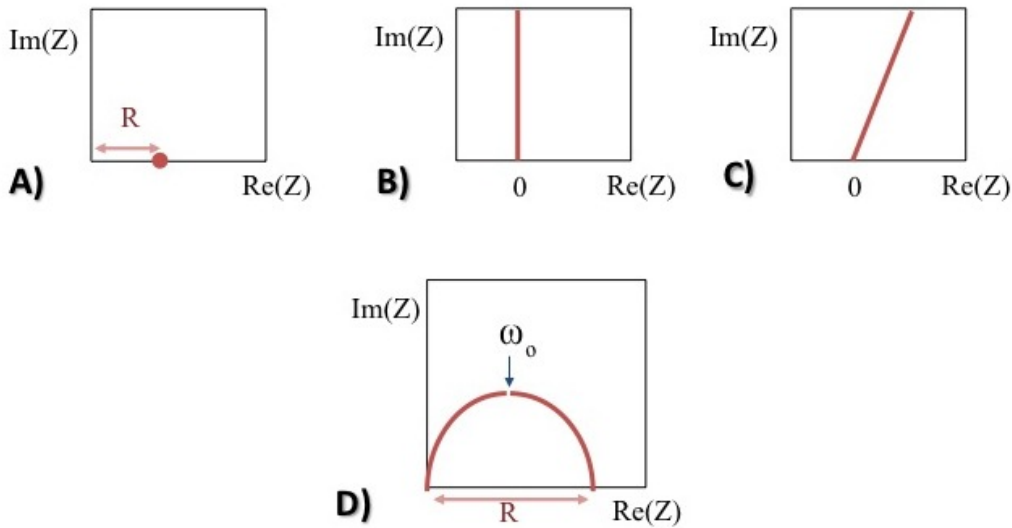


Figure 2.11: Graphical representations of certain electric circuit elements on the complex impedance plane. A) Resistor is a point on the real axis, because it does not have the imaginary part. B) Capacitor is a line parallel to the y-axis. C) Constant-phase element (CPE) is a line with a slope, which accounts for a $\theta \neq \frac{\pi}{2}$. D) A semicircle representing an $R \parallel C$ element with ω_0 being the characteristic frequency.

measurement the voltage amplitude is small (a few mV, typically 10 mV) so that the linearity of the response is preserved and the resulting impedance is independent of the amplitude of the perturbation. Linearity, causality and stationarity of the system are the necessary requirements to apply the Fourier transform^k to the parameters and move to the frequency domain, as the analysis of so many processes in the time regime would be too complicated. Sets of frequency-varying measurements for many (20–30) steady-potential bias steps are collected, because only in this way one can follow the changes in the processes occurring in the cell upon changing quasi-Fermi levels. For each bias potential step a Nyquist plot is usually analyzed and fitted. The main issue of impedance data treatment is the application of a physically relevant model, where each fitted circuit element describes the process that is suspected to happen in the device under operation. Apparently, the one and only fit to an impedance curve does not exist, therefore a heavy burden of the wise choice of the fitting parameters and their interpretation lies on the shoulder of the experimentalist.

DSC electric circuit models. A very comprehensive guide for application of EIS to DSCs is

^k $\hat{f}(\xi) = \int_{-\infty}^{\infty} f(x) \exp(-2\pi i x \xi) dx$

2.4. Theoretical background of the processes within the devices and characterization methods

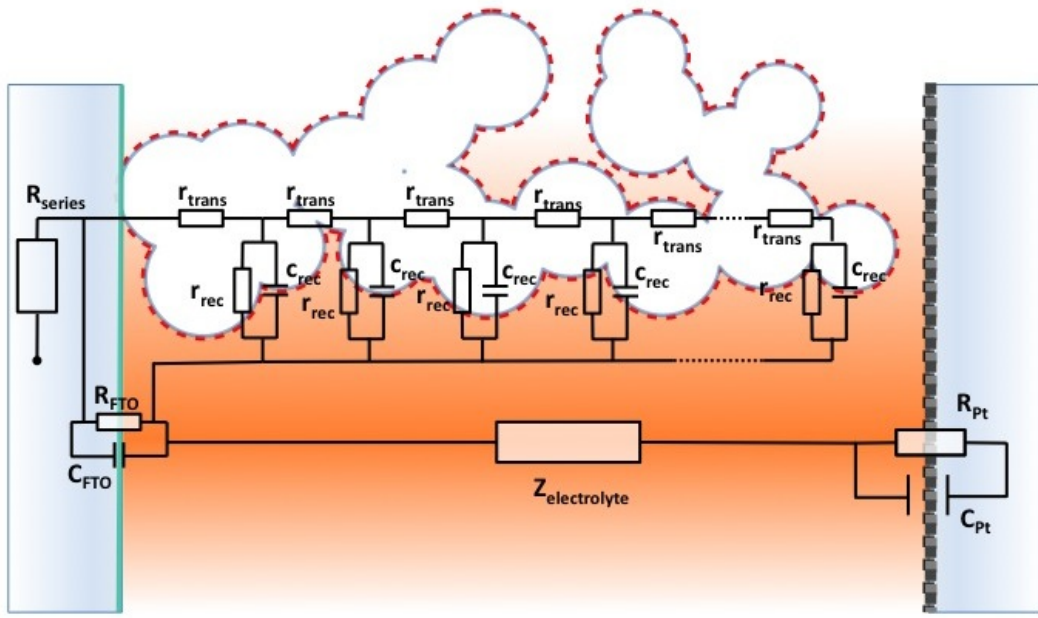


Figure 2.12: A scheme od a DSC combined with its equivalent circuit including the transmission line with one reflecting boundary conditions. The particular elements are described in more detail in the text below.

given by Bisquert and Fabregat-Santiago, who gathered all the know-how developed in the past few years⁵⁵. As mentioned above, it is crucial to identify the elements of the equivalent circuit of dye-sensitized solar cell according to their physical significance.

It has been shown that a minimal equivalent circuit describing a solar cell consists of a resistor connected in parallel with a capacitor and a current generator⁵⁶. The capacitor is at the heart of the device, because therein originates the difference in potentials, which is related to the splitting of Fermi levels. The operation of a solar cell is based on the promotion of charges from low energy levels to high energy levels via the energy of absorbed photons, therefore the reverse process is thermodynamically possible (or even probable!) and that is why the capacitor is accompanied by a resistor (leakage). Moreover, this capacitor is closer to the concept of chemical capacitance than the classic electrostatic capacitor⁴⁰, because the charge storage does not necessarily imply the change of the electric field - as it was stated before that the electrons in the conduction band of TiO_2 are effectively screened by the ions in the electrolyte.

Chapter 2. Fundamentals of dye-sensitized solar cells

Nevertheless, the DSC is a more complex system consisting of tailored components in-between which various processes occur at wide range of timescales. EIS cannot resolve the ultrafast phenomena like electron absorption and injection and the power of the technique lies in monitoring the behaviour of the electrons in the electron-transporting media (TiO_2 and electrolyte). The full equivalent circuit of DSC is presented in the Figure 2.12. The elements used for fitting the impedance data are as follows:

- **R_{series}** - is a series resistance, which groups all the external contacts to the cell (wires, metal contacts, sheet resistance FTO, electrolyte resistance). In a data plot it is the distance from the origin on the x-axis.
- **Counter-electrode, $R_{Pt} \parallel C_{Pt}$** - since it appears as a semicircle, an RC element is used for its fitting. It incorporates the information about the effectiveness of the I_3^- regeneration and the related with it Helmholtz layer in the vicinity of the counter-electrode.
- **$TiO_2/electrolyte interface$** - describing mainly the recombination processes. The total capacitance, C_{ct} , is in reality a combination of the chemical capacitance of TiO_2 and the capacitance of the Helmholtz layer in the electrolyte, $C = (C_{TiO_2}^{-1} + C_H^{-1})^{-1}$. In fact, each TiO_2 grain in contact with the electrolyte is described locally by a simple $R \parallel C$ circuit, which are collectively treated as a transmission line (vide infra). Nevertheless, a single semicircle is observed in the measurement results, so that a one cumulative circuit is used for a fitting model.
- **FTO/electrolyte interface, $R_{FTO} \parallel C_{FTO}$** - does not appear as a separate semicircle at high forward bias, however, the influence of the FTO capacitance on the overall cell capacitance has to be taken into consideration especially under low light conditions, when TiO_2 acts as an insulator.
- **Electrolyte** - diffusion of ions characterized by the Warburg resistance (short, because the diffusion is finite). Can only be seen at high forward current flow.

Additionally, as seen in the Figure 2.12, the nanostructured and mesoporous semiconductor layer is modelled by a transmission line including diffusion and recombination processes with

2.4. Theoretical background of the processes within the devices and characterization methods

reflecting boundary conditions at the end of the electron transport channel. The impedance for this element is given by the Equation 2.41⁵⁷.

$$Z(\omega) = \left(\frac{R_{trans} R_{rec}}{1 + \frac{i\omega}{\omega_{rec}}} \right)^{\frac{1}{2}} \coth \left[\left(\frac{R_{trans}}{R_{rec}} \right)^{\frac{1}{2}} \left(1 + \frac{i\omega}{\omega_{rec}} \right)^{\frac{1}{2}} \right] \quad (2.41)$$

The shape of the spectrum of this element is in general a semicircle, but in particular it depends on the ratio of the R_{rec} to R_{trans} . If $R_{rec} > R_{trans}$, the cell should be giving high efficiencies, since the main electron loss channel is blocked. The transmission line manifests itself as a straight line of a slope of 45° in addition to the semicircle and the value of R_{trans} can be extracted, following the Equation 2.42. However, on the contrary, when the recombination processes dominate the cell and the injected electrons are transferred to the electrolyte, the spectrum shape does not allow for the deconvolution of the values of the resistances (Equation 2.43).

$$Z = \frac{R_{trans}}{3} + \frac{R_{rec}}{1 + \frac{i\omega}{\omega_{rec}}} \quad (2.42)$$

$$Z = \left(\frac{R_{trans} R_{rec}}{1 + \frac{i\omega}{\omega_{rec}}} \right)^{\frac{1}{2}} \quad (2.43)$$

Parameters obtained from the EIS measurements. The full model presented in the section above in practice is simplified in order to reduce the number of parameters during fitting process. Typically, the interface between the FTO and TiO_2 , which would be represented by an $R \parallel C$ element, is omitted, because the contact between these materials is ohmic. There are in general three applied potential regions, where different simplifications of the equivalent circuit could be introduced. The application of the simplified models lies with the person treating the data and is mainly based on the experience.

- I. **High applied potentials** cause the Fermi level to move close to the conduction band and increase the population of electrons therein. Therefore the conductivity of the semiconductor is high (R_{trans} is low) and the transmission line is reduced to a simple $R_{ct} \parallel C_{ct}$ element. Three semicircles are observed in the spectrum corresponding to (in order of appearance) counter-electrode processes, charge-transfer processes at the

TiO₂/electrolyte interface and ion diffusion in the electrolyte.

II. **Intermediate potentials** enable the full expression of the complicated nature of the TiO₂/electrolyte interface in the form of the transmission line recognized by the straight line of the slope of 45° between the counter-electrode and charge-transfer semicircles. In this region also the capacitance of FTO starts to play more important role and is included in the fitting model. The Warburg element could be omitted, as the semicircle associated with the ion diffusion is very small with regards to the growing charge-transfer semicircle and these two merge.

III. At **low potentials** the TiO₂ becomes an insulator and the recombination processes take place at the FTO/electrolyte interface. The spectrum appears as an arc of a very large radius. The counter-electrode arc in some cases could still be distinguished and fitted, however, it is extremely small in comparison with the charge-transfer semicircle.

After fitting a set of IS spectra there is much useful information that can be derived from the fitted parameters. There are also some corrections that need to be applied in order to obtain true characteristics of the device.

First correction that should be applied is the correction of the applied potential (V_{app}). The potential set by the potentiostat is not precisely the same that is experienced by the interface due to the transport resistances connected in series (Equation 2.44). The IR drop correction (Equation 2.45) is therefore smaller at high bias and increases with its decrease. A certain value is obtained for each potential step and then subtracted from it.

$$R_{all} = W_{el} + R_{series} + R_{Pt} + \frac{1}{3}R_{trans} \quad (2.44)$$

$$\Delta V = \int R_{all} dI \quad V_{corr} = V_{app} - \Delta V \quad (2.45)$$

During the fitting of the data, some of the capacitances are replaced by constant-phase element to account for the non-ideality of the system. Nevertheless, it is important to observe the variation of the exponent n (Equation 2.40), which gives an estimate of how far from ideal is the behaviour of a particular capacitive component. Typically the value should be kept in

2.4. Theoretical background of the processes within the devices and characterization methods

0.8–0.95 range. To account for the use of CPE elements and as well for the fact that it is not easy to clearly distinguish between the contributions from TiO₂ and FTO, Equation 2.46 is used to calculate the overall capacitance of the device.

$$C_{all} = \underbrace{\frac{(R_{rec} CPE_{TiO_2}^T)^{\frac{1}{CPE_{TiO_2}^P}}}{R_{rec}}}_{C_{ct}} + \frac{(R_{rec} CPE_{FTO}^T)^{\frac{1}{CPE_{FTO}^P}}}{R_{rec}} \quad (2.46)$$

The calculated capacitance can be used to derive the density of states following the Equation 2.47.

$$DOS = \frac{C_{ct}}{qd(1-p)} \quad (2.47)$$

Recombination resistance, similarly to the capacitance, could be analyzed within the three potential regions. Low bias implies small number of charges, therefore the recombination rate is low. The recombination resistance here originates purely from the electrochemical reactions at the blocking layers applied to FTO substrate not covered with the mesoporous TiO₂ layer. The slope in this region is not large, because the resistance of this layer stays relatively constant. When the steepness of the curve is increasing and a linear behaviour is observed while going to the high applied potentials, the recombination via TiO₂ starts to play an important role. The recombination resistance in combination with the corrected capacitance (or CPE_{rec}) give the apparent electron lifetime (Equation 2.48) - a parameter which can be directly compared with the result obtained from the transient techniques.

$$\tau_n = (R_{rec} CPE_{rec})^{\frac{1}{n}} \approx R_{rec} C_{all} \quad (2.48)$$

The transport resistance, R_{trans}, can be only obtained in a regime of potentials (high-intermediate or only intermediate). Nevertheless, it enables the derivation of a set of useful parameters for

the direct comparisons between different systems.

Transport time: $\tau_{trans} = R_{trans} C_{all}$ (2.49)

Diffusion coefficient: $D_{coeff} = \frac{d^2}{R_{trans} C_{all}}$ (2.50)

Diffusion length: $D_l = \sqrt{\tau_n D_{coeff}}$ (2.51)

Conductivity $\sigma = \frac{d}{R_{trans} A(1-p)}$ (2.52)

Charge collection efficiency: $\eta_{col} = \frac{1}{1 + \frac{R_{trans}}{R_{rec}}}$ (2.53)

The characteristics resulting from EIS measurement gives a very detailed picture of the DSC, however, the interpretation of the data is not trivial. Although the IR correction is introduced to the applied potential, one should remember that comparison of the cells should be made under the conditions when the quasi-Fermi levels are displaced against the conduction band edge by the same value, i.e. the distribution and filling of the trap states are equal. The results from EIS measurement could be used independently, but also either as complimentary or as a cross-check to the transient techniques. It is also worth noting, that the idea of application of this particular technique to DSCs triggered many discussions, brain-storming and shed bright light on the interfacial processes within this complex device.

2.5 Bibliography

- [1] W. Shockley and H.-J. Queisser, *Journal of Applied Physics*, 1961, **32**, 510–519.
- [2] B. O'Regan and M. Grätzel, *Nature*, 1991, **353**, 737–740.
- [3] H. W. Vogel, *Photographische Mittheilungen*, 1873, **10**, 233–237.
- [4] H. Gerischer and F. Willig, in *Topics in Current Chemistry: Physical and Chemical Applications of Dyestuffs*, Springer, Germany, 1976, vol. 61, ch. Reaction of Excited Dye Molecules at Electrodes, pp. 31–84.

-
- [5] H. Tributsch and M. Calvin, *Photochemistry and Photobiology*, 1971, **14**, 95–112.
- [6] H. Tributsch, *Photochemistry and Photobiology*, 1972, **16**, 261–269.
- [7] A. Yella, H.-W. Lee, H. N. Tsao, C. Yi, A. K. Chandiran, M. Nazeruddin, E. W.-G. Diau, C.-Y. Yeh, S. M. Zakeeruddin and M. Grätzel, *Science*, 2011, **334**, 629–634.
- [8] M. K. Nazeruddin, A. Kay, I. Rodicio, R. Humphry-Baker, E. Müller, P. Liska, N. Vlachopoulos and M. Grätzel, *Journal of the American Chemical Society*, 1993, **115**, 6382–6390.
- [9] M. K. Nazeruddin, S. M. Zakeeruddin, R. Humphry-Baker, M. Jirousek, P. Liska, N. Vlachopoulos, V. Shklover, C.-H. Fischer and M. Grätzel, *Inorganic Chemistry*, 1999, **38**, 6298–6305.
- [10] M. K. Nazeruddin, P. Péchy and M. Grätzel, *Chemical Communications*, 1997, 1705–1706.
- [11] P. Wang, S. Zakeeruddin, J.-E. Moser, M. Nazeruddin, T. Sekiguchi and M. Grätzel, *Nature Materials*, 2003, **2**, 402–407.
- [12] Y. Cao, Y. Bai, Q. Yu, Y. Cheng, S. Liu, D. Shi, F. Gao and P. Wang, *The Journal of Physical Chemistry C*, 2009, **113**, 6290–6297.
- [13] N. Robertson, *Angewandte Chemie International Edition*, 2006, **45**, 2338–2345.
- [14] C.-Y. Chen, M. Wang, J.-Y. Li, N. Pootrakulchote, L. Alibabaei, C. ha Ngoc-le, J.-D. Decoppet, J.-H. Tsai, C. Grätzel, C.-G. Wu, S. M. Zakeeruddin and M. Grätzel, *ACS NANO*, 2009, **3**, 3103–3109.
- [15] M. K. R. Fischer, S. Wenger, M. Wang, A. Mishra, S. M. Zakeeruddin, M. Grätzel and P. Bäuerle, *Chemistry of Materials*, 2010, **22**, 1836–1845.
- [16] J. Burschka, A. Dualeh, F. Kessler, E. Baranoff, N.-L. Cevey-Ha, C. Yi, M. K. Nazeruddin and M. Grätzel, *Journal of the American Chemical Society*, 2011, **133**, 18042–18045.
- [17] H. Nusbaumer, J.-E. Moser, S. M. Zakeeruddin, M. K. Nazeruddin and M. Grätzel, *The Journal of Physical Chemistry B*, 2001, **105**, 10461–10464.
- [18] G. Oskam, B. V. Bergeron, G. J. Meyer and P. C. Searson, *The Journal of Physical Chemistry B*, 2001, **105**, 6867–6873.
- [19] Z. Yu, N. Vlachopoulos, M. Gorlov and L. Kloo, *Dalton Transactions*, 2011, **40**, 10289.
- [20] S. M. Feldt, E. A. Gibson, E. Gabrielsson, L. Sun, G. Boschloo and A. Hagfeldt, *Journal of the American Chemical Society*, 2010, **132**, 16714–16724.

-
- [21] T. Daeneke, T.-H. Kwon, A. B. Holmes, N. W. Duffy, U. Bach and L. Spiccia, *Nature Chemistry*, 2011, **3**, 211–215.
- [22] M. Wang, N. Chamberland, L. Breau, J.-E. Moser, R. Humphry-Baker, B. Marsan, S. M. Zakeeruddin and M. Grätzel, *Nature Chemistry*, 2010, **2**, 385–389.
- [23] C. Law, S. C. Pathirana, X. Li, A. Y. Anderson, P. R. F. Barnes, A. Listorti, T. H. Ghaddar and B. C. O'Regan, *Advanced Materials*, 2010, **22**, 4505–4509.
- [24] T. Daeneke, Y. Uemura, N. W. Duffy, A. J. Mozer, N. Koumura, U. Bach and L. Spiccia, *Advanced Materials*, 2012, **24**, 1222–1225.
- [25] Y. Bai, Y. Cao, J. Zhang, M. Wang, R. Li, P. Wang, S. M. Zakeeruddin and M. Grätzel, *Nature Materials*, 2008, **7**, 626–630.
- [26] L. Kavan, J.-H. Yum and M. Grätzel, *Nano Letters*, 2011, **11**, 5501–5506.
- [27] H. N. Tsao, J. Burschka, C. Yi, F. Kessler, M. K. Nazeeruddin and M. Grätzel, *Energy and Environmental Science*, 2011, **4**, 4921–4924.
- [28] J. B. Asbury, R. J. Ellingson, H. N. Ghosh, S. Ferrere, A. J. Nozik and T. Lian, *The Journal of Physical Chemistry B*, 1999, **103**, 3110–3119.
- [29] S. Wenger, P.-A. Bouit, Q. Chen, J. Teuscher, D. D. Censo, R. Humphry-Baker, J.-E. Moser, J. L. Delgado, N. Martin, S. M. Zakeeruddin and M. Grätzel, *Journal of the American Chemical Society*, 2010, **132**, 5164–5169.
- [30] S. Pelet, J.-E. Moser and M. Grätzel, *The Journal of Physical Chemistry B*, 2000, **104**, 1791–1795.
- [31] J. N. Clifford, E. Palomares, M. K. Nazeeruddin, M. Grätzel and J. R. Durrant, *The Journal of Physical Chemistry C*, 2007, **111**, 6561–6567.
- [32] 2013, http://en.wikipedia.org/wiki/Solar_cell.
- [33] *Practical handbook of photovoltaics: fundamentals and applications*, ed. A. McEvoy, T. Markvart and L. Castañer, Elsevier Ltd., 2nd edn., 2012.
- [34] S. Ito, M. K. Nazeeruddin, P. Liska, P. Comte, R. Charvet, P. Péchy, M. Jirousek, A. Kay, S. M. Zakeeruddin and M. Grätzel, *Progress in Photovoltaics: Research and Applications*, 2006, **14**, 589–601.
- [35] H. J. Snaith, *Energy and Environmental Science*, 2012, **5**, 6513–6520.

-
- [36] P. R. F. Barnes, A. Y. Anderson, S. E. Koops, J. R. Durrant and B. C. O'Regan, *The Journal of Physical Chemistry C*, 2009, **113**, 1126–1136.
 - [37] S. Ardo and G. J. Meyer, *Chemical Society Reviews*, 2009, **38**, 115–164.
 - [38] P. R. F. Barnes, A. Y. Anderson, J. R. Durrant and B. C. O'Regan, *Physical Chemistry Chemical Physics*, 2011, **13**, 5798–5816.
 - [39] N. Kopidakis, E. A. Schiff, N.-G. Park, J. van de Lagemaat and A. J. Frank, *The Journal of Physical Chemistry B*, 2000, **104**, 3930–3936.
 - [40] L. Dloczik, O. Ileperuma, I. Lauermann, L. M. Peter, E. A. Ponomarev, G. Redmond, N. J. Shaw and I. Uhendorf, *The Journal of Physical Chemistry B*, 1997, **101**, 10281–10289.
 - [41] L. M. Peter, *Journal of Electroanalytical Chemistry*, 2007, **599**, 233–240.
 - [42] P. E. de Jongh and D. Vanmaekelbergh, *Physical Review Letters*, 1996, **77**, 3427–3430.
 - [43] J. Bisquert and V. S. Vkhrenko, *The Journal of Physical Chemistry B*, 2004, **108**, 2313–2322.
 - [44] M. J. Cass, F. L. Qiu, A. B. Walker, A. C. Fisher and L. M. Peter, *The Journal of Physical Chemistry B*, 2003, **107**, 113–119.
 - [45] S. Soedergren, A. Hagfeldt, J. Olsson and S.-E. Lindquist, *The Journal of Physical Chemistry*, 1994, **98**, 5552–5556.
 - [46] N. Duffy, L. Peter and K. Wijayantha, *Electrochemistry Communications*, 2000, **2**, 262–266.
 - [47] A. B. Walker, L. M. Peter, K. Lobato and P. J. Cameron, *The Journal of Physical Chemistry B*, 2006, **110**, 25504–25507.
 - [48] L. M. Peter, *The Journal of Physical Chemistry C*, 2007, **111**, 6601–6612.
 - [49] J. Bisquert, F. Fabregat-Santiago, I. Mora-Sero, G. Garcia-Belmonte and S. Giménez, *The Journal of Physical Chemistry C*, 2009, **113**, 17278–17290.
 - [50] B. C. O'Regan, K. Bakker, J. Kroese, H. Smit, P. Sommeling and J. R. Durrant, *The Journal of Physical Chemistry B*, 2006, **110**, 17155–17160.
 - [51] R. de Levie, *Electrochimica Acta*, 1963, **8**, 751–780.
 - [52] J. Bisquert, G. Garcia-Belmonte, F. Fabregat-Santiago, N. S. Ferriols, P. Bogdanoff and E. C. Pereira, *The Journal of Physical Chemistry B*, 2000, **104**, 2287–2298.

-
- [53] G. Schlichthörl, S. Y. Huang, J. Sprague and A. J. Frank, *The Journal of Physical Chemistry B*, 1997, **101**, 8141–8155.
 - [54] *Impedance Spectroscopy Theory, Experiment, and Applications*, ed. E. Barsoukov and J. R. Macdonald, John Wiley and Sons, Inc., 2nd edn., 2005.
 - [55] J. Bisquert and F. Fabregat-Santiago, in *Dye-Sensitized Solar Cells*, ed. K. Kalayanasundaram, EPFL Press, 1st edn., 2010, ch. Impedance spectroscopy: a general introduction and application to dye-sensitized solar cells.
 - [56] J. Bisquert, *Physical Chemistry Chemical Physics*, 2003, **5**, 5360–5364.
 - [57] J. Bisquert, *The Journal of Physical Chemistry B*, 2002, **106**, 325–333.

3 Experimental methods

3.1 UV-Vis spectroscopy, dye loading experiments

UV-Vis spectra were recorded with CARY 5 UV-Vis-NIR spectrophotometer (Varian, Inc., USA) For the dyes dissolved in a respective solvent a standard fluorescence cuvette (Suprasil quartz, 111-QS, Hellma, Germany) with a path length 10×10 mm was used. Measurements of the dyes adsorbed on the film were realized with the transparent TiO_2 films. The nanoparticles of $20 \text{ nm} \varnothing$ were screen-printed on the thin glass. For various experiments films of different thicknesses were used - the thinnest being $1.8 \mu\text{m}$ and the thickest - $5.5 \mu\text{m}$. A non-stained film of a similar thickness was typically used as a blank.

Dye desorption studies were realized also with the aid of CARY 5 spectrophotometer. The experiment procedure is organized in a few steps:

1. **Dye adsorption on the film.** The film is sintered and additionally heated (if needed) prior to the immersion in the dye solution. The dye solution is no different than the one used for cell preparation.
2. **Measurement of the UV-Vis absorption spectrum of the dye adsorbed on the film.** The films are rinsed in the pure solvent to remove the excess of the dye and then dried in the air to remove the solvent.
3. **Dye desorption.** The still-stained films are placed in the known volume of the solution

Chapter 3. Experimental methods

of TBAOH (tetrabutylammonium hydroxide) in a respective solvent (0.5 g/50 ml solvent). The desorption time varies from 4 to 18 hours.

4. UV-Vis measurement of the solution of the desorbed dye.

For data evaluation the fundamental Beer-Lambert law was applied (Equation 3.1).

$$A = l \times c \times \varepsilon, \quad (3.1)$$

where A is absorbance, l - the length of the optical path, c - the concentration of the species, ε - the molar extinction coefficient of the dye. For the standard absorption measurement of the dyes a cuvette of an optical pathlength of 10 mm was used (*see supra*). As for dye loading measurements on the film, the film thickness was used as a "cuvette" pathlength. In order to estimate the concentration of the dye adsorbed on the surface a few assumptions must be taken. Due to the fact that the precise value for the surface area cannot be obtained (nanoparticulate film with voids and channels distributed randomly), we were using the films prepared within the same batch. In this way the parameters of paste (e.g. viscosity) determining the final pore size and their distribution within the film were kept constant, so that the layers can be compared directly. The thickness of each film was measured separately. In conclusion, the values of measured dye concentrations on the film normalized to the films' thicknesses allow for a direct comparison if and only if the films that were used during the experiment were from the same batch. This condition was always rigorously fulfilled.

3.2 Electrochemistry

The experimental evaluation of redox potentials of the dyes was obtained via a typical three-electrode setup placed in an Ar filled glovebox. Measurements were performed on a PC-controlled Autolab system (PGSTAT30, Metrohm, Switzerland). A glassy carbon electrode was used as a working electrode, accompanied by a Pt plate as an auxilliary electrode. Pt wire served as a quasi-reference electrode. Ferrocene/ferrocenium couple was additionally used as an internal standard. The concentration of the dye in the solution was at the level of 0.1–0.5 mM; the solution contained also the supporting electrolyte salt: 0.1 M TBAPF₆

3.3. Viscosity measurements

(tetrabutylammonium hexafluorophosphate). Cyclic Voltammetry (CV), as well as Differential Pulse Voltammetry (DPV) were used to observe the reversibility of the redox processes and precise determination of the potentials, respectively.

3.3 Viscosity measurements

The viscosities of the electrolytes, especially the ionic-liquid-based ones, were determined by using HAAKE Rheostress 1 Rheometer (Thermo Scientific) equipped with a HAAKE DC50 Thermostat (Thermo Scientific). Experiments and data acquisition were supported by the HAAKE RheoWin software. A Ti cone of a diameter of 20 mm and an angle of 0.5° was used for all the measurements. Samples were measured at 20°C. The applied shear rate was in the range 10–8000 s⁻¹ for electrolytes (10–2000 s⁻¹ for pure ionic liquids), and equilibration time of 30 s was used for each shear rate step. The ionic-liquid-based electrolytes are non-newtonian fluids, exhibiting thixotropic behaviour. In order to obtain comparable values for all the samples, a straight line was fitted to a plateau in the low shear rate region for each plot. A point for the lowest applied shear rate (10 s⁻¹) was neglected.

3.4 Fourier Transformed Infrared Spectroscopy

ATR-FTIR (Attenuated Total Reflection FTIR) technique was used to study the binding mode on the TiO₂ surface of the dyes in the Chapter 6. The spectra were recorded on the FTS7000 FTIR spectrometer (Digilab, USA) equipped with a "Golden Gate" diamond anvil. The anvil was pressed firmly against the sample (powder or dye adsorbed on the film) so that the intimate contact between these two was maintained during the experiment. Spectra was integrated from 64 individual scans at a resolution of 2 cm⁻¹. No ATR correction was applied to the data. The films used for measurements were rinsed with acetonitrile and dried prior to measuring the spectra. Obtained data was processed by subtraction of the absorption spectrum of TiO₂, surface water and carbon dioxide.

3.5 Device fabrication

At the heart of the device there is a mesoporous layer of TiO_2 nanoparticles. It is deposited on the fluorine doped SnO_2 (FTO) glass (NSG10, Nippon Sheet Glass, Japan) by the screen-printing method. The nanoparticles (of various sizes) are made into a paste, where the ethyl cellulose content determines the porosity of a resulting film. The glass has to be carefully cleaned beforehand (rinsing with ethanol, acetone, sonification in a detergent solution, Hellmanex®, 2% in H_2O , finally - ozone cleaning for 60 min with the UVO-Cleaner®, Model No. 256–220, Jelight Company Inc., USA) and a thin layer of nanocrystalline TiO_2 is then deposited hydrothermally. Typically, a solution of 40 mM TiCl_4 is used in a bath where the glass panes are immersed and the whole thing is heated at 70°C for 30 min. Thus formed TiO_2 layer is sintered at 500°C. This ensures better adhesion of the following layers on FTO, increasing the roughness of the surface, but also it blocks the unwanted electron recombination channel (interception of the electron in the conductive transparent oxide exposed directly to the electrolyte with triiodide, which undergoes reduction). The actual screen-printing of the nanoparticulate paste is performed stepwise. The geometry of a single electrode was either circular ($\sim 0.28 \text{ cm}^2$) or square ($4 \text{ mm} \times 4 \text{ mm}$). A single screen-printed layer has $1.8\text{--}3.3 \mu\text{m}$ thickness and in order to obtain $13\text{--}15 \mu\text{m}$ film the layers have to be printed multiple times. In between each paste deposition (printing) the freshly deposited layer is levelled for 3–6 min, allowing for an even distribution of the paste, and then sintered for 10 min at 125°C. Many different films were prepared, according to the purpose they were supposed to serve:

- for optical measurements thin transparent films (particles of $20 \text{ nm} \varnothing$, home-made paste^{1–3}, thickness: $1.8\text{--}5.5 \mu\text{m}$) were made;
- for transparent cells typically $5\text{--}8 \mu\text{m}$ films of 20–23 nm-sized nanoparticles (home-made pastes⁴, pore size: 23–32 nm) were printed;
- for high-performance cells a double-layer configuration was employed: 20–23 nm-sized particulate layer was placed (thickness: $8 \mu\text{m}$) at the bottom - to ensure high dye loading due to the large surface area; this transparent layer was covered by a scattering layer consisting of much larger nanoparticles ($\varnothing 400 \text{ nm}$, CCIC, Japan)

Table 3.1: Dye solution parameters.

| Dye | Concentration mM | Solvent | Additive (mM) | Dipping time |
|--------------------------|---------------------|--|----------------------------------|--------------|
| Dye 1 , Chapter 4 | 0.3 | chlorobenzene | CDCA (2 mM) | 5 h |
| Dye 2 , Chapter 4 | 0.3 | chlorobenzene | CDCA (2 mM) | 5 h |
| Dye 3 , Chapter 4 | 0.3 | chlorobenzene | CDCA (2 mM) | 5 h |
| Dye 4 , Chapter 4 | 0.3 | chlorobenzene | CDCA (2 mM) | 5 h |
| WS-2 , Chapter 5 | 0.3 | CH ₂ Cl ₂ or CHCl ₃ | no or 2 or 20 mM CDCA | 6 h |
| WS-9 , Chapter 5 | 0.3 | CH ₂ Cl ₂ or CHCl ₃ | no or 2 or 20 mM CDCA | 6 h |
| Dye 6 , Chapter 6 | 0.3 | DMSO/EtOH (1:9, v/v) | CDCA (10 mM) | 2 h |
| Dye 7 , Chapter 6 | 0.3 | DMSO/EtOH (1:9, v/v) | CDCA (10 mM) | 2 h |
| V4 , Chapter 7 | 0.1 | CH ₂ Cl ₂ | | 16 h |
| V5 , Chapter 7 | 0.3 | <i>t</i> -BuOH/MeCN (1:1, v/v) | | 16 h |
| V7 , Chapter 7 | 0.3 | CH ₂ Cl ₂ /EtOH (9:1, v/v) | | 16 h |
| V11 , Chapter 7 | 0.1 | CH ₂ Cl ₂ | | 16 h |
| Z907 , Chapter 8 | 0.3 | <i>t</i> -BuOH/MeCN (1:1, v/v) | phenylpropionic acid (0.3 mM) | 16 h |

The film is then sintered up to 500°C in a stepwise procedure under the oxygen flow ^a, carefully optimized in order to avoid cracking of the layers. Then the photoanodes undergo another TiCl₄ treatment (typically in 40 mM aqueous solution) for 30 min at 70°C. The films can be used immediately after the TiCl₄ post-treatment or stored in a dry place. They are being heated up to 450°C with a regular heat-gun just prior to the immersing in the dye solution, in order to remove water and CO₂. This last-step sintering lasts 20–30 min. The photoanodes are subsequently cooled down to ~80°C and then placed in the vial containing dye solution. The solution conditions for the dyes presented in this work are gathered in the Table 3.1.

The stained electrodes were rinsed in the pure solvents (each as used for a particular dye) prior to the assembly in order to remove the loosely bound dye molecules (unwanted aggregates). The sandwich cell structure is completed by a platinized counter-electrode made of a piece of conducting glass as well (TEC7, Pilkington, UK). The glass piece contains a hole, drilled

^aThe sintering procedure: 15 min at 125°C, 5 min ramp and 5 min at 150°C, 10 min ramp and 5 min at 325°C, 5 min ramp and 5 min at 450°C, 5 min ramp and 30 min at 500°C and then free cooling down.

Chapter 3. Experimental methods

with a sand-blaster, via which the electrolyte is introduced into the cell after sealing these two electrodes together. Platinum, acting as a catalyst for reduction of I_3^- , is deposited thermally: a drop of 8 mM solution of hexachloroplatinic acid ($[H_3O]_2[PtCl_6] \cdot 4 H_2O$) in *n*-propanol was cast onto the glass surface heated previously for 3–5 min, uniformly spread and dried in the air. Then the electrode was placed under the heat gun and fired for 15 min in 415°C; this step was repeated once more in order to ensure good coverage of the surface by the catalyst. The assembly of the two electrodes together was done with the aid of a polymer binder - in a form of a ring or a frame - made of 25- μm -thick Surlyn® (DuPont™, USA), which was placed on the counter-electrode around the hole, and the photoanode was put on the top of it. Everything was pressed together and heated from the bottom for 9–12 s, so that the polymer could melt and then solidify after a while, leaving the two pieces of glass sealed. The electrolyte was introduced via the pre-drilled hole using back-vacuum system. This step is required to be performed relatively quickly, especially when using volatile electrolytes, in order not to alter the concentrations of the electrolyte ingredients. In case of viscous electrolytes the problem arises when sometimes a small air bubble is trapped within the device. It was found that it does not have influence on the stability of the device. Finally, the metal contacts made of low-melting-temperature alloy (186–246°C, Cerasolzer, MBR Electronics GmbH, Switzerland), deposited on the free space of both electrodes. Most of the cells was equipped with a UV-cut-off and antireflecting filter ($\lambda < 380$ ARKTOP, Asahi Glass Co., Ltd, Japan) on the top and a back reflector made of an aluminum tape at the back.

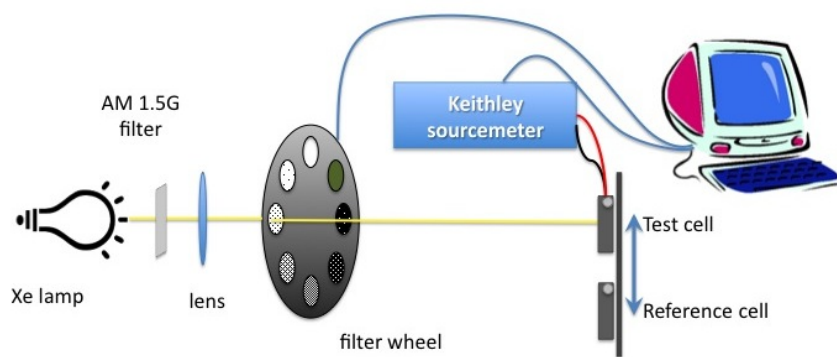


Figure 3.1: A schematic illustration of the basic components of the home-built setup for I-V characterization. For a detailed description see the text.

3.6 Photovoltaic characterization

A standard photovoltaic characterization (I-V curves) was performed on the home-made setup (Figure 3.1). The lamp used in this setup was a 450 W xenon lamp (LOT Oriel, USA), which spectral output was corrected in the region between 350 and 750 nm with a Schott K113 Tempax sunlight filter (Präzisions Glas & Optik GmbH, Germany) in order to reduce the mismatch between the simulated and real solar spectra (AM 1.5G) to less than 2%. The beam intensity was varied through additional filters not affecting the wavelength (mesh attenuators giving 0.63, 0.5, 0.3, 0.1 and 0.01 Sun intensity) and referenced by the calibrated silicon photodiode (Fraunhofer ISE, Freiburg, Germany and NREL, Boulder, CO, USA) equipped with a KG5 Schott filter to better approximate the absorption profile of the dyes. The current-voltage characteristics of the cell under these conditions were obtained by applying external potential bias to the cell and measuring the generated photocurrent with a Keithley 2400 digital source-meter (Keithley, USA). The potential scanning rate was optimized in such a way to ensure steady-state conditions and avoid current "overshoots". Typically it was 100 ms per voltage step (10 mV); for some of the cells with ionic-liquid-based electrolytes the scan rate was extended up to 1 s per voltage step. The cells were masked properly with a black metal mask⁵ that also defined the cells' active area to 0.159 cm² (round TiO₂ layers) or 0.16 cm² (square geometry).

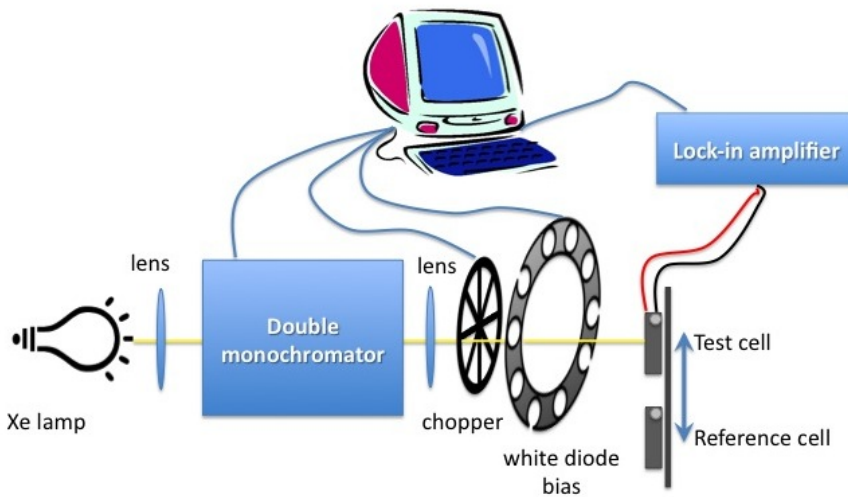


Figure 3.2: A schematic illustration of the basic components of the home-built setup to measure external quantum efficiency. For a detailed description see the text.

3.7 External quantum efficiency - IPCE

A spectral response to different incident wavelengths is essential information in evaluation of a new dye. External quantum efficiency, termed also Incident Photon-to-current Conversion Efficiency (IPCE) is measured in our lab with the use of another home-built setup (Figure 3.2). The light from a 300 W xenon arc lamp (ILC Technology, USA) is focused through a Gemini-180 double monochromator (Jobin Yvon Ltd., UK) and additionally modulated with a chopper (frequency range: 1–4 Hz). The intensity of the incident beam is rather low (~ 0.01 Sun), therefore in some cases additional DC white light bias (1–10%) provided by the diode array is applied in order to obtain measurable signal with an acceptable signal-to-noise ratio. A lock-in amplifier (SR 830, Stanford Research System, USA) measured the modulated AC photocurrent under short-circuit conditions.

3.8 Transient photocurrent/photovoltage measurements

Transient measurements were all performed on the home-built setup (Figure 3.3) consisting of a light source, a Keithley 2602 source-meter (Keithley, USA) and a computer. The white, steady-state light was provided by the LED array, intensity of which was controlled automatically

3.9. Fluorescence spectroscopy and Time-correlated Single Photon Counting

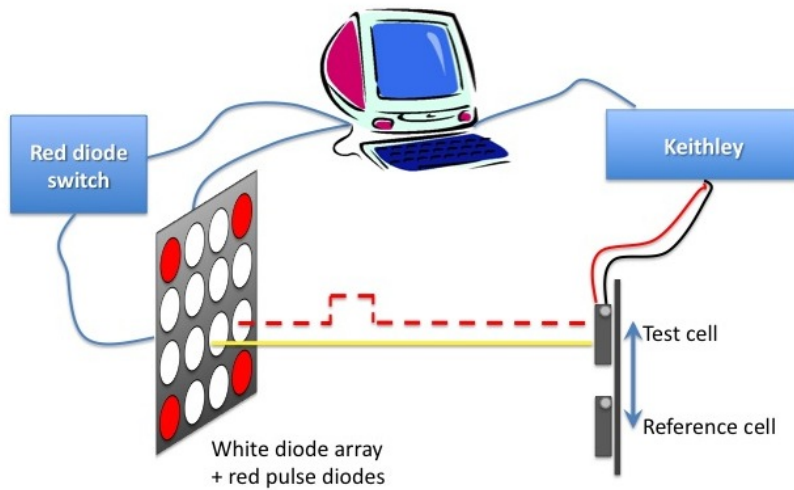


Figure 3.3: A schematic illustration of the basic components of the home-built setup for transient photovoltage/photocurrent measurements. For a detailed description see the text.

by the computer software. A red light (LED array) perturbation pulse, whose intensity was controlled manually so that the perturbation is less than 10% (typically it was controlled to be $\sim 1\%$ with regards to the V_{OC}), was superimposed on the white bias light. The superimposed pulses were adjusted in this way in order to maintain single-exponential voltage decay. Varying the intensity of the white light bias allowed the estimate of recombination rate constant (and thus apparent electron lifetime) at different open-circuit potentials by controlling the concentration of the free charges in TiO_2 .

3.9 Fluorescence spectroscopy and Time-correlated Single Photon Counting

For some dye molecules in solution and adsorbed on TiO_2 films a fluorescence study was conducted. Fluorescence steady-state emission and emission dynamics was measured at a right-angle with the use of Fluorolog-312 spectrofluorimeter (Horiba Jobin Yvon, Japan). The basic system is built with a 450 W xenon arc lamp, double-grating excitation and emission monochromators and an emission photomultiplier with photon-counting detection TBX-04. The emission lifetime was measured using the Time-correlated Single Photon Counting add-on FluoroHub in a front-face detection mode. The excitation beam was provided by the

Chapter 3. Experimental methods

NanoLED pulsed laser diode, emitting at 406 nm.

3.10 Photoinduced Absorption Spectroscopy

The photoinduced absorption spectra of the whole cells were recorded using a home-built setup. A white light probe beam falls on a sample and is intercepted by another one coming from the modulated pump light source. Here, a 20W halogen lamp was used as a probe source. The beam was filtered and focused on the sample prior to being refocused on the slits of a double monochromator (Gemini-180, Jobin Yvon Ltd., UK). A cooled dual colour solid-state detector (Si/InGaAs) was placed on the exit slits of the monochromator. The effective spectral range for investigation was 300—1650 nm. In order to resolve AC signals, a dual phase lock-in amplifier (SR 830, Stanford Research System, USA) was employed. The measured signal was the change in transmission as a function of the wavelength ($\frac{\Delta T}{T}(\lambda)$)

3.11 Electrochemical Impedance Spectroscopy

The electrochemical measurements were performed not only on the whole DSCs, but also on the symmetrical "dummy" cells - electrolyte sandwiched between two platinized pieces of FTO glass (see eg. Chapter 8). The setup, Autolab Frequency Analyzer (Metrohm, Switzerland), consists of a potentiostat (Autolab PGSTAT30) and a Frequency Response Analyzer Module. A sinusoidal AC potential perturbation of 10 mV with a frequency ranging between 1 MHz and 0.1 Hz was superimposed on a DC potential bias. Forward bias potentials were varied between 0 and 600—800 mV, depending on the V_{OC} of a particular device with potential step of 25 or 50 mV. While measuring, the devices were kept in a dark Faradaic cage, however, for the measurement in light conditions, the illumination was provided by the white LED (LXM3-PW51, Luxeon Rebel, Philips, Netherlands). The resulting data was analysed and fitted using the ZView software (Scribner Associates Inc., USA). The data was fitted using 1 to 3 models (equivalent circuits)^{6,7}, taking into consideration the appearance of the transmission line within a given potential range, presented in the Figure 3.4. **R_series** is a series resistance of all the connections made "outside" the cell, ie. wires, metal clips. Platinum counter-electrode is represented by a semicircle and described by two elements: a resistor (**R_Pt**) and a general

3.11. Electrochemical Impedance Spectroscopy

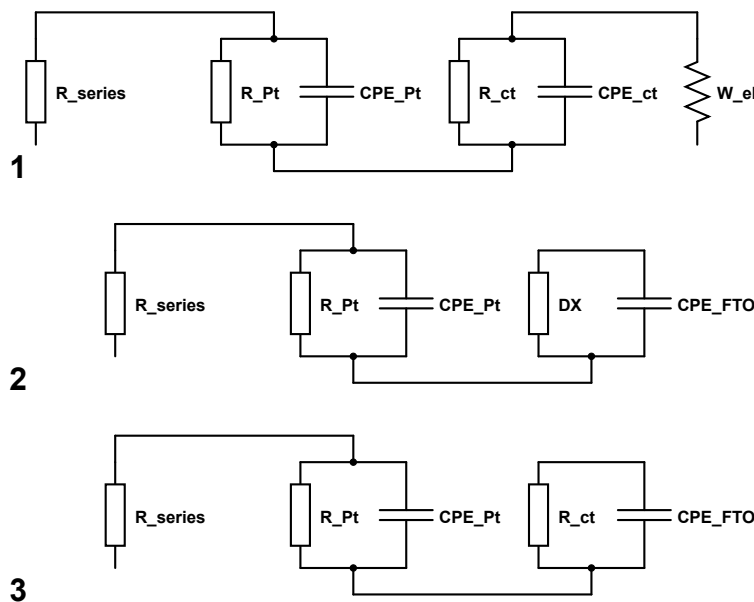


Figure 3.4: Equivalent circuits used for fitting impedance data of DSCs. (1) A model used at high applied potentials, where TiO_2 is conducting and no transmission line is seen, however, a semicircle originating from Warburg resistance of electrolyte is distinguishable. (2) A model with a transmission line incorporated in an extended element DX . (3) A model used at low applied potentials, where the conductivity of TiO_2 is rather low.

capacitor - constant phase element (**CPE_Pt**), because of its non-ideality (frequency dispersion). The TiO_2 -dye-electrolyte interface is another semicircle and is described analogously by two passive elements (R_{ct} and **CPE_ct**). As the applied potentials decrease, the appearance of a transmission line is observed in-between the semicircles of the counter-electrode and the TiO_2 -dye-electrolyte interface. In order to treat it properly an extended element, **DX11** which describes the transport in the mesoporous semiconductor was used. The parameters of the extended element include transport resistance of TiO_2 , **R_tr**, charge transfer resistance, **R_ct** and corresponding capacitive element, **CPE_ct**. Under low applied potentials the TiO_2 behaves as a very bad conductor and the capacitance of FTO starts to dominate (**CPE_FTO**). Another thing worth mentioning is the presence of a semicircle originating from the resistance of electrolyte - it is typically a limited Warburg element (**W_el**). It is only resolvable under high applied potentials.

3.12 Bibliography

- [1] S. Ito, T. N. Murakami, P. Comte, P. Liska, C. Grätzel, M. K. Nazeeruddin and M. Grätzel, *Thin Solid Films*, 2008, **516**, 4613–4619.
- [2] C. J. Barbé, F. Arendse, P. Comte, M. Jirousek, F. Lenzmann, V. Shklover and M. Grätzel, *Journal of American Ceramic Society*, 1997, **80**, 3157–3171.
- [3] P. Wang, S. M. Zakeeruddin, P. Comte, R. Charvet, R. Humphry-Baker and M. Grätzel, *The Journal of Physical Chemistry B*, 2003, **107**, 14147–1430.
- [4] H. N. Tsao, P. Comte, C. Yi and M. Grätzel, *ChemPhysChem*, 2012, **13**, 2976–2981.
- [5] H. J. Snaith, *Energy and Environmental Science*, 2012, **5**, 6513–6520.
- [6] F. Fabregat-Santiago, J. Bisquert, G. Garcia-Belmonte, G. Boschloo and A. Hagfeldt, *Solar Energy Materials and Solar Cells*, 2005, **87**, 117–131.
- [7] F. Fabregat-Santiago, G. Garcia-Belmonte, I. Mora-Seró and J. Bisquert, *Physical Chemistry Chemical Physics*, 2011, **13**, 9083–9118.

4 The influence of the structural modifications of D- π -A dyes containing benzothiadiazole as a spacer.

This part is adapted from a peer reviewed publication by Stephan Haid & Magdalena Marszalek, Amaresh Mishra, Mateusz Wielopolski, Joël Teuscher, Jacques-E. Moser, Robin Humphry-Baker, Shaik M. Zakeeruddin, Michael Grätzel and Peter Bäuerle published in 2012 in Advanced Functional Materials, Vol. 22, pp 1291–1302

4.1 Introduction

Organic dyes – metal-free donor-acceptor systems – are less expensive compared to the ruthenium complexes and offer almost unlimited design possibilities. So called D- π -A concept of a scheme for a molecule is required to ensure efficient and long-lived charge separation over a certain distance. Upon photon absorption, the electronic cloud is displaced from the donor (D) to the acceptor (A) part and the π -conjugated bridge facilitates the process. Dyes used for DSCs have their anchors located at the acceptor end, so that the electron injection to the conduction band of the sensitized semiconductor can take place. The diversity of donors, bridges and acceptors is large, which makes it feasible to tune and optimize the optical and electronic properties of the dyes.

Chapter 4. The influence of the structural modifications of D- π -A dyes containing benzothiadiazole as a spacer.

In this chapter, the study on D- π -A molecules containing a benzothiadiazole unit is presented. 2,1,3-benzothiadiazole is a bicyclic compound with unsaturated 6-membered ring fused to a 5-member heterocycle and has 10π electrons. It has been widely used as a building block in a number of materials such as polymers for organic light emitting diodes (OLEDs), liquid crystal displays (LCDs), two-photon absorbing materials, biosensors and for photovoltaic devices.

The whole study can be divided into two steps. Firstly, a set of three molecules with different π -bridges was synthesized. The compounds were characterised optically and electrochemically and subsequently used to fabricate photovoltaic devices. Although the physical properties (e.g. broad absorption range, large optical cross-section) of the compounds looked very promising, the overall devices' performance was not satisfying. Detailed characterization of the fundamental processes within the devices gave more insight into the problematic issues and showed a clear sign of an unusually short electron lifetime, translating directly into very low V_{OC} s. Additionally, the J_{SC} would be expected to be higher, given the optical properties of the compounds.

The best performing molecule was then modified by the introduction of a phenyl ring between the benzothiadiazole unit and the anchoring group. The increase in the performance was remarkable, even though the absorption spectra of the pure molecules would give more preferences to the unmodified one. A scrutinized investigation involving many tools (transient methods, EIS, laser studies) allowed for a careful elimination of the possible factors that influence the performance of the cell and led to the establishment of the crucial role of a phenyl unit as a necessary conjunction with a benzothiadiazole in a π -conjugated spacer.

4.2 Preliminary studies with thieno[3,2-b]thiophene, bithiophene and biselenophene as bridging units

4.2.1 Synthesis and characterization of the dyes

Synthesis of sensitizers. A series of low band gap D- π -A dyes (**1–3**) was synthesized for application in dye-sensitized solar cells as shown in Figure 4.1. 4-bromo-7-(bromomethyl)-benzo[c][1,2,5]-thiadiazole **4** was reacted with potassium carbonate in dioxane/water to

4.2. Preliminary studies with thieno[3,2-b]thiophene, bithiophene and biselenophene as bridging units

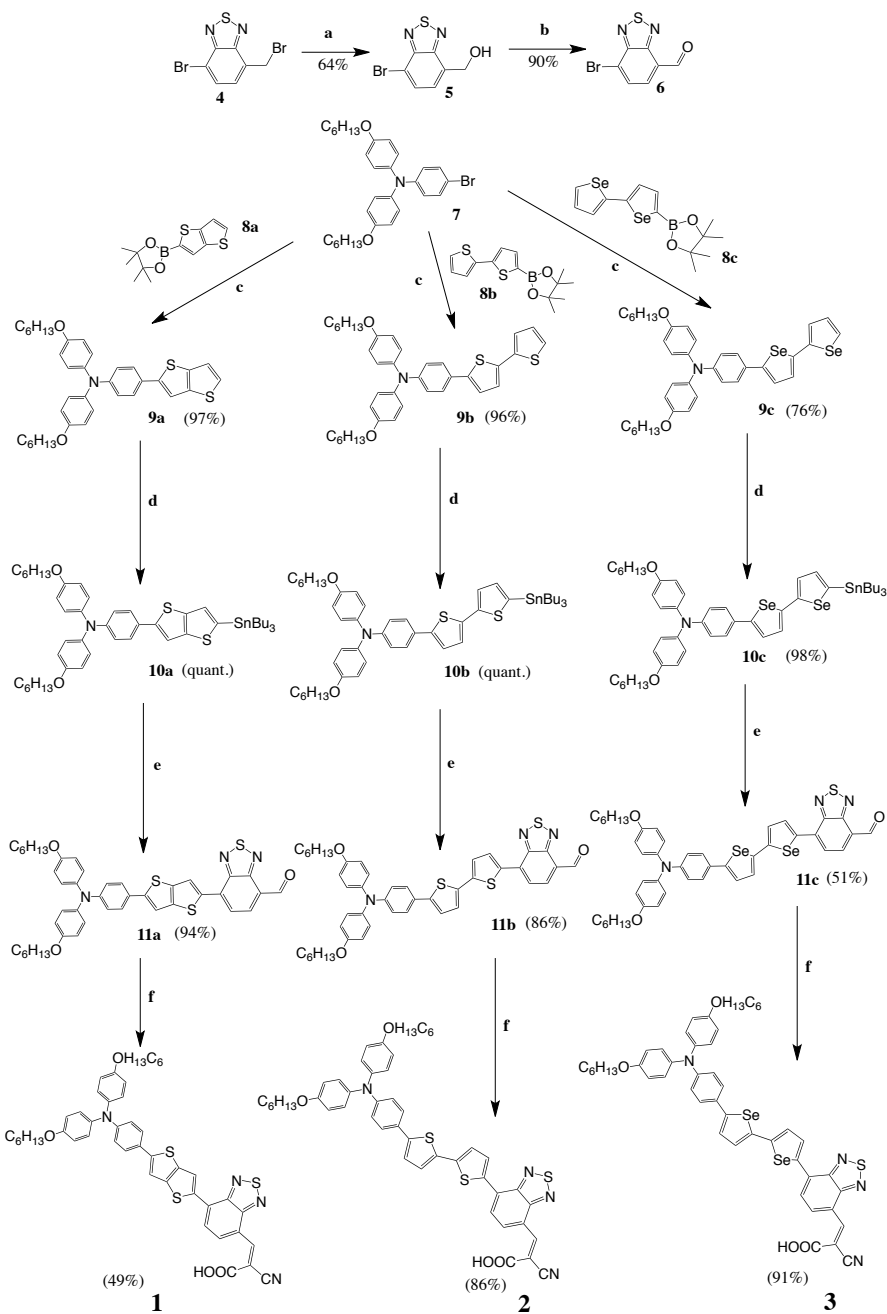


Figure 4.1: Synthesis of investigated dyes **1–3**. (a) 3 eq. K_2CO_3 , dioxane/water (1:1), reflux, 1 h (b) 4 eq. MnO_2 , CHCl_3 , reflux, 3 h (c) $\text{Pd}_2(\text{dba})_3 \cdot \text{CHCl}_3$, $\text{HPtBu}_3\text{BF}_4$, 2 M aq. K_3PO_4 (4 eq.), THF , r.t. (d) (i) $n\text{-BuLi}$, THF , -78°C (ii) SnBu_3Cl (e) $\text{Pd}(\text{PPh}_3)_2\text{Cl}_2$, THF , reflux, 4–22 h (f) cyanoacetic acid, NH_4OAc or piperidine, $\text{CH}_2\text{Cl}_2/\text{CH}_3\text{CN}$, reflux.

provide alcohol **5** in 64% yield. Alcohol **5** was oxidized to benzothiadiazole carbaldehyde **6** with MnO_2 in chloroform under reflux conditions in 90% yield. Bromotriphenylamine **7** was coupled with pinacolboronic esters **8 a-c** in a Suzuki-Miyaura cross-coupling reaction using

Chapter 4. The influence of the structural modifications of D- π -A dyes containing benzothiadiazole as a spacer.

Pd₂(dba₃)·CHCl₃/HPtBu₃BF₄ as a catalyst system. The coupling products were obtained in good (76% for biselenophene **9 c**) to excellent yields (97% for thienothiophene **9 a** and 96% for bithiophene **9 b**). Lithiation of compounds **9 a-c** with *n*-BuLi in THF at -78°C and subsequent quenching with tributyltin chloride afforded stannylyl compounds **10 a-c** in quantitative yields. Stille-type coupling reaction of the stannylated compounds **10 a-c** with benzothiadiazole derivative **6** using Pd(PPh₃)₂Cl₂ as a catalyst gave aldehydes **11 a** and **11 b** in very good yields of 94% and 86%, respectively. For aldehyde **11 c**, only a moderate yield of 51% could be obtained. Final Knoevenagel condensation of aldehyde **11 a** with cyanoacetic acid in the presence of piperidine as a catalyst yielded dye **1** in 51% yield. For the Knoevenagel condensation of aldehydes **11 b** and **11 c**, ammonium acetate was used instead of piperidine, and the yields were improved to 86% for dye **2** and 91% for dye **3**.

Optical properties. The dyes were characterized by UV-Vis absorption spectroscopy. Figure 4.2 shows the absorption spectra of dyes **1-3** measured in dichloromethane solutions and the data is tabulated in Table 4.1. All dyes exhibited three absorption transitions over a range of 300 to 800 nm. The absorption band between 350 to 450 nm corresponds to the π - π^* transitions of the conjugated system. The low energy bands between 570 nm and 610 nm were assigned to the charge transfer (CT) transitions. The CT transition is shifted from 569 nm for the thienothiophene dye **1** over 579 nm for the bithiophene dye **2** to 609 nm for the biselenophene dye **3**. Thus, the replacement of thiophene by selenophene leads to a significant red-shift of 30 nm. The insertion of benzothiadiazole as a low band gap chromophore between the linker and acceptor cyanoacrylic acid caused a red shift of 30–110 nm compared to corresponding dyes without this chromophore^{1–3}. Furthermore, the attachment of the benzothiadiazole unit directly to the acceptor resulted in a bathochromic shift of the spectral response compared to the dyes comprising a central benzothiadiazole unit⁴.

Redox properties. The redox properties of the three sensitizers **1-3** were measured by cyclic voltammetry in dichloromethane solutions with 0.1 M tetrabutylammonium hexafluorophosphate as a supporting electrolyte. The three dyes **1-3** showed two reversible oxidation potentials (Figure 4.3). The first oxidation potential at ca. 0.20 V (vs. Fc/Fc⁺) corresponds to the oxidation of the triphenylamino moiety. The second oxidation potential is assigned to the corresponding π -conjugated systems with decreasing values from 0.72 V for **1** over 0.61 V for **2**

4.2. Preliminary studies with thieno[3,2-b]thiophene, bithiophene and biselenophene as bridging units

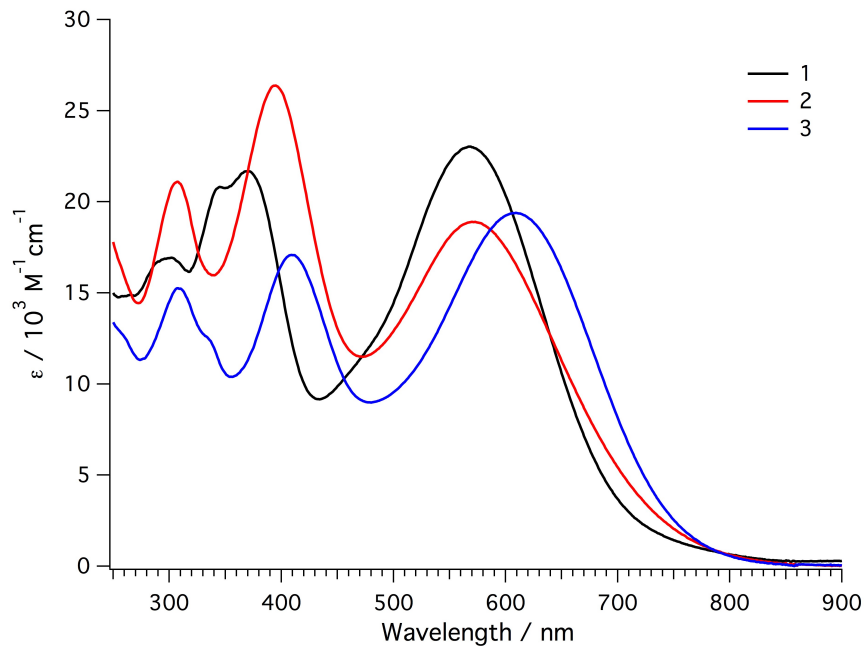


Figure 4.2: UV-Vis spectra of dyes **1**, **2** and **3** in dichloromethane.

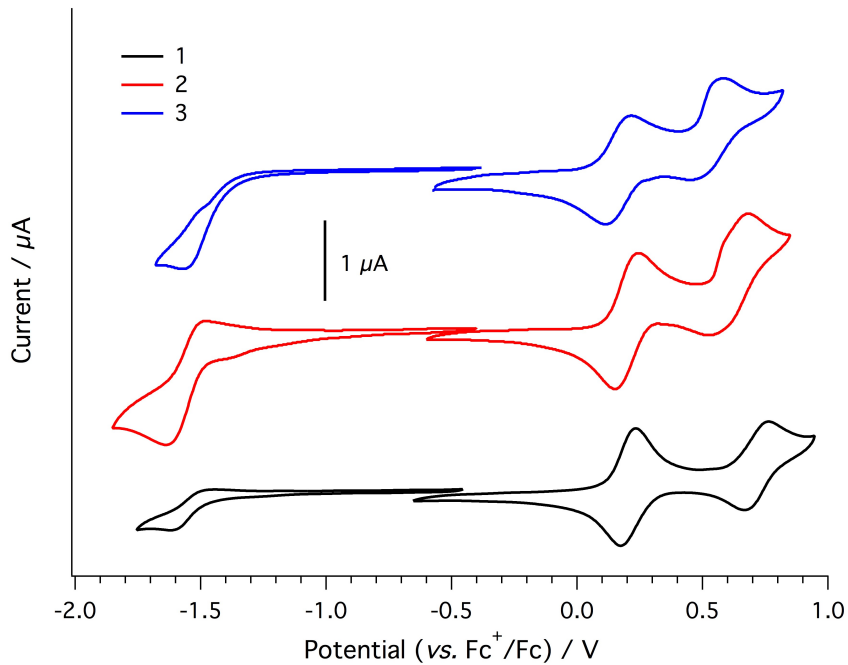


Figure 4.3: Cyclic voltammograms of **1**, **2** and **3**; DCM/TBAH PF_6 (0.1 M), $c = 5 \times 10^{-4}$ M, 295 K, scan rate = 100 mV s $^{-1}$, vs. Fc^+/Fc .

to 0.52 V for **3**. This indicates an increasing degree of conjugation going from thienothiophene to 2,2'-bithiophene and 2,2'-biselenophene. From the onset of the first oxidation potential,

Chapter 4. The influence of the structural modifications of D- π -A dyes containing benzothiadiazole as a spacer.

Table 4.1: Optical and electrochemical data of sensitizers **1**, **2** and **3** in dichloromethane.

| Dye | $\lambda_{abs} (\varepsilon)$ nm ($M^{-1}cm^{-1}$) | E_g^{opt} eV | E_{Ox1}^0 V ^a | E_{Ox2}^0 V ^a | E_{Red}^0 V ^a | HOMO eV ^b | LUMO eV ^b |
|----------|---|-------------------|-------------------------------|-------------------------------|-------------------------------|-------------------------|-------------------------|
| 1 | 302 (16900) | 1.76 | 0.20 | 0.72 | -1.55 | -5.20 | -3.63 |
| | 371 (21700) | | | | | | |
| | 569 (23000) | | | | | | |
| 2 | 308 (21000) | 1.70 | 0.21 | 0.61 | -1.51 | -5.20 | -3.74 |
| | 395 (26400) | | | | | | |
| | 570 (18900) | | | | | | |
| 3 | 308 (15300) | 1.65 | 0.16 | 0.52 | -1.53 | -5.17 | -3.71 |
| | 410 (17100) | | | | | | |
| | 609 (19400) | | | | | | |

^a Measured in $CH_2Cl_2/TBAH\text{PF}_6$ (0.1 M), $c \approx 1 \times 10^{-3}$ M, 295 K, scan rate = 100 mV s⁻¹, vs. Fc^+ . ^b Calculated from E_{Ox1}^{onset} and from E_{Red}^{onset} ; set $E_{LUMO}(\text{Fc}^+/\text{Fc}) = -5.1$ eV vs. vacuum⁵.

HOMO energy levels of ca. -5.20 eV vs. vacuum were calculated for the dyes. In the reductive region, the three dyes **1–3** show one reduction wave at around -1.5 to -1.6 V. From the onset of this reduction potential LUMO energy levels were calculated, the values being between -3.60 eV and -3.75 eV vs. vacuum. These LUMO levels lie above the conduction band edge of titanium dioxide (~4.0 eV vs. vacuum), which should ensure a sufficiently high driving force for the electron injection from the excited dye into the conduction band of the semiconductor. Compared to the corresponding dyes without benzothiadiazole^{1–3}, sensitizers **1–3** showed a lower band gap (~1.6–1.7 eV) due to a lowering of the LUMO energy levels.

Quantum chemical calculations. Semi-empirical methods were utilised for the quantum chemical calculation of molecular electronic structures to confirm the CT character of the dyes observed in solutions. The Austin Model 1 (AM1) method for dye **1** and **2** and parameterized Model 3 (PM3) for dye **3** under restricted Hartree-Fock conditions were used to analyse the electron distribution of the frontier orbitals of all dyes (Figure 4.4). The electron density distribution of the HOMO of all molecules is mainly located at the oligothiophene/oligoselenophene and triphenylamine moieties, whereas the electron density of the LUMO is primarily located at the benzothiadiazole and cyanoacrylic acid acceptor units, and, to a small extent, on the neighbouring thiophene/selenophene ring. Hence, strong electron density relocation between HOMO and LUMO is present, supporting the occurrence of an intramolecular charge transfer transition (ICT) in the UV-Vis spectra. In general, the calculations reveal that the

4.2. Preliminary studies with thieno[3,2-b]thiophene, bithiophene and biselenophene as bridging units

HOMO to LUMO excitations move the electron density distribution from electron donating triaryl moieties to the TiO₂ film via terminal cyanoacrylic acids efficiently.

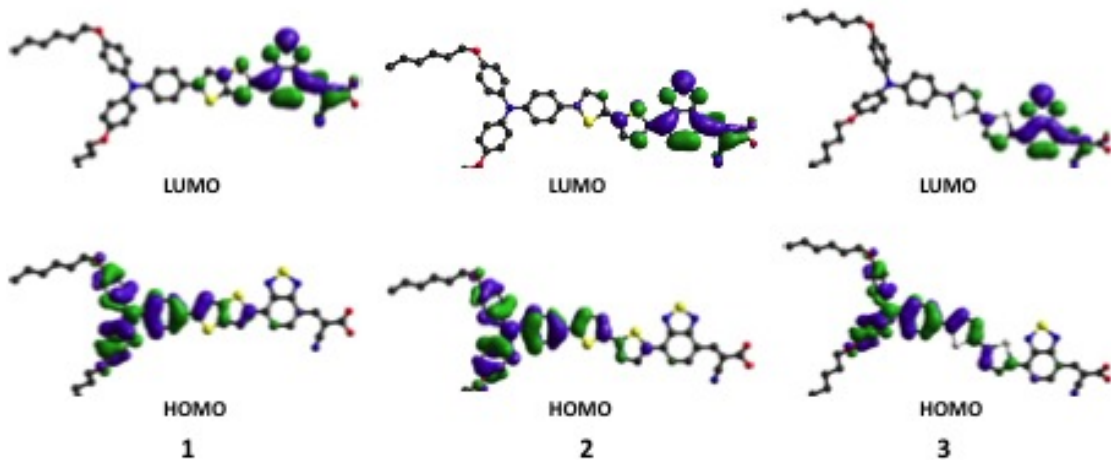


Figure 4.4: Frontier orbital electron distributions for dyes **1**, **2** and **3** calculated by AM1 and PM3 methods.

4.2.2 Application in DSCs

Photovoltaic performance. Screen-printed 5 μm thick, transparent layers of TiO₂ nanoparticles were used as photoelectrodes in this study. The preparation followed the procedure described in the Chapter 3, section 2.5 Device fabrication. After sintering at 500°C and cooling to 80°C, the sintered TiO₂ electrodes were sensitized by dipping for 5 h in the respective dye solutions (0.3 mM of the dye with 2 mM of chenodeoxycholic acid, CDCA, in chlorobenzene), and then assembled in a device using a thermally platinized FTO/glass counterelectrode. Sandwich-type devices were prepared according to the procedure presented in Chapter 3, section 2.5 Device fabrication, and were filled with the electrolyte coded as Z1040. The composition of Z1040 is as following: 1.0 M lithium iodide, 0.044 M I₂ and 0.25 M *tert*-butylpyridine (TBP) in acetonitrile:valeronitrile (85:15 v/v) solvent mixture.

The J-V characteristics of the solar cells sensitized with dyes **1–3** were measured under illumination with standard AM 1.5G simulated sunlight (100 mWcm⁻²) and are displayed in the Figure 4.5, left. On the right of the Figure 4.5 the incident photon to conversion efficiency (IPCE) plots of devices with dyes **1–3** are presented, which exhibit a broad spectral coverage

Chapter 4. The influence of the structural modifications of D- π -A dyes containing benzothiadiazole as a spacer.

Table 4.2: Detailed photovoltaic parameters of DSCs made with three different dyes and Z1040 electrolyte using 5 μm TiO₂ films.

| Dye | J_{SC} mA cm^{-2} | V_{OC} mV | FF | η % |
|-----|---------------------------------|----------------|------|-------------|
| 1 | 6.07 | 426 | 0.65 | 1.68 |
| 2 | 6.04 | 423 | 0.70 | 1.78 |
| 3 | 4.83 | 397 | 0.68 | 1.30 |

from 400 nm to 750 nm. Table 4.2 summarizes the photovoltaic parameters for devices made with all three synthesized dyes using the volatile electrolyte Z1040. The short circuit current density and open circuit potential of devices with dye **1** and **2** have almost the same values, except a small difference in the fill factor (FF). Device with dye **3** (selenothiophene derivative) yielded lower photocurrent density and open-circuit voltage that led to lower overall efficiency.

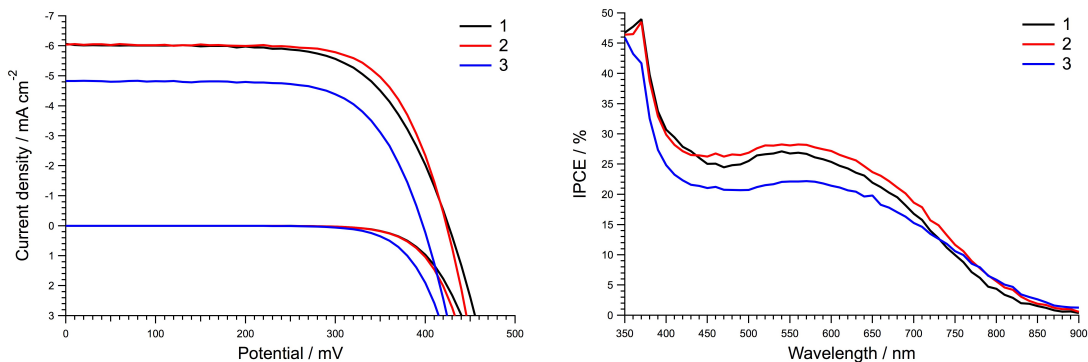


Figure 4.5: *Left:* J-V curves of cells sensitized with dyes **1**, **2** and **3** using Z1040 electrolyte on 5 μm TiO₂ films. *Right:* IPCE of the same devices.

Transient photovoltage measurements performed on the above-mentioned devices revealed that the charge densities generated upon illumination are surprisingly low (Figure 4.6). Their absorption spectrum is rather wide, but IPCE values were low, which means that this may be a sign of a poor electron injection or collection, ergo there is a small electron population in the conduction band of TiO₂ and low current densities are generated. Taking into consideration the high content of LiI in the electrolyte, believed to shift the conduction band of titania downwards, and the position of LUMO of the dyes, there should be no problem with the electron injection. The issue of the charge collection still persists.

4.2. Preliminary studies with thieno[3,2-b]thiophene, bithiophene and biselenophene as bridging units

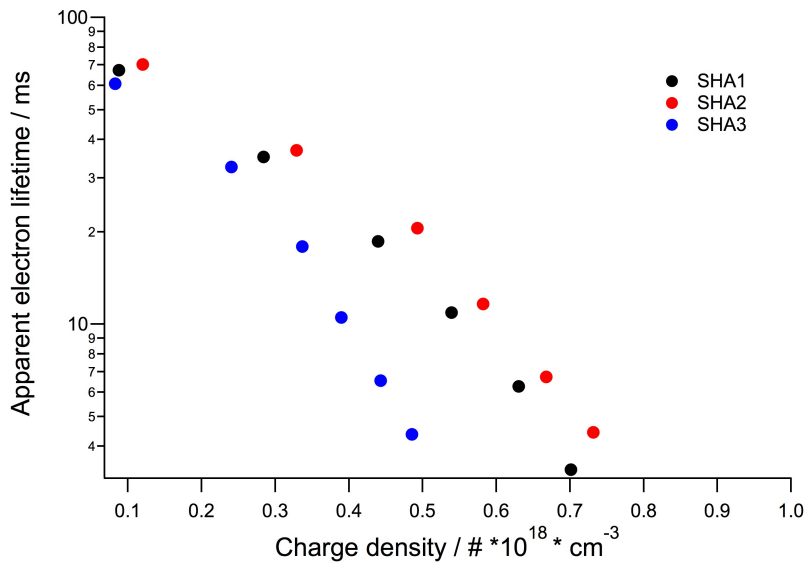


Figure 4.6: Apparent electron lifetime calculated from transient photovoltage decays of the devices with dyes **1**, **2** and **3** plotted against charge density.

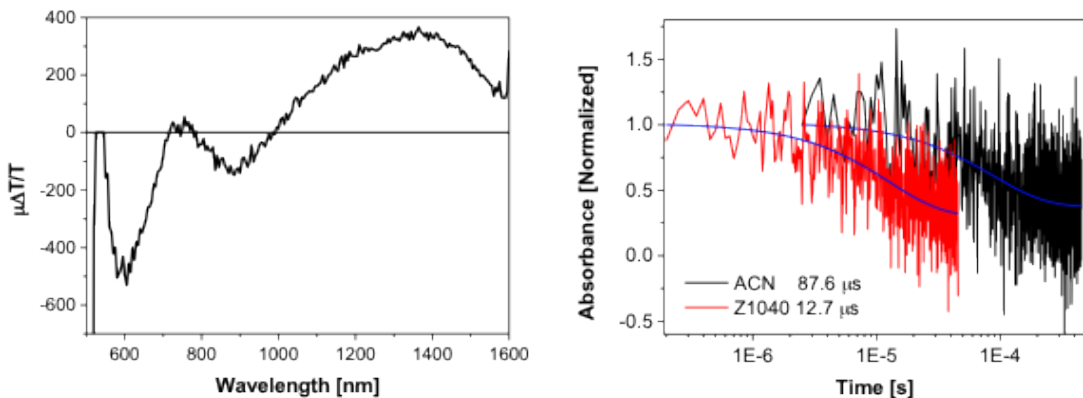


Figure 4.7: *Left:* Photoinduced absorption spectrum of the dye **1**. *Right:* Transient decays for the devices with dye **1** with Z1040 electrolyte (red) and acetonitrile (black).

A series of laser measurements (Photoinduced Absorption Spectroscopy, PIA) was performed on the complete cells with Z1040 electrolyte, as well as with pure acetonitrile. In all cases the residual fluorescence was detected within the range of 750–800 nm. This weak, however still present, signal may be attributed to the loosely bound molecules (physisorption), which do not sensitize the TiO₂ surface effectively (Figure 4.7, left: only dye **1**). Transient decays of the oxidized states of the dye **1** molecules adsorbed onto transparent TiO₂ films are presented in the Figure 4.7, right, as a representation of the dye family in question. In comparison with highly efficient dyes, the charge recombination rate seems to be much higher for the dyes **1–3**.

Chapter 4. The influence of the structural modifications of D- π -A dyes containing benzothiadiazole as a spacer.

Calculated interception efficiency reaches up to 88%, which means that the remaining 12% is lost.

Conclusions. The introduction of a benzothiadiazole unit in D- π -A sensitizers lowers the HOMO-LUMO energy gap to 1.6–1.7 eV. While the three dyes comprise the same donor and acceptor units, the bridging units were thieno[3,2-b]thiophene in **1**, bithiophene in **2**, and biselenophene in **3**. Photophysical and electrochemical properties of the dyes were investigated by UV-Vis spectroscopy and cyclic voltammetry. Photovoltaic devices including these dyes showed a moderate overall conversion efficiency of 1.8% under full sunlight (AM 1.5G, 100 mWcm²) irradiation, despite a broad monochromatic incident photon-to-current-efficiency, covering a region from 350 to 850 nm. Nanosecond transient absorption spectroscopy study revealed that the reason for this low performance is mainly an increase in the rate of recombination of injected electron from TiO₂ with the dye cation.

4.3 The effect of phenyl ring inserted between the benzothiadiazole and cyanoacrylic acid

4.3.1 Synthesis and characterization of the phenyl-bearing dye

Synthesis of a sensitizer. A small structural modification was done on the dye **2**, namely a phenyl ring was placed in-between the benzothiadiazole and the cyanoacrylic group (Figure 4.8). Starting from the common core **10 b**, Stille coupling with 7-bromobenzo[c][1,2,5]thiadiazole-4-carbaldehyde **6** or 4-(7-bromobenzo[c][1,2,5]thiadiazol-4-yl)benzaldehyde **12**⁶ gave intermediates **11 b** and **13** in yields of 86% and 92%, respectively. Final Knoevenagel condensation of **11 b** and **13** with cyanoacetic acid in the presence of ammonium acetate as a catalyst gave dye **2** in 86% yield and dye **4** in 38% yield.

Optical properties. The UV-Vis absorption spectra of dyes **2** and **4** are presented in the Figure 4.9 and the detailed data is gathered in the Table 4.3. Dye **4** dissolved in dichloromethane also exhibits three absorption bands, however, in comparison to the dye **2**, the CT-band is significantly blue-shifted (55 nm). This was not expected, because dye **4** contains an additional phenyl ring, which should lead to a more extended conjugated system and, consequently, to a

4.3. The effect of phenyl ring inserted between the benzothiadiazole and cyanoacrylic acid

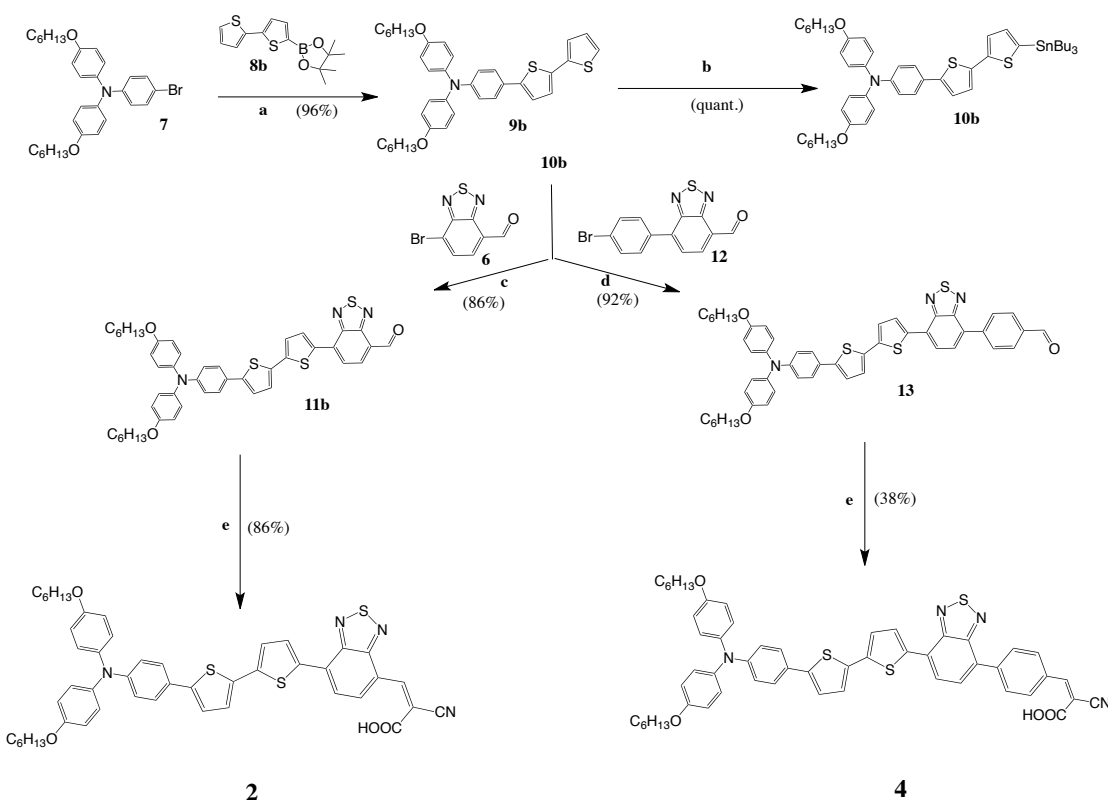


Figure 4.8: Synthesis of dyes **2** and **4**. (a) $\text{Pd}_2(\text{dba})_3 \cdot \text{CHCl}_3$, $\text{HP}^t\text{Bu}_3\text{BF}_4$, 2 M aq. K_3PO_4 (4 eq.), THF, rt (b) (i) $n\text{-BuLi}$, THF, -78°C (ii) Bu_3SnCl (c) $\text{Pd}(\text{PPh}_3)_2\text{Cl}_2$, THF, 70°C , 15 h (d) $\text{Pd}(\text{PPh}_3)_2\text{Cl}_2$, THF, 75°C , 4.5 h (e) cyanoacetic acid, NH_4OAc or piperidine, $\text{CH}_2\text{Cl}_2/\text{CH}_3\text{CN}$, reflux.

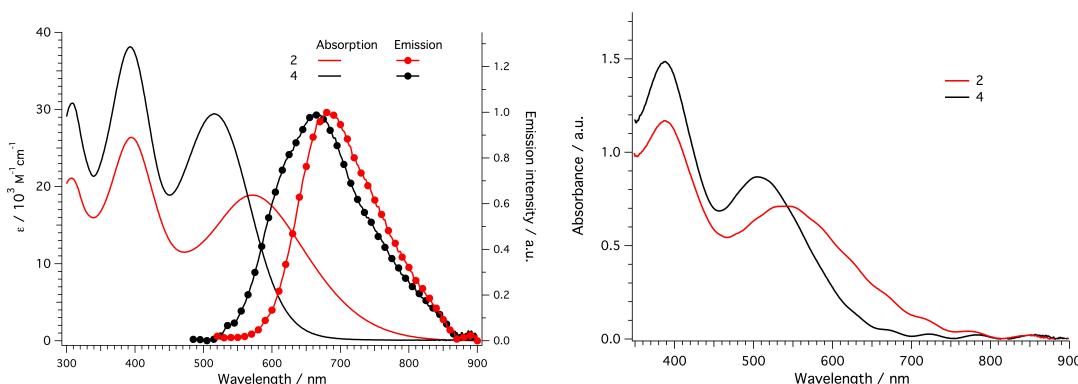


Figure 4.9: *Left:* UV-vis and normalized emission spectra of dyes **2** and **4** in dichloromethane ($c = 10^{-5} \text{ M}$). Emission spectra measured upon excitation at 500 nm (**2**) and 460 nm (**4**). *Right:* UV-vis spectra of dyes **2** and **4** adsorbed on a transparent TiO_2 film.

Chapter 4. The influence of the structural modifications of D- π -A dyes containing benzothiadiazole as a spacer.

Table 4.3: Optical and electrochemical data of sensitizers **2** and **4** in dichloromethane.

| Dye | $\lambda_{abs} (\varepsilon)$ nm ($M^{-1}cm^{-1}$) | λ_{em} nm | E_g^{opt} eV ^a | E_{Ox1}^0 V | E_{Ox2}^0 V | E_{Red}^0 V | HOMO eV ^b | LUMO eV ^b |
|-----|---|----------------------|--------------------------------|------------------|------------------|------------------|-------------------------|-------------------------|
| 2 | 308 (21 000) | 681 | 1.70 | 0.21 | 0.61 | -1.51 | -5.20 | -3.74 |
| | 395 (27 200) | | | | | | | |
| | 579 (21 900) | | | | | | | |
| 4 | 308 (30 800) | 665 | 1.98 | 0.30 | 0.64 | -1.57 | -5.33 | -3.66 |
| | 392 (38 000) | | | | | | | |
| | 515 (29 400) | | | | | | | |

^a Estimated using the onset of the UV-vis spectra in dichloromethane. ^b set $E_{LUMO}(Fc^+/Fc) = -5.1$ eV vs. vacuum.

red-shifted absorption. Furthermore, the molar extinction coefficient for the CT transition of dye **4** ($\varepsilon = 29\,400\,M^{-1}cm^{-1}$) is increased by a factor of 1.6 compared to dye **2** ($\varepsilon = 18\,900\,M^{-1}cm^{-1}$). The emission maxima of dyes **2** and **4** can be found at 681 and 665 nm, respectively. Dye **4** showed a much larger Stokes shift ($4\,379\,cm^{-1}$) in comparison to **1** ($2\,860\,cm^{-1}$) which is an indication of a significant structural reorganization of the dye **4** upon photoexcitation. The UV-Vis spectra of dyes **2** and **4** adsorbed on transparent TiO₂ films (Figure 4.9, left) showed a slight blue-shift of the CT band for dye **4** (506 nm) compared to the solution spectra, while the shift is more pronounced for dye **2** (540 nm). Hence, the steady-state results clearly hint to a reduction of the overall π -conjugation in the cationic form of **4** due to a possible torsion of the additional phenyl ring.

Redox properties. Dye **4** was characterized electrochemically as well (Figure 4.10). Dissolved in dichloromethane, with the addition of 0.1 M tetrabutylammonium hexafluorophosphate as a supporting electrolyte and ferrocene couple as an internal standard, exhibited two reversible oxidation waves and one irreversible reduction wave (detailed data is provided in the Table 4.3). Compared to dye **2** ($E_{Ox1}^0 = 0.21$ V), the first oxidation potential of dye **4** ($E_{Ox1}^0 = 0.30$ V) is shifted to more negative values. This is another hint for the weaker donor-acceptor interaction in dye **4** due to probable torsion of the phenyl ring.

4.3.2 Quantum chemical calculations

Due to the suspicion of the significant changes in geometry of the molecules after the implementation of a phenyl ring, the quantum chemical calculations were performed for the two

4.3. The effect of phenyl ring inserted between the benzothiadiazole and cyanoacrylic acid

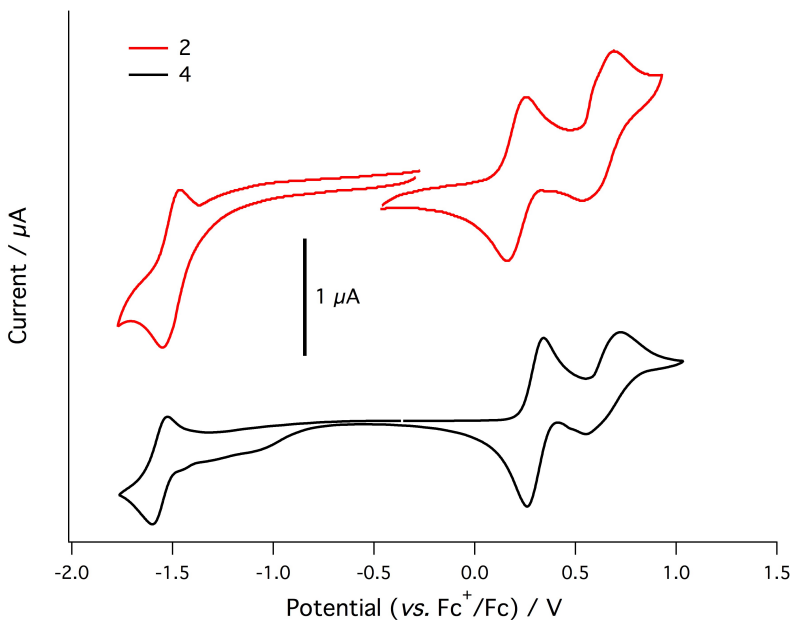


Figure 4.10: Cyclic voltammograms of dyes **2** and **4** in $\text{CH}_2\text{Cl}_2/\text{TBAHFP}$ (0.1 M) solution $c=5 \times 10^{-4}\text{M}$, 295 K, scan rate = 100 mV s^{-1} , vs. Fc^+/Fc .

dyes, which additionally gave insights into the electron density distribution of their frontier orbitals. Density functional theory (DFT) using the B3LYP hybrid functional with 6-31G* basis set was the method of choice⁷. First, the ground state geometries of molecule **2** and **4** were optimized using the restricted Hartree-Fock conditions. The calculations showed that the CT absorption bands of these dyes were due to the HOMO→LUMO transition in the ground state. The calculated HOMO and LUMO energies were -4.96 and -3.36 eV, respectively, for **2** and -4.81 and -3.01 eV for **4**. In comparison to HOMO and LUMO energies determined by electrochemical methods the calculated values are by 0.3–0.4 eV higher, but the same trend is observed, i.e. the values for dye **4** are lowered in comparison to dye **2**. In the neutral form both molecules do not exhibit significant differences in the electron density distribution of the orbitals (Figure 4.11).

For dye **2**, the HOMO and LUMO orbitals are slightly more delocalized, giving rise to a better conjugation between the donor and acceptor moiety, which corroborates well with the outcome of the UV-Vis studies. On the other hand, in dye **4** the additional phenyl ring induces a slight out-of-plane torsion (18°) with respect to the BTDA moiety. As a consequence, the HOMO is no longer extended to the cyanoacrylic acid carbon as in the case of the dye **2**. How-

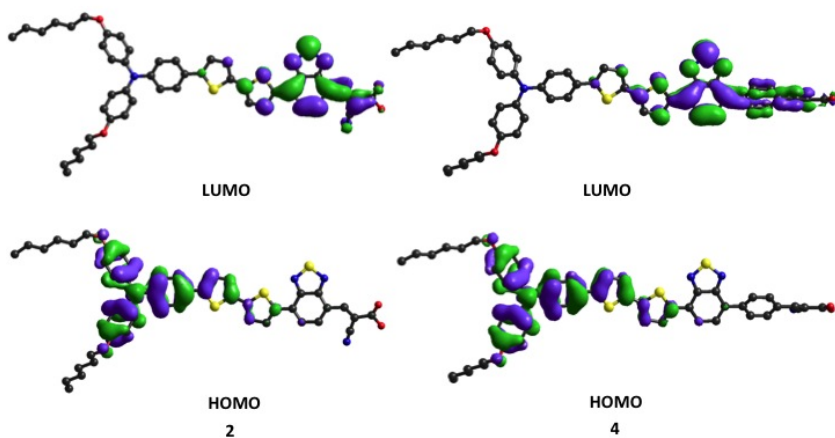


Figure 4.11: HOMO and LUMO electron density distributions for frontier orbitals of dyes **2** and **4** calculated using DFT methods (B3LYP/6-31G*).

ever, this does not impact the HOMO-LUMO overlap, which is reflected by the extension of the LUMO orbital coefficient over the thiophene units. Hence, both orbitals provide sufficient overlap between donor and acceptor to guarantee a fast charge transfer transition. Therefore, excitation from the HOMO to the LUMO should lead to an efficient photoinduced electron transfer from the electron donating triarylamine moiety to the TiO₂ film via the terminal cyanoacrylic acid. This nicely follows the trends of the almost identical charge separation rates for **2** and **4** as stated in the photophysical section (*vide infra*). Significant differences arise when considering the cationic form of **2** and **4**, as calculated using the unrestricted Hartree-Fock method. The optimized cationic structure of **2** becomes completely planar with dihedral angles of ~1° each (Figure 4.12). In contrast, the BTDA unit and the adjacent phenyl rings in the cation of dye **4** are twisted out-of-plane by 48°. It should be noted that, in the cationic form of the dye **4**, the phenyl ring is twisted by almost 30° more compared to the neutral conformation (dihedral angle = 18°). This deviation from planarity, as suggested by the large Stokes shift of **4** as compared to **2**, has an impact on the orbital energies. In fact, the energies of the singly-occupied molecular orbital (SOMO) are lowered to a higher extent in **4** than in **2**. The SOMO in **4** (-6.80 eV) is 0.2 eV lower in energy than the SOMO in **2** (-6.61 eV). This brings to the conclusion that releasing an electron leads to a more stable cation

4.3. The effect of phenyl ring inserted between the benzothiadiazole and cyanoacrylic acid

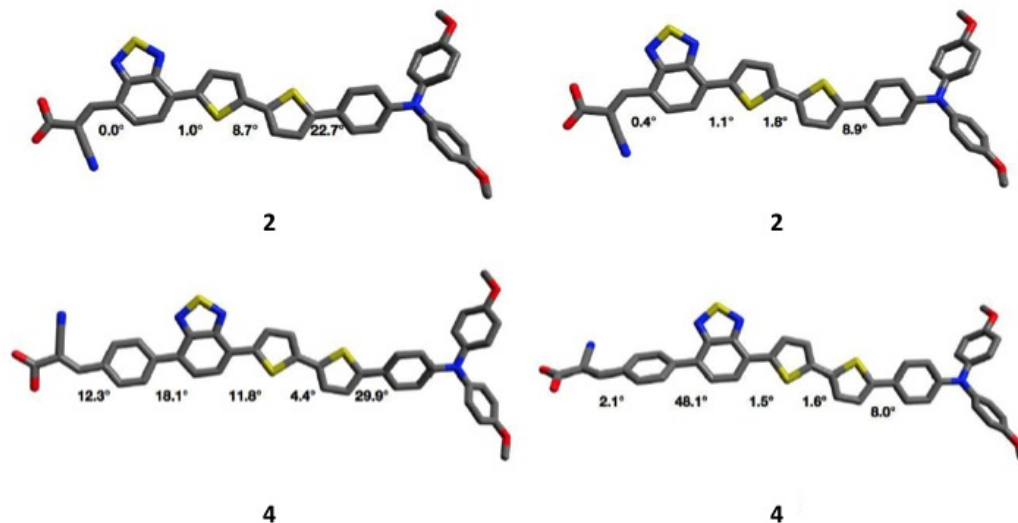


Figure 4.12: Geometry optimized structures of the neutral (*left*) and cationic (*right*) species of **2** and **4** with the corresponding dihedral angles between each plane.

of **4** than that of **2**. This corroborates well with the difference in solar cell performance of devices with **2** vs. **4**, as discussed in the photovoltaic section. As shown below, the charge recombination rates in **4** are remarkably slower due to a better stabilization of its cationic form. Furthermore, the insertion of the phenyl ring in **4** and the consequential out-of-plane torsion of the adjacent plane upon oxidation leads to an interruption of the π -conjugation between donor and anchoring group. On the contrary, the cationic form of **2** remains entirely planar and the π -conjugation is preserved as shown in the Figure 4.12. This fact is clearly in favour of an intramolecular electron back-transfer process as the deactivation pathway of the charge separated state. In other words, the electron back-transfer from TiO₂ to the acceptor moieties of **2** is energetically possible and facilitated.

Chapter 4. The influence of the structural modifications of D- π -A dyes containing benzothiadiazole as a spacer.

Table 4.4: Composition of electrolytes used for optimization of the performance of the devices with dye **4**. The components were dissolved in a solvent mixture of acetonitrile and valeronitrile (85:15, v/v).

| Code | DMII / M | I ₂ / M | GuNCS / M | TBP / M | LiI / M |
|-----------|----------|--------------------|-----------|---------|---------|
| E1 | 0 | 0.044 | 0 | 0.25 | 1 |
| E2 | 1 | 0.3 | 0.1 | 0.5 | 0 |
| E3 | 1 | 0.3 | 0.1 | 0.5 | 0.05 |
| E4 | 1 | 0.3 | 0.1 | 0.5 | 0.1 |

4.3.3 Application in DSC

Photovoltaic performance. The J-V characteristics of the solar cells sensitized with dyes **2** and **4** on 5 μm TiO₂ films with the volatile electrolyte **E1** measured under standard AM 1.5G conditions (100 mW cm⁻²) are displayed in the Figure 4.13, left. The electrolyte compositions are presented in the Table 4.4. Dye **4** sensitized cells provided an overall power conversion efficiency (η) of 5.59% with a high short-circuit current density (J_{SC}) of 16.26 mA cm⁻², while dye **2** sensitized cells showed a relatively poor performance with an overall η of 1.78% due to lower J_{SC} and open-circuit potential (V_{OC}) values (Table 4.5). The dramatically increased J_{SC} value for dye **4** was also clearly seen in the incident photon-to-current conversion efficiency (IPCE) spectra reaching ~78%@570 nm compared to only ~28%@550 nm for **2** (Figure 4.13, right). The concentration of dye **2** and **4** on the TiO₂ surface is found to be 39.8 μM and 35.5 μM , respectively. Dye loading experiments showed that there is not much difference in the concentration of the two dyes on the surface, indicating that this is not the reason for the lower J_{SC} of the device with dye **2**.

In order to optimize the conditions of the photovoltaic performance for dye **4**, we employed a thicker TiO₂ layer with scattering nanoparticles on the top (8 μm transparent + 5 μm scattering) and varied the LiI content in the electrolyte (coded as **E1** to **E4**). This allowed us to reach a very high J_{SC} value of 18.97 mA cm⁻² for a LiI concentration of 1 M (**E1**). Unfortunately, V_{OC} and the fill factor decreased with increasing Li⁺ concentration in the electrolyte and on the TiO₂ surface⁸. It was found that the system is very sensitive to the change of Li⁺ concentration in the electrolyte and the short-circuit current density saturates even with small amounts of Li⁺. At an optimal LiI concentration of 100 mM (electrolyte **E4**), an excellent η of 8.21%

4.3. The effect of phenyl ring inserted between the benzothiadiazole and cyanoacrylic acid

Table 4.5: Photovoltaic parameters of dye **2** and **4** adsorbed on nanocrystalline TiO_2 films of different thicknesses. Electrolyte optimization by varying the LiI content and its influence on the photovoltaic parameters of the cells sensitized with dye **4**. Devices were made using single ($5\ \mu\text{m}$) and double layered TiO_2 film ($8\ \mu\text{m}$ transparent + $5\ \mu\text{m}$ scattering layer).

| Dye | Electrolyte | LiI content mM | TiO_2 film thickness μm | J_{SC} mA cm^{-2} | V_{OC} mV | FF | η % |
|----------|-------------|-------------------|--|---------------------------------|----------------|------|-------------|
| 2 | E1 | 1000 | 5 | 6.04 | 423 | 0.70 | 1.78 |
| 4 | E1 | 1000 | 5 | 16.26 | 593 | 0.57 | 5.59 |
| 2 | E4 | 100 | 8+5 | 3.40 | 489 | 0.74 | 1.24 |
| 4 | E2 | 0 | 8+5 | 14.26 | 688 | 0.73 | 7.19 |
| 4 | E3 | 50 | 8+5 | 17.52 | 655 | 0.65 | 7.26 |
| 4 | E4 | 100 | 8+5 | 18.47 | 640 | 0.69 | 8.21 |
| 4 | E1 | 1000 | 8+5 | 18.97 | 558 | 0.55 | 5.91 |

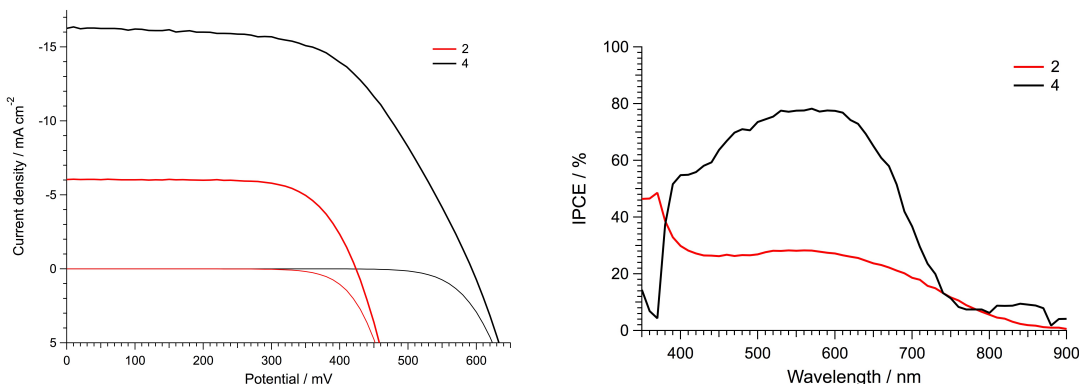


Figure 4.13: *Left:* J-V curves of cells sensitized with dyes **2** and **4** and using **E1** electrolyte on $5\ \mu\text{m}$ TiO_2 films. *Right:* IPCE of the same devices.

was achieved. The significant difference in the photogenerated current densities obtained for electrolytes containing various concentrations of Li^+ may be ascribed to an extended electron lifetime in the titania and change in the conduction band position induced by the using the electrolyte with higher concentration of Li^+ . For the cells with lower content of Li^+ , the electron lifetime is one order of magnitude shorter than for the one with $100\ \text{mM Li}^+$ (Figure 4.14).

The molecular structures of dye **2** and **4** differ only by an additional phenyl ring placed between the BTDA unit and the anchoring group in dye **4**. Nevertheless, this subtle modification has a significant impact on the photovoltaic performance. In a direct comparison with the above-

Chapter 4. The influence of the structural modifications of D- π -A dyes containing benzothiadiazole as a spacer.

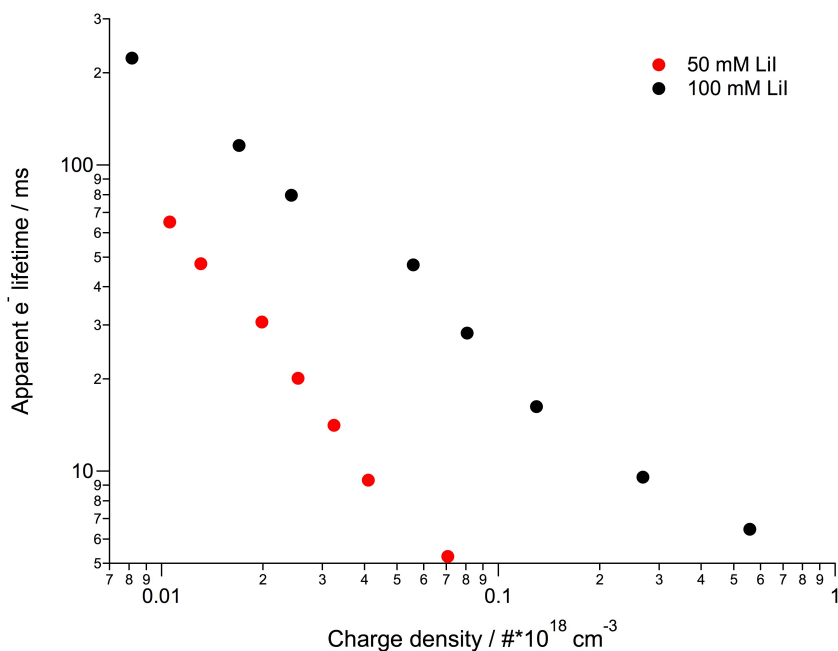


Figure 4.14: Influence of the concentration of Li^+ in the electrolyte on the apparent electron lifetime in TiO_2 for cells sensitized with dye 4.

mentioned champion cell, using electrolyte **E4**, dye **2** exhibited a more than 5 times lower J_{SC} and the resulting η was almost 7 times lower, as shown in the Figure 4.15, left, and Table 4.5. The difference in J_{SC} was further confirmed by IPCE spectra. Both dyes showed a wide spectral coverage of the 380–750 nm region (Figure 4.15, right), but the maximum IPCE at 600 nm for dye **2** is only 20% as compared to >90% for dye **4**.

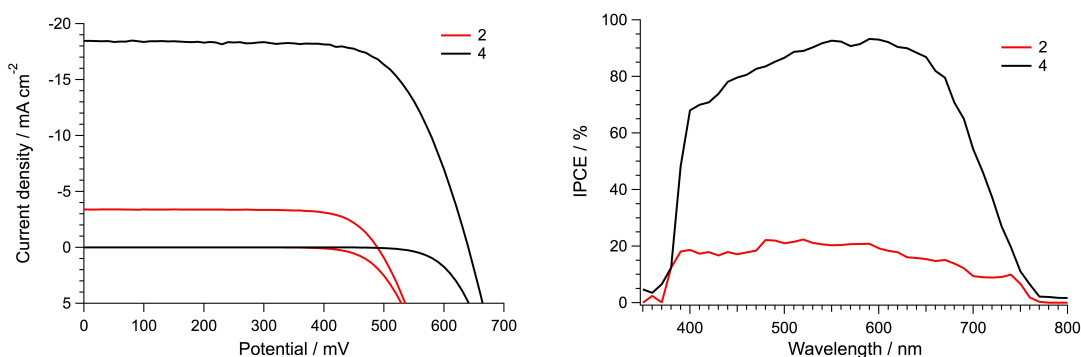


Figure 4.15: J-V curves (*left*) and IPCE spectra (*right*) for devices sensitized with dye **2** and **4** using a double-layered TiO_2 film (8+5 μm) and electrolyte **E4**.

4.3. The effect of phenyl ring inserted between the benzothiadiazole and cyanoacrylic acid

4.3.4 Detailed investigation: transient measurements, laser study and EIS

Transient measurements. Transient photovoltage and photocurrent measurements revealed that the apparent electron lifetime in the case of the device with dye **4** exhibits typical exponential behaviour when plotted against charge density in the film. It seems that for dye **2** an asymptotic-like saturation limit exists for the amount of charges injected into TiO₂. Above this limit, the recombination processes are vastly enhanced, thus reducing the lifetime of injected electrons (Figure 4.16).

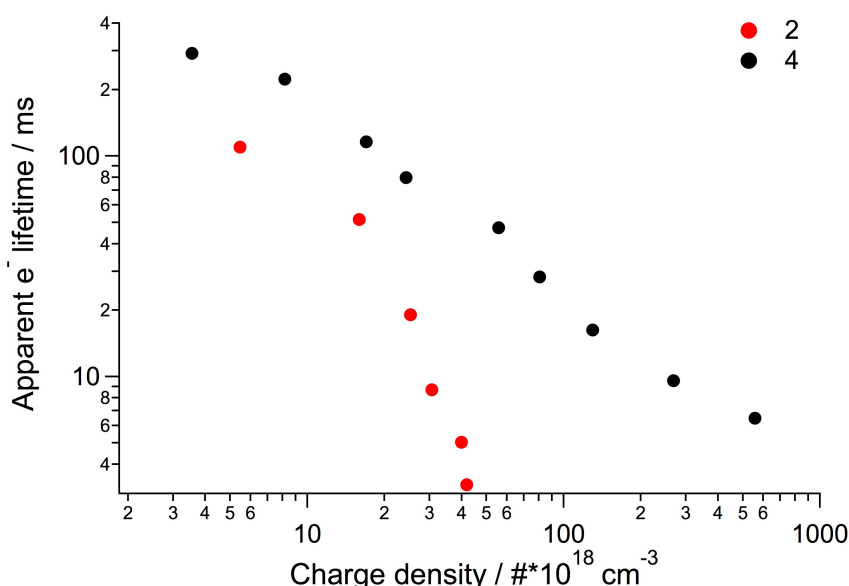


Figure 4.16: Apparent electron lifetimes of the dyes **2** and **4** measured with a transient photovoltage technique.

Electron injection study. Time-correlated single photon counting (TCSPC) technique was used to study the excited state lifetimes of dyes **2** and **4** in an acetonitrile solution and adsorbed on the TiO₂ surface (Figure 4.17). Lifetimes of the species in solution are in the nanosecond range, 5.6 ns for dye **2** and 7 ns for dye **4**. In the case of molecules adsorbed on the TiO₂ layer, the lifetime decreased significantly as a result of the injection of the electron into the conduction band of the semiconductor. Dye **2** adsorbed on the TiO₂ substrate is characterized by an excited state lifetime, τ_{TiO_2} of 296 ps, whereas dye **4** is slightly longer-lived ($\tau_{TiO_2} = 373$ ps). The estimated electron injection efficiencies for both dyes were found to be fairly similar (dye **2**: 94.8%; dye **4**: 94.7%) (Eq. 4.1). The lack of a significant difference between

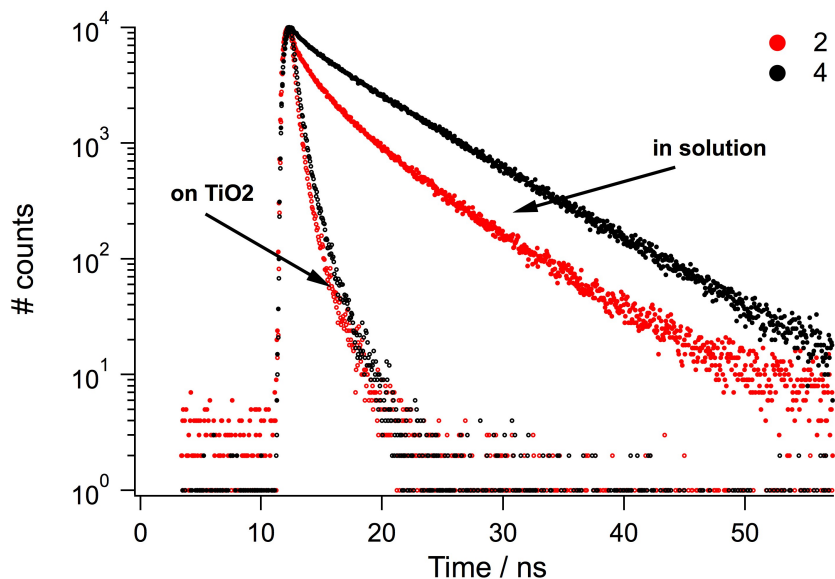


Figure 4.17: Histograms of the dyes **2** and **4** dissolved in acetonitrile and adsorbed on the surface of TiO_2 film. Faster exponential decays in case of dyes adsorbed on TiO_2 are indication of efficient electron injection into the semiconductor. There is no significant difference between the injection yields of the two dyes.

electron injection efficiencies for the two systems may turn the focus on the charge collection efficiency or enhanced recombination processes as main reasons for the dramatically different performance of the two dyes in DSC application.

$$\eta_{inj} = 1 - \frac{\tau_{TiO_2}}{\tau_{solution}} \quad (4.1)$$

Ultrafast laser spectroscopy. Nanosecond laser photolysis experiments focusing on the decay of the oxidized state of the dye performed on TiO_2 films covered with dye **2** and **4** in the absence and presence of the redox electrolyte have confirmed 5 times faster recombination (half-reaction time $\tau_{1/2} = 12 \mu s$) in the case of dye **2** (Figure 4.18). Spectra recorded in the presence of redox electrolyte exhibited a fast decay ($9 \mu s$) due to the efficient regeneration of the oxidized dye molecules by iodide. Nevertheless, in the absence of the redox couple, the dye cations can only be reduced by the dye-injected electrons from TiO_2 (electron back-transfer). In the case of well-performing device, in order to ensure quantitative electron collection at the back contact of the cell, this process is expected to be rather slow and non-competing with the dye regeneration by I^- . This requirement is fulfilled in case of the dye **4** and allows

4.3. The effect of phenyl ring inserted between the benzothiadiazole and cyanoacrylic acid

for the generation of high current densities in the device. In contrast, dye **2** recombines with electrons from TiO_2 in the absence of a redox couple at a time-scale comparable to that of the dye regeneration rate. This undesirable behaviour may indicate a facilitated electron flow from the TiO_2 back to the dye cation. Furthermore, this is in agreement with the planar molecular geometry of the cation of dye **2** as compared to the twisted structure of dye **4** cation as discussed above. Apart from the TCSPC and nanosecond flash photolysis studies, further

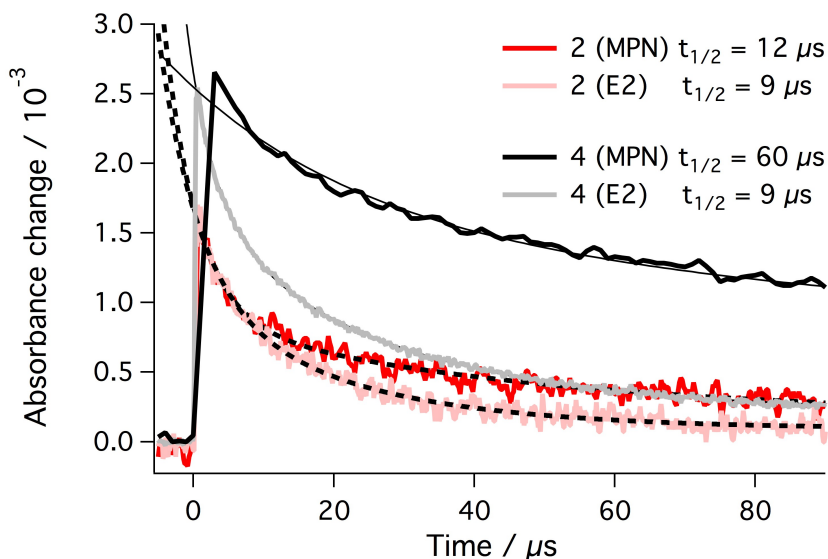


Figure 4.18: Transient absorption data following the decay of the oxidized states of the dyes **2** and **4** adsorbed on a transparent TiO_2 nanocrystalline film in presence and absence of a redox couple.

insight into the excited state deactivation processes was provided by transient absorption measurements. Dyes **2** and **4** were studied on TiO_2 films in the absence of a redox electrolyte. This permits to focus particularly on the interactions between the dyes and TiO_2 . 530 nm laser excitation was used, which directs the light energy mainly to the CT absorption band of both dyes. At this wavelength, both dyes exhibit similar extinction coefficients, which allows for a good comparison even at slight variations of the TiO_2 film thickness. Immediately after laser excitation, the instantaneous formation of the singlet-excited states of the dyes is observed. Specifically, the singlet-excited states of the dyes **2** and **4** are characterized by a maximum at 501 nm and a transient bleach between 535 and 598 nm. After only 0.6 ps singlet-excited features of both dyes transform into new bands (Figure 4.19). This transduction of singlet-excited state energy is then identified by the shift of the minimum of the transient bleach from

Chapter 4. The influence of the structural modifications of D- π -A dyes containing benzothiadiazole as a spacer.

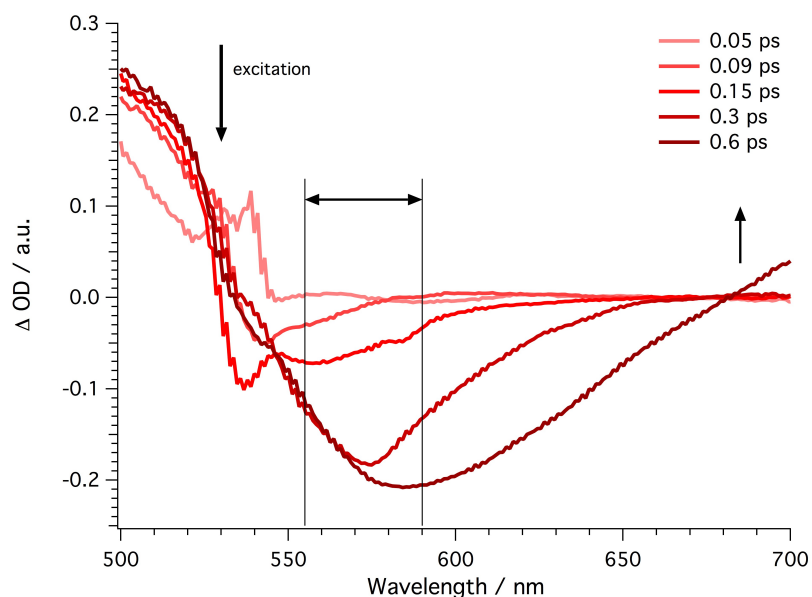


Figure 4.19: Differential absorption spectrum obtained upon femtosecond pump-probe spectroscopy ($\lambda_{exc} = 530$ nm) of a film of the dye **2** on 5 μ m thick TiO₂ with several time delays between 0 and 0.6 ps at room temperature illustrating the radical cation formation with the ground-state transient bleaching between 555 and 590 nm and the triarylamine cation (TA•⁺) beyond 680 nm.

555 to 584 nm and a broadening of the signal. The bleaching is attributed to the ground-state bleaching due to the radical cation formation of the triarylamine (TA•⁺), which is represented by the appearance of a new absorption band beyond 680 nm (Figure 4.19). For both dyes these features appear on a time-scale of less than 2 ps. Hence, after a rapid transfer of singlet-excited state energy, the formation of the charge separated state occurs with equal rate constants for both dyes. Averaging first-order fits of the time-absorption profiles leads to singlet-excited state lifetimes of 0.95 ps for **2** and 0.79 ps for **4**. This supports comparable charge-separation dynamics for both dyes and nicely complies with the fact that the charge-injection efficiencies will be equal when a redox electrolyte is present. The analysis of the decay dynamics reveals the key difference between both dyes (Figure 4.20). For dye **2** the ground-state bleaching and the radical cation signature are vanished after 300 ps, whereas in **4** they remain visible beyond this time scale. The results clearly revealed the faster recombination process in devices prepared using dye **2** compared to dye **4** sensitized devices.

In particular, in the dye **2** absorption profile the radical cation features decay with a lifetime of 18 ps. On the contrary, for the dye **4** it is persistent on the time-scale of our experiment (1100

4.3. The effect of phenyl ring inserted between the benzothiadiazole and cyanoacrylic acid

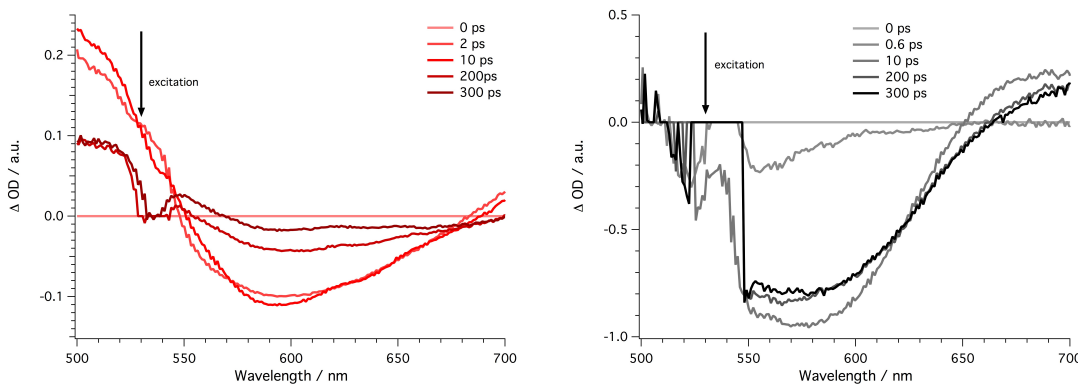


Figure 4.20: Differential absorption spectra obtained upon femtosecond flash photolysis ($\lambda_{exc} = 530 \text{ nm}$) of films of dye **2** (left) and **4** (right) on $5 \mu\text{m}$ thick TiO_2 with several time delays between 0 and 300 ps at room temperature illustrating the difference decay dynamics of the radical cation signatures as stated in the text.

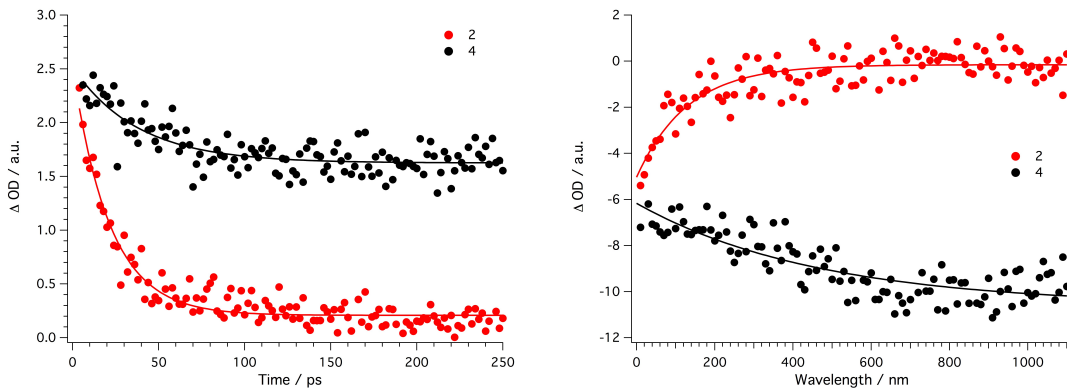


Figure 4.21: First-order-fits of the time-absorption profiles obtained from the femtosecond pump-probe studies of the dyes **2** and **4** illustrating the different charge recombination dynamics of the radical cation signatures at 700 nm (left) and the ground-state bleaching at 580 nm (right).

ps) and give rise to a lifetime of 526 ps (Figure 4.21). Conclusively, charge recombination for the dye **2** occurs almost 30 times faster than for the dye **4**, which is in line with the fact that in the cationic form of **2** the electron back-transfer is facilitated due to the preserved planarity of the π -conjugated system. In other words, dye **2** recombines with electrons from TiO_2 in the absence of a redox couple due to a facilitated electron flow from the TiO_2 back to the dye cation. On the contrary, the electron back-transfer in **4** is hindered by the out-of-plane twist of the additional phenyl ring upon oxidation. This leads to longer lifetimes of the charge-separated state and thus may explain the improved device performances. Importantly, in this context the charge recombination lifetimes do not match the lifetimes obtained by nanosecond laser

Chapter 4. The influence of the structural modifications of D- π -A dyes containing benzothiadiazole as a spacer.

photolysis. The reason for this is that the laser intensities used for the transient absorption studies exceed the laser power of the nanosecond experiment by 2 orders of magnitude. As a consequence, interfacial back electron flow is facilitated due to the high intensities and the generation of many more electrons per laser pulse. This, on the other hand, leads to study much faster charge recombination dynamics as compared with the nanosecond experiments.

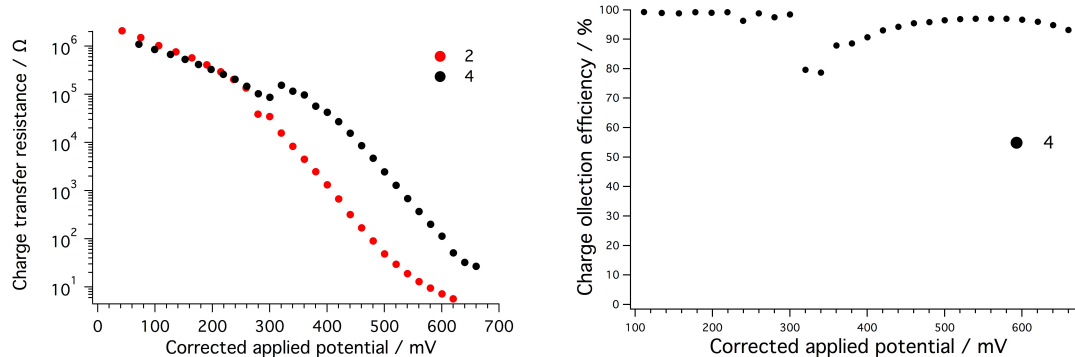


Figure 4.22: *Left:* Charge transfer resistance as a function of the corrected applied potential at the TiO₂/electrolyte interface measured by EIS in the dark on the complete cells. *Right:* Charge collection efficiency for a cell with the dye **E4** as a function of the corrected applied potential calculated from EIS measurement under 0.5 Sun illumination.

Impedance study. Electrochemical impedance spectroscopy (EIS) measurements performed on complete cells in the dark revealed that the charge transfer resistance of the TiO₂/electrolyte interface in the cell sensitized with dye **2** is lower than that with dye **4** (Figure 4.22, left). This may be the reason for faster recombination in the device with dye **2**, which is in accordance with our above-mentioned results. Using the Equation 4.2, where R_{ct} stands for a charge transfer resistance and R_{tr} is a transport resistance, the charge collection efficiency for the best performing cell measured under 0.5 Sun with dye **4** was found to be over 90% (Figure 4.22, right). The fitting of EIS measurements could not provide the values required to calculate the charge collection efficiency for the cell with dye **2**, because a Gerischer-type impedance was observed, where the transport resistance, R_{tr}, and recombination resistance, R_{ct}, cannot be resolved explicitly⁹. Nevertheless, the presence of Gerischer impedance confirms that the electron back-transfer reaction is faster than the transport of charge carriers through the film, which explains the very low J_{SC} measured for the device with dye **2**.

$$\eta_{col} = \frac{R_{ct}}{R_{ct} + R_{tr}} \quad (4.2)$$

4.4 Conclusions

It is of crucial importance to understand the role of the dyes' building blocks so as to improve the molecular design in the future. Incorporation of a BTDA unit close to the anchoring acceptor group led to a bathochromic shift of the CT bands in the UV-Vis spectra, as was shown in the examples of the dyes **1–3**. However, the promising capability of harvesting a broader range of photons by these dyes did not translate into improved cell performance. Cells with the dyes **1–3** exhibited ample electron injection efficiencies and suffered from unusually fast recombination with the electrons from TiO₂, which was reflected by the low PCEs. Insertion of a phenyl ring in order to electronically separate the anchoring group and the BTDA unit in the dye **4** turned out to be a good solution to improve J_{SC} and the overall performance. The additional phenyl ring in the dye **4** seems not to be co-planar with the π -conjugated donor and BTDA part. Theoretical studies revealed that upon formation of the cation of the dye **4**, the out-of-plane torsion of the adjacent BTDA and cyanoacrylic acid unit is enhanced, leading to an interruption of the π -conjugation between donor and anchoring group. The results lead to the conclusion that this configuration inhibits the electron back-transfer. In particular, the electron injection rate was barely affected, but the geminate recombination reaction was slowed down over 5 times.

Extensive laser studies revealed that dye **2** adsorbed on TiO₂ film exhibits a very fast fast decay of its oxidized state even in the absence of the redox couple. In this case, the reduction of the dye **2** has to be realized via the electrons from TiO₂, since the anchoring part of the molecule is flat and the extended LUMO may be overlapping with the TiO₂ conduction band (the electrons flow goes in two directions: dye \rightleftharpoons TiO₂). The geometry of the dye cation **2** allows for this process to occur. In the case of the dye **4** adsorbed on TiO₂, the oxidized state is long-lived in the absence of redox couple, which indicates that the recombination with the conduction band electrons is negligible. The inserted phenyl ring fulfills its role of creating the unidirectional electron flow (dye \rightarrow TiO₂) by introducing a torsion angle in the anchoring unit. Thus, the insertion of the phenyl ring maintains near to quantitative electron injection. Electrochemical impedance spectroscopy confirmed a very low charge transfer resistance for the devices sensitized with the dye **2**. Moreover, in their spectra the Gerischer-type impedance was observed - a clear sign of the back electron transfer reaction being faster than the electron

transport within the TiO₂ film. Blocking this electron leak by structural dye modification with a twisted and electronically decoupling unit may be a possible way to obtain high J_{SCs}s and efficiencies in DSCs.

4.5 Bibliography

- [1] M. Xu, R. Li, N. Pootrakulchote, D. Shi, J. Guo, Z. Yi, S. M. Zakeeruddin, M. Grätzel and P. Wang, *The Journal of Physical Chemistry C*, 2008, **112**, 19770–19776.
- [2] R. Li, X. Lv, D. Shi, D. Zhou, Y. Cheng, G. Zhang and P. Wang, *The Journal of Physical Chemistry C*, 2009, **113**, 7469–7479.
- [3] J.-H. Yum, D. Hagberg, S.-J. Moon, K. Karlsson, T. Marinado, L. Sun, A. Hagfeldt, M. Nazeeruddin and M. Grätzel, *Angewandte Chemie International Edition*, 2009, **48**, 1576–1580.
- [4] M. Velusamy, K. R. J. Thomas, J. T. Lin, Y.-C. Hsu and K.-C. Ho, *Organic Letters*, 2005, **7**, 1899–1902.
- [5] T. Johansson, W. Mammo, M. Svensson, M. R. Andersson and O. Inganäs, *Journal of Materials Chemistry*, 2003, **13**, 1316–1323.
- [6] A. S. D. Sandanayaka, Y. Taguri, Y. Araki, T. Ishi-i, S. Mataka and O. Ito, *The Journal of Physical Chemistry B*, 2005, **109**, 22502–22512.
- [7] M. J. Frisch, G. W. Trucks, H. B. Schlegel, G. E. Scuseria, M. A. Robb, J. R. Cheeseman, G. Scalmani, V. Barone, B. Mennucci, G. A. Petersson, H. Nakatsuji, M. Caricato, X. Li, H. P. Hratchian, A. F. Izmaylov, J. Bloino, G. Zheng, J. L. Sonnenberg, M. Hada, M. Ehara, K. Toyota, R. Fukuda, J. Hasegawa, M. Ishida, T. Nakajima, Y. Honda, O. Kitao, H. Nakai, T. Vreven, J. J. A. Montgomery, J. E. Peralta, F. Ogliaro, M. Bearpark, J. J. Heyd, E. Brothers, K. N. Kudin, V. N. Staroverov, R. Kobayashi, J. Normand, K. Raghavachari, A. Rendell, J. C. Burant, S. S. Iyengar, J. Tomasi, M. Cossi, N. Rega, J. M. Millam, M. Klene, J. E. Knox, J. B. Cross, V. Bakken, C. Adamo, J. Jaramillo, R. Gomperts, R. E. Stratmann, O. Yazyev, A. J. Austin, R. Cammi, C. Pomelli, J. W. Ochterski, R. L. Martin, K. Morokuma, V. G. Zakrzewski, G. A. Voth, P. Salvador, J. J. Dannenberg, S. Dapprich, A. D. Daniels, O. Farkas, J. B. Foresman, J. V. Ortiz, J. Cioslowski and D. J. Fox, *Gaussian 09, Revision A.02*, Gaussian, Inc., Wallingford CT, 2009.
- [8] N. Kopidakis, K. D. Benkstein, J. van de Lagemaat and A. J. Frank, *The Journal of Physical Chemistry B*, 2003, **107**, 11307–11315.
- [9] J. Bisquert, *The Journal of Physical Chemistry B*, 2002, **106**, 325–333.

5 Molecular engineering on D-A- π -A dyes featuring indoline donor and benzothiadiazole bridge.

This part is adapted from a peer reviewed publication by Yongzhen Wu, Magdalena Marszalek, Shaik M. Zakeeruddin, Qiong Zhang, He Tian, Michael Grätzel and Weihong Zhu published in 2012 in Energy and Environmental Science, Vol. 5, pp 8261–8272

5.1 Introduction

Amongst various strategies for improving the power conversion efficiency of dye-sensitized solar cells, successful molecular engineering of the photosensitizers has remarkably contributed to the light harvesting and interfacial environment optimization. Organic dyes with donor- π -acceptor (D- π -A) configuration are the most common among metal-free organic sensitizers^{1–4}. Generally, D- π -A molecules with short π -conjugation length only absorb short wavelength photons, while long π -conjugated dye molecules easily form unfavourable π -stacks⁵ and are not very stable when irradiated with high-energy photons⁶. To further improve the performance of DSCs, including efficiency and stability, it is necessary to remodel the molecular design of organic sensitizers. One of the new design concepts is to realize broad spectral response on relatively small and sturdy organic molecules.

Chapter 5. Molecular engineering on D-A- π -A dyes featuring indoline donor and benzothiadiazole bridge.

Along this line, Tian et al. have recently proposed a novel D-A- π -A configuration for the design of novel organic dyes which are different from the traditional organic D- π -A dyes due to the incorporation of an additional electron-withdrawing unit in the π -spacer⁷. The idea of the specific design of D-A- π -A molecules was based on several deliberate considerations: firstly, the electron-withdrawing unit is usually a low-band gap unit, which is helpful to decrease the HOMO-LUMO gap of organic dyes, and extends their absorption spectra^{8,9}; secondly, the extension of absorption to longer wavelengths, introducing a low-band gap unit to replace a long conjugated structure between D and A is beneficial for the photostability of organic dyes¹⁰; thirdly, it is easy to realize long wavelength absorption in short and small organic molecules, simplifying the synthesis and reducing the material cost.

WS-2 (Figure 5.1, left)⁷, one of the D-A- π -A dyes, employing an indoline derivative as electron donor, cyanoacrylic acid as an electron acceptor and a benzothiadiazole as the additional acceptor in the π -bridge, showed a broad spectral response (IPCE onset > 800 nm), high efficiency ($\eta = 8.7\%$) and good photostability. The **WS-2** based device could be kept for long time without dye desorption and decoloration. The short-circuit current density (J_{SC}) of **WS-2** is comparable with that of a standard Ru-dye N719; however, its open-circuit voltage (V_{OC}) is unsatisfactory. The reason for this relatively lower V_{OC} is that **WS-2** possesses a good co-planarity across the π -conjunction, making it prone to forming unfavourable π -stacks, namely aggregation. This unfavourable aggregation may lead to intermolecular quenching or back reaction of the injected electron, limiting the electron accumulation in the TiO_2 conduction band and resulting in low V_{OC} output. Therefore, controlling dye-aggregation is an important issue for D-A- π -A dyes in order to obtain highly efficient DSCs. Bearing this in mind, a novel D-A- π -A indoline dye **WS-9** (Figure 5.1, right) was designed by introducing an *n*-hexyl substituted thiophene subunit into the π -conjunction of **WS-2** to retard the strong aggregation tendency of the latter.

We carefully studied the differences between **WS-2** and **WS-9** caused by the *n*-hexylthiophene modification, including their absorption spectra, energy levels and photovoltaic performance. The aggregation effect of the two dyes was carefully investigated. The aggregates are formed during dye adsorption in the bath solution, and the types of solvents or coadsorbent have a significant influence on the dye adsorption as well as its aggregation. In this work

5.2. Synthesis and characterization of the dyes WS-2 and WS-9

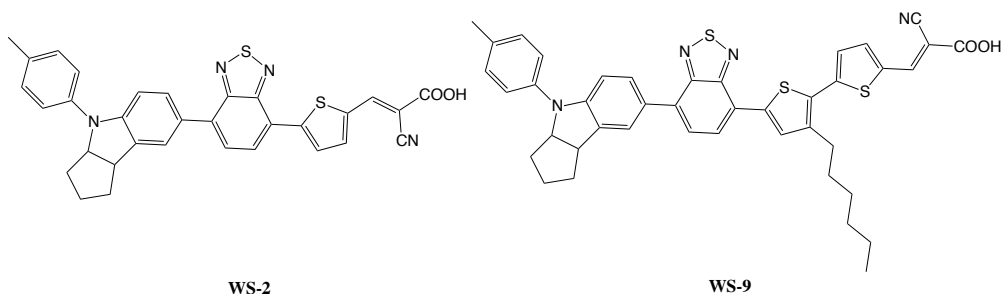


Figure 5.1: Chemical structures of D- π -A sensitizers **WS-2** and **WS-9**.

dichloromethane (CH_2Cl_2) and chloroform (CHCl_3) were used as the bath solvents, and chenodeoxycholic acid (CDCA) was added to the dye bath as the coadsorbent. The **WS-9** based DSCs system shows better performance than that of **WS-2**, regardless of the dye bath solvents employed and the addition of CDCA coadsorbent. Impressively, when coadsorbed with 20 mM CDCA, **WS-9** based DSCs showed remarkable PV performance ($J_{\text{SC}} > 18.0 \text{ mA cm}^{-2}$, $V_{\text{OC}} > 700 \text{ mV}$, and $\eta > 9\%$). Transient photovoltage and photocurrent decay measurements show that the apparent electron lifetime of **WS-2** based DSCs increases an order of magnitude upon CDCA coadsorption. In contrast, there is only a minor variation in the electron lifetime for **WS-9** after CDCA addition. As demonstrated, the introduction of *n*-hexylthiophene can significantly improve the potential anti-aggregation ability of D- π -A organic dye, proving that a small chemical modification on the sensitizer structures can largely affect its photovoltaic performance. Our research indicates that the D- π -A featured organic dyes are promising candidates in the development of highly efficient DSCs.

5.2 Synthesis and characterization of the dyes WS-2 and WS-9

5.2.1 Design and synthesis

In the previous work of Tian et. al, they found that the D- π -A configuration dyes showed several merits with respect to the common D- π -A organic dyes^{7,11}. Especially, **WS-2** with an indoline unit as the electron donor, cyanoacrylic acid as the electron acceptor, a thiophene group as π -conjunction and a benzothiadiazole as the additional acceptor, showed extremely high photovoltaic performance after coadsorption with CDCA. To further improve the performance of this organic sensitizer, we specifically introduced a hexylthiophene group into

Chapter 5. Molecular engineering on D-A- π -A dyes featuring indoline donor and benzothiadiazole bridge.

the structure of **WS-2** for the design of **WS-9**. The sterically hindering hexyl chain was expected to suppress the serious aggregation tendency of **WS-2** on the TiO₂ film. The novel dye **WS-9** was synthesized according to the synthetic route in the Figure 5.2. The starting material **2** is an important intermediate for preparing **WS-2**. After Suzuki coupling with a pinacol ester of 4-hexylthiophene-2-boronic acid (**1**), the pivotal hexylthiophene unit was successfully incorporated into the target system. It is widely known that the introduction of long alkyl chains into dyes can not only inhibit the dye aggregation¹²⁻¹⁴ but also improve the solubility¹⁵, which is of great benefit to the synthesis and purifications. For further grafting another thiophene unit, a simple bromination was done on the reactive hexylthiophene unit. Suzuki coupling with a low cost and commercially available 5-formylthiophene-2-boronic acid resulted in the aldehyde precursor. Finally, the obtained intermediate **5** was converted to sensitizer **WS-9** by Knoevenagel condensation with cyanoacrylic acid by reflux in acetonitrile in the presence of piperidine. The important intermediates **3**, **4**, **5** and the target sensitizer were well characterized by ¹H NMR, ¹³C NMR, and HRMS. The obtained **WS-9** is dark in solid state and can be dissolved in dichloromethane, chloroform, and THF.

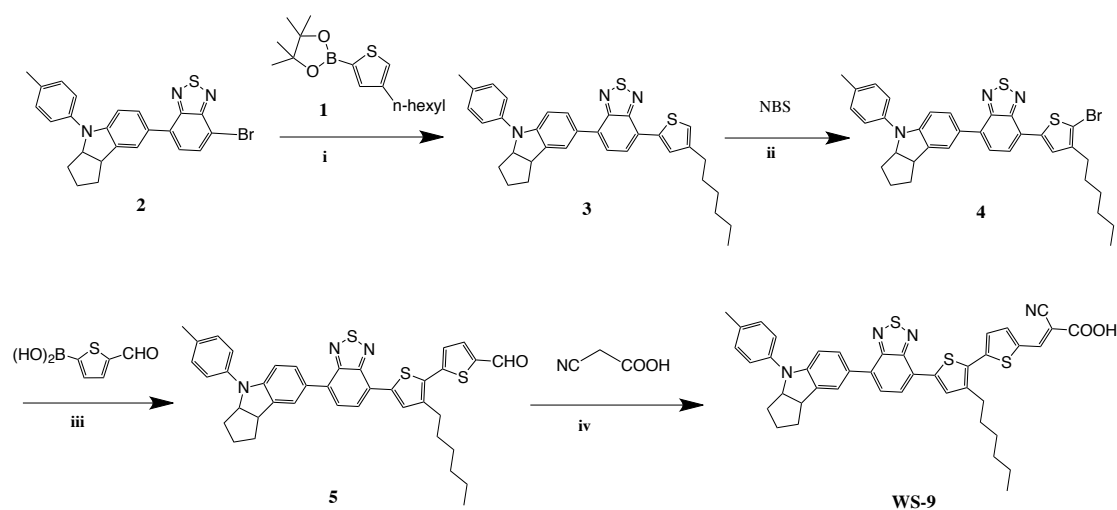
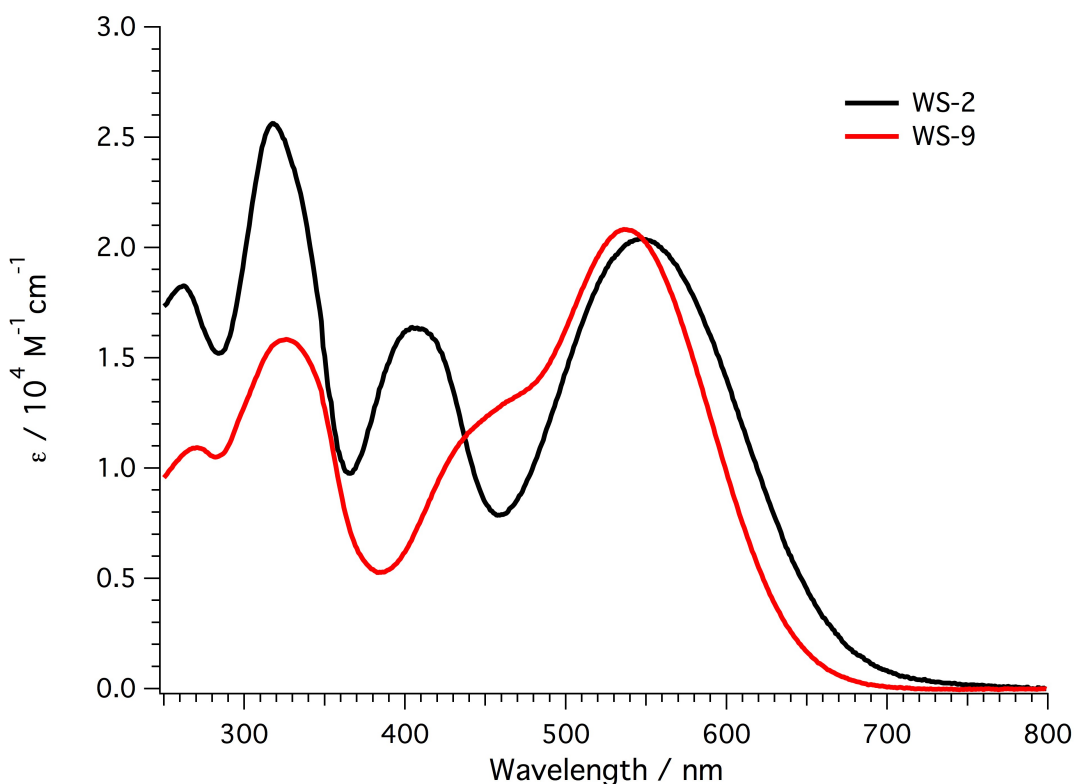


Figure 5.2: Synthetic route of dye **WS-9**. Reaction conditions: (i) Pd(PPh₃)₄, 2 M K₂CO₃ aqueous solution, THF, Ar, 80°C; (ii) NBS CH₂Cl₂, 0°C; (iii) Pd(PPh₃)₄, 2 M K₂CO₃ aqueous solution, THF, Ar, 80°C; (iv) piperidine, acetonitrile, Ar, 80°C.

Figure 5.3: Absorption spectra of **WS-2** and **WS-9** in CH_2Cl_2 .

5.2.2 Optical and redox properties

The UV-vis absorption spectra of **WS-2** and **WS-9** in CH_2Cl_2 solution are shown in the Figure 5.3. The absorption peaks as well as their extinction coefficients are summarized in the Table 5.1. In general, commonly used D- π -A organic dyes show two principle groups of absorption bands: one intramolecular charge transfer (ICT) absorption in the visible region and one local π - π^* absorption band in the UV region¹⁶. However, it is interesting to find that the two D-A- π -A dyes show three major electronic absorption bands in the UV and visible regions. It is worthwhile to investigate the origins of the additional absorption band and to evaluate its contribution to the photo-induced charge separation. In addition, although **WS-9** contains one more thiényl unit in the π -conjunction, its ICT absorption peak is not red-shifted, but blue-shifted by 10 nm with respect to that of **WS-2**. Meanwhile, the most significant difference in absorption spectra between **WS-9** and **WS-2** is the band around 400 nm, where the former shows a 50 nm red shift compared to the latter. Obviously, the elongation of the π -conjunction does not broaden the ICT band, but red-shifts the absorption band around 400 nm, evoking

Chapter 5. Molecular engineering on D-A- π -A dyes featuring indoline donor and benzothiadiazole bridge.

further interest on that specific absorption band. The density functional theory (DFT) is employed for further study on the absorption bands of D-A- π -A dyes.

Table 5.1: Absorption and electrochemical properties of **WS-2** and **WS-9** measured in CH_2Cl_2 .

| Dye | $\lambda_{abs} (\varepsilon)^a$ nm ($\text{M}^{-1}\text{cm}^{-1}$) | HOMO V ^b | E_{0-0}^c V | LUMO V ^d |
|------|---|------------------------|------------------|------------------------|
| WS-2 | 318 (25600) | 0.67 | 2.02 | -1.35 |
| | 408 (16400) | | | |
| | 546 (20400) | | | |
| WS-9 | 327 (15800) | 0.66 | 2.05 | -1.39 |
| | 458 (12700) | | | |
| | 536 (20800) | | | |

^a Absorption peaks (λ_{abs}) and molar extinction coefficients (ε) were measured in CH_2Cl_2 (10^{-5} M). ^b The first formal oxidation potentials (vs. NHE) were internally calibrated with ferrocene, and taken as the HOMO. ^c E_{0-0} was estimated from the differences between the redox peaks of dyes in anodic and cathodic voltammograms. ^d The LUMO was calculated with the expression of LUMO = HOMO - E_{0-0} .

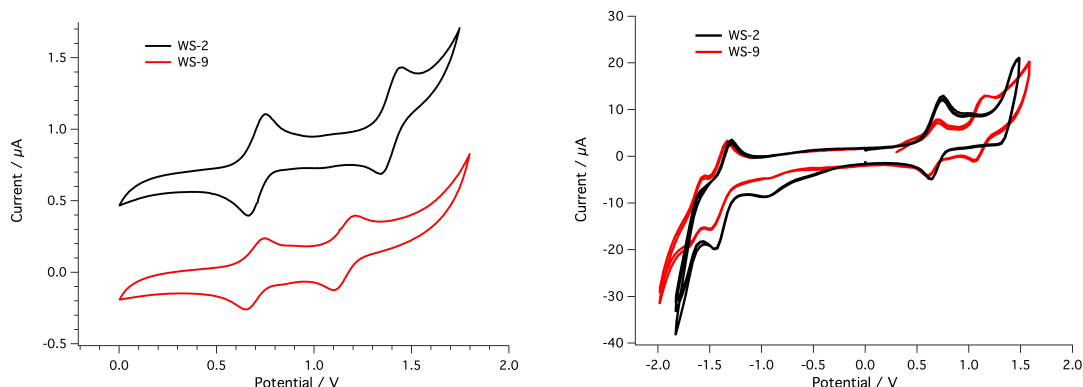


Figure 5.4: Cyclic voltammetry scans of the dyes **WS-2** and **WS-9** measured in CH_2Cl_2 (left: anodic scans, right: cathodic scans).

5.2.3 Theoretical calculations

To understand the origins of the additional absorption band in D-A- π -A dyes and the absorption variation of **WS-9** with respect to **WS-2** caused by the additional thiényl unit, TD-DFT calculations were performed on the B3LYP optimized ground-state geometries taking into consideration the solvent effect (CH_2Cl_2)¹⁷. Theoretically, the D-A- π -A dyes show three groups of absorption bands (Table 5.2):

5.2. Synthesis and characterization of the dyes WS-2 and WS-9

- i) the lowest energy absorption bands (S1 transition) for both dyes correspond to the HOMO→LUMO transition
- ii) the additional absorption band around 400 nm (S2 transition) is composed of the electronic excitations of HOMO→LUMO+1 and HOMO-1→LUMO
- iii) the absorption band in the UV region (S3 transition) is ascribed to other high energy transitions, such as HOMO→LUMO+2 or HOMO-1→LUMO+1

The energy level values, including HOMO-2, HOMO-1, HOMO, LUMO, LUMO+1 and LUMO+2, were further likewise simulated and are displayed in the Figure 5.5. The HOMO and LUMO levels of both dyes are similar, resulting in a nearly identical ICT absorption band at around 540 nm. However, the HOMO-1 and LUMO+1 levels of **WS-9** drift significantly with respect to that of **WS-2**. Considering the upward shift in HOMO-1 and downward shift in LUMO+1 of **WS-9** (Figure 5.5), it is easy to understand that the HOMO→LUMO+1 and HOMO-1→LUMO transition energy become smaller, resulting in the observed red shift in absorption band at 458 nm.

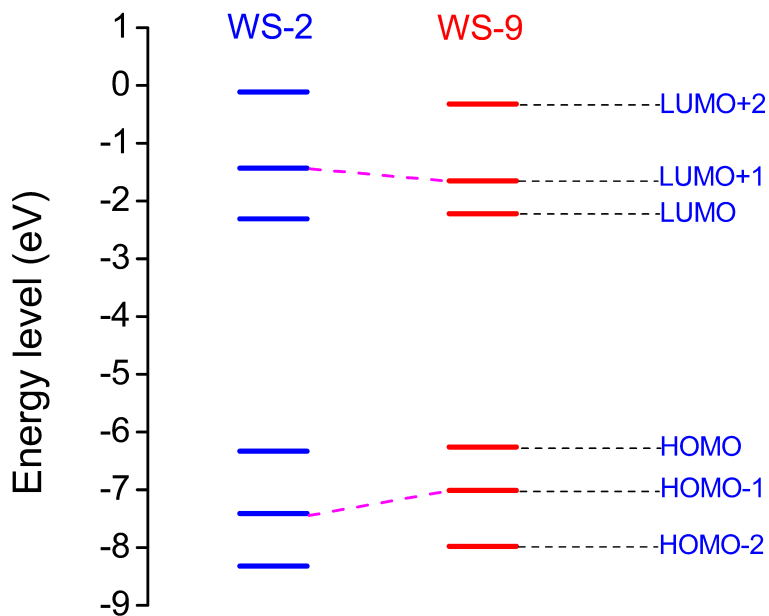


Figure 5.5: The calculated molecular orbital energy levels of **WS-2** and **WS-9**, including HOMO-2, HOMO-1, HOMO, LUMO, LUMO+1 and LUMO+2.

Chapter 5. Molecular engineering on D-A- π -A dyes featuring indoline donor and benzothiadiazole bridge.

Table 5.2: Calculated TDDFT (CAMB3LYP) excitation energies for the lowest transition (eV, nm), oscillator strengths (f), composition in terms of molecular orbital contributions, and experimental absorption maxima.

| Dye | State | Composition ^a | E eV (nm) | f | Exp. eV (nm) |
|------|-------|--------------------------|--------------|--------|-----------------|
| WS-2 | S1 | 77%H→L | 2.31 (535.9) | 1.2417 | 2.27 (546) |
| | S2 | 34%H→L+1 48%H-1→L | 3.16 (391.8) | 0.3657 | 3.04 (408) |
| | S3 | 28%H-1→L+1 | 4.07 (304.3) | 0.1083 | 3.89 (318) |
| WS-9 | S1 | 61%H→L | 2.32 (533.5) | 1.7286 | 2.31 (536) |
| | S2 | 44%H→L+1 36%H-1→L | 2.87 (432.3) | 0.2035 | 2.71 (458) |
| | S3 | 33%H→L+2 | 4.06 (305.7) | 0.4483 | 3.79 (327) |

^a H = HOMO, L = LUMO, H-1 = HOMO-1, H-2 = HOMO-2, L+1 = LUMO+1, L+2 = LUMO+2.

Here, the upward shift of HOMO-1 orbital can be cross-checked by the cyclic voltammetry (CV) measurement. Figure 5.4, left, shows the anodic CV scans of **WS-2** and **WS-9** in CH₂Cl₂. Both dyes reveal two groups of redox process in the anodic region. The first one around 0.7 V (vs. NHE, same below) corresponds to HOMO level, while the second peak couple can be attributed to the redox potential of the HOMO-1 orbital. The second redox couple peak of **WS-9** was apparently negatively shifted by 0.24 V with respect to **WS-2** from +1.397 V to +1.156 V. For experimentally determining the HOMO-LUMO gap, namely E₀₋₀, the cathodic CV scans were also carried on these two dyes in CH₂Cl₂ solutions (Figure 5.4, right). It is worth noting that both of the two dyes are redox stable since their CV curves are almost overlapping after repeatedly scanning. The HOMO and LUMO levels (calibrated with the internal ferrocene reference) are shown in the Table 5.1. The slight upward shift of HOMO and LUMO for **WS-9** in experimental results is in agreement with the theoretical calculations.

It is important to evaluate the contributions of the absorbed photons from different transitions to the effective charge separation, hence the ground-state geometries of **WS-2** and **WS-9** were optimized in the gas phase by DFT with the *Gaussian09* package¹⁷, using the hybrid B3LYP functional and the standard 6-31G(d) basis set. The electron distributions of the frontier orbitals (HOMO-2, HOMO-1, HOMO, LUMO, LUMO+1, LUMO+2) in the systems of **WS-2** and **WS-9** are shown in the Figure 5.6. Due to the similar configuration, the most frontier orbitals of two dyes possess similar spatial distribution, except for the LUMO+2 orbital. For both dyes,

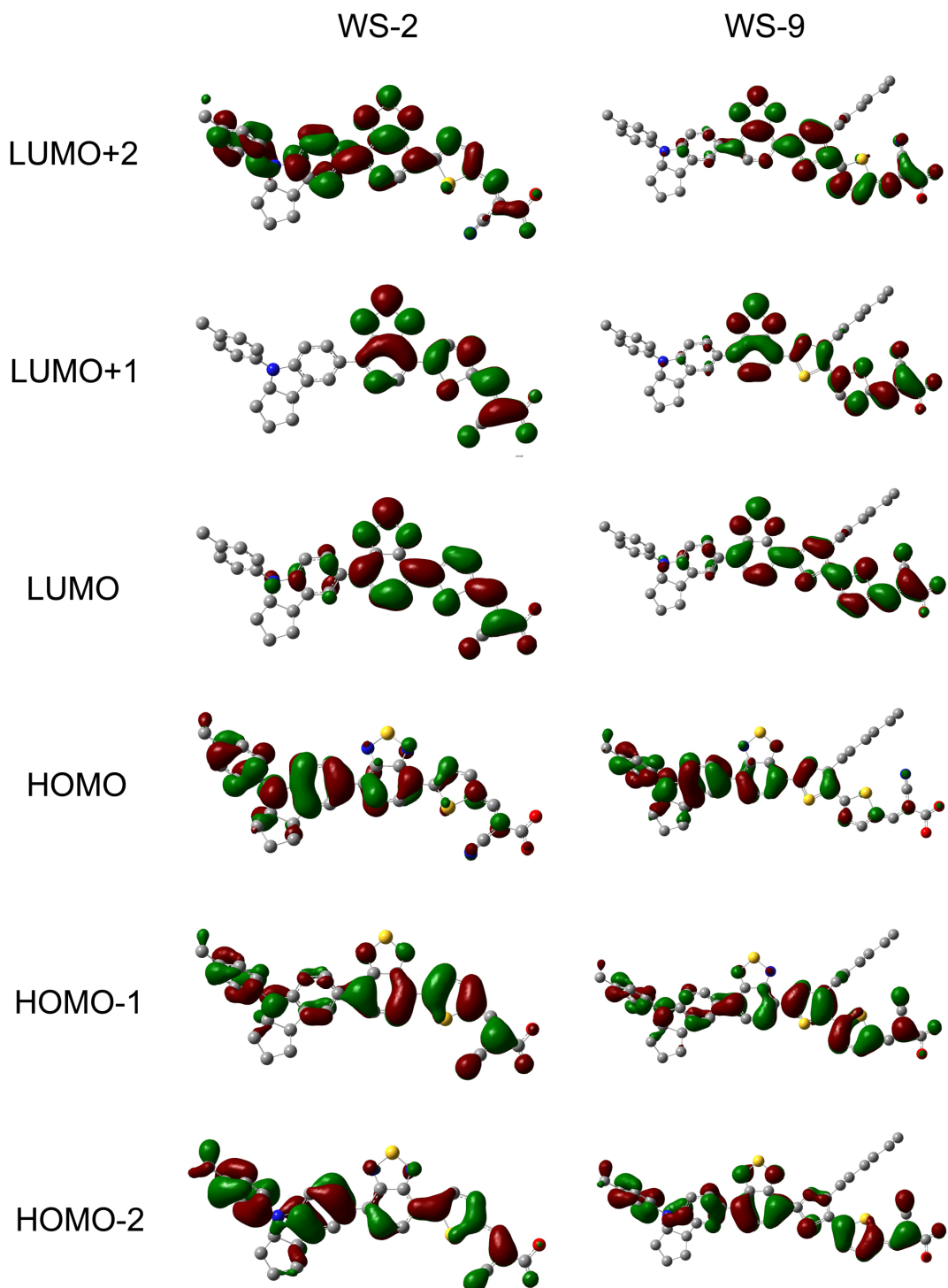


Figure 5.6: The frontier orbitals of sensitizers **WS-2** and **WS-9** (isodensity = 0.020 a.u.).

Chapter 5. Molecular engineering on D-A- π -A dyes featuring indoline donor and benzothiadiazole bridge.

the HOMO orbitals are mainly located on the indoline and benzothiadiazole skeleton, while HOMO-1 orbitals are distributed on the whole molecules. Interestingly, for the two dyes, the LUMO and LUMO+1 orbitals are almost the same, covering the whole A- π -A conjunction, with a distinct overlap with the HOMO and HOMO-1 orbitals on the benzothiadiazole core. Notably, the LUMO and LUMO+1 are very important for the two dyes, because most of their electron transition bands involve transporting electrons to these two orbitals. Apparently, besides the HOMO→LUMO absorption band, the observed additional absorption bands at 408 and 458 nm for **WS-2** and **WS-9**, respectively, are also favourable to the photon-to-electron conversion since they correspond to efficient electron-transitions to the LUMO or LUMO+1 orbitals, where electrons could be smoothly injected into the semiconductor. The origins of the additional absorption band in the D-A- π -A dye and the electron distributions for the frontier molecular orbitals are well understood with the aid of DFT and TDDFT calculations. The featured D-A- π -A dyes are preferable to use in DSCs, as compared to common D- π -A dyes for the light harvesting, since they possess an additional absorption band for efficient charge separation.

5.2.4 The effect of an additional acceptor on the optical properties of the deprotonated form of the dye

In the previous work, it was found that the strong electron-withdrawing unit in the D-A- π -A dyes could weaken the large blue-shift in ICT band caused by the deprotonation of the carboxylic acid group ($-COOH$). For instance, when organic dyes adsorbed onto the TiO_2 film, the free $-COOH$ group became a $-COOTi$ form, which equals to the deprotonation of the COOH. Most D- π -A organic dyes show a large blue-shift in absorption spectra during this process, which is unfavourable to the long wavelength light harvesting. Taking the triphenylamine dye C219 as an example, its ICT peak was observed at 584 nm in a chloroform solution, but distinctly blue-shifted to <500 nm after adsorption on a $2.4\ \mu m$ TiO_2 film¹⁸. The blue-shift was not as apparent in the D-A- π -A featuring dyes. Previously, we only compared the absorption spectra of D-A- π -A dyes in solutions and on TiO_2 films⁷. Considering that the absorption spectra of sensitizer dyes on TiO_2 film were also affected by the dye-aggregation and scattering effect of the nanoparticles, here we use triethylamine (TEA) to neutralize the $-COOH$ in the

5.2. Synthesis and characterization of the dyes WS-2 and WS-9

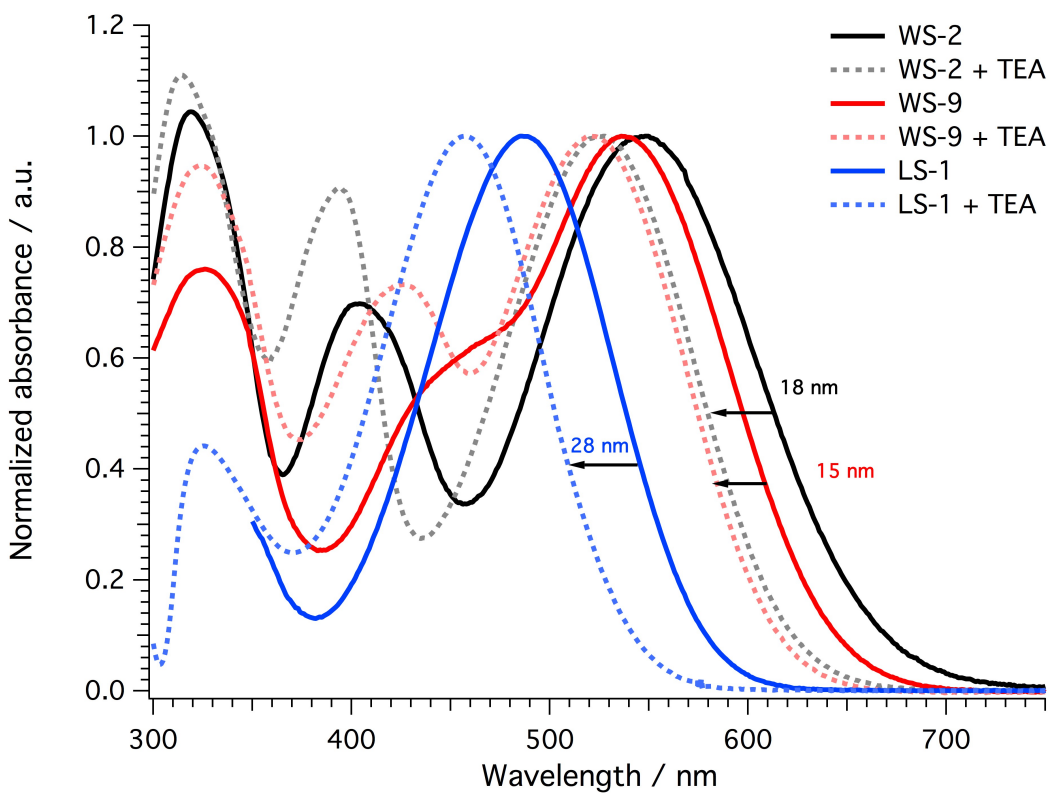


Figure 5.7: The effect of TEA on absorption spectra of dyes in dichloromethane solutions.

CH_2Cl_2 solutions and investigate the deprotonation directly. Note that the amount of TEA was excessive for dyes in solution. A reference D- π -A dye LS-1⁷ having a similar structure to **WS-2** with the exception of benzothiadiazole unit was used in this experiment. The absorption spectra of the three dyes (**WS-2**, **WS-9** and LS-1) in the presence and absence of TEA in CH_2Cl_2 solutions are shown in the Figure 5.7. After the addition of TEA, the absorption spectra of all three dyes showed a blue-shift to various extent. The degree of this blue-shift is also illustrated in the Figure 5.7, ie., 15, 18 and 28 nm for **WS-9**, **WS-2** and LS-1, respectively. The reference D- π -A dye LS-1 exhibits a larger blue-shift than **WS-2** and **WS-9**, indicating the weakening of the deprotonation effect by the additional 'A' unit in D-A- π -A dyes. The electron transition in D- π -A structure dyes is facilitated by the push-pull effect of the electron donor and acceptor. The deprotonation of the -COOH group will decrease the electron withdrawing ability of the acceptor group, leading to an inevitable blue-shift in the absorption spectra¹⁹. The longer π -bridge will lead to a larger blue-shift. However, in the D-A- π -A dyes, the additional electron-withdrawing group in the structure assists the electron transition process. The deprotonation

Chapter 5. Molecular engineering on D-A- π -A dyes featuring indoline donor and benzothiadiazole bridge.

induced blue-shift is thus not as evident for D-A- π -A dyes. In addition, it is interesting to find that the shoulder peak of **WS-9** at around 450 nm was significantly blue-shifted by the addition of TEA, resulting in three changed absorption bands in 300, 400 and 500 nm intervals to form a broad and high absorption. By contrast, **WS-2** showed similar absorption width, but low absorbance in region of 400–500 nm; LS-1 showed a much narrower absorption range in the presence of TEA.

5.3 Optimization of the photovoltaic performance

5.3.1 General PV characterization including the effects of the dye-bath solvent and coadsorbents

Preliminary photovoltaic performance comparison between WS-2 and WS-9. In the first set of experiments, **WS-2** and **WS-9** were adsorbed onto the TiO₂ electrode from a dye solution using CH₂Cl₂ as solvent. The devices were filled with a volatile electrolyte (Z960). In order to check the difference in aggregation between the two dyes, parallel experiments were also conducted by adding 2 mM chenodeoxycholic acid (CDCA) into the dye solutions. The J-V curves of DSCs based on both dyes in the presence and absence of CDCA are shown in the Figure 5.8, left. Photovoltaic parameters such as J_{SC}, V_{OC}, FF and η are collected in the Table 5.4. As expected, CDCA is effective in increasing photovoltaic performance for both dyes. However, the improvement witnessed in presence of coadsorbent for **WS-2** is much greater than that of **WS-9**. For **WS-2**, 2 mM CDCA increases the photovoltaic performance significantly: J_{SC} augments from 8.46 to 17.50 mA cm⁻², V_{OC} from 601 to 657 mV and the power conversion efficiency (η) improved from 3.86% to 8.56%. For **WS-9**, 2 mM CDCA has only small influence on J_{SC} and η . The significant increase in J_{SC} following CDCA coadsorption with **WS-2** can be explained by the incident photon-to-electron conversion efficiency (IPCE) (Figure 5.8, right). The IPCE of **WS-2** was almost doubled after CDCA treatment, while for **WS-9** there was only a small variation. The manifestly different influence that coadsorption of CDCA in presence of **WS-2** and **WS-9** based DSCs is a strong indication that the structural differences of the two dyes have a great impact on dye aggregation. A comparison between **WS-2** and **WS-9** photovoltaic data shows that the introduction of *n*-hexylthiophene leads to

5.3. Optimization of the photovoltaic performance

an increase in the V_{OC} of **WS-9** device regardless of the presence of CDCA. It is indicative that the introduction of the *n*-hexylthiophene in **WS-9** yields a V_{OC} value of 692 mV, which is 91 mV higher than that of **WS-2** without CDCA. Although the presence of 2 mM CDCA increased the V_{OC} value of **WS-2** based DSCs from 601 to 657 mV, it is still far lower than that of **WS-9**.

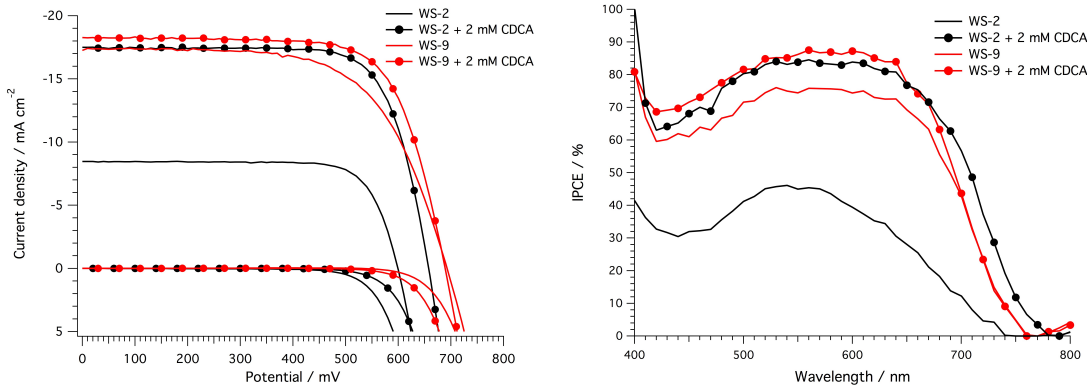


Figure 5.8: *Left:* J-V curves of devices with dyes **WS-2** and **WS-9** in the dark and under 1 Sun illumination. The dyes were deposited from CH_2Cl_2 solutions. *Right:* IPCE of the same devices, with volatile Z960 electrolyte. TiO_2 film consisted of an 8 μm transparent layer and 5 μm scattering layer.

Table 5.3: The effect of CDCA addition to the dye-bath on dye loading.

| Dye | Solvent | Γ^a | |
|------|--------------------------|---|-----------|
| | | $\times 10^{20} \mu\text{m}^{-1}$ pure dye | with CDCA |
| WS-2 | CH_2Cl_2 | 6.37 | 4.82 |
| | CHCl_3 | 4.45 | 3.97 |
| WS-9 | CH_2Cl_2 | 5.34 | 4.96 |
| | CHCl_3 | 4.18 | 3.43 |

^a Γ : number of dye molecules normalized to the film thickness.

Dye-bath solvent effect on photovoltaic performance. The adsorption and aggregation of sensitizer dyes on TiO_2 films are strongly dependent on the solvent used as a dye bath²⁰. Consequently, we systematically studied the aggregation effect of the two dyes on TiO_2 photoanodes stained from two dye solutions containing either in CH_2Cl_2 or CHCl_3 . A dye loading experiment was performed in order to determine the number of molecules grafted on the TiO_2 surface. For each dye, either a CH_2Cl_2 or CHCl_3 solution of pure dye, and another one containing 10 mM of CDCA were prepared. Transparent TiO_2 electrodes were immersed in

Chapter 5. Molecular engineering on D-A- π -A dyes featuring indoline donor and benzothiadiazole bridge.

these solutions, following the standard cell preparation procedure. Before treating the samples with desorbing solution, the photoanodes were thoroughly rinsed using the corresponding solvent in order to remove the loosely bound molecules, not chemically attached to the TiO₂ surface. The number of adsorbed molecules was determined by UV-Vis spectrometry and the values were normalized to the film thickness (assuming that other film parameters, namely porosity and specific surface area, were identical for the same batch of the substrates). As shown in the Table 5.3, it is evident that the number of **WS-2** molecules deposited from pure CH₂Cl₂ is significantly higher than for all other samples in both solvents. However, this augmentation of surface coverage does not lead to an increase of the photocurrent density (Table 5.4). The addition of CDCA decreased the total number of **WS-2** molecules by almost 25%. Nevertheless, the current drawn from the corresponding solar cell is more than doubled. **WS-9** is not very much affected by the presence of the coadsorbent, regardless of the solvent used; the dye loading is somewhat lower due to the occupation of the adsorption sites by CDCA. A significant increase in photovoltaic performance is not to be expected, since the structure of **WS-9** should ensure sufficient steric repulsion between the molecules. We also present the results of the dye adsorption from different solvent, CHCl₃. When using CHCl₃ as a dye bath, surprisingly, the number of **WS-2** molecules is diminished to a level comparable to **WS-9** (without CDCA). CHCl₃ is a non-polar solvent and appears to solvate the dye molecules better, resulting in lower dye loading, but in better spatial distribution, preventing the undesired $\pi - \pi$ stacking. The addition of CDCA in CHCl₃ has no significant effect on the number of adsorbed dye molecules.

The electrodes stained from CHCl₃ solutions (with and without the addition of 2 mM CDCA) were used to fabricate solar cells, according to the previously described procedure (see: Chapter 3 Experimental methods). The η of DSC stained by **WS-2** (without CDCA) from CHCl₃ (7.22%) was almost 2 times higher than that stained from CH₂Cl₂ (3.86%) (Table 5.4). However, in the case of coadsorption with 2 mM CDCA the solvent has negligible influence on the photovoltaic parameters. It indicates that **WS-2** easily forms aggregates on the surface of TiO₂ when adsorbed from CH₂Cl₂ solution in the absence of CDCA. In contrast to **WS-2**, **WS-9** based DSCs show comparable photovoltaic performance whether CH₂Cl₂ or CHCl₃ is used as bath solvent for sensitization. In the case of **WS-2** based devices, coadsorption with CDCA

5.3. Optimization of the photovoltaic performance

Table 5.4: Photovoltaic characteristics of DSCs based on **WS-2** and **WS-9** using CH_2Cl_2 or CHCl_3 as sensitizing bath solvent and Z960 (volatile) as electrolyte, with or without CDCA as a coadsorbent.

| Dye | Solvent | CDCA mM | J_{SC} mA cm^{-2} | V_{OC} mV | FF | η % |
|------|--------------------------|------------|---------------------------------|----------------|------|-------------|
| WS-2 | CH_2Cl_2 | 0 | 8.46 | 601 | 0.76 | 3.86 |
| | | 2 | 17.50 | 657 | 0.74 | 8.56 |
| | CHCl_3 | 0 | 16.25 | 618 | 0.72 | 7.22 |
| | | 2 | 17.82 | 646 | 0.72 | 8.29 |
| WS-9 | CH_2Cl_2 | 0 | 17.26 | 692 | 0.64 | 7.63 |
| | | 2 | 18.28 | 689 | 0.71 | 8.99 |
| | CHCl_3 | 0 | 16.99 | 689 | 0.70 | 8.15 |
| | | 2 | 17.88 | 702 | 0.67 | 8.40 |

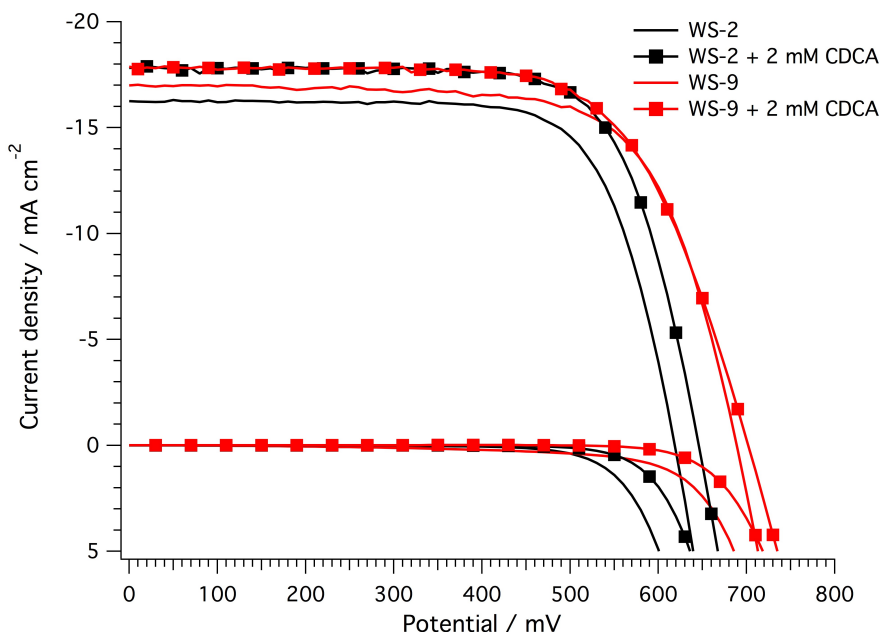


Figure 5.9: J-V curves of devices with dyes **WS-2** and **WS-9** in the dark and under 1 Sun illumination. The dyes were deposited from CHCl_3 .

is helpful in breaking this kind of aggregates, resulting in a significant increase in J_{SC} , V_{OC} and η . In addition, CDCA may also adsorb on the surface of TiO_2 , and is believed to hinder the recombination of injected electrons from the TiO_2 surface to the oxidized species of the redox electrolyte. Coadsorption of **WS-9** with 2 mM CDCA increased the J_{SC} of DSCs stained in CH_2Cl_2 and CHCl_3 by around 5%. It is worth noting, that in the case of **WS-9** changing the solvent from CH_2Cl_2 to CHCl_3 did not induce formation of aggregates, indicating that the

Chapter 5. Molecular engineering on D-A- π -A dyes featuring indoline donor and benzothiadiazole bridge.

presence of a hexyl chain on the thiophene spacer can likewise be helpful in retarding the recombination process. CDCA coadsorption has a marginal influence on the **WS-9** sensitized devices. The dye aggregation on the TiO₂ surface is simultaneously influenced both dye structure and bath solvent used for sensitization and coadsorbent. Backing our primary purpose in the specific design of **WS-9** it is observed that this dye exhibits superior anti-aggregation capacities and gives better overall performance than **WS-2**.

Table 5.5: Photovoltaic characteristics for DSCs based on **WS-2** and **WS-9** using CH₂Cl₂ or CHCl₃ as a dye-loading solvent and Z960 (volatile) as electrolyte, with 20 mM CDCA as a coadsorbent.

| Dye | Solvent | J _{SC} mA cm ⁻² | V _{OC} mV | FF | η % |
|------|---------------------------------|--|-----------------------|------|-------------|
| WS-2 | CH ₂ Cl ₂ | 17.95 | 649 | 0.73 | 8.56 |
| | CHCl ₃ | 17.93 | 661 | 0.74 | 8.90 |
| WS-9 | CH ₂ Cl ₂ | 18.15 | 702 | 0.71 | 9.02 |
| | CHCl ₃ | 18.00 | 696 | 0.72 | 9.04 |

Coadsorption with the excess of CDCA (20 mM). As discussed above, addition of 2 mM CDCA to the dye solution is helpful in suppressing unfavourable dye aggregation and augmenting the DSCs performance. Since 2 mM CDCA used as a coadsorbent had a major influence on the photovoltaic parameters of **WS-2** in CH₂Cl₂, we decided to study the influence of saturated solution of CDCA on photovoltaic parameters. Another set of experiments, where the concentration of CDCA in dye solution is increased to 20 mM was performed. As the solubility of CDCA in CH₂Cl₂ and CHCl₃ is not high, much time was required to dissolve 20 mM CDCA into these solvents using ultrasonic bath, meaning that the concentration of CDCA in the dye solution was close to saturation. As shown in the Table 5.5, following coadsorption with 20 mM CDCA, the photovoltaic performances of both **WS-2** and **WS-9** devices were further improved. Specifically, **WS-9** based DSCs show J_{SC} > 18 mA cm⁻², V_{OC} > 700 mV, and η > 9%. Importantly, we found that the V_{OC} of **WS-2** was limited to around 660 mV, regardless of the CDCA concentration. Therefore, the V_{OC} is the key parameter hindering the efficiency improvement of **WS-2** based DSCs. For **WS-2**, an increase in V_{OC} was observed with CDCA (600 mV for dye alone and 660 mV with CDCA coadsorbed), whereas the V_{OC} of **WS-9** dye was relatively high, and not influenced by CDCA concentration in the dye solution (690 mV for no CDCA and 700 mV for CDCA coadsorbed). The reason why **WS-9** shows higher V_{OC} will be

studied by transient photovoltage and photocurrent decay experiments and electrochemical impedance spectroscopy analysis.

5.3.2 Apparent electron lifetime and electrochemical impedance spectroscopy

As discussed above, the lower device performance of **WS-2** with respect to **WS-9** dye in presence and absence of the CDCA coadsorbent results mainly from the dye aggregation in addition to enhanced electron recombination. Transient photovoltage and photocurrent experiments performed on the above-discussed set of cells with various concentrations of CDCA confirm the recombination-blocking effect of the coadsorbent. **WS-2** dye, which lacks a hexyl chain on its π -conjugated moiety, requires the addition of a coadsorbent to prevent the back electron transfer. The V_{OC} of **WS-2** sensitized devices is low compared to either **WS-2** or **WS-9** based devices with a coadsorbent. Open-circuit voltage is defined as a difference between the redox potential of the electrolyte and the quasi-Fermi level of TiO_2 . As the redox potential was kept constant during the experiment through using the same electrolyte, the quasi-Fermi level of TiO_2 must be changing. The population of electrons in the semiconductor under illumination determines the position of quasi-Fermi level, thus, by assuming constant electron injection rate for each dye, it can be concluded that the difference in the V_{OC} between the two dyes results from the existence of more electron leakage paths in the case of **WS-2** based devices. Bare TiO_2 sites exposed directly to the redox electrolyte are examples of such leakage paths. Closer packing of dye molecules on the surface of TiO_2 would prevent this exposure, but it would also cause the undesirable aggregation, allowing for dye-dye interactions, and most probably a decrease in the electron injection efficiency. Coadsorbents, like CDCA, are believed to adsorb on the TiO_2 surface along with the dye molecules, as well as separating them from each other. It is also possible that coadsorbents break dye aggregates already in the solution. This role may be as well attributed to the presence of hexyl chain on the thiophene of **WS-9** dye. This concept proved to work – the difference in the V_{OC} is well pronounced in comparison to **WS-2**. At the same charge density, the electron lifetime of **WS-9** is approximately an order of magnitude longer than that of **WS-2** (Figure 5.10, left). As expected, the hexyl chain helps in shielding the non-sensitized TiO_2 surface and retarding the electron loss channel. The addition of CDCA results in an order of magnitude increase of the electron lifetime in case of

Chapter 5. Molecular engineering on D-A- π -A dyes featuring indoline donor and benzothiadiazole bridge.

the **WS-2** dye, while for the **WS-9** dye it remained almost unchanged. This could happen due to the coadsorbed CDCA occupying the free spaces on TiO_2 surface in **WS-2** sensitized device, thus retarding the recombination processes.

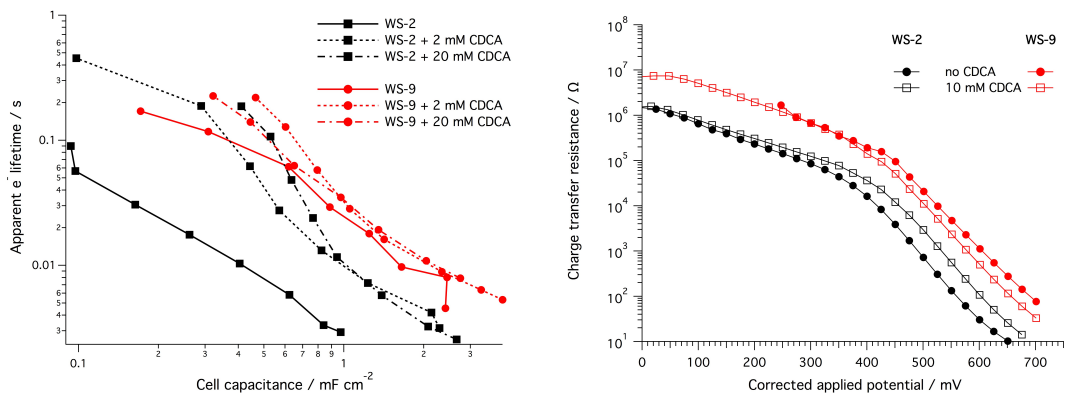


Figure 5.10: *Left:* Apparent electron lifetime as a function of the cell capacitance, which corresponds to the density of states in TiO_2 . The devices within each dye series contained increasing amount of CDCA in the CH_2Cl_2 dye solution used for staining the photoanodes. Lines are only guides for eyes. *Right:* The effect of the coadsorbent (CDCA) on the charge transfer resistance of DSC devices with the dyes **WS-2** and **WS-9**.

Electrochemical impedance spectroscopy (EIS) measurements give a direct access to the charge transfer resistance of the TiO_2 -dye-electrolyte interface²¹. A set of devices with and without CDCA was investigated using **WS-2** and **WS-9** dyes. The lowest charge transfer resistance was found for the **WS-2** dye alone cell (Figure 5.10, right), which confirms that injected electrons are more likely to undergo recombination with the oxidized form of the redox species present in the electrolyte. The addition of 10 mM CDCA to the dye solution is helpful to increase the interfacial resistance, mainly due to the blocking of recombination sites, correlating to the higher V_{OC} . **WS-9** sensitized cells exhibit an order of magnitude higher charge transfer resistance at the same potentials, regardless of the presence of the coadsorbent.

5.3.3 Stability of the dyes and the devices

For the practical application of DSCs, the long lifetime of the devices is an important prerequisite, besides the high η . Among many factors controlling the lifetime of DSCs, the stability of sensitizers is an especially critical factor. Katoh and coworkers²² have developed a simple and efficient method to evaluate the stability of sensitizers. Since the most unstable state of

5.3. Optimization of the photovoltaic performance

the sensitizers is their oxidized state, the corresponding sensitizers must remain stable in the cation state for at least 10 s to be capable of realizing a 10-year operation cycle²². Actually, we can accelerate the dye aging process upon light irradiation on dye-loaded TiO₂ film without redox electrolyte, because the dye regeneration process under this condition occurs in the millisecond time range, thus taking 10⁴ to 10³ times longer than that in a complete solar cell device (100 ns – 1 ms). Figure 5.11 shows the absorption curves of dyes **WS-2**, **WS-9** and **LS-1** with aging upon light irradiation of AM 1.5 light (5 or 30 min). Obviously, the photostability of benzothiadiazole-containing **WS-2** and **WS-9** is much higher than that of the reference dye **LS-1**. Moreover, the photostability of **WS-2** seems a little higher than that of **WS-9** (Figure 5.11), suggesting that the existence of the hexyl chain on the thiophene group in **WS-9** may decrease its intrinsic photostability^{23,24}. However, according to Katoh's experience, the benzothiadiazole-incorporating dyes **WS-2** and **WS-9** are stable enough, without any distinct absorption peak shift, for DSCs application, because the variation in absorption curves before and after irradiation is smaller than that of the MK-2²².

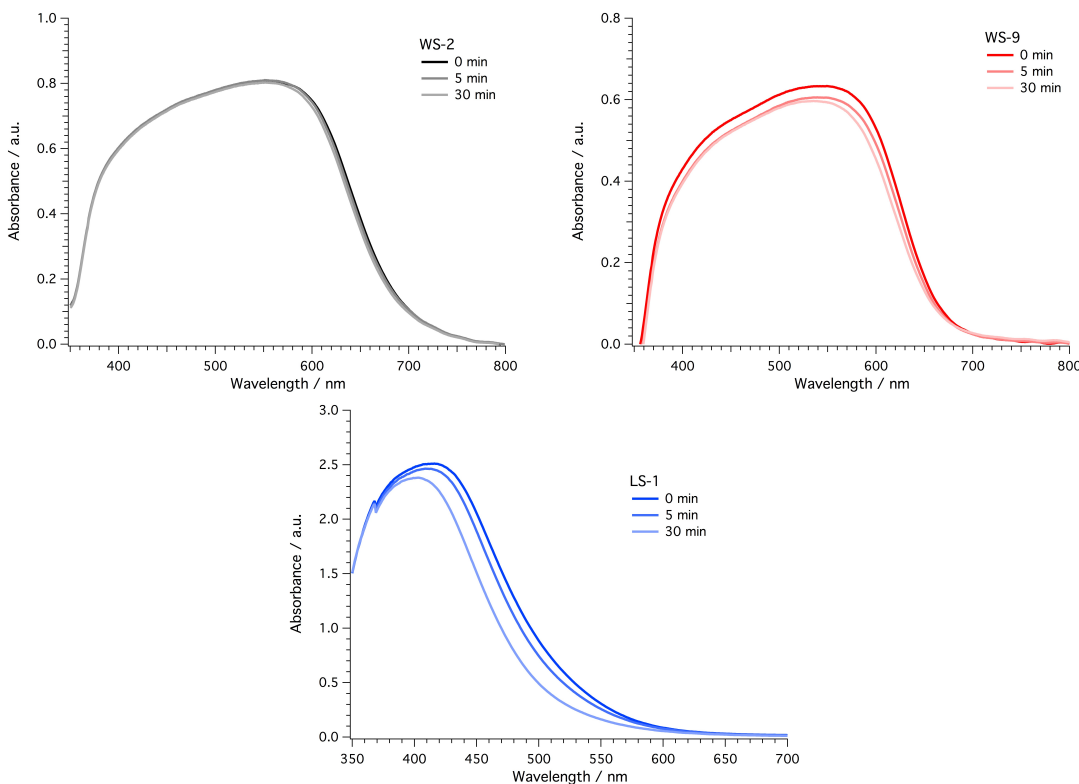


Figure 5.11: Absorption spectra of **LS-1**, **WS-2** and **WS-9** adsorbed on nanocrystalline TiO₂ films before(0 min) and after light irradiation for 5 and 30 minutes.

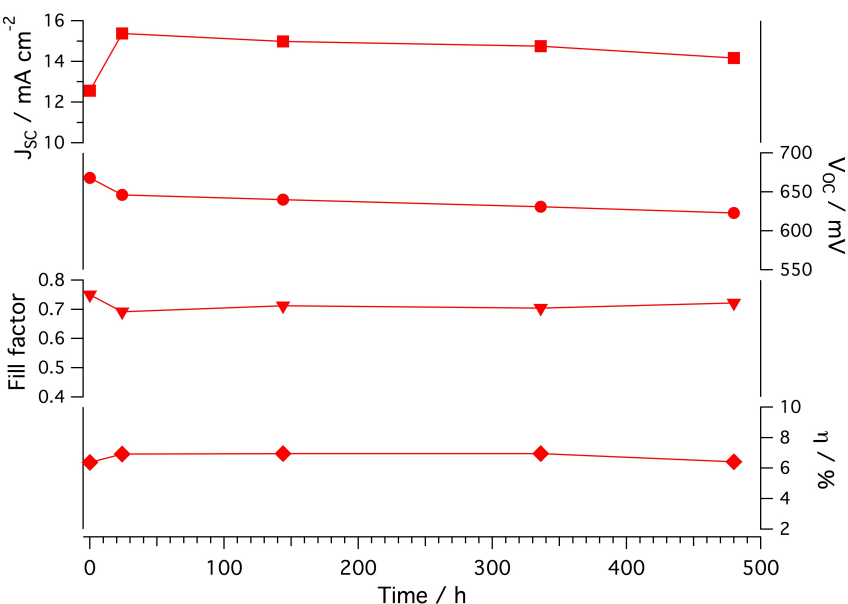


Figure 5.12: Variations of the photovoltaic parameters (J_{SC} , V_{OC} , fill factor and η) with ageing time for the DSC based on **WS-9** and ionic liquid electrolyte Z952 under AM 1.5 light soaking.

On the other hand, the composition of redox electrolytes as well as the encapsulation of the devices also influence the device stability. For the long term test of device's stability, we chose a more stable ionic liquid electrolyte Z952 to fabricate solar cells. Figure 5.12 shows the photovoltaic performance during a long term accelerated aging of a **WS-9** sensitized solar cell under AM 1.5 irradiation. As shown in the Figure 5.12, the J_{SC} , V_{OC} , FF and η values were recorded, indicating that the **WS-9** based DSC is stable under AM 1.5 light for at least 500 h. These preliminary stability tests indicate that the overall device efficiency increased from 6.38% to 6.95% in ionic liquid electrolyte, then slowly dropped, but was still higher than at the starting point after 500 h of light soaking.

5.4 Conclusions

In summary, we have successfully designed and synthesized a new D-A- π -A organic dye **WS-9**, solving the aggregation problem of the dye **WS-2** through incorporation of a hexylthiophene unit on the π -bridge. The absorption, energy levels and frontier orbitals of **WS-9** and **WS-2** were studied in detail. We found that D-A- π -A organic dyes show more complicated electronic absorption behavior in comparison to the common D- π -A dyes, resulting in a broader

absorption range. The high performance of **WS-2** sensitized DSCs relies on the appropriate choice of dye bath solvent as well as the addition of coadsorbents to diminish its tendency to form aggregates. In contrast, **WS-9** exhibits inherent anti-aggregation ability resulting in high performance independent of the use of coadsorbent and the choice of dye bath solvent. Transient photovoltage and photocurrent decay experiments and electrochemical impedance spectroscopy showed that the injected electron lifetime and charge recombination resistance were increased for **WS-9** devices. These results can be attributed to the introduction of a hexylthiophene unit in the π -bridge of **WS-2**, resulting in a higher V_{OC} and a promising high power conversion efficiency of 9.04% for the **WS-9** dye. The dye photostability in accelerated conditions was tested upon light irradiation of a dye-adsorbed TiO₂ film in the absence of redox electrolyte, and a **WS-9**-based DSC device with ionic liquid redox electrolyte. These findings pave a new way in the design of novel efficient D–A– π -A organic dye sensitizers.

5.5 Bibliography

- [1] S. Kim, J. K. Lee, S. O. Kang, J. Ko, J.-H. Yum, S. Fantacci, F. D. Angelis, D. D. Censo, M. K. Nazeerud-din and M. Grätzel, *Journal of the American Chemical Society*, 2006, **128**, 16701–16707.
- [2] A. Hagfeldt, G. Boschloo, L. Sun, L. Kloo and H. Pettersson, *Chemical Reviews*, 2010, **110**, 6595.
- [3] A. Listorti, B. O'Regan and J. R. Durrant, *Chemistry of Materials*, 2011, **23**, 3381–3399.
- [4] Z.-M. Tang, T. Lei, K.-J. Jiang, Y.-L. Song and J. Pei, *Chemistry – An Asian Journal*, 2010, **5**, 1911–1917.
- [5] T. Marinado, K. Nonomura, J. Nissfolk, M. K. Karlsson, D. P. Hagberg, L. Sun, S. Mori and A. Hagfeldt, *Langmuir*, 2010, **26**, 2592–2598.
- [6] K. Hara, Z.-S. Wang, T. Sato, A. Furube, R. Katoh, H. Sugihara, Y. Dan-oh, C. Kasada, A. Shinpo and S. Suga, *The Journal of Physical Chemistry B*, 2005, **109**, 15476–15482.
- [7] W. Zhu, Y. Wu, S. Wang, W. Li, X. Li, J. Chen, Z. sheng Wang and H. Tian, *Advanced Functional Materials*, 2011, **21**, 756–763.
- [8] J.-Y. Li, C.-Y. Chen, C.-P. Lee, S.-C. Chen, T.-H. Lin, H.-H. Tsai, K.-C. Ho and C.-G. Wu, *Organic Letters*, 2010, **12**, 5454–5457.

-
- [9] C. Risko, M. D. McGehee and J.-L. Brédas, *Chemical Science*, 2011, **2**, 1200–1218.
- [10] Z.-S. Wang, Y. Cui, K. Hara, Y. Dan-oh, C. Kasada and A. Shinpo, *Advanced Materials*, 2007, **19**, 1138–1141.
- [11] Y. Cui, Y. Wu, X. Lu, X. Zhang, G. Zhou, F. B. Miapeh, W. Zhu and Z.-S. Wang, *Chemistry of Materials*, 2011, **23**, 4394–4401.
- [12] J. E. Kroese, N. Hirata, S. Koops, M. K. Nazeeruddin, L. Schmidt-Mende, M. Grätzel and J. R. Durrant, *Journal of the American Chemical Society*, 2006, **128**, 16376–16383.
- [13] Z.-S. Wang, N. Koumura, Y. Cui, M. Takahashi, H. Sekiguchi, A. Mori, T. Kubo, A. Furube and K. Hara, *Chemistry of Materials*, 2008, **20**, 3993–4003.
- [14] Y. Wu, X. Zhang, W. Li, Z.-S. Wang, H. Tian and W. Zhu, *Advanced Energy Materials*, 2012, **2**, 149–156.
- [15] S. Qu, W. Wu, J. Hua, C. Kong, Y. Long and H. Tian, *The Journal of Physical Chemistry C*, 2010, **14**, 1343–1349.
- [16] B. Liu, W. Zhu, Q. Zhang, W. Wu, M. Xu, Z. Ning, Y. Xie and H. Tian, *Chemical Communications*, 2009, 1766–1768.
- [17] M. J. Frisch, G. W. Trucks, H. B. Schlegel, G. E. Scuseria, M. A. Robb, J. R. Cheeseman, G. Scalmani, V. Barone, B. Mennucci, G. A. Petersson, H. Nakatsuji, M. Caricato, X. Li, H. P. Hratchian, A. F. Izmaylov, J. Bloino, G. Zheng, J. L. Sonnenberg, M. Hada, M. Ehara, K. Toyota, R. Fukuda, J. Hasegawa, M. Ishida, T. Nakajima, Y. Honda, O. Kitao, H. Nakai, T. Vreven, J. J. A. Montgomery, J. E. Peralta, F. Ogliaro, M. Bearpark, J. J. Heyd, E. Brothers, K. N. Kudin, V. N. Staroverov, R. Kobayashi, J. Normand, K. Raghavachari, A. Rendell, J. C. Burant, S. S. Iyengar, J. Tomasi, M. Cossi, N. Rega, J. M. Millam, M. Klene, J. E. Knox, J. B. Cross, V. Bakken, C. Adamo, J. Jaramillo, R. Gomperts, R. E. Stratmann, O. Yazyev, A. J. Austin, R. Cammi, C. Pomelli, J. W. Ochterski, R. L. Martin, K. Morokuma, V. G. Zakrzewski, G. A. Voth, P. Salvador, J. J. Dannenberg, S. Dapprich, A. D. Daniels, O. Farkas, J. B. Foresman, J. V. Ortiz, J. Cioslowski and D. J. Fox, *Gaussian 09, Revision A.02*, Gaussian, Inc., Wallingford CT, 2009.
- [18] W. Zeng, Y. Cao, Y. Bai, Y. Wang, Y. Shi, M. Zhang, F. Wang, C. Pan and P. Wang, *Chemistry of Materials*, 2010, **22**, 1915–1925.
- [19] T. Dentani, Y. Kubota, K. Funabiki, J. Jin, T. Yoshida, H. Minoura, H. Miura and M. Matsui, *New Journal of Chemistry*, 2009, **33**, 93–101.

-
- [20] H. Tian, X. Yang, R. Chen, R. Zhang, A. Hagfeldt and L. Sun, *The Journal of Physical Chemistry C*, 2008, **112**, 11023–11033.
 - [21] J. Bisquert, *Journal of Electroanalytical Chemistry*, 2010, **646**, 43–51.
 - [22] R. Katoh, A. Furube, S. Mori, M. Miyashita, K. Sunahara, N. Koumura and K. Hara, *Energy and Environmental Science*, 2009, **2**, 542–546.
 - [23] M. Jørgensen, K. Norrman, S. A. Gevorgyan, T. Tromholt, B. Andreasen and F. C. Krebs, *Advanced Materials*, 2012, **24**, 580–612.
 - [24] M. Manceau, S. Chambona, A. Rivatona, J.-L. Gardette, S. Guillerez and N. Lemaître, *Solar Energy Materials and Solar Cells*, 2010, **94**, 1572–1577.

6 Donor- π -Acceptors containing a 10-(1,3-dithiol-2-ylidene)anthracene unit for dye-sensitized solar cells.

This part is adapted from a peer reviewed publication by Pierre-Antoine Bouit, Magdalena Marszalek, Robin Humphry-Baker, Rafael Viruela, Enrique Ortí, Shaik M. Zakeeruddin, Michael Grätzel, Juan Luis Delgado and Nazario Martín published in 2012 in Chemistry A European Journal, Vol. 18, pp 11621–11629

6.1 Introduction

Within the field of organic sensitizers, a large variety of organic dyes including coumarins¹, indolines², tetrahydroquinolines³, hemicyanines⁴, boron-dipyrromethenes⁵, oligothiophenes⁶, and triarylaminies⁷, anthracenes and heteroanthracenes⁸ have been reported. Recently, the use of π -extended tetrathiafulvalene (exTTF, 2-[9-(1,3-dithiol-2-ylidene)anthracen-10(9H)-ylidene]-1,3-dithiol)^{9–13} as a donor unit in a sensitizer (**1**, Figure 6.1) have been introduced for the preparation of DSCs that show an efficient photovoltaic conversion as well as unusual electrochemical and kinetic properties¹⁴. The donor ability of the exTTF unit increases the HOMO level of the organic dye and significantly reduces the required energy for the regeneration of the dye by the electrolyte to 150 mV. Stimulated by these results, we decided to explore the closely related 10-(1,3-dithiol-2-ylidene) anthracene group as an appealing electron-donor

Chapter 6. Donor- π -Acceptors containing a 10-(1,3-dithiol-2-ylidene)anthracene unit for dye-sensitized solar cells.

unit for the preparation of efficient DSCs.

Figure 6.1 shows the structure of a push-pull chromophore (**2**) incorporating the 10-(1,3-dithiol-2-ylidene) anthracene electron-donor unit¹⁵. Interestingly, molecule **2** is highly distorted from planarity due to the strong S···H steric repulsions, which is crucial to prevent dye aggregation. Additionally, compound **2** shows strong UV-vis absorption owing to the efficient intramolecular charge transfer (ICT) transition that takes place from the donor to the acceptor unit upon excitation. Molecular engineering using the 10-(1,3-dithiol-2-ylidene)anthracene core allows the design of dyes featuring two anchoring groups, which was previously shown to enhance the performance and the stability of the photovoltaic (PV) devices^{16,17}.

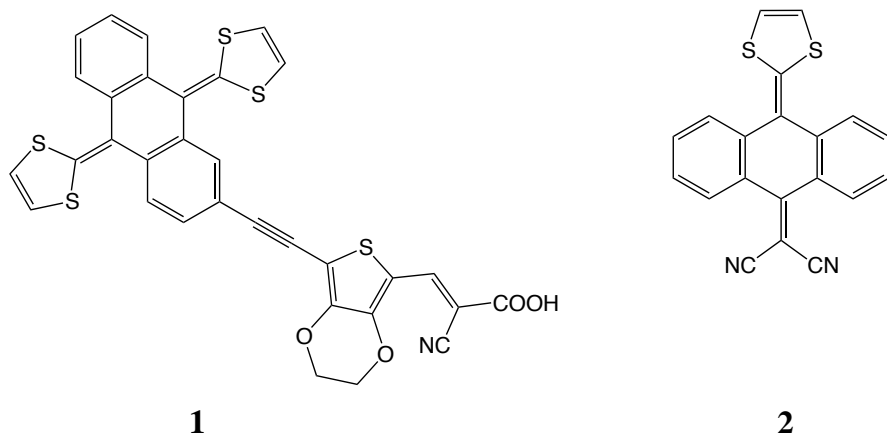


Figure 6.1: A previously reported exTTF-based sensitizer for DSCs (**1**) and a push-pull chromophore based on the 10-(1,3-dithiol-2-ylidene)anthracene core (**2**).

Considering all these precedents, we designed two new push-pull sensitizers (**6** and **7**) based on the 10-(1,3-dithiol-2-ylidene)anthracene core as electron-donor group with two cyanoacrylic acid units as acceptor/anchor groups. To modulate the absorption properties, each sensitizer contained a different π -bridge between the donor group and the anchoring units: two benzene rings in compound **6** and two 3,4-ethylenedioxythiophene (EDOT) units for **7**. EDOT spacers have been successfully employed for red-shifting the spectral response and enhancing the molar extinction coefficient of triphenylamine and exTTF-based sensitizers^{7,14,18}. Theoretical calculations have been carried out at the density functional theory (DFT) level to gather information about the geometrical and electronic properties of the new sensitizers. Their photovoltaic potential in DSCs has been investigated by J-V measurements. The

differences between the performances of these two molecules were scrutinized by transient-photovoltage technique. This technique supported the existence of enhanced recombination processes within devices that were functionalized by the compound **7**.

6.2 Synthesis and characterization of the dyes

6.2.1 Synthetic route

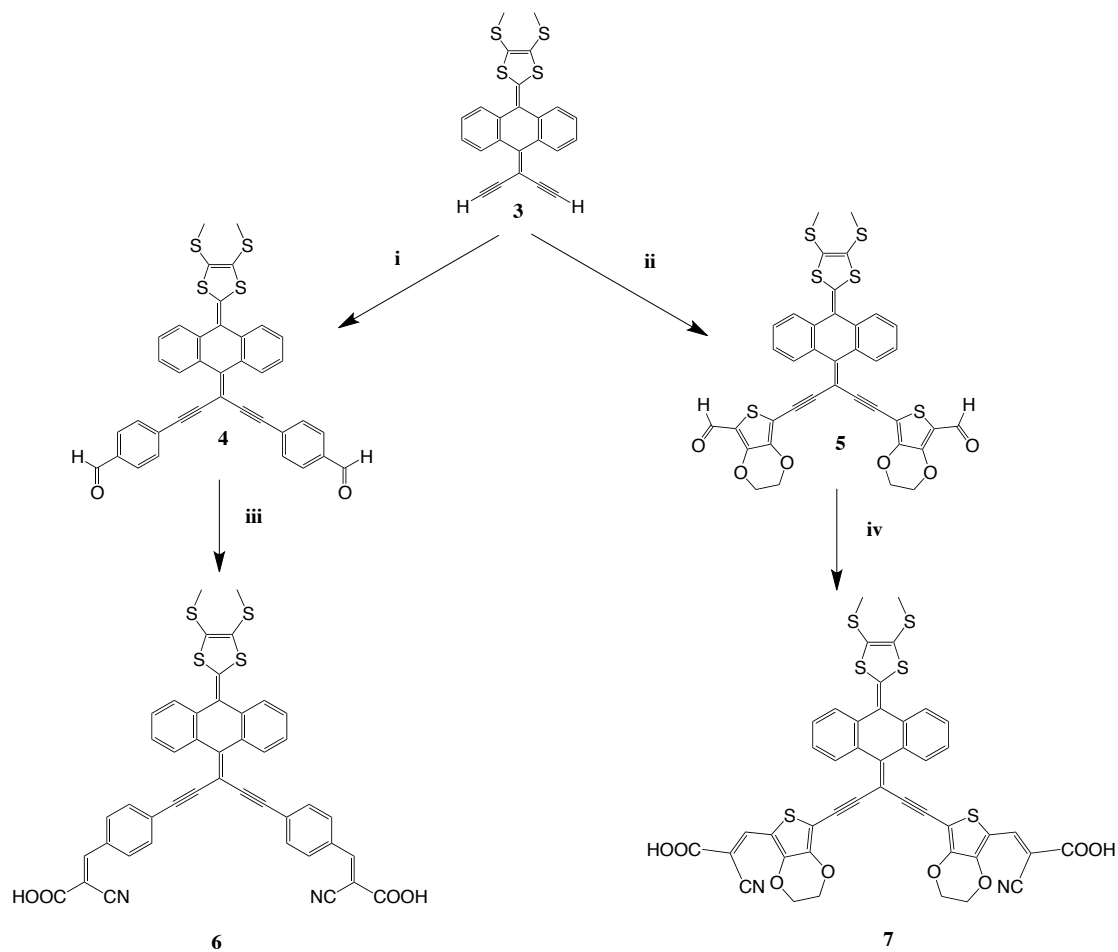


Figure 6.2: Synthesis of the new sensitizers **6** and **7**. Reagents and conditions: (i, ii) $\text{PdCl}_2(\text{PPh}_3)_2$, CuI , $\text{THF}/\text{Et}_3\text{N}$ (4:1), reflux overnight. (iii, iv) cyanoacetic acid, $\text{NH}_4(\text{CH}_3\text{COO})$, CH_3COOH , reflux overnight.

The synthesis of the two new sensitizers was accomplished according to a multistep synthetic procedure (described in the Supporting Information of the corresponding publication). The intermediate **3**, which featured two terminal alkyne groups (Figure 6.2), was synthesized in

Chapter 6. Donor- π -Acceptors containing a 10-(1,3-dithiol-2-ylidene)anthracene unit for dye-sensitized solar cells.

four steps in good yield according to modified previously published procedures¹⁹.

The conjugated bridges were introduced by means of the Sonogashira cross-coupling reaction using $[\text{PdCl}_2(\text{PPh}_3)_2]$ and CuI as catalysts. Thus, reaction of **3**, with either 4-iodobenzaldehyde or with 7-bromo-3,4-ethylenedioxythiophene-5-carbaldehyde²⁰, afforded compounds **4** and **5**, respectively, in moderate yields (both ~50%). The introduction of the acceptor/anchor units was achieved by two-fold Knoevenagel condensation of aldehydes **4** and **5** with cyanoacetic acid, to afford the new sensitizers **6** and **7** in moderate yields (40 and 64%, respectively). The structures of all the new compounds and the new sensitizers were confirmed by ¹H and ¹³C NMR spectroscopy. Furthermore, their chemical structures were ascertained by high-resolution mass spectrometry measurements [**6**: $[\text{M}]^+ = 774.051$ (Calculated for $\text{C}_{44}\text{H}_{26}\text{N}_2\text{O}_2\text{S}_4$: 774.077) and **7**: $[\text{M}]^+ = 901.964$ (Calculated for $\text{C}_{44}\text{H}_{26}\text{N}_2\text{O}_8\text{S}_6$: 902.001)].

6.2.2 Optical and electrochemical properties

The optical properties of sensitizers **6** and **7** were studied by means of UV-vis spectroscopy. The absorption spectra of both compounds display two absorption bands (Figure 6.3). The first band with maximum at 354 nm for **6** and 440 nm for **7** is in the region of the $\pi - \pi^*$ transitions of the anthracene core¹⁵. The weaker, broad band in the visible region, with absorption maximum at 495 nm for **6** and 540 nm for **7**, is assigned to an internal charge transfer (ICT) transition from the donor to the acceptor moieties¹⁵. As expected, extending the conjugation with EDOT in compound **7** allowed for a red-shift of the absorption spectrum up to 700 nm. Compared to the previously reported exTTF sensitizers, which mainly absorb in the 400–500 nm region¹⁴, this extension represents a significant improvement in the optical properties of the sensitizer. The HOMO-LUMO gap was determined from the combination of the UV-Vis absorption and emission measurements (Figure 6.4). The gap, in fact corresponding to the E_{0-0} transition, was taken as the interception of the UV-Vis and fluorescence spectra.

Electrochemical characterization of the new dyes was performed by cyclic voltammetry and differential pulse voltammetry in dimethylformamide (DMF) solution using tetrabutylammonium hexafluorophosphate (TBAPF_6) as a supporting electrolyte and a typical three-electrode setup in controlled Ar atmosphere. Both molecules show reversible redox behaviour. Accord-

6.2. Synthesis and characterization of the dyes

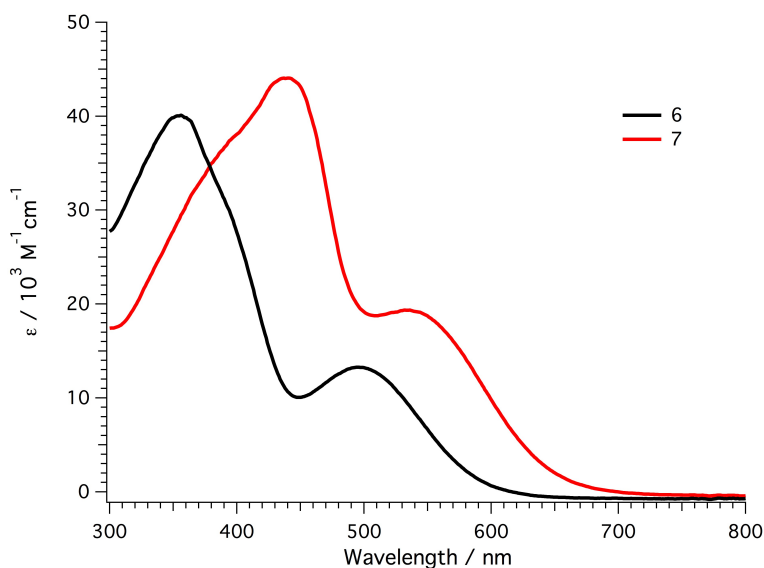


Figure 6.3: UV-vis absorption spectra of **6** (black) and **7** (red) in diluted dimethyl sulfoxide (DMSO) solution (2×10^{-5} M).

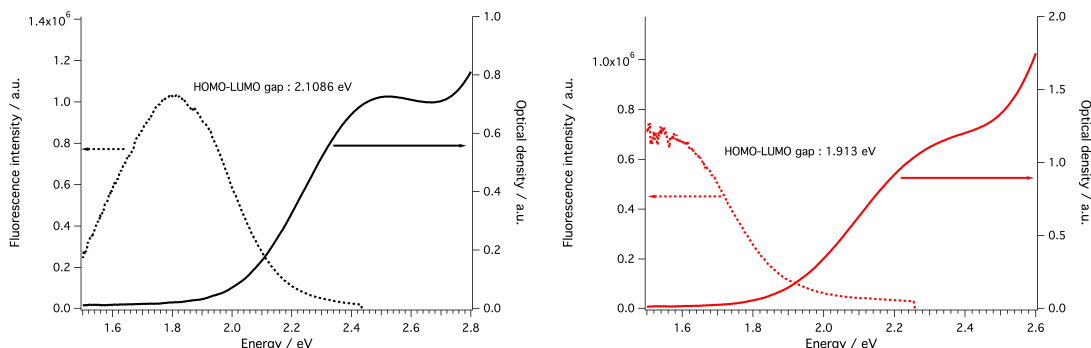


Figure 6.4: Determination of the HOMO-LUMO gap from the UV-Vis absorption and fluorescence spectra for the dye **6** (left) and the dye **7** (right) adsorbed on a transparent $5.5 \mu\text{m}$ TiO_2 film.

ing to the optical measurements, a decrease of the gap is observed when the phenyl spacer in **6** is replaced by the EDOT in **7** (Table 6.1). The oxidation potential for both compounds (Table 6.1), related to the highest occupied molecular orbital (HOMO), is around 0.25 V vs. ferrocenium/ferrocene (Fc^+/Fc) couple and is sufficiently more positive than the redox potential of the I^-/I_3^- electrolyte (-0.21 V vs Fc^+/Fc in ionic liquid)²¹ for efficient dye regeneration. The reduction potential of the dyes, related to the lowest unoccupied molecular orbital (LUMO), is considerably more negative than the TiO_2 conduction band, providing enough driving force for electron injection.

Chapter 6. Donor- π -Acceptors containing a 10-(1,3-dithiol-2-ylidene)anthracene unit for dye-sensitized solar cells.

Table 6.1: Oxidation and reduction potentials and experimental/theoretical HOMO-LUMO energy gaps (E_g) for dyes **6** and **7**.

| Dye | E_{ox} V ^a | E_{red} V ^a | E_g^{elect} eV ^b | E_g^{opt} eV ^c | E_g^{DFT} eV ^d |
|----------|----------------------------|-----------------------------|----------------------------------|--------------------------------|--------------------------------|
| 6 | 0.25 | -1.76 | 2.01 | 2.10 | 2.25 |
| 7 | 0.23 | -1.69 | 1.92 | 1.95 | 2.11 |

^a Values determined by differential pulse voltammetry in DMF versus Fc^+/Fc . ^b Estimated as $E_{ox}-E_{red}$. ^c Taken as the intersection of the absorption and emission spectra. ^d Obtained from DFT calculations (B3LYP/6-31G**) in DME.

6.3 Theoretical calculations

6.3.1 Geometry of the molecules

The molecular geometries of the two dyes were fully relaxed, both as isolated systems and in the presence of the solvent, by using DFT calculations performed at the B3LYP/6-31G** level. Figure 6.5 displays three minimum-energy conformations computed for the dye **6** at the B3LYP/6-31G** level. The conformations differ in the relative orientation of the cyanoacrylic acid groups. Calculations predict that these conformations are very close in energy and all of them should coexist in solution. Conformations C1 and C2 are almost isoenergetic, both in the gas phase and in the solution. Conformation C3 is slightly higher in energy (3.50 kcal mol⁻¹ in the gas phase and 1.76 kcal mol⁻¹ in DMSO) due to relative orientation of the C=O group that prefers to be in an *s-trans* disposition with respect to the C≡N group. The relative orientation of the carboxylic groups could, in principle, have an influence on the anchoring mode (unidentate or bidentate) of the dye on the semiconductor oxide surface, and, depending on the conformation, the anchoring of one group could even impede the anchoring of the other group. For instance, if one COOH group of a molecule with conformation C1 is anchored on the TiO₂ surface, the anchoring of the second COOH group would not be possible. In contrast, conformations C2 and C3 favour the unidentate anchoring of both COOH groups and they become equivalent upon deprotonation on the semiconductor surface. Conformation C2 has therefore been adopted for the calculations.

A mixing of conformations is also expected for the molecule **7**, for which the three most stable conformations are depicted in the Figure 6.6 (other conformations with higher energies were

6.3. Theoretical calculations

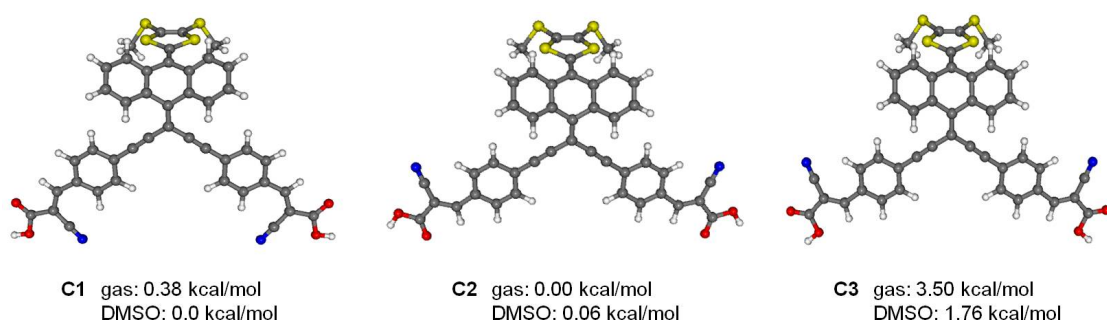


Figure 6.5: Minimum-energy optimized conformations (C1 to C3) calculated for the dye 6. Relative B3LYP/6-3G** energies calculated in gas phase and in DMSO are given.

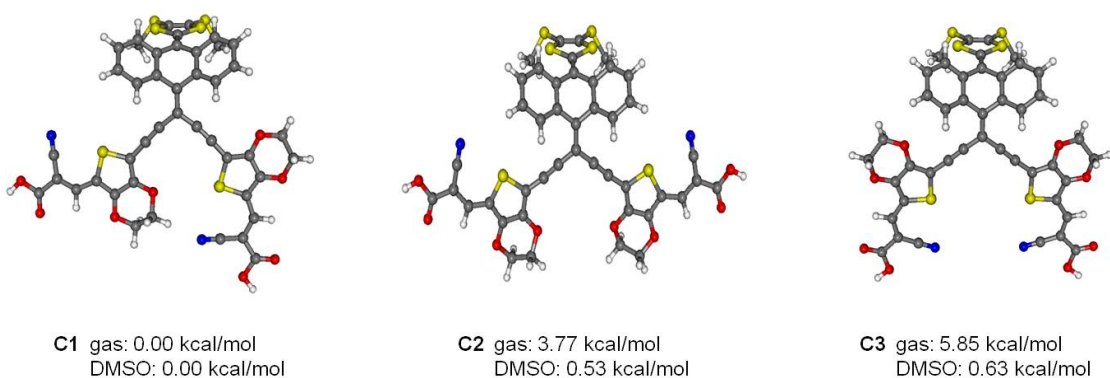


Figure 6.6: Minimum-energy optimized conformations (C1 to C3) calculated for the dye 7. Relative B3LYP/6-3G** energies calculated in gas phase and in DMSO are given.

also calculated). The presence of EDOT groups leads to the appearance of less symmetric structures, like C1, that results to be more stable than the symmetric structures C2 and C3. The energy differences between conformations C1-C3 are significant when calculated for the isolated system, but they almost disappear when solvent effects (DMSO) are included in the calculation. In this case, conformation C2 would favour the bidentate anchoring of only one COOH group, whereas the unidentate anchoring of both COOH groups is favoured for conformation C3 and this conformation has been adopted in the calculations. The molecular conformation can indeed evolve after the anchoring of one COOH group on the TiO₂ surface, since the interconversion between the different possible structures implies internal rotations around single bonds with low energy barriers.

Among the various possible conformations discussed shortly above, due to the internal rotation and relative orientation of the cyanoacrylic acid groups (Figures 6.5 and 6.6), the Figure

Chapter 6. Donor- π -Acceptors containing a 10-(1,3-dithiol-2-ylidene)anthracene unit for dye-sensitized solar cells.

6.7 displays the minimum-energy structures calculated for dyes **6** and **7** that favoured the unidentate anchoring of both carboxylate groups. As shown in the Figure 6.7,b , for the dye **6**, the molecule adopts the typical butterfly- or saddle-like shape observed for exTTFs^{15,22–28}. To relieve the short-range interactions of the *peri* hydrogen atoms of the anthracene core with the sulfur atoms of the dithiol ring and the carbon atoms of the acetylene units, the central ring of the anthracene core with both of the sulfur atoms of the dithiol ring and the carbon atoms of the acetylene units, the central ring of the anthracene unit folds in a boat conformation along the C9–C10 vector by an average angle of 36.9° for both dyes **6** and **7** in the gas phase. This value is very similar to that determined by X-ray crystallography for tetramethylthio-exTTF (38°)¹⁵, for which an almost identical value (38.3°) was calculated at the B3LYP/6-31G** level^{26–28}. The dithiol ring and the diacetylene unit are tilted down by 33.3 and 31.9°, respectively, with respect to the plane defined by the anthracene atoms C11-C12-C13-C14. Almost identical tilting angles are computed for compound **7** (34.0 and 31.2°, respectively). The molecular structures of dyes **6** and **7** are therefore highly distorted from planarity, which helps to prevent molecular aggregation.

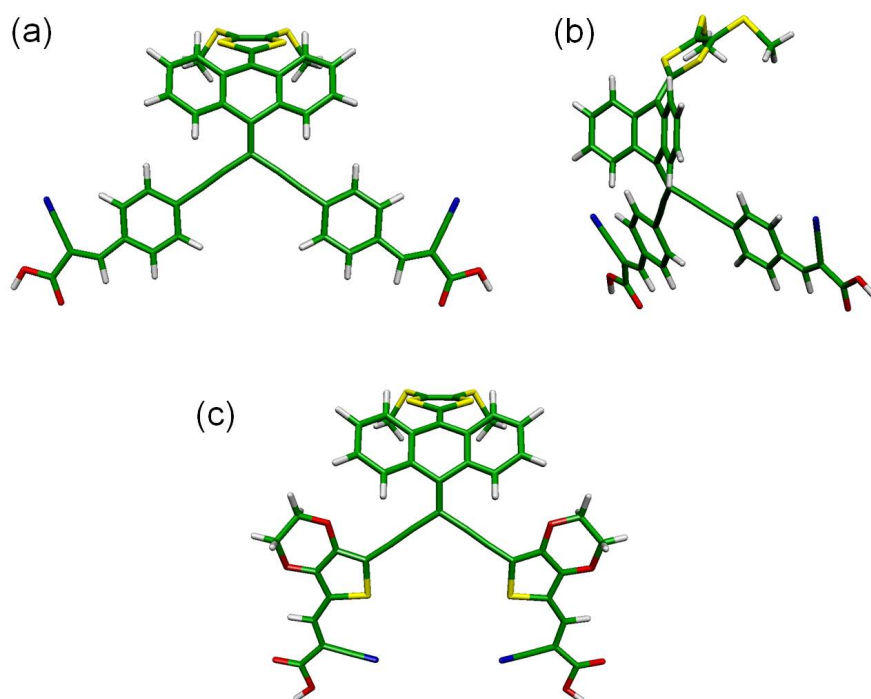


Figure 6.7: Optimized B3LYP/6-31G** structures calculated for the dye **6**, front view (a) and side view showing the distortion from planarity (b), and the dye **7** (c).

6.3.2 The character of the molecular orbitals

The Figure 6.8 shows the atomic orbital (AO) composition of the highest-occupied (HOMO–2 to HOMO) and lowest unoccupied (LUMO and LUMO+1) molecular orbitals calculated for the dye **6** in DMF. Identical MO topologies are obtained for the isolated dyes in the gas phase. The HOMO (-5.14 eV) is mainly localized on the electron-donor dithiol unit and is calculated at lower energy than the HOMO of the tetramethylthio-exTTF molecule (-4.90 eV) that contains two dithiol units²⁹. The HOMO–1 (-5.75 eV) spreads over the dithiol and the diacetylene units and is separated by 0.64 eV from the HOMO–2 (-6.39 eV), which is fully localized over the acceptor part of the molecule. The LUMO (-2.89 eV) and LUMO+1 (-2.63 eV) are close in energy and correspond to the symmetric and antisymmetric combination of the LUMOs of the two molecular arms that constitute the acceptor moiety, respectively. An equivalent MO distribution is obtained for the molecule **7**. Therefore, dyes **6** and **7** present small HOMO-LUMO energy gaps of 2.25 and 2.11 eV, respectively, and low-energy charge-transfer (CT) absorption bands are to be expected - which is in agreement with that observed in the electronic spectra (Figure 6.3).

The nature of the HOMO and LUMO indicates that oxidation should mainly affect the dithiol moiety, whereas reduction concerns the acetylene/benzene/cyanoacrylic acid units (see Figure 6.8). DFT calculations support the observed experimental trends found for the redox potentials (Table 6.1). In passing from the dye **6** to the dye **7**, the HOMO increases in energy slightly from -5.14 to -5.10 eV, which is in good agreement with the small cathodic shift of 0.02 V recorded experimentally for the first oxidation potential. In contrast, the LUMO decreases in energy from -2.89 eV (**6**) to -2.99 eV (**7**), which justifies the less negative reduction potential measured for the dye **7** (-1.69 V) compared with the dye **6** (-1.76 V). The shift of the HOMO to higher energy and of the LUMO to lower energy leads to a narrowing of the HOMO-LUMO gap in passing from the dye **6** (2.25 eV) to the dye **7** (2.11 eV), which is in good accordance with the electrochemical (**6**: 2.01 eV, **7**: 1.92 eV) and spectroscopical (**6**: 2.10 eV, **7**: 1.95 eV) estimates.

To investigate the nature of the electronic transitions that give rise to the absorption bands observed in the electronic spectra, the lowest-energy singlet excited states (S_n) of dyes **6** and **7** were calculated by using the time-dependent DFT (TDDFT) approach and the B3LYP/6-31G**-

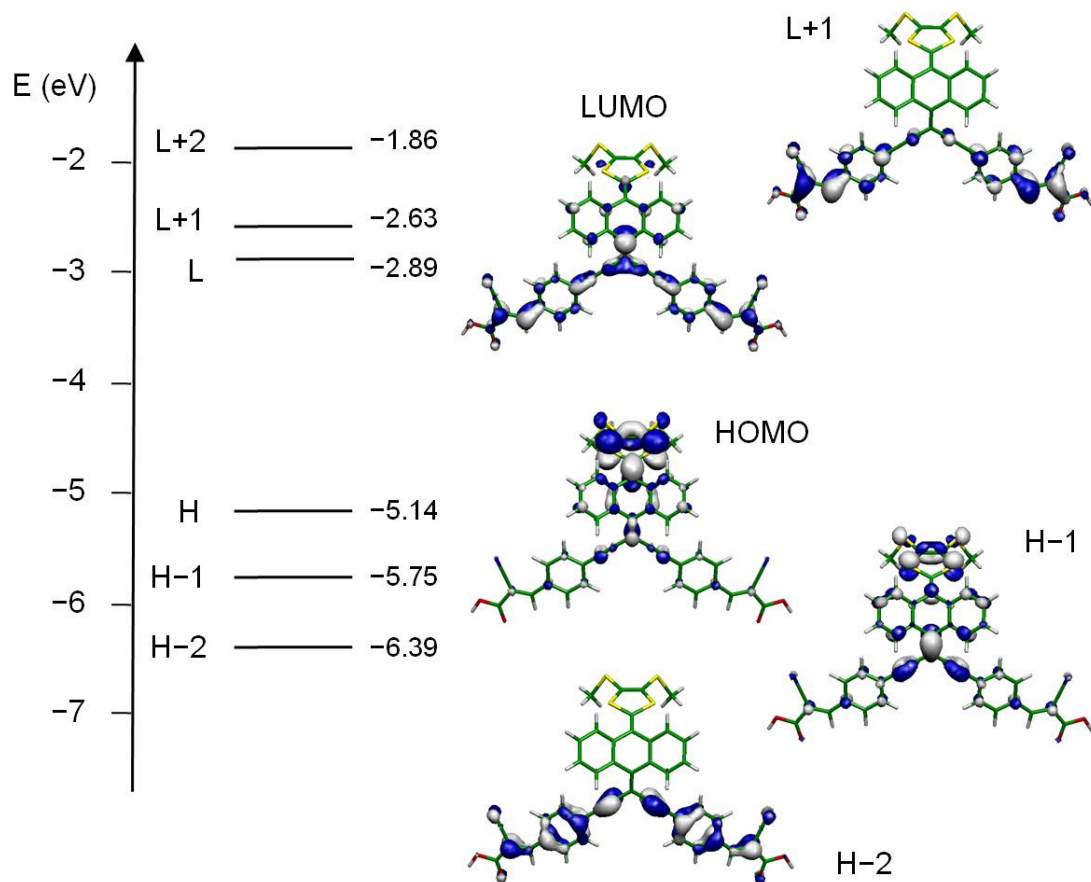


Figure 6.8: Electron density contours ($0.025 \text{ e bohr}^{-3}$) and orbital energies calculated for the HOMOs and LUMOs of the dye **6** at the B3LYP/6-31G** level in DMF solution. H and L denote HOMO and LUMO, respectively.

optimized ground-state geometries. All parameters obtained for the lowest-energy singlet states of the molecule **6** using the B3LYP and PBE0 functionals together with the 6-31G** basis set and the geometry optimized for conformation C2 in the ground electronic state are presented in the Table 6.2. Both functionals led to an identical description of the lowest-energy singlets, yet the PBE0 functional yields slightly higher excitation energies. TDDFT calculations at the B3LYP/6-31G** level were also performed in the presence of the solvent (DMSO). The description of the excited states in terms of molecular orbitals remains the same in DMSO, the only significant change being the reduction of the excitation energies by about 0.1 eV.

TDDFT calculations predict that the low-energy absorption band that is observed experimentally at 495 nm (2.50 eV) for the dye **6** and 540 nm (2.30 eV) for the dye **7** (Figure 6.3) mainly results from the electronic transition to the first excited singlet state, S_1 , at 2.12 eV.

6.3. Theoretical calculations

Table 6.2: Lowest singlet excited states calculated at the TDDFT level for the dye **6**. Vertical excitation energies (E), oscillator strengths (*f*), dominant monoexcitations with contributions (within parentheses) greater than 10%, and description of the excited states are given.

| State | E eV | <i>f</i> | Monoexcitations | Description |
|----------------------|---------|----------|-----------------|----------------------------------|
| B3LYP/6-31G** | | | | |
| S₁ | 1.94 | 0.34 | H→L (98%) | Donor→Acceptor CT |
| S₂ | 2.20 | 0.26 | H→L+1 (100%) | Donor→Acceptor CT |
| S₃ | 2.61 | 0.40 | H-1→L (97%) | Donor→Acceptor CT |
| S₄ | 2.80 | 0.37 | H-1→L+1 (99%) | Donor→Acceptor CT |
| S₅ | 2.89 | 0.10 | H→L+2 (94%) | Donor→Acceptor CT |
| S₆ | 3.13 | 0.96 | H-2→L (96%) | $\pi \rightarrow \pi^*$ Acceptor |
| PBE0/6-31G** | | | | |
| S₁ | 2.04 | 0.41 | H→L (89%) | Donor→Acceptor CT |
| S₂ | 2.39 | 0.31 | H→L+1 (96%) | Donor→Acceptor CT |
| S₃ | 2.73 | 0.45 | H-1→L (87%) | Donor→Acceptor CT |
| S₄ | 3.01 | 0.42 | H-1→L+1 (95%) | Donor→Acceptor CT |
| S₅ | 3.05 | 0.10 | H→L+2 (89%) | Donor→Acceptor CT |
| S₆ | 3.27 | 0.81 | H-2→L (90%) | $\pi \rightarrow \pi^*$ Acceptor |

(**6**) and 1.94 eV (**7**) with oscillator strengths (*f*) of 0.34 and 0.54, respectively. The calculated S₀→S₁ transition supports both: the shift to the red and the higher intensity of the low-energy absorption band for the dye **7**. The second excited singlet state, S₂, computed at slightly higher energies (**6**: 2.34 eV *f* = 0.26; **7**: 2.25 eV; *f* = 0.16), could also contribute to that band. The S₁ and S₂ states originate in the HOMO→LUMO and HOMO→LUMO+1 monoexcitations, respectively, and imply an electron density transfer from the dithiol moiety, where the HOMO mainly resides, to the acceptor part of the molecule, where the LUMO and LUMO+1 are located (Figure 6.8). Therefore, calculations confirm the CT nature of the low-energy absorption band observed in the electronic spectra of the new dyes **6** and **7**. The higher intensity, that was experimentally observed and theoretically calculated for this band in the compound **7**, can be ascribed to the better electronic communication existing between the donor and acceptor units through the EDOT bridge. The high-energy absorption band recorded in the spectra of **6** and **7** (Figure 6.3) results from the excited states associated with the HOMO-2→LUMO excitation, that is localized on the acceptor part of the molecule, and the HOMO-1→LUMO and LUMO+1 excitations, which also imply some intramolecular electron density transfer

Chapter 6. Donor- π -Acceptors containing a 10-(1,3-dithiol-2-ylidene)anthracene unit for dye-sensitized solar cells.

(Figure 6.8).

The calculations clearly show that the molecules **6** and **7** become more polarized in the S_1 state. The acceptor part of the dye **6** accumulates a charge of -0.54 e in the S_1 state, which is extracted from the anthracene moiety (+0.31 e) and the dithiol unit (+0.23 e). The charge transfer that is associated with the S_1 state is also reflected by the computed value for the molecular dipole moment, which increases from 1.41 D in S_0 to 12.94 D in S_1 . The charge that is transferred from the donor unit to the acceptor unit in the S_1 state is slightly smaller for the dye **7** (acceptor unit: -0.43 e; anthracene moiety: +0.27 e; dithiol unit: +0.16 e). The polarization of the dye in the excited state S_1 facilitates the electron injection in the semiconductor TiO_2 conduction band.

6.4 Dye adsorption and photovoltaic performance

6.4.1 Adsorption of the two-anchor dyes

ATR-FTIR studies. The surface-binding mode of the sensitizer on titania is an interesting aspect to investigate since two anchoring groups are present in the dyes **6** and **7**, which may allow these dyes to attach onto the semiconductor surface through either one or two anchoring groups. ATR-FTIR measurements performed on the dye powders and the sensitized films (Figure 6.9) revealed that, most likely, both dyes **6** and **7** were bound to the surface via both anchoring groups. In the ATR-FTIR spectra of the dye powders, the peaks at 1680–1720 cm^{-1} are attributed to the carboxylic acid groups. The spectra obtained for the dyes adsorbed on transparent TiO_2 films do not contain these peaks, which indicates that both anchoring groups form bonds with the surface of titania. Moreover, the symmetric stretching modes of the carboxylate groups can be identified at 1340–1380 cm^{-1} and the asymmetric stretching at about 1600 cm^{-1} . The position of these frequencies is consistent with the unidentate form of binding of the carboxylate to the TiO_2 surface³⁰.

6.4. Dye adsorption and photovoltaic performance

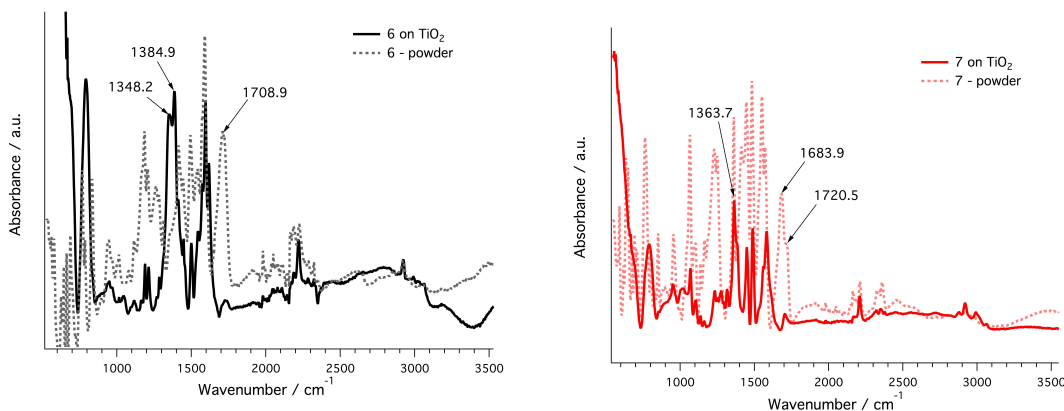


Figure 6.9: FTIR spectra of the dye **6** (left) and **7** (right) as powders (dotted lines) and adsorbed on a transparent TiO₂ layer (solid lines). The spectra were corrected for residuals of CO₂, surface-adsorbed water and TiO₂ itself.

6.4.2 General PV characterization

The photovoltaic performance of dyes **6** and **7** was tested with a volatile acetonitrile-based electrolyte and a solvent-free ionic liquid electrolyte. The devices were fabricated using a transparent, 5.5-μm-thick TiO₂ (200 nm sized nanoparticles). Photoanodes were immersed in the dye solutions (0.3 mM in DMSO/EtOH, 1:9 v/v with 10 mM chenodeoxycholic acid, CDCA) for 2 h upon prior heating at 500°C for 30 min. In this study two types of electrolytes were used; a volatile electrolyte coded Z960 (1.0 M 1,3-dimethylimidazolium iodide, 0.03 M iodine, 0.1 M guanidinium thiocyanate, 0.5 M *tert*-butylpyridine, 0.05 M lithium iodide in acetonitrile:valeronitrile, 85:15, v/v) and ionic-liquid-based Z952 (1,3-dimethylimidazolium iodide/ 1-ethyl-3-methylimidazolium iodide/ 1-ethyl-3-methylimidazolium tetracyanoborate/ iodine/ N-butylbenzimidazole/ guanidinium thiocyanate, 12:12:16:1.67:3.33:0.67). The J-V curves for the volatile systems are presented in the Figure 6.10. The devices sensitized

Table 6.3: Photovoltaic parameters of devices with volatile and ionic liquid electrolytes under simulated AM 1.5G illumination (100 mW cm⁻²)

| Dye | Electrolyte | J _{SC} mA cm ⁻² | V _{OC} mV | FF | η % |
|----------|-------------|--|-----------------------|------|--------|
| 6 | Z960 | 8.8 | 560 | 0.75 | 3.7 |
| | Z952 | 7.4 | 520 | 0.71 | 2.8 |
| 7 | Z960 | 6.3 | 500 | 0.70 | 2.2 |
| | Z952 | 6.1 | 490 | 700 | 2.1 |

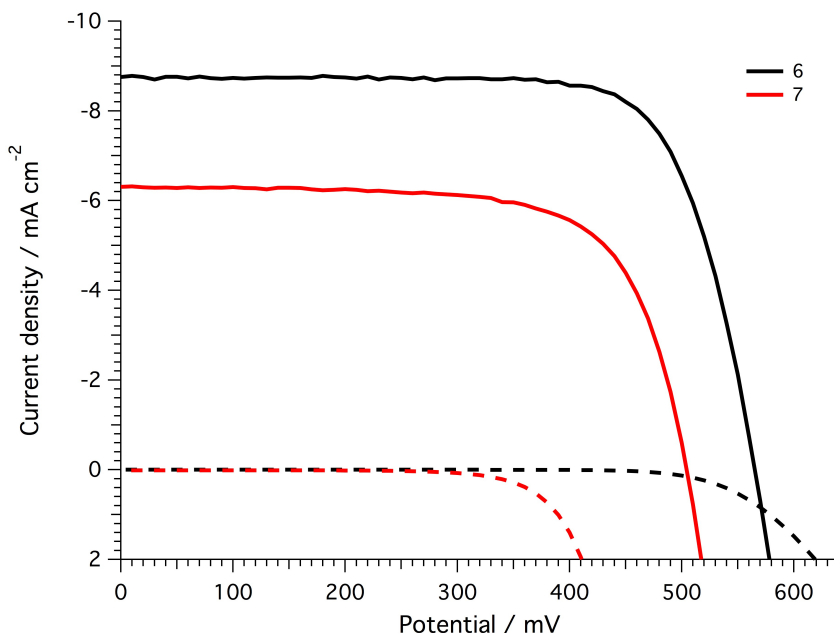


Figure 6.10: J-V plots for the DSCs sensitized with dyes **6** (black) and **7** (red) measured under 1 Sun (AM 1.5G, 100 MWcm^{-2}) conditions (solid line) and in the dark (dashed line).

with the dye **6** yielded better photovoltaic performance, due to higher J_{SC} and V_{OC} . This result seems somewhat surprising, since the absorption spectra of the dyes either in solution (Figure 6.3) or adsorbed on a transparent TiO_2 layer (Figure 6.11) show a better spectral response for the dye **7**. The bathochromic shift of 40 nm accompanied by a significant broadening of the spectra on the film would suggest better performance for the device that contain compound **7**. However, the J_{SC} is $1.3\text{--}2.5 \text{ mA cm}^{-2}$ lower, depending on the electrolyte used, than that obtained for the device containing **6**. Detailed photovoltaic parameters of both the devices are given in the Table 6.3.

The absorption spectrum of the dye **6** adsorbed on the titania surface seems to be notably broadened in the complete device (filled with electrolyte). The incident photon-to-current conversion efficiency (IPCE) spectra of the complete devices are also shown in the Figure 6.11. The integrated current obtained from the IPCE spectrum of the device containing the dye **7** (35%) is significantly smaller than that measured for the device that incorporated the dye **6** (60%). This result is consistent with the lower current densities measured from the J-V curves for the device contained dye **7** (Figure 6.10 and Table 6.3). To calculate the amount of dye that was adsorbed onto the surface of TiO_2 , we stained transparent 2 μm -thick films

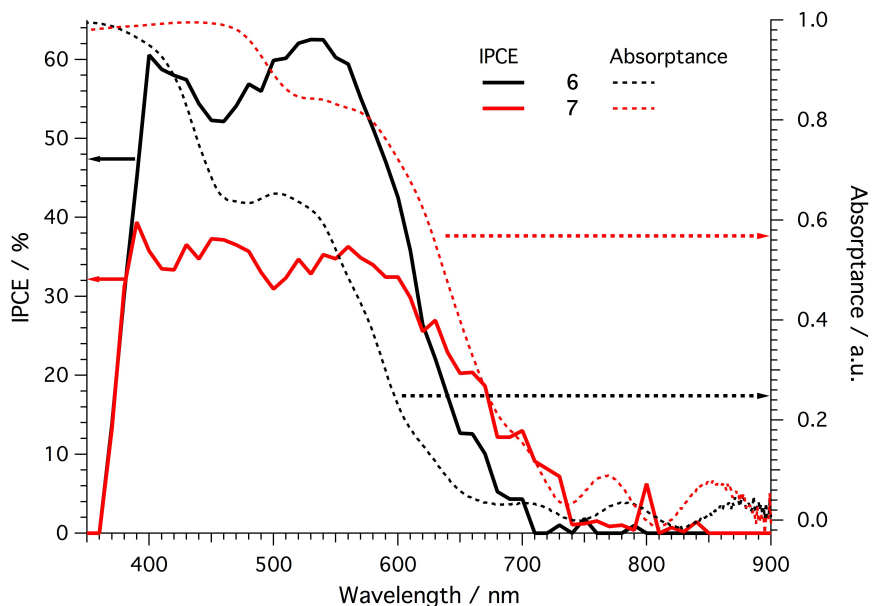


Figure 6.11: Comparison of the absorption spectra of **6** and **7** adsorbed on a transparent 1.9 μm TiO_2 film (dotted line, right axis) and the IPCE spectra of the devices with a 5.5 μm TiO_2 layer (solid line, left axis).

with the dyes and measured their optical density by using UV-vis spectroscopy. By using the Lambert-Beer law (Equation 3.1), we calculated the concentration of the dye within this 2 μm -thick volume, assuming that the film porosity and the surface area were exactly the same for all of the samples. This result entitled us to compare the calculated concentrations 150 mM for the dye **6** and 158 mM for the dye **7**. Because the dye-loading results show that there is no difference between the number of molecules that effectively sensitize the semiconductor, the differences between the performances of devices based on the dyes **6** and **7** should originate from other factors that affect the processes in the cell, such as charge recombination.

6.4.3 Charge recombination problem

In addition to the above-observed difference in J_{SC} , there is also a substantial difference in the V_{OC} of the two devices: at 1 Sun illumination, the V_{OC} for the cell sensitized with the dye **6** is 60 mV (Z960 electrolyte) higher than that with the dye **7**. This difference is even more pronounced when comparing the onset of the dark currents. The logarithmic plot of the dark currents of both devices (Figure 6.12) reveals that there is a tenfold difference between the current densities, which can be interpreted as a sign of enhanced charge recombination in the

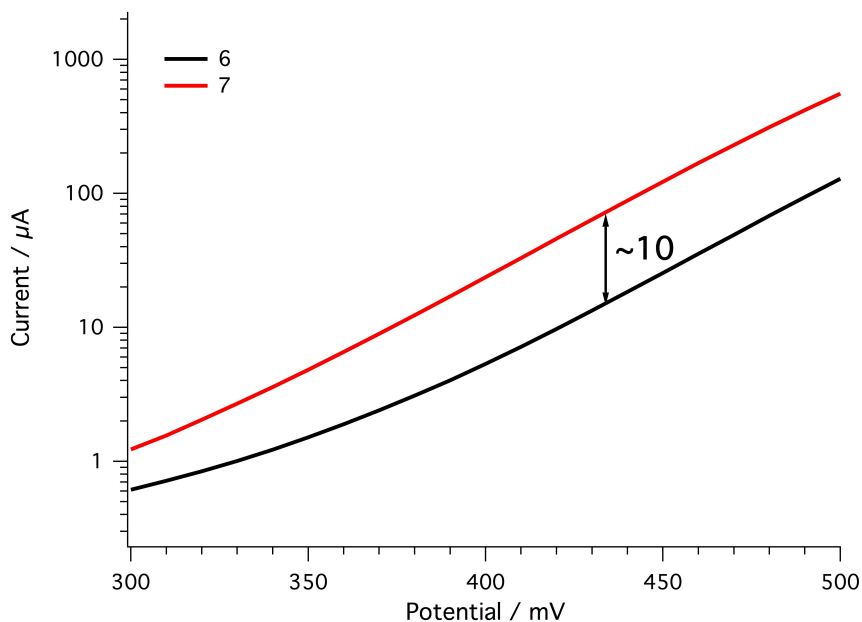


Figure 6.12: Dark currents of the DSCs that incorporated dyes **6** and **7**, which show the undesired behaviour (“leak”) of the dark current in the case of the device sensitized with the dye **7**, thus indicating additional channels for recombination.

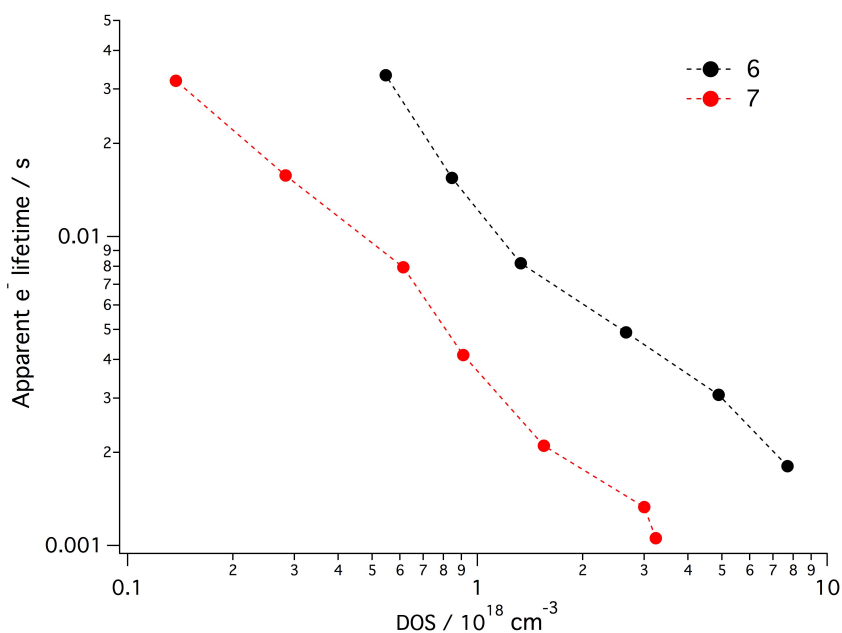


Figure 6.13: Apparent electron lifetime plotted against density of states for DSCs with dyes **6** and **7**.

device sensitized with the dye **7**. To investigate this behaviour, a transient photovoltage decay measurement was performed on both devices. The apparent electron lifetimes measured at the same density of states level are much shorter for the DSCs incorporating the dye **7** (Figure 6.13). By assuming that the position of TiO₂ conduction band remains at the same level in both cases, these results support the previous suggestion that a much faster recombination takes place in the case of the device sensitized with the dye **7** and explains the lower photovoltaic performances obtained when using this dye.

6.5 Conclusions

The work presented in this chapter focuses on the investigation of the synthesis, characterization and application of new dye molecules based on the exTTF core. They were designed in such a way to improve their spectral responses, which makes them more attractive to incorporate in the DSCs. For instance, inserting EDOT in the structure has led to the extension of the spectrum up to 700 nm, which in comparison with the previously reported analogous molecules gives a 200–300 nm of red-shift. FTIR measurements revealed that both dyes are bound to the TiO₂ surface through the two anchoring groups in a unidentate binding form. The preferable conformations that were obtained from the DFT calculations support this binding mode and showed that the molecular geometry is highly distorted from planarity, mainly due to the saddle-like-shaped exTTF core, with the anthracene core being folded in a boat-type structure. In the light of this spatial arrangement, lower aggregation is expected. Optical and electrochemical characterization of these new materials satisfied the criteria for their successful incorporation into photovoltaic devices. The highest obtained efficiency reached 3.7%, while the IPCE being stretched out beyond 700 nm for the dye **6** sensitized device. EDOT-containing molecule, the dye **7**, despite having a slightly broader UV-Vis spectrum, was inferior to the phenyl-substituted one in terms of the overall PV performance. The main reason behind this discrepancy is the higher recombination rate manifested in a higher dark current and a shorter electron lifetime.

6.6 Bibliography

- [1] K. Hara, Z.-S. Wang, T. Sato, A. Furube, R. Katoh, H. Sugihara, Y. Dan-oh, C. Kasada, A. Shinpo and S. Suga, *The Journal of Physical Chemistry B*, 2005, **109**, 15476–15482.
- [2] S. Ito, H. Miura, S. Uchida, M. Takata, K. Sumioka, P. Liska, P. Comte, P. Péchy and M. Grätzel, *Chemical Communications*, 2008, 5194–5196.
- [3] R. Chen, X. Yang, H. Tian and L. Sun, *Journal of Photochemistry and Photobiology A: Chemistry*, 2007, **189**, 295–300.
- [4] Z. Wang, Y. Huang, C. Huang, J. Zheng, H. Cheng and S. Tian, *Synthetic Metals*, 2000, **114**, 201–207.
- [5] S. Erten-Ela, M. D. Yilmaz, B. Icli, Y. Dede, S. Icli and E. U. Akkaya, *Organic Letters*, 2008, **10**, 3299–3302.
- [6] S. Tan, J. Zhai, H. Fang, T. Jiu, J. Ge, Y. Li, L. Jiang and D. Zhu, *Chemistry – A European Journal*, 2005, **11**, 6272–6276.
- [7] G. Zhang, H. Bala, Y. Cheng, D. Shi, X. Lv, Q. Yu and P. Wang, *Chemical Communications*, 2009, 2198–2200.
- [8] H. Tian, X. Yang, R. Chen, Y. Pan, L. Li, A. Hagfeldt and L. Sun, *Chemical Communications*, 2007, 3741–3743.
- [9] J. L. S. und Nazario Martín, *Angewandte Chemie*, 2001, **113**, 1416–1455.
- [10] N. Martín, L. Sánchez, M. Á. Herranz, B. Illescas and D. M. Guldi, *Accounts of Chemical Research*, 2007, **40**, 1015–1024.
- [11] D. Canevet, M. Sallé, G. Zhang, D. Zhang and D. Zhu, *Chemical Communications*, 2009, 2245–2269.
- [12] P.-A. Bouit, C. Villegas, J. L. Delgado, P. M. Viruela, R. Pou-Amérigo, E. Ortí and N. Martín, *Organic Letters*, 2011, **13**, 604–607.
- [13] F. G. Brunetti, J. L. López, C. Atienza and N. Martín, *Journal of Materials Chemistry*, 2012, **22**, 4188–4205.
- [14] S. Wenger, P.-A. Bouit, Q. Chen, J. Teuscher, D. D. Censo, R. Humphry-Baker, J.-E. Moser, J. L. Delgado, N. Martín, S. M. Zakeeruddin and M. Grätzel, *Journal of the American Chemical Society*, 2010, **132**, 5164–5169.

-
- [15] A. S. Batsanov, M. R. Bryce, M. A. Coffin, A. Green, R. E. Hester, J. A. K. Howard, I. K. Lednev, N. Martín, A. J. Moore, J. N. Moore, E. Ortí, L. Sanchez, M. Saviron, P. M. Viruela, R. Viruela and T.-Q. Ye, *Chemistry – A European Journal*, 1998, **4**, 2580–2592.
- [16] C. Y. Lee, C. She, N. C. Jeong and J. T. Hupp, *Chemical Communications*, 2010, **46**, 6090–6092.
- [17] A. Abbotto, N. Manfredi, C. Marinzi, F. D. Angelis, E. Mosconi, J.-H. Yum, Z. Xianxi, M. K. Nazeerud-din and M. Grätzel, *Energy and Environmental Science*, 2009, **2**, 1094–1101.
- [18] M. Xu, S. Wenger, H. Bala, D. Shi, R. Li, Y. Zhou, S. M. Zakeeruddin, M. Grätzel and P. Wang, *The Journal of Physical Chemistry C*, 2009, **113**, 2966–2973.
- [19] G. Chen, L. Wang, D. W. Thompson and Y. Zhao, *Organic Letters*, 2008, **10**, 657–660.
- [20] W.-H. Liu, I.-C. Wu, C.-H. Lai, C.-H. Lai, P.-T. Chou, Y.-T. Li, C.-L. Chen, Y.-Y. Hsu and Y. Chi, *Chemical Communications*, 2008, 5152–5154.
- [21] R. Kawano and M. Watanabe, *Chemical Communications*, 2003, 330–331.
- [22] N. Martín, L. Sánchez, C. Seoane, E. Ortí, P. M. Viruela and R. Viruela, *The Journal of Organic Chemistry*, 1998, **63**, 1268–1279.
- [23] M. C. Díaz, B. M. Illescas, N. Martín, R. Viruela, P. M. Viruela, E. Ortí, O. Brede, I. Zilberman and D. M. Guldi, *Chemistry – A European Journal*, 2004, **10**, 2067–2077.
- [24] D. Canevet, M. Gallego, H. Isla, A. de Juan, E. M. Pérez and N. Martín, *Journal of the American Chemical Society*, 2011, **133**, 3184–3190.
- [25] E. M. Pérez and N. Martín, *Chemical Society Reviews*, 2008, **37**, 1512–1519.
- [26] M. R. Bryce, A. J. Moore, M. Hasan, G. J. Ashwell, A. T. Fraser, W. Clegg, M. B. Hursthouse and A. I. Karaulov, *Angewandte Chemie International Edition*, 1990, **29**, 1450–1452.
- [27] C. A. Christensen, A. S. Batsanov, M. R. Bryce and J. A. K. Howard, *The Journal of Organic Chemistry*, 2001, **66**, 3313–3320.
- [28] A. E. Jones, C. A. Christensen, D. F. Perepichka, A. S. Batsanov, A. Beeby, P. J. Low, M. R. Bryce and A. W. Parker, *Chemistry – A European Journal*, 2001, **7**, 973–978.
- [29] J. Santos, B. M. Illescas, N. Martín, J. Adrio, J. C. Carretero, R. Viruela, E. Ortí, F. Spänig and D. M. Guldi, *Chemistry – A European Journal*, 2011, **17**, 2957–2964.
- [30] K. S. Finnie, J. R. Bartlett and J. L. Woolfrey, *Langmuir*, 1998, **14**, 2744–2749.

7 Tuning the photovoltaic performance of the D- π -A dyes with a phenothia- zine and carbazole donor in dye- sensitized solar cells.

This part is adapted from a peer reviewed publications

1. *Magdalena Marszalek, Satyawan Nagane, Amol Ichake, Robin Humphry-Baker, Vincent Paul, Shaik M. Zakeeruddin and Michael Grätzel published in 2012 in Journal of Materials Chemistry, Vol. 22, pp 889-894*
2. *Magdalena Marszalek, Satyawan Nagane, Amol Ichake, Robin Humphry-Baker, Vincent Paul, Shaik M. Zakeeruddin and Michael Grätzel published in 2013 in RSC Advances, Vol. 3, pp 7921-7927*

7.1 Introduction

Phenothiazine, containing electron-rich sulphur and nitrogen atoms, is particularly interesting as an electron donor, mainly because of a non-planar geometry and good thermal and electrochemical stability. However, it has not been investigated much as a potential donor unit for D- π -A for DSCs. A few simple molecules containing phenothiazine were tested by Sun et al.¹, but the efficiencies reached with the devices were reaching only 5.5%. In this work we decided to revisit this particular donor, at the same time applying all the known concepts for

Chapter 7. Tuning the photovoltaic performance of the D- π -A dyes with a phenothiazine and carbazole donor in dye-sensitized solar cells.

the design of an efficient dye for dye-sensitized solar cells.

First we designed and synthesized two new dyes (**V5** and **V7**) using 10-butyl-(2-methylthio)-10*H*-phenothiazine as a donor with/without vinyl thiophene group as a π -bridge and one with a cyanoacrylic acid as an acceptor. The photophysical properties of these dyes were characterized by UV-Vis spectroscopy and electrochemical techniques. Additionally, theoretical calculations were performed in order to optimize geometry and visualize HOMO and LUMO. The dyes were then used as sensitizers in DSCs and the devices' performances were evaluated under standard AM 1.5G conditions, yielding up to 7.3% efficiency. The extension of the π -conjugated bridge has led to an increase in the efficiency and we explain this effect using transient photovoltage and photocurrent decays techniques, and electrochemical impedance spectroscopy (EIS). Nevertheless, the increase in the current density (mainly due to the widening of the absorption spectra upon introducing a thiophene unit) was tied with the significant drop in the V_{OC} . That is why a follow-up dye (**V11**) containing a π -bridge with alkyl chains was synthesized, as the introduction of more bulky group close to the semiconductor surface may improve its effective shielding from the redox species in the electrolyte. Additionally, following the increased interest in the dyes with a carbazole donor group²⁻⁴, we synthesized a dye which is similar to the **V11** dye, where the donor part is a 9-butyl-9*H*-carbazole in place of the phenothiazine. With this set of dyes the comparisons in two directions could be made: the influence of the extending the π -bridge on the phenothiazine dyes (**V5**, **V7** and **V11**) and the effect of the donor part (**V11** and **V4**), where in this configuration the difference is just one additional sulphur atom in the ring.

7.2 Synthesis and characterization of the dyes V5, V7, V11 and V4

7.2.1 Chemical synthesis of the dye molecules

In the Figure 7.1 we present the synthetic approach for the two sensitizers: **V5** and **V7**. Alkylation of 2-methylthiophenothiazine, followed by Vilsmeier-Haack formylation, provided the common aldehyde intermediate **2**. Knoevenagel condensation with cyanoacetic acid in the presence of piperidine resulted in the sensitizer **V5** (91% yield) as a product. The Horner-Wadsworth-Emmons coupling reaction between the aldehyde **2** and diethyl-(thio-

7.2. Synthesis and characterization of the dyes V5, V7, V11 and V4

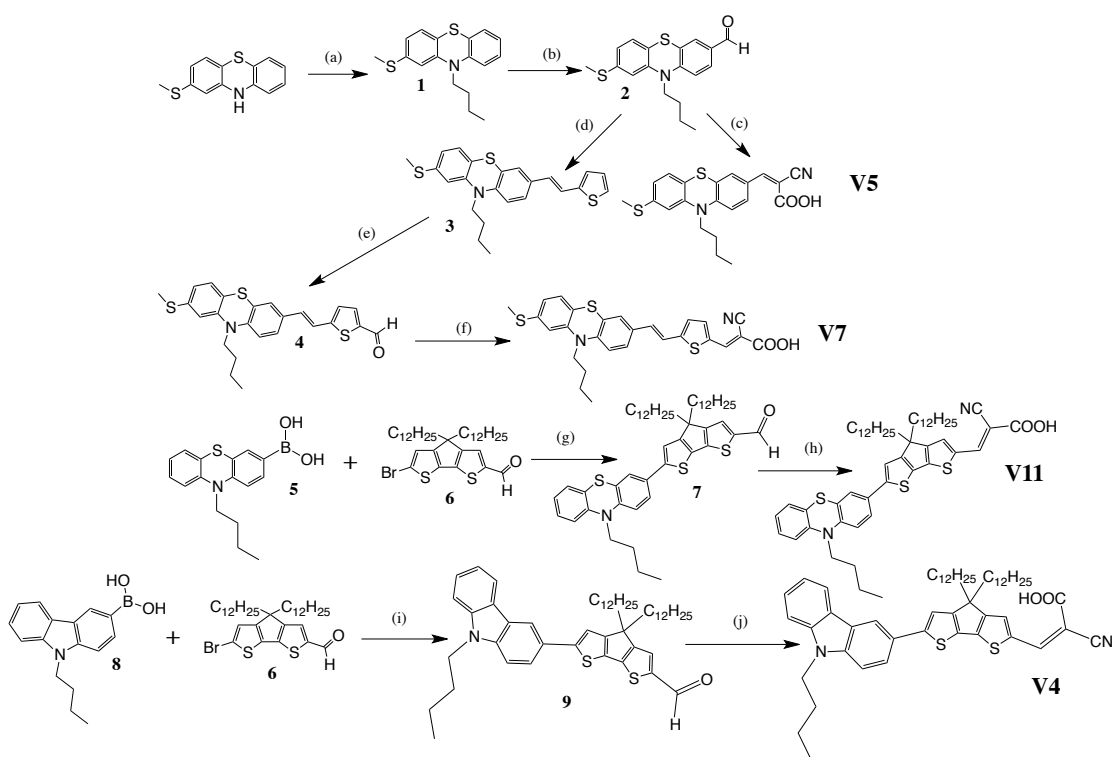


Figure 7.1: Synthetic route for V-dyes. (a) 1-bromobutane, KOH, KI, DMSO, rt; (b) POCl_3 , DMF, 80°C; (c) cyanoacetic acid, piperidine, toluene, reflux; (d) diethyl-(thiophen-2-yl)-methylphosphonate, NaH, THF, rt; (e) POCl_3 , DMF, 1,2-dichlorobenzene; (g)/(i) $\text{Pd}(\text{PPh}_3)_4$, K_2CO_3 , THF, H_2O , 80°C; (h)/(j) cyanoacetic acid, piperidine, toluene, reflux 7 hrs.

phen-2-yl)-methylphosphonate afforded crude **3** in 89% yield. Several attempts to purify the product by column chromatography could not afford pure single product. NMR measurement indicated a mixture of two compounds, of which 90–95% was the desired product **3**. Hence, the crude product was taken as it is without purification for further reaction. The compound **3** underwent a reaction with phosphorus oxychloride (POCl_3) and N,N-dimethyl formamide (DMF) to give the aldehyde **4** in 82% yield. The sensitizer **V7** in 85% yield (after silica gel column chromatography) was obtained after a condensation with cyanoacetic acid in the presence of piperidine.

V11 dye was synthetised by Suzuki coupling of the (10-butyl-10*H*-phenothiazin-3-yl)boronic acid, **5**, with the aldehyde **6**, followed by Knoevenagel condensation with cyanoacetic acid. The reaction yield was rather high (81%) and resulted in the dye as red solid.

Additionally, the dye **V4** bearing the carbazole donor was synthesized along with the previous

Chapter 7. Tuning the photovoltaic performance of the D- π -A dyes with a phenothiazine and carbazole donor in dye-sensitized solar cells.

three phenothiazine dyes. A compound **8** was prepared according to the reported methods⁵. Suzuki coupling reaction of the aldehyde **6** with (9-butyl-9*H*-carbazol-3-yl)boronic acid, **8**, afforded compound **9** in 89% yield after column chromatography. Knoevenagel condensation of the aldehyde **9** with cyanoacetic acid afforded the desired sensitizer **V4** as a red solid in 81% yield.

7.2.2 Optical properties

All measured photophysical properties of the molecules are summarized in the Table 7.1. UV-visible spectra of the dyes in dichloromethane are presented in the Figure 7.2. **V7** dye exhibits a bathochromic shift of 27 nm in respect to the dye **V5**. The insertion of a vinyl thiophene unit clearly extends the absorption spectrum of the dye **V7** – the onset of the spectral response reaches up to 700 nm. The insertion of the CPDT unit clearly has some impact on the absorption spectrum of the dyes. The lowest energy absorption band for the **V4** and **V11** dyes is located at 532 nm, corresponding to intramolecular charge transfer from the N-butyl-carbazole or the N-butyl-phenothiazine donor to the cyanoacrylic acid, providing efficient charge separation at the excited state. Emission measurements in combination with UV-Visible spectra show that the Stokes shift is much larger for the dyes without the CPDT units reaching almost 200 nm, whereas for the dyes **V4** and **V11** it is two times smaller.

Table 7.1: Absorption, emission and electrochemical properties of dyes **V4**, **V5**, **V7** and **V11** in dichloromethane solution.

| Dye | V4 | V5 | V7 | V11 |
|--|-----------|-----------|-----------|------------|
| λ_{max} / nm (abs) | 532 | 451 | 478 | 532 |
| $\epsilon(\lambda_{max})$ / M ⁻¹ cm ⁻¹ | 57 500 | 11 500 | 29 300 | 46 500 |
| λ_{max} / nm (em) | 636 | 644 | 665 | 610 |
| E_{ox} / V | 1.15 | 1.09 | 0.97 | 0.97 |
| E_{0-0} / eV | 2.11 | 2.03 | 1.85 | 2.20 |
| $E_{ox}-E_{0-0}$ / V | -0.96 | -0.94 | -0.88 | -1.23 |

Oxidation potentials measured with ferrocene as an internal standard and the values are given vs. NHE (Fc/Fc⁺ = +0.7 V NHE). E_{0-0} transition energy was estimated from the emission and absorption spectra.

7.2.3 Electrochemistry - experimental determination of HOMO/LUMO

It is important to determine the highest occupied molecular orbital (HOMO) and lowest unoccupied molecular orbital (LUMO) energy of the dye molecules to know whether there is enough driving force to inject electrons into the TiO_2 conduction band and to afford the regeneration of the dye cation with the redox electrolyte. First, the cyclic voltammograms recorded for the four molecules have shown that the compounds undergo reversible reduction/oxidation reactions. The electrochemical properties of the dyes were then studied with differential pulse voltammetry to obtain formal redox potentials of the molecules and are presented in the Table 7.1. The oxidation potential of **V11** dye is observed at 0.97 V, which is in agreement with the values of **V7** that has the N-butyl-(2-methylthio)-phenothiazine as a donor. The oxidation potential of **V4** dye is 180 mV more positive than that of **V7** dye indicating that the HOMO is stabilized more in the presence of the N-butyl-carbazole donor than that of the N-butyl-(2-methylthio)-phenothiazine donor moiety. The excited state reduction potentials of all dyes are obtained by combining the oxidation potentials with the energy of the transition

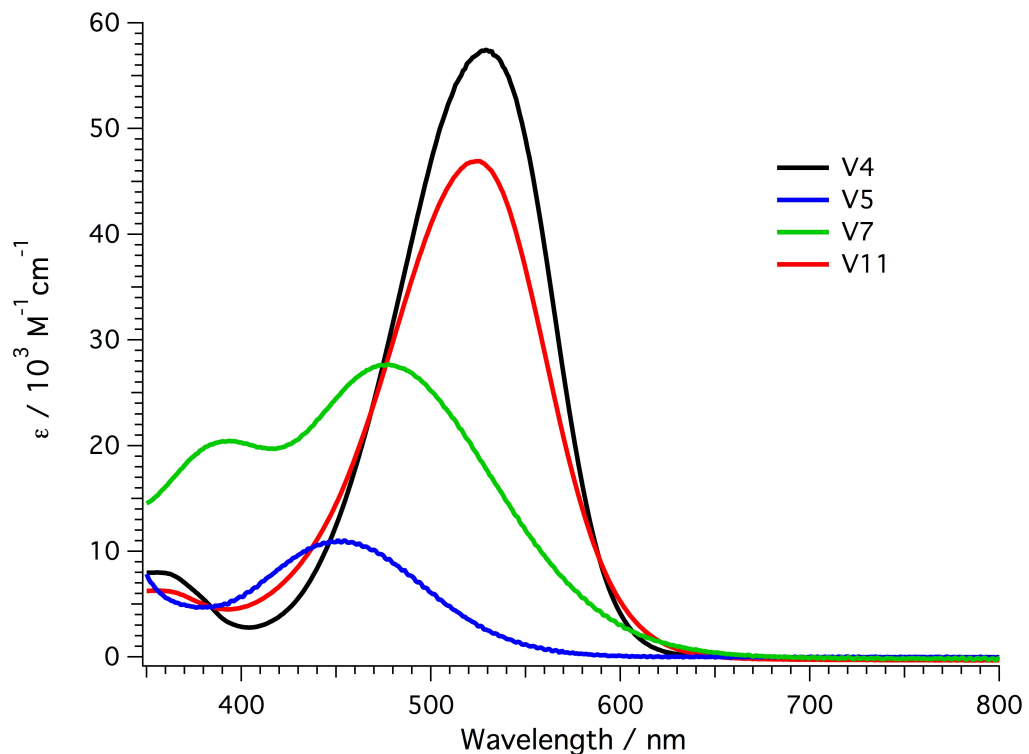


Figure 7.2: UV-Vis spectra of the dyes **V4**, **V5**, **V7** and **V11** in dichloromethane solution.

Chapter 7. Tuning the photovoltaic performance of the D- π -A dyes with a phenothiazine and carbazole donor in dye-sensitized solar cells.

upon light absorption (the HOMO-LUMO energy difference was taken as an intersection of the absorption and emission plots after normalization). The excited state potentials are placed sufficiently above the TiO_2 conduction band edge (-0.5 V vs. NHE) to ensure no energetic barriers for the electron injection. Since the HOMO energy levels of the dyes are both below 0.90 V vs NHE, i.e. lower than the redox energy level of I^-/I_3^- couple (0.35 V vs NHE), there should be enough driving force for the dye regeneration.

7.2.4 Quantum chemical calculations

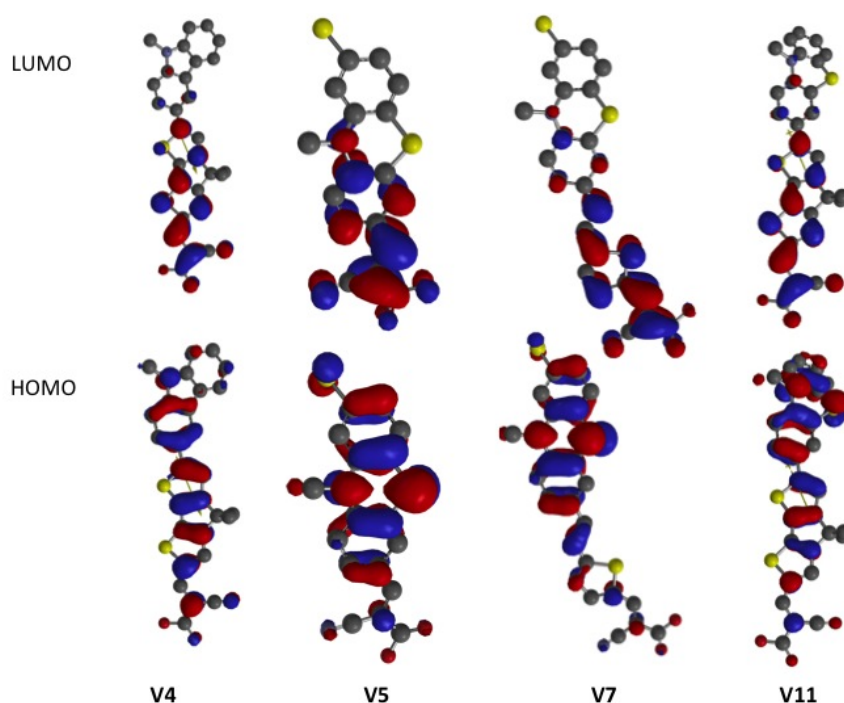


Figure 7.3: Frontier molecular orbitals of the **V**-dyes calculated with DFT (B3LYP/6-31G*) in vacuum.

In order to get more insight into the molecular structure and electron distribution within the molecules, DFT calculations were performed. These analyses were carried out using B3LYP/6-31G* basis set (Spartan'10, Wavefunction) to optimize dye geometries and energies in vacuum. The molecules were simplified by replacing alkyl chains attached to the CPDT, carbazole and phenothiazine units by methyl groups to reduce the number of basis functions. Initial optimization of the geometry of the molecules reveals that the carbazole donor (**V4**) is the least distorted from planarity. Phenothiazine donor (**V5**, **V7** and **V11**) exhibits a fold along

7.3. Evaluation of the photovoltaic performance

Table 7.2: Summarized photovoltaic parameters of DSCs sensitized with the **V** dyes and incorporating a volatile electrolyte

| Dye | V4 | V5 | V7 | V11 |
|--------------------------------|-----------|-----------|-----------|------------|
| J_{SC} / mA cm ⁻² | 13.1 | 11.2 | 15.2 | 12.9 |
| V_{OC} / mV | 770 | 768 | 691 | 774 |
| Fill factor | 0.73 | 0.75 | 0.70 | 0.70 |
| η / % | 7.50 | 6.53 | 7.44 | 7.00 |

the sulphur-nitrogen axis going through the middle ring. As can be seen in the Figure 7.3, the HOMO orbitals are mainly located at the donor end of the molecule. There is some extension of the HOMO onto the π -conjugated building block. Nevertheless, the LUMO is confined to the π -bridge and acceptor in all cases, which confirms that there should be no problem with effective charge separation and subsequent unidirectional electron transfer to the titania conduction band.

7.3 Evaluation of the photovoltaic performance

7.3.1 Overall photovoltaic characterization

A set of dye-sensitized solar cells fabricated as described in the Chapter 3 Experimental methods was tested under standard conditions (AM 1.5G, 100 mW cm⁻²) in order to investigate the photovoltaic performance of the dyes. The cells consisted of a double-layered TiO₂ photoanode (8 μ m transparent and 5 μ m scattering layer) and standard Pt counter-electrode and electrolyte that was used in the experiment was a standard volatile electrolyte containing 1.0 M 1,3-dimethylimidazolium iodide, 0.03 M I₂, 0.05 M lithium iodide, 0.1 M guanidinium thiocyanate and 0.5 M *tert*-butylpyridine. The J-V curves of the devices are shown in the Figure 7.4 and the photovoltaic parameters are presented in the Table 7.2.

There is a substantial difference between the performances of the devices with the dyes **V5** and **V7** containing volatile electrolyte. The extension of the π -conjugated bridge, by inserting a vinyl thiophene unit into the **V5** structure to obtain the **V7** molecule has led to the increase of the photocurrent drawn from the cell with the latter by 4 mAcm⁻². This effect can be ascribed to the enhanced optical properties of the latter, namely a bathochromic shift accompanied

Chapter 7. Tuning the photovoltaic performance of the D- π -A dyes with a phenothiazine and carbazole donor in dye-sensitized solar cells.

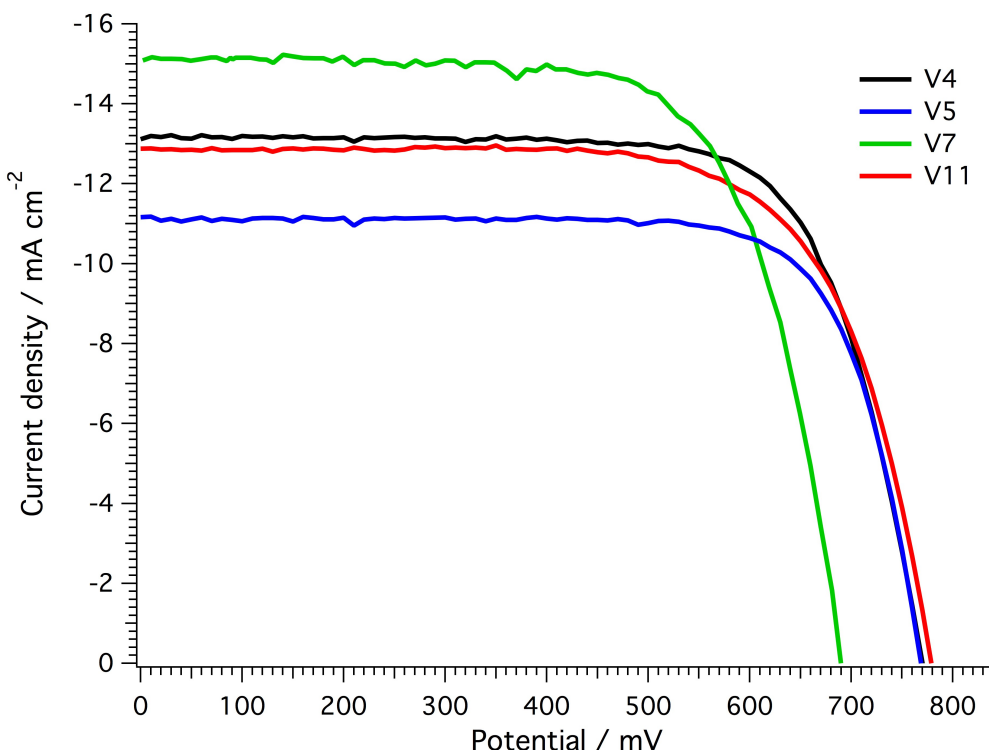


Figure 7.4: J-V curves of the devices sensitized with the **V**-dyes measured at 1 Sun intensity.

with doubling the absorption cross-section (vide infra).

Devices with **V4** and **V11** dyes yielded a power conversion efficiency (η) of 7.5 and 7.0% at full sunlight intensity under standard AM 1.5G condition. Both these devices show comparable η with similar J_{SC} and V_{OC} values as shown in the Table 7.2. This shows that there is not much influence of the donor group on the devices η values, whether it is N-butyl-carbazole or N-butyl-phenothiazine. Here we would like to make a comparison with a similar D- π -A dye **V7**, which has N-butyl-(2-methylthio)-phenothiazine as a donor and its π -conjugated spacer is vinyl thiophene in place of the CPDT on the **V11** dye. Maintaining identical TiO_2 films, redox electrolyte and counter-electrodes, the only difference in the devices is in the structure of two dyes, which have different π -conjugated spacer. This comparison gives us more insight into the structure-performance relationship of D- π -A dyes within the context of photovoltaic performance. The photovoltaic parameters of **V7**-sensitized devices compared to **V11**-sensitized ones show larger differences in the J_{SC} and V_{OC} values.

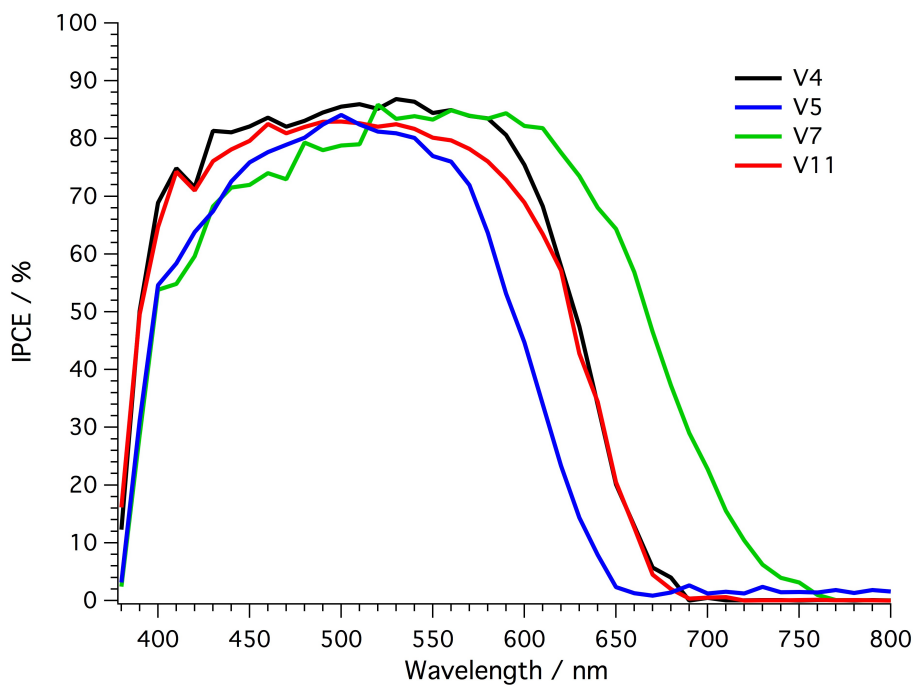


Figure 7.5: Incident photon-to-current efficiency spectra for the champion devices sensitized with the **V**-dyes.

7.3.2 IPCE comparison

The incident-photon-to-current efficiency (IPCE) plots for the above-mentioned devices are presented in the Figure 7.5. Despite the difference in the molar extinction coefficient, the dyes **V5** and **V7**, when incorporated in the DSC, exhibit a plateau of 80% from 450 nm up to 550 nm and 640 nm (**V5** and **V7**, respectively). In the IPCE plot, the bathochromic shift of the dye **V7** is even more pronounced (in comparison to the UV-Vis spectrum of the pure dye), the onset of the plot reaching 750 nm.

The incident photon-to-conversion efficiency (IPCE) of devices sensitized with **V4** and **V11** also exhibit a plateau of 70 to 80% from 450 nm to 600 nm as shown in the Figure 7.5. The **V11** dye sensitized device exhibits somewhat lower IPCE values compared to the **V4** dye. The maximum IPCE of 86% at 600 nm was obtained with **V4** dye, which is in agreement with the proposed optical loss mechanisms for DSC. In the absence of antireflection UV cut-off film on top of the devices, the reflections from the glass surface account for ~10% of the losses. Since IPCE is a product of the efficiencies of three consecutive processes occurring within the cell:

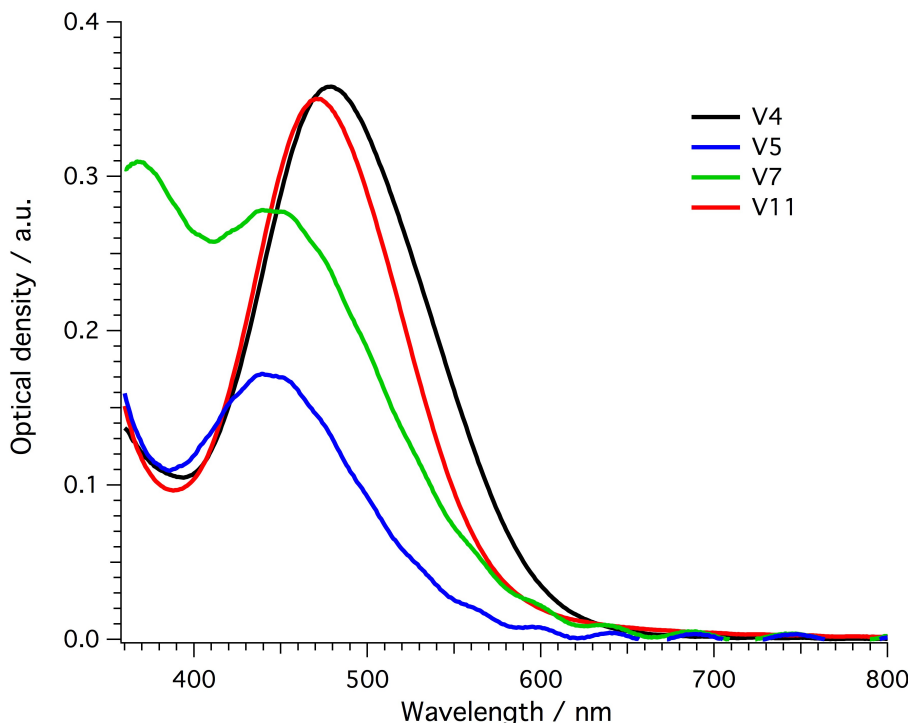


Figure 7.6: UV-vis absorption spectra of the **V**-dyes adsorbed on the 3- μm thick TiO₂ layers.

light harvesting, electron injection and charge collection, it could then be inferred that none of the above listed phenomena impedes the work of the devices, and they are close to their peak performance. The IPCE spectral response for the **V4** and **V11** dyes reach up to 700 nm whereas for the **V7** device it extends up to 750 nm. The higher J_{SC} values obtained with the **V7** dye are due to its broader spectral response. The difference in the IPCE spectra of **V7** dye compared to **V4** and **V11** is in agreement with the red shift in the absorption spectra adsorbed on a transparent TiO₂ film, respectively (as shown in the Figure 7.6). In addition to the red shifted spectral response, the concentration of **V7** dye adsorbed on the TiO₂ film is ~ 234 mM and is higher than that of the **V4/V11** dyes (111 and 157 mM) due to smaller molecular size, which is contributing to the higher J_{SC} value that was observed in the J-V measurements.

7.4 Controlling the TiO₂ interface - recombination rate and conduction band shift

7.4.1 V5-V7 comparison

The **V7** dye could be perceived as an extended version of a very simple molecule **V5**. The incorporation of the thiophene unit close to the anchoring group of the dye seems to have influence on the electronic processes in the fabricated devices. The significant difference of the obtained open-circuit voltages (77 mV) could be a sign of the enhanced recombination at the TiO₂/dye/electrolyte interface. In order to investigate further this issue, a series of transient photovoltage and photocurrent experiments as well as electrochemical impedance spectroscopy (EIS) characterization were performed for the complete devices. EIS measurement conducted under 0.5 Sun illumination reveals that the charge transfer resistance of the cell with the **V7** dye is approximately 1 order of magnitude lower (initially), which may hint to facilitated recombination (Figure 7.7, **V5** - blue and **V7** - green). Even though there are many more electrons harvested and injected into the mesoporous structure of **V7** sensitized cell, there are still some losses that influence the V_{OC} . Additionally, there is a shift of the conduction band detected by both: EIS and transient photovoltage decay, which agree very well with the J-V data that we have presented before. This conduction band shift is significant and has to be included in the R_{ct} plot from EIS (horizontal shift towards higher potential). The difference in the charge transfer resistance, after the correction, is not as much pronounced. The plots obtained from the two measurements are presented in the Figure 7.8, left and Figure 7.9, where the potential is plotted against the capacitance, which can be directly scaled up to obtain DOS (see: Equation 2.47). Thus, the difference in the V_{OC} can result from both: downward shift of the conduction band (because the relative position of the Fermi level in regards to the conduction band stays fairly close in both of the cells) and lowered charge transfer resistance leading to easier recombination in case of the cell sensitized with **V7**.

Despite the enhanced recombination observed for the **V7** sensitized DSC, which manifests itself in the lower charge collection efficiency (Figure 7.8, right) in comparison with the **V5** sensitized device, the short-circuit current drawn from the cell is much higher. Having analysed the processes in the cells and probing the properties of the interfaces, we ascribe the

Chapter 7. Tuning the photovoltaic performance of the D- π -A dyes with a phenothiazine and carbazole donor in dye-sensitized solar cells.

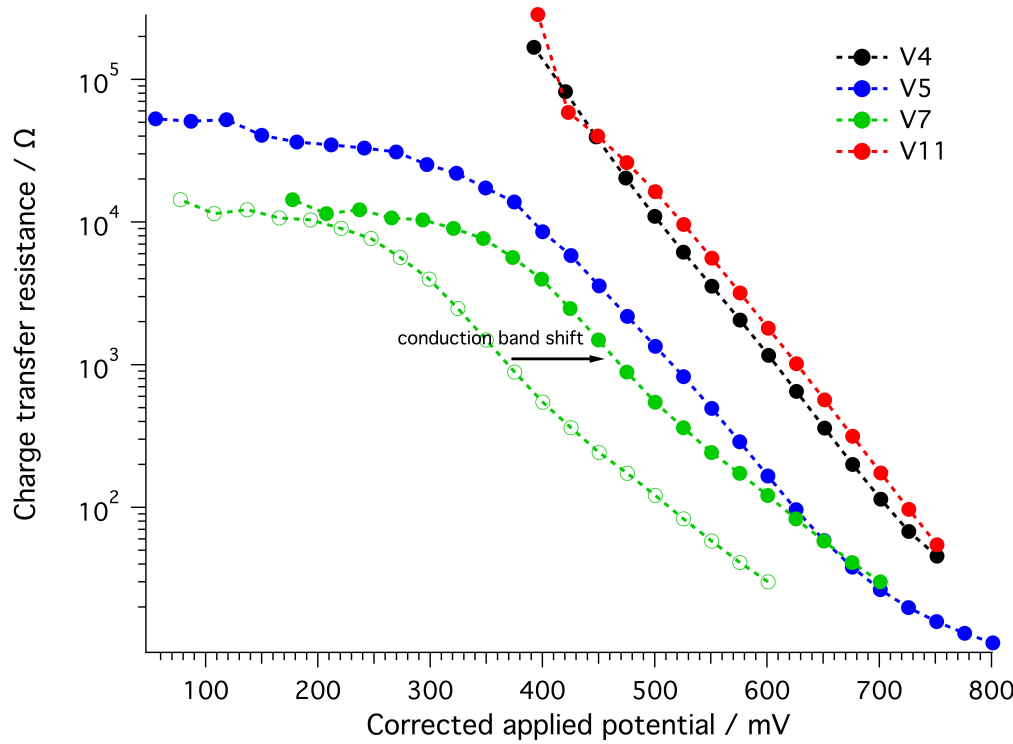


Figure 7.7: Charge transfer resistance derived from the electrochemical impedance spectroscopy plotted against applied potential corrected for the IR drop.

increase in the current purely to the extended spectral response of the dye V7.

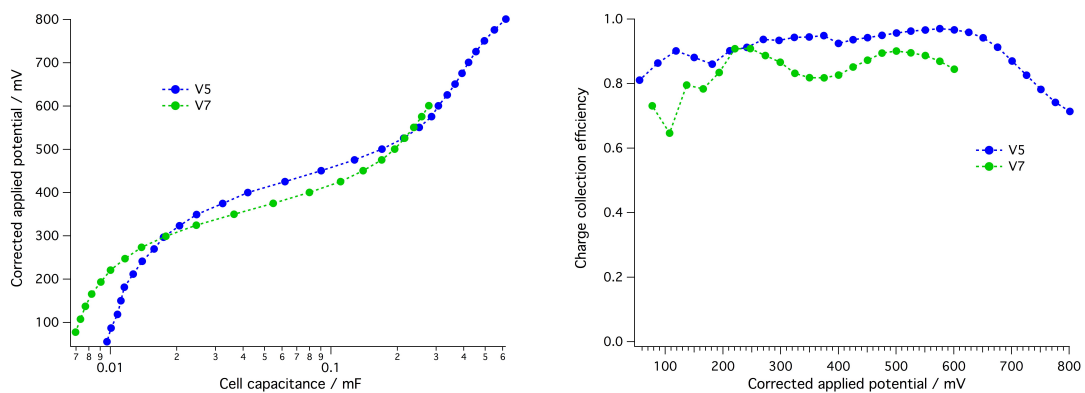


Figure 7.8: *Left:* Cell capacitance measured with the electrochemical impedance spectroscopy under 0.5 Sun light bias for the cells with V5 and V7 dyes. *Right:* Charge collection efficiency derived from the same EIS experiment for the V5 and V7-sensitized devices.

7.4. Controlling the TiO₂ interface - recombination rate and conduction band shift

7.4.2 Introduction of CPDT with alkyl side-chains

Again, in order to better understand the difference in the V_{OC} of the **V7** and **V4/V11**-sensitized devices, transient photovoltage decay characterization was the technique of choice. The **V7** cell, with the 80 mV lower V_{OC} than **V4/V11**, exhibited the highest current density. The trapped electron density estimated from the short-circuit current density in the cell with **V7** is higher than for **V4/V11**. At short-circuit conditions, the recombination flux is negligible, thus the J_{SC} is a good measure of the electrons in the film⁶. Taking the ratio of the number of charges approximated from the corresponding short-circuit current densities (Table 7.2) we find that the calculated change in V_{OC} between **V4/V11** and **V7** is about 10 mV. This suggests that a 70 mV difference is arising due to a shift in the conduction band position. For all devices the V_{OC} measured under decreasing light intensity against cell capacitance is plotted in the Figure 7.9. The **V7** sensitized cell shows the lowest lying quasi-Fermi level as compared to the other devices, which is in line with the V_{OC} as measured during a standard J-V characterization. As a consequence of the higher molecular concentration on the TiO₂ surface of the **V7** dye, an increased concentration of protons on that surface might be expected. This could be responsible for shifting the DOS of the **V7** device.

7.4.3 Electrochemical impedance study

The DSCs were further subjected to EIS investigation. The obtained results confirm the hypothesis of an upward shift of the conduction band for **V4/V11** dyes, when compared with **V7**. Fitting the impedance data as presented in Figure 7.7, the important circuit element, electron transfer resistance at the dye-sensitized TiO₂/electrolyte interface, R_{ct} , was derived. As reported previously, the electron transfer resistance is related to the densities of electrons in the conduction band and that of oxidized state of redox couple^{7,8}. The parallel displacement of the plots along the bias voltage (corrected for the IR drop, see Figure 7.7) follows the order of **V7<V4≈V11**. The resistance from the device with **V7** is shifted downward from that of devices with **V4** and **V11**. As presented in Figure 7.7, the difference among the three devices will be very small if the resistances of **V7** are shifted positively by 70 mV, indicating that the interfacial recombination of these devices is similar under an identical quasi-Fermi level of the electrons. This can also be supported by the apparent electron lifetime plot (Figure 7.10), where the

Chapter 7. Tuning the photovoltaic performance of the D- π -A dyes with a phenothiazine and carbazole donor in dye-sensitized solar cells.

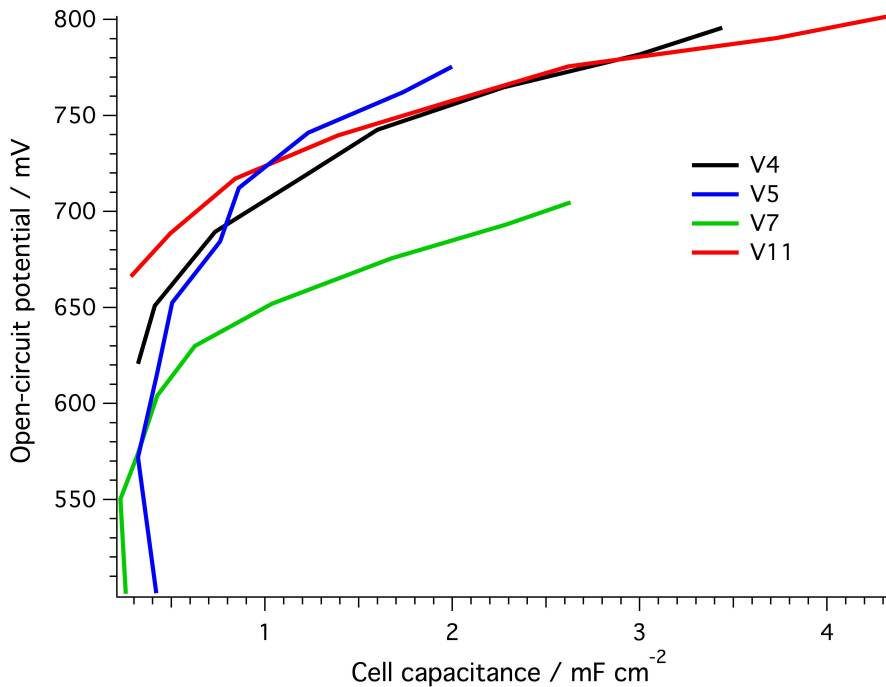


Figure 7.9: Cell capacitance measured with transient photocurrent and photovoltage techniques under varying light intensity.

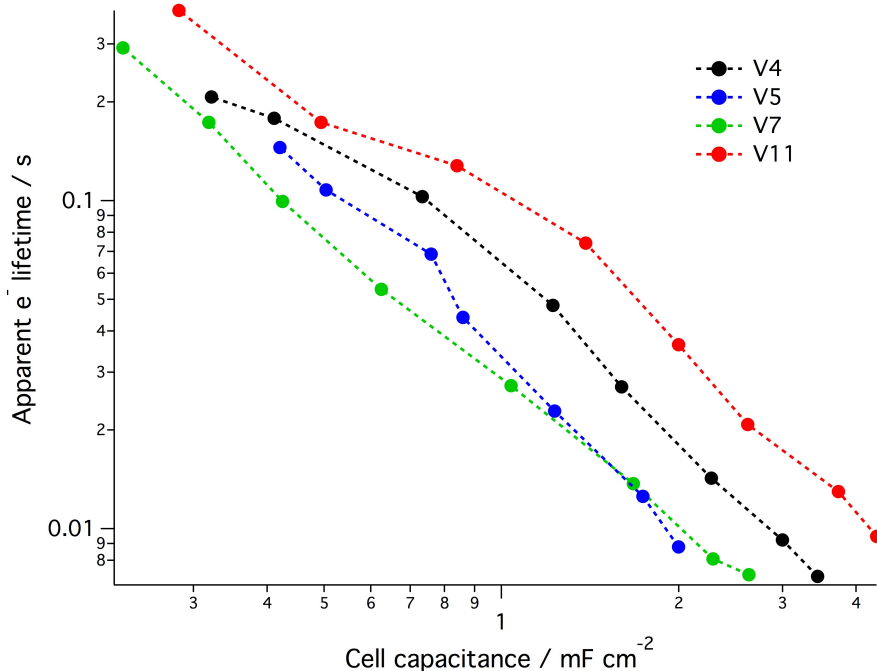


Figure 7.10: Apparent electron lifetimes as a function of cell capacitance for the devices sensitized with **V4**, **V5**, **V7** and **V11** dyes.

plots lie relatively close to each other, especially at the high capacitance conditions. Under these conditions the contribution of the recombination rate difference on the device V_{OC} is insignificant.

When compared the two dyes with CPDT as a spacer (**V4** and **V11**), the electronic properties of the interface remained unchanged – the devices sensitized with them exhibit similar capacitances and charge transfer resistances. One can conclude that the donor part of the dye is not affecting the nature of the interface and device performance. The molecules' structural units, like alkyl chains substituted on the chromophore of the CPDT, have more impact on the dye loading and conduction band edge position.

7.5 Conclusions

In this chapter I have gathered the studies performed on the D- π -A dyes with a phenothiazine unit as an electron donor where the π -bridge was consequently extended - starting from one double bond (**V5**), through the vinylthiophene (**V7**) to the alkyl-substituted cyclopentadithiophene unit (**V11**). The last dye was directly compared with another synthesized molecule (**V4**), because both molecules have the same π -bridge and acceptor part, differing only in the donor: phenothiazine vs. carbazole.

It has been shown, that gradual extending of the conjugated bridge enhances the optical properties of the molecules. First of all, a bathochromic shift of the peak of the absorption spectrum of the dyes is noticed (from 451 nm to 532 nm). Additionally, the molar extinction coefficient value has increased 4 times. After applying the dyes to DSCs it can be seen that the best performing molecule with phenothiazine donor is **V7**, yielding an efficiency of 7.44%. The **V7**-stained cells exhibited the largest photocurrent density, which originates from the broadest absorption spectrum. The IPCEs of these cells stretch up to 750 nm - at least 50 nm more than the other dyes in question. Having analysed the processes inside the cells by the means of transient techniques and EIS, one can clearly attribute the best efficiency among the phenothiazine dyes presented in this work to this particular feature of the dye. It was observed that the electron recombination rate in this case is high, which is manifested in the considerably lower V_{OC} . The augmented recombination processes are most probably

enhanced by the proximity of the sulphur on the thiophene unit to the TiO_2 surface. Sulphur atoms are thought to associate with triiodide and be responsible for its local concentration increase, resulting in higher probability of an electron being recaptured by the I_3^- . Thiophene unit in the **V7** dye at the TiO_2 /electrolyte interface has clearly an impact on the charge transfer resistance, as concluded from the EIS measurements. Lowered charge transfer resistance contributes to the significantly increased recombination rate, which can be further deduced from the comparison of the apparent electron lifetime plots. This phenomenon is accompanied by a slight downward shift of the conduction band of the TiO_2 for the **V7** cell. The cell-probing experiments explain very well the parameters that have been obtained from the J-V measurements.

V7-sensitized devices, in spite of great overall performance, suffered from the low V_{OC} . That is why a strategy of employing the state-of-the-art π -bridge unit was employed in the course of the project (molecule **V11**). CPDT unit with long alkyl chain proved to be efficient in shielding the TiO_2 surface and decreasing the recombination rate and simultaneously raising the conduction band edge upwards - effectively increasing the V_{OC} . In direct comparison of the two donors - carbazole and phenothiazine - attached to the exactly same core of the dye, the carbazole was shown to be slightly more efficient than the phenothiazine. The photovoltaic parameters are very similar for the devices sensitized with dyes **V11** and **V4**, which leads to the conclusion that in this case the donor part of the dye has insignificant influence on the overall performance of DSCs.

7.6 Bibliography

- [1] H. Tian, X. Yang, R. Chen, Y. Pan, L. Li, A. Hagfeldt and L. Sun, *Chemical Communications*, 2007, 3741–3743.
- [2] D. Kim, J. K. Lee, S. O. Kang and J. Ko, *Tetrahedron*, 2007, **63**, 1913–1922.
- [3] N. Koumura, Z.-S. Wang, S. Mori, M. Miyashita, E. Suzuki and K. Hara, *Journal of the American Chemical Society*, 2008, **128**, 14256–14257.
- [4] Z.-S. Wang, N. Koumura, Y. Cui, M. Takahashi, H. Sekiguchi, A. Mori, T. Kubo, A. Furube

-
- and K. Hara, *Chemistry of Materials*, 2008, **20**, 3993–4003.
- [5] W. Zhang, G. M. Ng, H. L. Tam, M. S. Wong and F. Zhu, *Journal of Polymer Science Part A: Polymer Chemistry*, 2011, **49**, 1865–1873.
- [6] N. Kopidakis, K. D. Benkstein, J. van de Lagemaat and A. J. Frank, *The Journal of Physical Chemistry B*, 2003, **107**, 11307–11315.
- [7] M. Wang, P. Chen, R. Humphry-Baker, S. M. Zakeeruddin and M. Grätzel, *ChemPhysChem*, 2009, **10**, 290–299.
- [8] M. Wang, X. Li, H. Lin, P. Pechy, S. M. Zakeeruddin and M. Grätzel, *Dalton Transactions*, 2009, 10015–10020.

8 Application of ionic liquids containing tricyanomethanide $[C(CN)_3]^-$ or tetracyanoborate $[B(CN)_4]^-$ anions in dye sensitized solar cells.

This part is adapted from a peer reviewed publication by Magdalena Marszalek, Zhaofu Fei, Dun-Ru Zhu, Rosario Scopelliti, Paul J. Dyson, Shaik M. Zakeeruddin and Michael Grätzel published in 2011 in Inorganic Chemistry, Vol. 50, pp 11561–11567

8.1 Introduction

Despite the on-going interest in ionic liquids (ILs)^{1–8}, the majority of the research is based on ILs containing a rather limited set of fluorine containing anions, notably tetrafluoroborate (BF_4^-), hexafluorophosphate (PF_6^-) and bis(trifluoromethylsulfonyl)imide (Tf_2N^-)⁹. In contrast, ILs based on non-fluorous anions, i.e. tricyanomethanide ($[C(CN)_3]^-$)^{10–12} and tetracyanoborate ($[B(CN)_4]^-$)^{13,14}, are somewhat under-explored. Indeed, it has been reported that ILs with $[C(CN)_3]^-$ and $[B(CN)_4]^-$ anions have low viscosities^{10,14}. For example, [EMI] $[C(CN)_3]$ (where EMI = 1-ethyl-3-methylimidazolium cation) has a viscosity of 18 cP at 22°C and a melting point of 11°C¹⁰ and [EMI] $[B(CN)_4]$ has a viscosity of 19 cP at 21°C¹⁴ both being lower than that of [EMI] $[Tf_2N]$, 27 cP at 20°C^{15,16}. N,N,N',N'-tetramethyl-N'',N''-dipentylguanidinium tricyanomethanide has a viscosity of 88 cP¹² the value being relatively low as in the case for this particular cation.

Chapter 8. Application of ionic liquids containing tricyanomethanide $[C(CN)_3]^-$ or tetracyanoborate $[B(CN)_4]^-$ anions in dye sensitized solar cells.

There is only a limited number of ILs that contain $[C(CN)_3]^-$ and $[B(CN)_4]^-$ anions and their applications have been scarcely explored, despite the high stability and interesting electrochemical and physicochemical properties of the $[B(CN)_4]^-$ anion^{17–20}. Indeed, in nearly all the applications, including electrolytes, as well as others^{21,22}, studies are almost exclusively conducted on the $[EMI]^+$ -based systems.

In this chapter the synthesis and characterization of a series of new ILs with $[C(CN)_3]^-$ and $[B(CN)_4]^-$ anions are described. The ionic liquids were characterized by NMR and IR spectroscopy and ESI-mass spectrometry, and their physical properties were investigated. Solid state structures of the N-propyl-N-methylpyrrolidinium and triethylpropylammonium tetracyanoborate salts were obtained by single crystal X-ray diffraction. The salts that are liquid at room temperature were evaluated as electrolyte additives in dye sensitized solar cells giving rise to efficiencies 7.35 and 7.85% under 100 and 10% Sun, respectively, in combination with the standard Z907 dye.

8.2 Synthesis and characterization of ionic liquids

8.2.1 Synthetic route

The preparation of ILs with BF_4^- , PF_6^- and Tf_2N^- anions is well established^{23–25}, whereas there are relatively few reports describing the synthesis of ILs with $[C(CN)_3]^-$ anions. Synthesis of ILs with $[B(CN)_4]^-$ anions is only covered in a patent and details of the anion exchange of the alkali metal salts of tetracyanoborate with imidazolium or pyridinium halides have not been reported¹³. In this work, we used a literature protocol to react 1-propyl-3-methylimidazolium chloride [PMI]Cl with $Na[C(CN)_3]$ in aqueous solution and the resulting IL, [PMI] $[C(CN)_3]$ (**1a**), was extracted with dichloromethane. Similarly, reaction of [PMI]Cl with $K[B(CN)_4]$ gives the IL [PMI] $[B(CN)_4]$ (**1b**). Using the same approach ILs containing N-propylpyridinium, N-propyl-N-methylpyrrolidinium and triethylpropylammonium cations with the $[C(CN)_3]^-$ anion **2a-4a** and the $[B(CN)_4]^-$ anion **2b-4b** were prepared (see Figure 8.1).

The $[C(CN)_3]^-$ containing ILs, **1a-4a**, are liquid at room temperature, whereas of the ILs containing the $[B(CN)_4]^-$ anion, i.e. **1b-4b**, only **1b** and **2b** are liquid at room temperature.

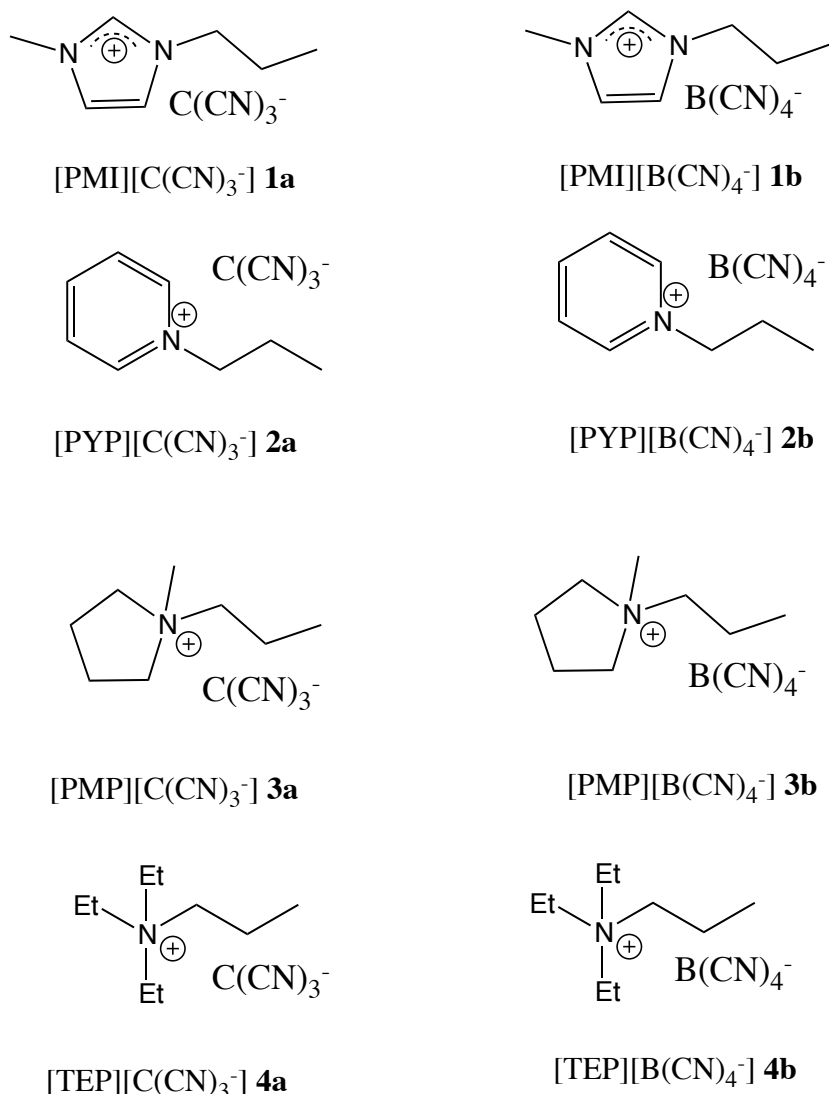


Figure 8.1: Structures and numbering scheme of the ionic liquids prepared in this study.

The 1H and ^{13}C NMR spectra of **1a-4a**, **1b** and **2b** are recorded as neat ILs in the absence of a co-solvent (only using a C_6D_6 capillary for external lock-in). Spectra of **3b** and **4b** were obtained in CD_2Cl_2 solution. In general, the signals do not differ much to those of the precursor salts – the variation being typical for ILs^{26,27}. The IR spectra of **1a-4a** contain absorptions between 2153 to 2164 cm^{-1} that correspond to the $C\equiv N$ bond; the absorptions lie in a rather smaller range compared to those observed in salts with metal cations²⁸⁻³¹. In **1b-4b** the absorptions of the CN group are observed at markedly higher wavenumbers (ca. 2222 cm^{-1}), and are significantly shifted from those containing metal cations which are found in the range 2250 to 2290 cm^{-1} ³²⁻³⁴, but nonetheless are close in value to those observed in tetrabutylammonium³⁵

Chapter 8. Application of ionic liquids containing tricyanomethanide $[C(CN)_3]^-$ or tetracyanoborate $[B(CN)_4]^-$ anions in dye sensitized solar cells.

and tetrabutylphosphonium³⁶ salts. It is known that the C≡N absorption in salts containing $[C(CN)_3]^-$ and $[B(CN)_4]^-$ anions are sensitive to the structure of the cations and is susceptible to $\pi \cdots \pi$ and/or $\pi \cdots H$ non-covalent interactions²⁸.

8.2.2 Crystallography

Although salts containing the tetracyanoborate anion were reported many years ago³⁷, the structure of simple lithium salt was reported only recently³⁸, followed by the structures of potassium³⁹, sodium, rubidium, cesium and ammonium³² salts, several transition metal salts^{33,34}, and somewhat more exotic salts⁴⁰. Single crystals of **3b** and **4b** were obtained by slow cooling from the liquid state from 110°C to room temperature over a period of 24 hours, and their structures were determined by X-ray diffraction. Data collection was performed on a KUMA CCD using graphite-monochromated Mo K α (0.71073 Å) radiation and a low temperature device [T = 140(2) K]. Data reduction was performed by CrysAlis RED⁴¹. The structure was solved with SHELX97⁴². Refinement was performed using the SHELX97 software package, and graphical representations of the structures were made with Diamond⁴³. The whole structure was solved by direct methods and successive interpretation of the difference Fourier maps, followed by full matrix least-squares refinement (against F^2). All non-hydrogen atoms were refined anisotropically. The contribution of the hydrogen atoms, in their calculated positions, was included in the refinement using a riding model. Relevant details for the structure refinements of **3b** and **4b** are listed in the Table 8.1.

Only very few salts with organic cations (e.g. tetrabutylphosphonium and tetrabutylammonium salts) have been reported^{35,36}, and the structures of **3b** and **4b** (Figure 8.2), represent the first examples of tetracyanoborate salts containing asymmetric cations. In **3b** and **4b** the anion adopts a nearly ideal tetrahedral structure with the C-B-C angles close to 109.4° and B-C-N angles close to 180°. The average C-N distance in the nitrile groups is 1.14 Å in **3b** and in **4b**, nearly the same as those observed in the lithium (1.14 Å)³⁸ and potassium (1.14 Å) salts³⁹. These values are in the range of found in the ammonium and phosphonium salts (1.141–1.143 Å)^{35,36}. In the crystal of **3b** the anions are connected by weak hydrogen bonds forming a C-H…N-C-B-C-N…H-C network (Figure 8.3). The D…A distances of the C-H…N hydrogen bonds range from 3.40 to 3.53 Å (Figure 8.3 and Table 8.2). These distances are rather longer

8.3. Photovoltaic application evaluation

Table 8.1: Crystal data and structure refinement details for **3b** and **4b**.

| empirical formula | C₁₂H₁₈BN₅ (3b) | C₁₃H₂₂BN₅ (4b) |
|--|--|--|
| fw | 243.12 | 259.17 |
| temperature / K | 140(2) | 140(2) |
| crystal size / mm ³ | 0.32 × 0.22 × 0.17 | 0.23 × 0.20 × 0.11 |
| crystal system | monoclinic | tetragonal |
| space group | P2 ₁ /c | P42(1)m |
| a / Å | 8.5730(17) | 11.9402(9) |
| b / Å | 16.777(3) | 11.9402(9) |
| c / Å | 9.822(2) | 5.5735(11) |
| β / deg | 94.74(3) | |
| V / Å ³ | 1407.9(5) | 794.60(18) |
| Z | 4 | 3 |
| D _{calc} / g cm ⁻³ | 1.147 | 1.083 |
| F (000) | 520 | 280 |
| abs coefficient / mm ⁻¹ | 0.072 | 0.067 |
| θ range / deg | 2.38–24.50 | 3.41–25.98 |
| h/k/l | -9, 9/-19, 19/0, 11 | -14, 14/-14, 14/-6, 6 |
| reflections collected | 2301 | 6902 |
| indexed reflections | 2301 [R _{int} =0.0] | 6902 [R _{int} =0.0447] |
| observed reflections | 1502 | 709 |
| data/restrained/parameters | 2301/0/165 | 833/0/57 |
| goodness-of-fit on F ² | 1.175 | 1.095 |
| R, wR indices [I>2σ(I)] | 0.0796, 0.2079 | 0.0494, 0.1142 |
| R, wR indices (all data) | 0.1225, 0.2315 | 0.0583, 0.1175 |
| largest difference peak and hole / e·Å ⁻³ | 0.225, -0.257 | 0.141, -0.107 |

than those that exist in series imidazolium salts with other anions such as Tf₂N⁻, BF₄⁻^{44,45}. The CH₃ group of the propyl substituent in **4b** is disordered, but hydrogen bonds are observed between CH₃ group of the ethyl substituents and the anion, with the shortest C-H···N-C distance being 2.638 Å.

8.3 Photovoltaic application evaluation

8.3.1 Electrolyte formulation and characterization

The room temperature ILs **1a/b**, **2a/b**, **3a** and **4a** were used to prepare electrolytes, and their viscosities and triiodide diffusion coefficients were determined. Finally, they were evaluated in dye sensitized solar cells following the procedure described for the standard eutectic

Chapter 8. Application of ionic liquids containing tricyanomethanide $[C(CN)_3]^-$ or tetracyanoborate $[B(CN)_4]^-$ anions in dye sensitized solar cells.

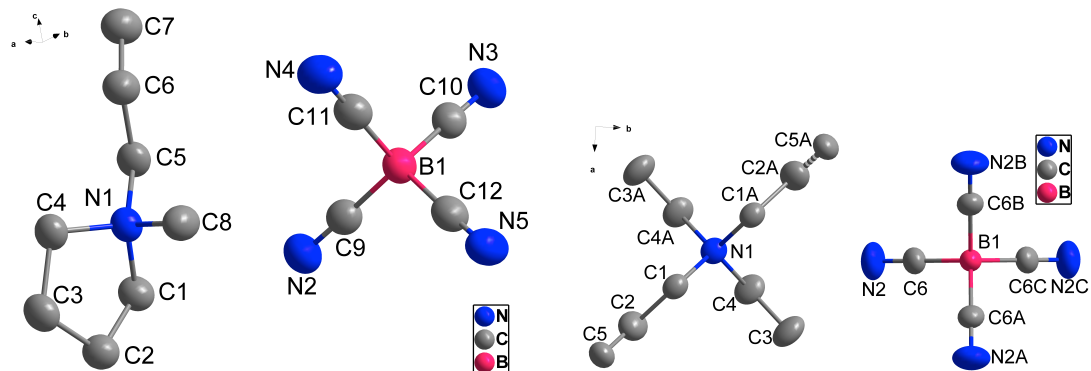


Figure 8.2: Solid state structures of **3b** (left) and **4b** (right) with the thermal ellipsoids at 50% probability; H atoms were omitted for clarity. Selected bond distances (\AA) and angles (deg). **3b** N(1)-C(5) 1.506(4), N(1)-C(1) 1.522(5), N(2)-C(9) 1.153(5), N(3)-C(10) 1.143 (5), B(1)-C(10) 1.590(6), B(1)-C(11) 1.594(7), C(10)-B(1)-C(11) 109.7(3), C(10)-B(1)-C(12) 108.7(3). **4b** N(1)-C(1) 1.518(3), N(1)-C(4) 1.522(3), N(2)-C(6) 1.143(2), B(1)-C(6) 1.5941(18), C(6)-B(1)-C(6A) 109.00(6).

Table 8.2: Principal hydrogen bond parameters in **3b**.

| D-H \cdots A | D-H | H \cdots A | D \cdots A | D-H \cdots A |
|---------------------------------|--------------|--------------|--------------|----------------|
| | \AA | \AA | \AA | deg |
| C4-H4B \cdots N5 ^a | 0.990 | 2.570 | 3.408(5) | 142.00 |
| C8-H8A \cdots N3 ^b | 0.980 | 2.560 | 3.536(5) | 171.00 |

^a Symmetry code: $x, 3/2-y, 1/2+z$. ^b Symmetry code: $-x, 1-y, -z$.

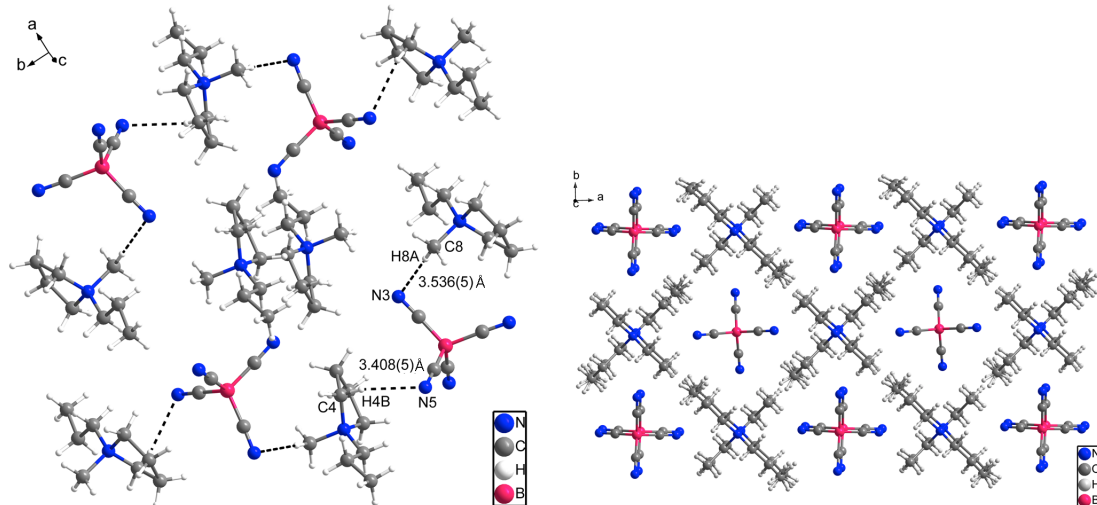


Figure 8.3: Crystal packing in **3b** (left) and **4b** (right).

melt electrolyte coded Z952²¹. For a more detailed picture, this state of the art eutectic ionic-liquid-based electrolyte was used as a model for further modifications. Its compo-

8.3. Photovoltaic application evaluation

sition comprises 1,3-dimethylimidazolium iodide ($[DMI][I]$)/1-ethyl-3-methylimidazolium iodide ($[EMI][I]$)/1-ethyl-3-methylimidazolium tetracyanoborate ($[EMI][B(CN)_4]$)/iodine/N-butylbenzimidazole/guanidinium thiocyanate (6:6:8:0.83:1.67:0.33). Essentially, the new ILs were incorporated into the electrolytes in place of 1-ethyl-3-methylimidazolium tetracyanoborate $[EMI][B(CN)_4]$ at the same molar ratio giving electrolytes termed **M-1a**, **M-1b**, **M-2a**, **M-2b**, **M-3a**, **M-4a**.

The electrolytes with $[C(CN)_3]^-$ are less viscous than their $[B(CN)_4]^-$ analogues (namely **M-1a** vs. **M-1b** and **M-2a** vs. **M-2b**). Diffusion coefficients of I_3^- were obtained by cyclic voltammetry and electrochemical impedance spectroscopy (EIS) performed on symmetric cells, and the results obtained by these two methods are shown in the Table 8.3. Electrolytes **M-1a** and **M-2a** have slightly higher triiodide diffusion coefficients presumably due to their lower viscosity.

Table 8.3: Comparison of the diffusion coefficients of I_3^- in electrolytes and their viscosities.^a

| Electrolyte | | M1-a | M2-a | M3-a | M1-b | M2-b |
|---|-----|------|------|------|------|------|
| $D_{I_3^-} / 10^{-7} \text{ cm}^2\text{s}^{-1}$ | CV | 2.51 | 2.27 | 3.42 | 2.39 | 2.09 |
| | EIS | 1.66 | 1.54 | 1.82 | 1.20 | 1.27 |
| Viscosity / cP at 20°C | | 49.8 | 49.4 | 59.1 | 56.5 | 53.0 |

^a Data for **M-4a** is not available because it is a quasi-solid substance.

8.3.2 Photovoltaic performance

The six new electrolytes have been formulated for use in DSCs in combination with Z907 dye as a sensitizer (Table 8.4). The best DSC contains the electrolyte **M-1a**, the open-circuit voltage (V_{OC}), short-circuit current density (J_{SC}), fill factor (FF) are 725 mV, 13.7 mAcm $^{-2}$ and 0.743, respectively, yielding an overall photoconversion efficiency (PCE) of 7.35% at full sunlight intensity. However, the PCE at 10% light intensity is as high as 7.85% due to diminished problems with diffusion connected with lower photocurrents under these light conditions. The J-V curves of the device with electrolyte **M-1a** are presented in the Figure 8.4. The incident photon-to-current efficiency (IPCE) of the device **M-1a** is shown in the inset of Figure 8.4. The maximum IPCE value at 550 nm is more than 70%. The DSCs exhibit rather linear performance with increasing intensity of irradiating light and only a small current drop (~5%) was noticed at 1 Sun presumably due to mass transport limitations of triiodide.

Chapter 8. Application of ionic liquids containing tricyanomethanide $[C(CN)_3]^-$ or tetracyanoborate $[B(CN)_4]^-$ anions in dye sensitized solar cells.

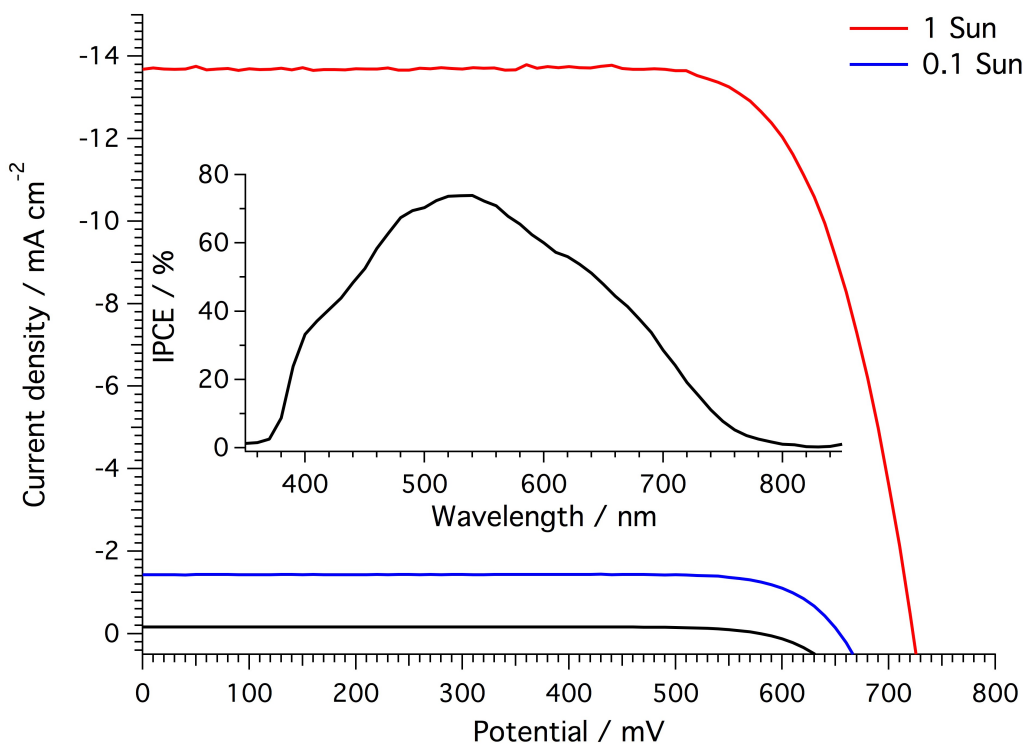


Figure 8.4: Current density-voltage characteristic of the device containing the electrolyte **M-1a** under various Sun intensity: 1 Sun (red), 0.1 Sun (blue) and in the dark (black). Incident photon-to-current conversion efficiency spectrum of the same cell (inset).

Table 8.4: Photovoltaic characteristics of the solar cells measured under AM 1.5G, 100% Sun and 10% Sun.

| Electrolyte | Sun intensity % | J_{SC} mA cm ⁻² | V_{OC} mV | Fill factor | η % |
|-------------|--------------------|---------------------------------|----------------|-------------|-------------|
| M-1a | 100 | 13.70 | 725 | 0.743 | 7.35 |
| | 10 | 1.43 | 655 | 0.802 | 7.85 |
| M-2a | 100 | 13.60 | 710 | 0.750 | 7.20 |
| | 10 | 1.41 | 645 | 0.797 | 7.60 |
| M-3a | 100 | 12.65 | 725 | 0.722 | 6.70 |
| | 10 | 1.32 | 655 | 0.798 | 7.20 |
| M-4a | 100 | 12.20 | 725 | 0.733 | 6.50 |
| | 10 | 1.36 | 660 | 0.806 | 7.50 |
| M-1b | 100 | 14.80 | 685 | 0.714 | 7.20 |
| | 10 | 1.54 | 620 | 0.779 | 7.70 |
| M-2b | 100 | 12.70 | 700 | 0.746 | 6.60 |
| | 10 | 1.36 | 635 | 0.805 | 7.25 |

8.3.3 Conduction band shift induced by the counter-anions in the electrolyte

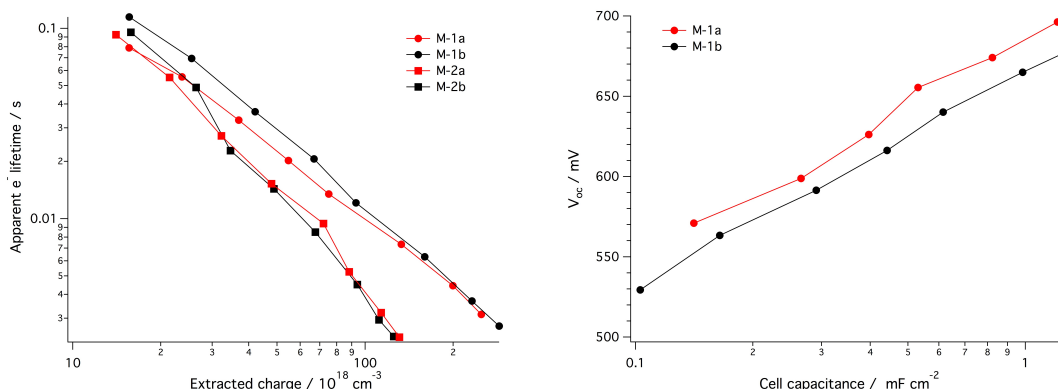


Figure 8.5: *Left:* Apparent electron lifetimes in DSCs with electrolytes **M-1a**, **M-1b**, **M-2a** and **M-2b**. The lines are only present to guide the eye. *Right:* The upward shift of the conduction band of TiO₂ induced by the different anions present in the electrolyte in a DSC.

There is a clear trend between the open circuit potential of the DSCs and the counteranion of the IL used in the electrolyte. Electrolytes containing the [C(CN)₃]⁻ anion exhibit higher V_{OC} values, by ~20 mV, compared to those with the [B(CN)₄]⁻ anion. We employed transient photovoltage decay measurements with different electrolytes to compare the rate of interfacial recombination of electrons from the TiO₂ conduction band to the oxidized form of the redox mediator, triiodide. In the Figure 8.5, left, the apparent electron lifetime calculated for cells with the different electrolytes is plotted against extracted charge, which provides a clearer comparison, because the difference between the quasi-Fermi level and the conduction band is kept constant for each measured point. The DSCs with electrolytes **1a**, **1b**, **2a** and **2b** were compared. It appears that the two anions, [C(CN)₃]⁻ and [B(CN)₄]⁻, do not influence the recombination rate, since the electron lifetimes for the cells with electrolytes sharing the same cation are practically identical. Nevertheless, the planar [C(CN)₃]⁻ anion⁴⁶ could potentially facilitate access to the TiO₂ surface as it could adsorb on it more easily than the tetrahedral [B(CN)₄]⁻ anion³⁹. Indeed, a more detailed comparison between the [B(CN)₄]⁻ and dicyanoamide, [N(CN)₂]⁻, anions has been reported⁴⁷. It was found that [N(CN)₂]⁻ containing electrolytes have higher open circuit potential than [B(CN)₄]⁻ based electrolytes, and this difference was ascribed to suppressed interfacial charge-transfer behaviour in addition to an increase in the conduction band edge position of TiO₂ due to the surface interaction with the [N(CN)₂]⁻ anion. While we did not observe similar differences in the recombination rates

the specific adsorption of $[\text{C}(\text{CN})_3]^-$ may be responsible for the upward shift of the conduction band of TiO_2 , especially as this difference corresponds very well with the difference between V_{OC} of the devices (Figure 8.5, right) at a given density of states.

8.4 Conclusions

In conclusion, we have prepared and characterized a series of new fluorous-free ILs containing imidazolium, pyridinium, pyrrolidinium and ammonium cations and $[\text{C}(\text{CN})_3]^-$ and $[\text{B}(\text{CN})_4]^-$ anions. These ILs were evaluated as electrolyte components in dye-sensitized solar cells, and the influence of the anion was found to be negligible, giving comparable results to those containing Tf_2N anions. Nevertheless, these results are likely to generate increased interest in ILs containing these anions.

8.5 Bibliography

- [1] K. R. Seddon, *Journal of Chemical Technology and Biotechnology*, 1997, **68**, 351–356.
- [2] T. Welton, *Chemical Reviews*, 1999, **99**, 2071–2084.
- [3] P. Wasserscheid and W. Keim, *Angewandte Chemie International Edition*, 2000, **39**, 3772–3789.
- [4] P. J. Dyson, *Applied Organometallic Chemistry*, 2002, **16**, 495–500.
- [5] J. Dupont, R. F. de Souza and P. A. Z. Suarez, *Chemical Reviews*, 2002, **102**, 3667–3692.
- [6] C. Chiappe and D. Pieraccini, *Journal of Physical Organic Chemistry*, 2005, **18**, 275–297.
- [7] Z. Fei, T. J. Gelbach, D. Zhao and P. J. Dyson, *Chemistry – A European Journal*, 2006, **12**, 2122–2130.
- [8] P. Migowski and J. Dupont, *Chemistry – A European Journal*, 2006, **13**, 32–39.
- [9] H. Xue, R. Verma and J. M. Shreeve, *Journal of Fluorine Chemistry*, 2006, **127**, 159–176.
- [10] Y. Yoshida, K. Muroi, A. Otsuka, G. Saito, M. Takahashi and T. Yoko, *Inorganic Chemistry*, 2004, **43**, 1458–1462.
- [11] P. Wang, B. Wenger, R. Humphry-Baker, J.-E. Moser, J. Teuscher, W. Kantlehner, J. Mezger, E. V. Stoyanov, S. M. Zakeeruddin and M. Grätzel, *Journal of the American Chemical Society*, 2005, **127**, 6850–6856.

-
- [12] P. Wang, S. Zakeeruddin, M. Grätzel, W. Kantlehner, J. Mezger, E. Stoyanov and O. Scherr, *Applied Physics A*, 2004, **79**, 73–77.
 - [13] U. Welz-Biermann, N. Ignatyev, E. Bernhardt, M. Finze and H. Willner, *Patent WO 2004/072089 A1*, Merck gmbh technical report, 2004.
 - [14] D. Kuang, P. Wang, S. Ito, S. M. Zakeeruddin and M. Grätzel, *Journal of the American Chemical Society*, 2006, **128**, 7732–7733.
 - [15] J. G. Huddleston, A. E. Visser, W. M. Reichert, H. D. Willauer, G. A. Broker and R. D. Rogers, *Green Chemistry*, 2001, **3**, 156–164.
 - [16] A. B. McEwen, H. L. Ngo, K. LeCompte and J. L. Goldman, *Journal of The Electrochemical Society*, 1999, **146**, 1687–1695.
 - [17] J. Tong, Q.-S. Liu, Y.-X. Kong, D.-W. Fang, U. Welz-Biermann and J.-Z. Yang, *Journal of Chemical and Engineering Data*, 2010, **55**, 3693–3696.
 - [18] D. Kuang, S. Uchida, R. Humphry-Baker, S. M. Zakeeruddin and M. Grätzel, *Angewandte Chemie International Edition*, 2008, **47**, 1923–1927.
 - [19] Y. Bai, Y. Cao, J. Zhang, M. Wang, R. Li, P. Wang, S. M. Zakeeruddin and M. Grätzel, *Nature Materials*, 2008, **7**, 626–630.
 - [20] D. Kuang, C. Klein, Z. Zhang, S. Ito, J.-E. Moser, S. M. Zakeeruddin and M. Grätzel, *Small*, 2007, **3**, 2094–2102.
 - [21] Z. Lei, B. Chen and C. Li, *Chemical Engineering Science*, 2007, **62**, 3940–3950.
 - [22] Pei-Fang, Y. M. Yang, X.-M. Liu, C. Wang, Z.-C. Tan and U. Welz-Biermann, *The Journal of Chemical Thermodynamics*, 2010, **42**, 817–822.
 - [23] M. J. Z. J. S. Wilkes, *Chemical Communications*, 1992, 965.
 - [24] P. A. Suarez, J. E. Dullius, S. Einloft, R. F. D. Souza and J. Dupont, *Polyhedron*, 1996, **15**, 1217–1219.
 - [25] P. Bonhôte, A.-P. Dias, N. Papageorgiou, K. Kalyanasundaram and M. Grätzel, *Inorganic Chemistry*, 1996, **35**, 1168–1178.
 - [26] F. Mazille, Z. Fei, D. Kuang, D. Zhao, S. M. Zakeeruddin, M. Grätzel and P. J. Dyson, *Inorganic Chemistry*, 2006, **45**, 1585–1590.

-
- [27] H. Brand, J. F. Liebman, A. Schulz, P. Mayer and A. Villinger, *European Journal of Inorganic Chemistry*, 2006, **2006**, 4294–4308.
- [28] J. H. Enemark and R. H. Holm, *Inorganic Chemistry*, 1964, **3**, 1516–1521.
- [29] F. A. Miller and W. K. Baer, *Spectrochimica Acta*, 1963, **19**, 73–84.
- [30] P. Andersen, B. Klewe and E. Thom, *Acta Chemica Scandinavica*, 1967, **21**, 1530–1542.
- [31] J. Witt and D. Britton, *Acta Crystallographica*, 1971, **B27**, 1835.
- [32] T. Küppers, E. Bernhardt, H. Willner, H. W. Rohm and M. Köckerling, *Inorganic Chemistry*, 2005, **44**, 1015–1022.
- [33] M. Neukirch, S. Tragl, H.-J. Meyer, T. Küppers and H. Willner, *Zeitschrift für anorganische und allgemeine Chemie*, 2006, **632**, 939–944.
- [34] C. Nitschke and M. Köckerling, *Zeitschrift für anorganische und allgemeine Chemie*, 2009, **635**, 503–507.
- [35] E. Bernhardt, G. Henkel and H. Willner, *Zeitschrift für anorganische und allgemeine Chemie*, 2000, **626**, 560–568.
- [36] A. Flemming, M. Hoffmann and M. Köckerling, *Zeitschrift für anorganische und allgemeine Chemie*, 2010, **636**, 562–568.
- [37] E. Bessler and J. Goubeau, *Zeitschrift für anorganische und allgemeine Chemie*, 1967, **352**, 67–76.
- [38] D. Williams, B. Pleune, J. Kouvetsakis, M. D. Williams and R. A. Andersen, *Journal of the American Chemical Society*, 2000, **122**, 7735–7741.
- [39] T. Küppers, M. Köckerling, and H. Willner, *Zeitschrift für anorganische und allgemeine Chemie*, 2007, **633**, 280–284.
- [40] K. Koppe, H.-J. Frohn, H. P. A. Mercier and G. J. Schrobilgen, *Inorganic Chemistry*, 2008, **47**, 3205–3217.
- [41] A. J. M. Duisenberg, L. M. J. Kroon-Batenburg and A. M. M. Schreurs, *Journal of Applied Crystallography*, 2003, **36**, 220–229.
- [42] M. Sheldrick, *SHELX-97*, Universität Göttingen, Göttingen, Germany, 1997.
- [43] L. J. Farrugia, *Journal of Applied Crystallography*, 1997, **30**, 565.

-
- [44] A. R. Choudhury, N. Winterton, A. Steiner, A. I. Cooper and K. A. Johnson, *Journal of the American Chemical Society*, 2005, **127**, 16792–16793.
 - [45] A. R. Choudhury, N. Winterton, A. Steiner, A. I. Cooper and K. A. Johnson, *CrystEngComm*, 2006, **8**, 742–745.
 - [46] K. W. Hipps and A. T. Aplin, *The Journal of Physical Chemistry*, 1985, **89**, 5459–5464.
 - [47] M. Zhang, J. Zhang, Y. Bai, Y. Wang, M. Su and P. Wang, *Physical Chemistry Chemical Physics*, 2011, **13**, 3788–3794.

9 Summary and final conclusions

The work presented within the scope of this thesis revolves around one of the most exciting and blooming 3rd generation photovoltaic systems - dye-sensitized solar cells. The technology, which is already entering the worldwide markets via companies like Sony, Dyesol-Tata, Solaronix, DyeTec Solar, Fujikura, g2e or G24i, is being constantly improved and optimized at the laboratory level. A DSC, which is a successful marriage of various materials, has to be studied simultaneously at very different angles, because a small change in one component has a non-negligible influence on the others.

Undoubtedly, the most extensively developing area is the dye design and synthesis. At the time this work was commenced, ruthenium sensitizers were dominating the field: in 2009 B11 dye giving 11.5% was published¹, surpassed in 2010 by C106 dye, reaching 12.1%². A cell of 1 cm² was fabricated by Sharp and certified at AIST, Japan (The National Institute of Advanced Industrial Science and Technology), giving the efficiency of 11.9%³. Parallelly, the purely organic sensitizers, utilizing D- π -A concept, were being developed - having the advantage of much larger freedom in the choice of the building blocks of the molecule. C219 dye, presented in 2009, yielded the efficiency of 10.0–10.3%⁴, but was then outperformed by the porphyrin dye YD-2 with 11% power conversion efficiency⁵. All above-mentioned records were achieved using electrolytes with iodide/triiodide redox couple and so are the systems that were the subjects of this thesis. In the ocean of countless possibilities for the design of dyes it is of crucial importance to understand the role of particular building blocks: donor, acceptor, π -conjugated bridge and the modifications introduced to them. As discussed in

Chapter 9. Summary and final conclusions

the respective chapters, valuable contributions to deeper understanding of dye design and application for DSCs could be stated briefly:

- **The use of benzothiadiazole (BTDA) unit in the π -bridge** is not trivial. The incorporation of this building block in the D- π -A molecule causes a desired bathochromic shift in the absorption spectrum. Nevertheless, the flat structure induced by the fused 6- and 5-membered rings close to the anchoring group results in an unusually fast recombination of the dye cation with the electrons previously injected in the TiO_2 . In order to ensure unidirectional electron flow from the excited state of the dye to the conduction band of TiO_2 , an out-of-plane torsion was introduced with a phenyl unit in between the BTDA and the anchoring group. This improvement granted the generation of a remarkably high current density (18.47 mA cm^{-2}) and power conversion efficiency of 8.21%, as compared with $3.40\text{ mA cm}^{-2} J_{SC}$ and η of 1.24% for the dye with BTDA attached directly to the anchoring group. It constitutes a very clear evidence of how much care has to be taken while designing dyes and which interactions within the molecule itself and at the sensitized interface can be influenced by the structure of the sensitizer. This concept was implemented already in a few molecules bearing porphyrin units. Especially in these cases BTDA proves to be very useful, because it fills in the absorption dip in the green region, while still stretching the spectrum into the red.
- **Preventing aggregation of the D-A- π -A dye containing BTDA** was realized by the introduction of hexyl chains on the π -bridge. This time the electron-accepting BTDA unit was placed next to the indoline donor, efficiently spaced from the anchoring group by bithiophene. π - π stacking of such molecules led to aggregation and, in order to achieve reasonable efficiencies (8.56%), an addition of coadsorbent was a necessity. Grafting a hexyl chain on one of the thiophenes allowed for obtaining similar efficiencies with much enhanced V_{OC} - a sign of reduced recombination rate. Inherent anti-aggregation ability and more freedom in the use of solvent are the advantages of the modified D-A- π -A molecule **WS-9**.
- **Exploring new donor unit - phenothiazine** - along with the study on the extending π -conjugated bridge. Starting from a very simple molecule with only a double bond between donor and acceptor, it was found that reasonable efficiencies (6.5%) can be

achieved. Absorption spectrum of the phenothiazine dyes was gradually extended by modification of the π -bridge with thiophene and cyclopentadithiophene and led to the significance increase in current density and η of 7.44%. This result is purely attributed to the broad absorption spectrum of molecule V7 reaching up to 750 nm.

- **Bianchoring dyes with exTTF donors** were investigated as a continuation of study on dyes with minimal driving force required for the regeneration⁶. The effect of employing a second anchoring group with either benzene or EDOT was studied first on the geometry of the dye via theoretical calculations, then the adsorption mode on TiO₂ and finally the photovoltaic performance. It was found - both, theoretically and experimentally - that in these cases the dyes favour the conformation that allows for anchoring with two carboxylic groups. This would definitely improve the stability of the molecule attached to the semiconductor surface. However, the choice of spacer groups (particularly EDOT) could affect the overall performance, by increasing the recombination rate. The concept of bianchors is not used very widely, however, it was proven that when applied correctly it inhibits the dye desorption⁷. Nevertheless, the electronic structure of the dye has to be taken into consideration while implementing a second anchor, because the widely spreading LUMO level covering both anchoring groups may not be very beneficial for unidirectional electron transfer, and this may explain rather short electron lifetimes. Probably if one of the groups would be electronically cut off from the charge-transfer path - serving purely as the attaching unit, it would help to make the LUMO more centralized on the other one, hopefully leading to a higher number of the electrons efficiently injected in the conduction band (higher current density and higher quasi-Fermi level directly related to V_{OC}).

As mentioned above, dye-sensitized solar cell is a combination of different materials and as a device can be studied at different angles of interests. Apart from high efficiency and low fabrication costs, stability is of the highest importance when one wants to shift from laboratory samples to a real market product. Implementation of ionic liquids as easy-to-handle, non-volatile electrolytes reached its peak interest after the introduction of binary eutectic melts in 2008⁸. Following this successful attempt a **series of ionic liquids with tricyanomethanide and tetracyanoborate anions with various cations was synthesized in**

Chapter 9. Summary and final conclusions

order to replace 1-ethyl-3-methylimidazolium tetracyanoborate. The electrolytes with tricyanomethanide were less viscous than the ones with tetracyanoborate and yielded better photovoltaic performance, unfortunately, at the expense of slightly lower stability. There was no influence of the anion exchange on the recombination rate, however, tricyanomethanide anion is believed to adsorb easier on TiO₂ surface and consequently raise its conduction band edge. Similar observations were also published on dicyanoamide anion employed in ionic-liquid based electrolyte⁹.

The research in DSC field is going on parallelly on many different tracks: semiconductor nanostructures, light absorbing materials, redox mediators and hole transporting materials, and - last but not least - developing theories and new methods of investigation to shed brighter light on the physical phenomena occurring in the cells. It should be made obvious, that one cannot progress fast without understanding the fundamentals of processes within the device. In the constant race for the highest efficiency it is worth to spend a while on trying to solve the problems which at first glance may not directly be related with realisation the ideal champion DSC. Nevertheless, the answers found during these investigations will certainly help to develop new strategies or concepts, which later can be combined with the state-of-the-art in order to continue the progress. While investigating, it should never be forgotten to look at the system from different perspectives or at various levels or scales: each cell's component should be carefully tailored, but what is of major importance, is the essence of the DSC system - the interfaces between the materials.

After 4 years of study and gaining experience in the dye-sensitized photovoltaics I stay strong in my opinion that this field still has a lot of potential and should be explored deeper. During my PhD stay I witnessed two major paradigm shifts: successful use of cobalt-based redox mediators in combination with porphyrin dye leading to the new record efficiency¹⁰ and the employment of hybrid organic-inorganic light absorber¹¹ - perovskite - which established the efficiency record¹² for both, conventional electrolyte containing and solid-state devices. I believe that the last word has not been said yet.

9.1 Bibliography

- [1] C.-Y. Chen, M. Wang, J.-Y. Li, N. Pootrakulchote, L. Alibabaei, C. ha Ngoc-le, J.-D. Decoppet, J.-H. Tsai, C. Grätzel, C.-G. Wu, S. M. Zakeeruddin and M. Grätzel, *ACS NANO*, 2009, **3**, 3103–3109.
- [2] Q. Yu, Y. Wang, Z. Yi, N. Zu, J. Zhang, M. Zhang and P. Wang, *ACS NANO*, 2010, **4**, 6032–6038.
- [3] M. A. Green, K. Emery, Y. Hishikawa, W. Warta and E. D. Dunlop, *Progress in Photovoltaics: Research and Applications*, 2012, **21**, 1–11.
- [4] W. Zeng, Y. Cao, Y. Bai, Y. Wang, Y. Shi, M. Zhang, F. Wang, C. Pan and P. Wang, *Chemistry of Materials*, 2010, **22**, 1915–1925.
- [5] T. Bessho, S. Zakeeruddin, C.-Y. Yeh, E.-G. Diau and M. Grätzel, *Angewandte Chemie International Edition*, 2010, **49**, 6646–6649.
- [6] S. Wenger, P.-A. Bouit, Q. Chen, J. Teuscher, D. D. Censo, R. Humphry-Baker, J.-E. Moser, J. L. Delgado, N. Martín, S. M. Zakeeruddin and M. Grätzel, *Journal of the American Chemical Society*, 2010, **132**, 5164–5169.
- [7] M. García-Iglesias, J.-H. Yum, R. Humphry-Baker, S. M. Zakeeruddin, P. Pechy, P. Vazquez, E. Palomares, M. Grätzel, M. K. Nazeeruddin and T. Torres, *Chemical Science*, 2011, **2**, 1145–1150.
- [8] Y. Bai, Y. Cao, J. Zhang, M. Wang, R. Li, P. Wang, S. M. Zakeeruddin and M. Grätzel, *Nature Materials*, 2008, **7**, 626–630.
- [9] M. Zhang, J. Zhang, Y. Bai, Y. Wang, M. Su and P. Wang, *Physical Chemistry Chemical Physics*, 2011, **13**, 3788–3794.
- [10] A. Yella, H.-W. Lee, H. N. Tsao, C. Yi, A. K. Chandiran, M. Nazeeruddin, E. W.-G. Diau, C.-Y. Yeh, S. M. Zakeeruddin and M. Grätzel, *Science*, 2011, **334**, 629–634.
- [11] M. M. Lee, J. Teuscher, T. Miyasaka, T. N. Murakami and H. J. Snaith, *Science*, 2012, **338**, 643–646.
- [12] J. Burschka, N. Pellet, S.-J. Moon, R. Humphry-Baker, P. Gao, M. K. Nazeeruddin and M. Grätzel, *Nature*, 2013, submitted.

Acknowledgements

I came to Lausanne 5 years ago to work with dye-sensitized solar cells. An Erasmus exchange stay turned into a full 4-year-long doctorate and resulted in the work you are reading. During all these years I receive a lot of support and so many positive emotions that I could never imagine. My gratitude towards all people accompanying me in my scientific journey is endless and cannot be fully express with words. I will try, however, taking into consideration my love for writing, this part may grow even longer than the thesis itself. Allow me for just briefly mentioning the most important people involved - although you all know how much I really, really owe you and how much I love you indeed.

This thesis would not have been done, if Professor Michael Grätzel once did not agree for me to come to EPFL. Thank you for letting me be a part of DSC history. For sharing a huge passion for science, inspiring and explaining problems with such simplicity. Many, many thanks go to my co-advisor, Dr Shaik M. Zakeeruddin for always keeping me busy, showering with million diverse projects, which allowed me to learn different aspects of DSC. I am grateful to both of you for the freedom you gave me while I was doing my research and fruitful, eye-opening discussions at the moments

It took me around a year to gather enough courage to talk to Dr Robin Humphry-Baker. And ever since I did, whenever I came to Robin with *just one question*, I would always leave with 10 more. But questions are the driving force for science and I thank you for them. I also thank you for sharing your enormously broad knowledge, your endless patience – especially during proofreading this piece of work – and this unique sense of humour. You taught me all the basics, transients and how to use almost all of the equipment we have. You made me and *IgorPro* best friends. You are my favourite kind of scientist – thank you!

I want to say *vielen Dank* to Dr Thomas Moehl for his constant support, believing in me,

Acknowledgements

cheering me up and reminding me that I am capable of doing all this. I will never forget my first encounter with the glovebox and you were laughing pretty hard because of my clumsiness and shaky hands, and me wearing high heels. You showed me that impedance spectroscopy is not a black magic (sometimes it still is, though) and was never annoyed with my persisting problems with electrochemical setup. Herzlichen Dank!

I spent loads of time in our labs, but it would not be so much fun if it were not for the people I had the pleasure to meet and collaborate with. Thank you, former and present LPI members, and also the numerous visitors, for the absolutely unique atmosphere! Special thanks go to Nuttapol, Dr Pootrakulchote, who showed me how to assemble my first cell. But even this one would not be done without the countless TiO₂ layers provided by the one and only Master Pascal, who was also very kind to share some of his precious tips on screen-printing – merci beaucoup, Pascal! I also appreciate very, very much the help and kindness from Marie and Jacky from the magasin and from Gaby, Supardi, Harald and Grégoire from the electronic workshop - merci! I am truly grateful to three wonderful ladies dealing with all the administration: Madame Gonthier, Madame Gourdou and Madame Odegaard. I cannot forget about four charming Messieurs, who were trying very hard to *convince* me to speak French: Pierre, Fred, Jean-David and Manuel - I still have to work on that, mais c'était toujours un plaisir de discuter avec vous! Davide, truly a renaissance man, thank you so much for all the help with electrochemistry, but also for discussions about music and being the most awesome piano teacher ever! Last, but not least I want to thank Fabienne from CIME, who patiently spent many hours training me on HR-SEM – I hope you will be proud of me one day!

This thesis is a result of the numerous international collaborations. I particularly want to thank Prof. Peter Bäuerle and his group at the Universität Ulm (Dr Stephan Haid, cheers!), Prof. He Tian and Prof. Weihong Zhu and the group at the East China University of Science and Technology, Prof. Nazario Martin and his group at Universidad Complutense de Madrid, Dr Enrique Ortí and Dr Rafael Viruela from Universitat de Valencia, Dr Vincent Paul and his group at the National Chemical Laboratory in Pune, Prof. Paul Dyson and Dr Zhaofu Fei and their group at EPFL, Prof. Jacques-Edouard Moser and his group at EPFL and Prof. Thomas Bein and his group at Ludwig-Maximilians-Universität in Munich (Dr Johann Szeifert, cheers!).

I was extremely lucky to be placed in the best office ever – CH B2 424. It felt like home, not only because of the big fridge. Francine, Jun-Ho and Julian - you are my second family, I love you so much. Thank you for making my stay here so awesome. I know you have been through

Acknowledgements

a lot: my constant talking and mood swings especially during the final stage of my doctorate. Thank you for not complaining about the music I was playing all the time and being the guinea pigs for my pastries. Francine, merci especially for helping me to sort out everyday problems. Jun-Ho – I am endlessly indebt to you for saving my life you know when, but I also thank you for being always – always – helpful. Julian, danke for all this time we spent working and talking till super late hours (until you were starving!). I cannot forget about Rebecca, who was a wonderful officemate and still is a friend. I always missed our girlie chats – with Julian it was not the same :)!

In addition to all scientific discussions and numerous hours spent in the labs, lunches, coffee breaks and just hanging out are the essentials of the daily university life. They would extend to BBQs, international food dinners, raclettes, games' sessions and many others exciting events and adventures, involving wonderful people: Aswani, Aravind, Amalie, Stephan, Nok, Rebecca, Sandy, Ines, Nuttapol, Takeru, Soo-Jin and Ji-Ah, Mateusz, Morgan and Julia, Fabrizio, Andrea, Michelle, and many others. Special thanks go to my "welcoming committee": Julian, Simon - the Master of Potions, Lauren and Tom. Good job :)!

I honestly would not survive this period without my friends and family. And skype, whatsapp and chats. I felt your support despite the distance all the time. Dominika, Marta, Kasia i Eryk, Darek, Justynka, Pan Sekwoja – thanks for all the awesome Polish parties and loads of fun. Ania – first in Lausanne, than in Cambridge – you were always there to remind me why I am here, always there to listen about my crazy life stories, and you are my best travelling buddy (A bientôt à Paris!). My family of engineers from Cracow whenever I went there, always made me feel like I had never left. You are so special, I missed you all the time: Michał, Ola, Ada, Kasia Makówka i Adam, Agatka, Mały i Marta, Jacuś i Diana, Natalia, Marcin, Dawid and all the others. Old times, good times!

Special thanks go to the emergency hot-lines: Ania, Dominika and Michał – I love you, you are the best, you kept me sane. This is precious.

I have to thank my sister Agata for constantly pointing out that I am too nerdy. Love you, lil'sis.

Mamo, Tato - kocham Was bardzo. Dziękuję Wam, że zawsze we mnie wierzyliście i pozwalaliście mi wierzyć, że mogę spełnić wszystkie moje marzenia.

Magdalena Anna Marszałek

Born 4th June 1985 in Świdnik, Poland

marszalekmagda@gmail.com

skype: madziulek_m

Education

Jul 2009 – Jul 2013

PhD in Chemistry and Chemical Engineering

Ecole Polytechnique Fédérale de Lausanne (EPFL),
Switzerland

Thesis title: “*Dye-sensitized Solar Cells: Detailed studies focused on the molecular engineering of D-π-A dyes and the optimization of the application of ionic-liquid based electrolytes*” under the supervision of Prof. Michael Grätzel and Dr Shaik M. Zakeeruddin.

Courses: Artificial Photosynthesis, Experimental methods in physics I, Experimental methods in physics II, Photochemistry II, Scientific writing, Intensive TEM and SEM training course

Teaching: Organic chemistry for Biotechnologists (1st year B.Sc.), Chemistry Laboratory for Physicists (1st year B.Sc.)

Oct 2004 – Jun 2009

M. Sc. Engineering in Materials Science,

GPA 5/5, rank 1

The Jagiellonian University (UJ), Cracow, Poland

Dissertation title: “*Photoelectrochemistry of semiconducting composites containing organic and organometallic electron donors*” under the supervision of Prof. Konrad Szaciłowski.

President of the Materials Engineering Society UJ

- Organised a conference for Materials Science students
- Arranged the financial support and coordinated the projects of the members of the association
- Wrote scientific articles for the brochures aimed at non-academics published by the Society

Member of Students' Self Government UJ and the Physics Faculty Council UJ, Class Representative

- Actively participated in creating the new study curriculum

- Organised the timetables and exam schedules for students
- Served as an official link between the students and professors/administration
- Participated actively in the annual Science Fairs with experiments demonstrations

Achievements & Awards

- The Award of the Polish Ministry of Science and Higher Education for outstanding grades and achievements (2008)
- The University Award for the best GPA (UJ, Cracow) (4 consecutive years 2005 – 2008)
- Erasmus scholarship (September 2008 – February 2009) at EPFL, Switzerland (established a connection between the universities – UJ and EPFL)

Skills & Competences

Languages

- Polish: native
- English: fluent (C2)
- French: intermediate (B1/B2)
- German: intermediate (B1/B2)

Research tools

- Fabrication and characterization of solar cells (JV characteristics, IPCE, transient techniques)
- Electrochemical Impedance Spectroscopy
- Electrochemical characterization of materials (CV, DPV)
- UV-Vis spectroscopy, fluorescence spectroscopy, time-correlated single photon counting
- Scanning Electron Microscopy (+ High Resolution), Transmission Electron Microscopy
- Classical piano (Music School Diploma)

Music

List of publications

1. **Structural variations of D-π-A dyes influence on the photovoltaic performance of dye-sensitized solar cells.**
M. Marszalek, S. Nagane, A. Ichake, R. Humphry-Baker, V. Paul, S. M. Zakeeruddin and M. Grätzel
RSC Advances, vol. 3, pp 7921-7927, 2013

2. **A structural study of DPP-based sensitizers for DSC applications.**
T.W. Holcombe, J.-H. Yum, J. Yoon, P. Gao, M. Marszalek, D. Di Censo, K. Rakstys, M. K. Nazeeruddin and M. Grätzel
Chemical Communications, vol. 48, num. 87, pp. 10724—10726, 2012
3. **High conversion-efficiency organic dye-sensitized solar cells: molecular engineering on D-A- π -A featured organic indoline dyes.**
Y. Wu, M. Marszalek, S. M. Zakeeruddin, Q. Zhang, H. Tian, M. Grätzel, and W. Zhu
Energy & Environmental Science, vol. 5, num. 8, pp. 8261—8272, 2012
4. **Donor- π -Acceptors containing the 10-(1,3-dithiol-2-ylidene)anthracene unit for dye-sensitized solar cells.**
P.-A. Bouit, M. Marszalek, R. Humphry-Baker, R. Viruela, E. Orti, S. M. Zakeeruddin, M. Grätzel, J. L. Delgado and N. Martin
Chemistry – A European Journal, vol. 18, num. 37, pp. 11621—11629, 2012
5. **Influence of the anchoring modes on the electronic and photovoltaic properties of D- π -A dyes.**
M. Katono, T. Bessho, M. Wielopolski, M. Marszalek, J.-E. Moser, R. Humphry-Baker, S. M. Zakeeruddin and M. Grätzel
The Journal of Physical Chemistry C, vol. 116, num. 32, pp. 16876—16884, 2012
6. **Significant improvement of dye-sensitized solar cell performance by small structural modification in π -conjugated donor-acceptor dyes.**
S. Haid, M. Marszalek, A. Mishra, M. Wielopolski, J. Teuscher, J.-E. Moser, R. Humphry-Baker, S. M. Zakeeruddin, M. Grätzel and P. Bäuerle
Advanced Functional Materials, vol. 22, num. 6, pp. 1291—1302, 2012
7. **Tuning spectral properties of phenothiazine based donor- π -acceptor dyes for efficient dye-sensitized solar cells.**
M. Marszalek, S. Nagane, A. Ichake, R. Humphry-Baker, V. Paul, S. M. Zakeeruddin and M. Grätzel
Journal of Materials Chemistry, vol. 22, pp. 889-894, 2012
8. **Application of ionic liquids containing tricyanomethanide $[C(CN)_3]^-$ or tetracyanoborate $[B(CN)_4]^-$ anions in dye-sensitized solar cells.**
M. Marszalek, Z. Fei, D.-R. Zhu, R. Scopelliti, P. J. Dyson, S. M. Zakeeruddin and M. Grätzel
Inorganic Chemistry, vol. 50, pp. 11561—11567, 2011
9. **Optimization of distyryl-Bodipy chromophores for efficient panchromatic sensitization in dye-sensitized solar cells.**
S. Kolemen, O. A. Bozdemir, Y. Cakmak, G. Barin, S. Erten-Ela, M. Marszalek,

J.-H. Yum, S. M. Zakeeruddin, M.K. Nazeeruddin, M- Grätzel and E. U. Akkaya
Chemical Science, vol. 2, pp. 949—954, 2011

10. **Synthesis, characterization and photovoltaic properties of novel molecules based on triarylamine dyes.**

S. Erten-Ela, M. Marszalek, S. Tekoglu, M. Can and S. Icli
Current Applied Physics, vol. 10, pp. 749—756, 2010